TESIS DE LA UNIVERSIDAD DE ZARAGOZA

2023

47

Álvaro Artiga Folch

Gold nanoparticles and chitosan encapsulation for therapy and sensing

Director/es

Martínez de la Fuente, Jesús

Mitchell, Scott G.

ISSN 2254-7606

Prensas de la Universidad Universidad Zaragoza

ISSN 2254-7606

Universidad Zaragoza
1542

Tesis Doctoral

GOLD NANOPARTICLES AND CHITOSAN ENCAPSULATION FOR THERAPY AND SENSING

Autor

Álvaro Artiga Folch

Director/es

Martínez de la Fuente, Jesús
Mitchell, Scott G.

UNIVERSIDAD DE ZARAGOZA
Escuela de Doctorado

Programa de Doctorado en Bioquímica y Biología Molecular

2020

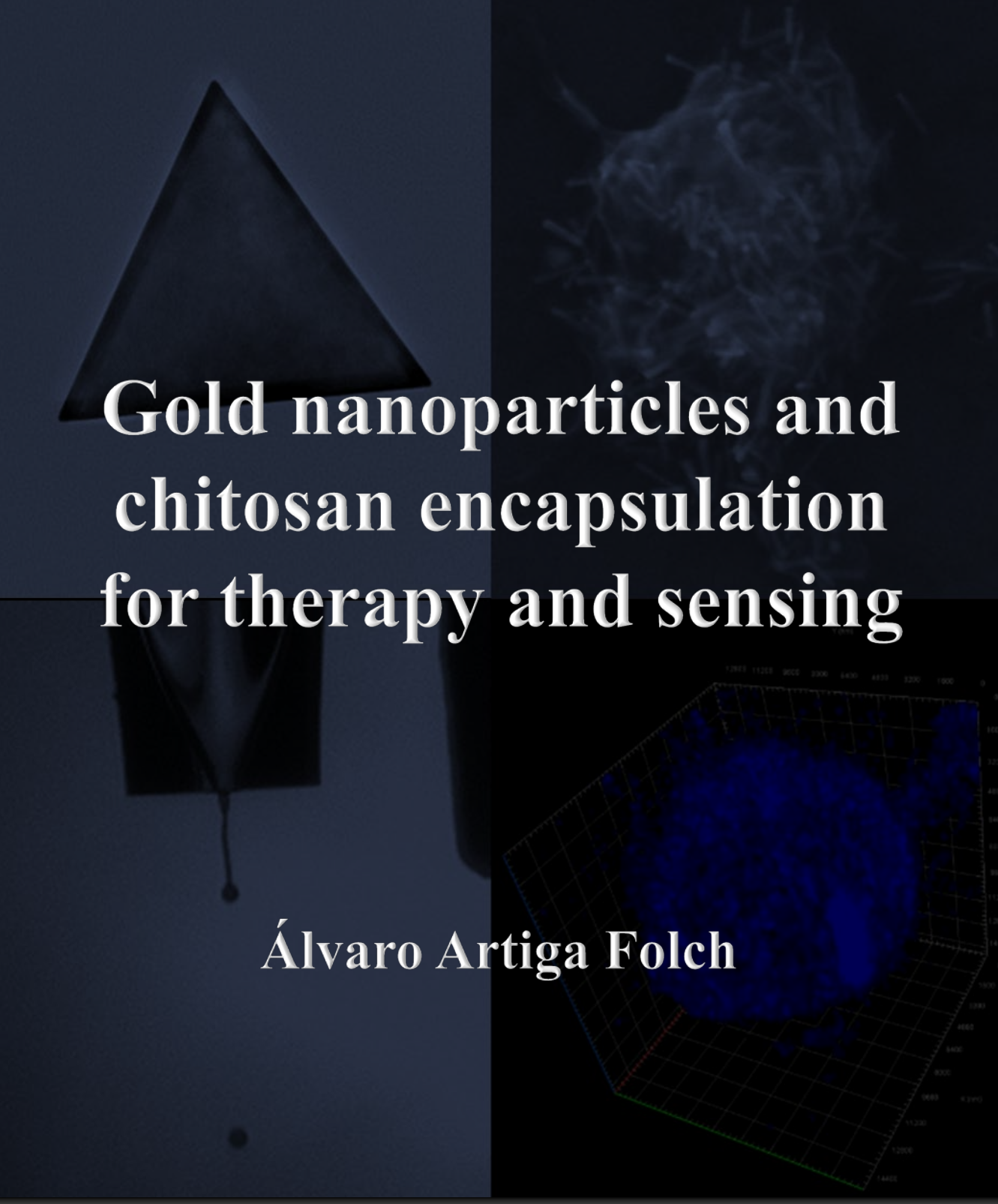

Gold nanoparticles and chitosan encapsulation for therapy and sensing

Álvaro Artiga Folch

Universidad Zaragoza
1542

INMA
INSTITUTO DE NANOCIENCIA Y MATERIALES DE ARAGÓN

CSIC
CONSEJO SUPERIOR DE INVESTIGACIONES CIENTÍFICAS

Gold nanoparticles and chitosan encapsulation for therapy and sensing

Memoria presentada para optar al grado de Doctor por la Universidad de Zaragoza

Álvaro Artiga Folch

Directores:

Jesús Martínez de la Fuente

Scott G. Mitchell

Universidad Zaragoza 1542

INMA INSTITUTO DE NANOCIENCIA Y MATERIALES DE ARAGÓN

CSIC Consejo Superior de Investigaciones Científicas

Programa de Doctorado en Bioquímica y Biología Molecular

Zaragoza 2020

D. Jesús Martínez de la Fuente, Profesor de Investigación del grupo de Biofuncionalización de Nanopartículas y Superficies del Instituto de Nanociencia y Materiales de Aragón del CSIC/Universidad de Zaragoza, y D. Scott George Mitchell, Científico Titular del mismo grupo de investigación

INFORMAN:

Que Álvaro Artiga Folch, graduado en Biotecnología y con título de Máster en Materiales Nanoestructurados para Aplicaciones Nanotecnológicas, ha realizado en el grupo de Biofuncionalización de Nanopartículas y Superficies del Instituto de Nanociencia y Materiales de Aragón bajo su dirección el trabajo descrito en la presente memoria, que lleva por título “Gold nanoparticles and chitosan encapsulation for therapy and sensing”, y que presenta para optar al grado de Doctor.

Zaragoza, 2020

Prof. Jesús Martínez de la Fuente

Dr. Scott George Mitchell

Agradecimientos

Además de gracias al programa FPU por el apoyo económico, esta tesis jamás habría sido posible sin la ayuda y colaboración de una larga lista de personas que merecen un gran reconocimiento.

En primer lugar, me gustaría agradecer la posibilidad que me han dado todos los colaboradores que se describen a lo largo de la tesis de poder trabajar junto a ellos. He aprendido mucho de ellos y según mi experiencia la ciencia mejora considerablemente cuando se trabaja en equipo y además se disfruta más. En particular me gustaría destacar a Renzo y Andrea por toda la ayuda y el apoyo durante mi estancia doctoral en Milán y a Carlos Sánchez por su confianza, sus enseñanzas y por tener su puerta siempre abierta para mí.

Pero gran parte de esta tesis se la debo a las personas que forman y han formado parte del grupo Bionanosurf, que durante estos años han sido para mí un equipo inmejorable no solo en el ámbito profesional sino también en el personal:

A Scott, jamás podré agradecerte lo suficiente como te mereces todo lo que me has ayudado, enseñado y confiado en mí (muchas veces incluso más que yo mismo), por todo el tiempo que te he hecho perder y por estar ahí cuando te he necesitado. A Jesús, por todas las oportunidades, enseñanzas y buenos consejos que me has dado y sobre todo por la gran confianza que has depositado en mí. A Mari Carmen, porque además de hacer uno de los trabajos más importantes del grupo siempre nos cuidas todo lo que puedes. A Laura de Matteis y María Moros por todo lo que he aprendido de vosotras y vuestra ética del trabajo, cada una con vuestro estilo. A Valeria, Raluca, Lucía, Rafa, Laura Asín, Elena y Andrés por toda la ayuda siempre que la he necesitado y el buen ejemplo que nos dais. A Rafi, por todo lo que hemos aprendido juntos trabajando codo con codo como equipo Oro, por tantísimos buenos ratos y por estar siempre dispuesto a echarme una mano dentro y fuera del laboratorio. A Sonia, por todas

las risas y buenos momentos, pero también por tus ideas y ayuda y por estar ahí siempre que te necesito. A Inés por todos los buenos ratos, pero también por los retos que nos han tocado afrontar juntos, siempre con una sonrisa y sacando lo mejor posible de cada situación. A Bea y a Lili, junto al resto de los compañeros de mi despacho, gracias por todo el tiempo de calidad que hemos pasado juntos, los viajes, experiencias, ratos increíbles y el apoyo que nos hemos dado unos a otros en los momentos más complicados. A María Pequeña e Isa por vuestro optimismo y por todas las veces que me hacéis reír, dentro y fuera del laboratorio. A Alba, Silvia, Francesca, Marcos, Vito, Héctor, Lou, David y y gran parte de los ya nombrados por todas las cervezas, tardes y noches de futbolín, juepintxos, cenas, conciertos y demás grandes momentos que han hecho que estos años mereciesen tanto la pena. A Fran por ser el mejor pupilo que he tenido nunca. Y a Regina, Zsuzsa, Ilaria, Gabi, Edu, Yilian, Bea T., Iñigo, Vanesa, Graz, Xabi, Eva, Arantxa, Sara R., Yulán, Carlos, Alfredo, que junto al resto de gente que ha formado parte de nuestro grupo, habéis sido responsables del gran ambiente que se respira en el laboratorio y de que el día a día sea mucho más ameno. Gracias a todos vosotros, que habéis hecho que estos años de doctorado sean una muy buena experiencia para mí que no cambiaría nunca.

Laura, una parte de esta tesis también te la debo a ti, por todas las veces que me soportas y me animas, por hacer que mi vida sea mucho más feliz y por estar ahí cuando te necesito, siempre apoyándome. No creo que pudiese haberlo conseguido sin ti.

Y sobre todo esta tesis se la debo a mis padres, que siempre habéis sido para mí un ejemplo de esfuerzo e integridad, y junto a mis hermanos siempre me habéis dado el apoyo, la libertad, la educación y los ánimos necesarios para intentar hacer con mi vida lo que creía mejor y afrontar cualquier reto que me propusiese.

Table of contents

Publications

The following articles and communications were published as a result of research undertaken over the course of this PhD programme:

(9) "*Rational design of chitosan nanocapsules as gold nanoparticle carriers for gastrointestinal protection and enhanced cellular internalisation"*

I. Serrano-Sevilla[§], **Á. Artiga**[§], L. De Matteis, Y. Hernández, S. G. Mitchell, & J. M. de la Fuente*,* 2020**,** *(In Preparation).*

(8) '*Inkjet-based technology for microencapsulation of gold nanoparticles within biocompatible hydrogels*'

Á. Artiga, F. Ramos-Sánchez, I. Serrano, L. De Matteis, S. G. Mitchell, C. Sánchez-Somolinos & J. M. de la Fuente, *Particle & Particle Systems Characterization*, 2020, 37, 2000026 (Back Cover)

(7) *'Surfactant-free synthesis and scalable purification of triangular gold nanoprisms with low non-specific cellular uptake'*

R. Ramirez-Jimenez, **Á. Artiga**, S. G. Mitchell, R. Martín-Rapún & J. M. de la Fuente, *Nanomaterials*, 2020, 10(3), 539.

(6) '*In vivo comparison of the biodistribution and long-term fate of colloids – gold nanoprisms and nanorods – with minimum surface modification*'

G. Alfranca, L. Beola, L. Gutiérrez, A. Zhang, **Á. Artiga**, D. Cui & J. M. de la Fuente, *Nanomedicine*, 2019, 14(23), 3035.

(5) '*A simple and universal enzyme-free approach for the detection of multiple microRNAs using a single nanostructured enhancer of surface plasmon resonance imaging'*

A. Sguassero[§], **Á. Artiga**[§], C. Morasso, R. Ramirez-Jimenez, R. Martín Rapún, R. Mancuso, S. Agostini, A. Hernis, A. Abols, A. Linē, A. Gualerzi, S. Picciolini, M. Bedoni, M. Rovaris, F. Gramatica, J. M. de la Fuente & R. Vanna, *Anal Bioanal Chem*, 2019, 411, 1873.

(4) '*Current status and future perspectives of gold nanoparticle vectors for siRNA delivery*'

Á. Artiga, I. Serrano, L. De Matteis, S. G. Mitchell, J. M. de la Fuente, *J. Mater. Chem. B*, 2019, 7, 876.

(3) '*Natural Polysaccharides for siRNA Delivery: Nanocarriers Based on Chitosan, Hyaluronic Acid, and Their Derivatives*'

I. Serrano-Sevilla, **Á. Artiga**, S. G. Mitchell, L. De Matteis, J. M. de la Fuente, *Molecules*, 2019, 24, 2570.

(2) '*Effective in Vitro Photokilling by Cell-Adhesive Gold Nanorods*'

Á. Artiga[§], S. García-Embid[§], L. De Matteis, S. G. Mitchell & J. M. de la Fuente, *Front. Chem.* 2018, 6, 234.

(1) '*Gold Nanoprism-Nanorod Face Off: Comparing heating efficiency, cellular internalisation and thermoablation capacity*'

G. Alfranca[§], **Á. Artiga**[§], G. Stepien, M. Moros, S. G. Mitchell & J. M. de la Fuente, *Nanomedicine* 2016, 11, 2903-2916**.**

[§]Both authors contributed equally to this work

Collaborations

I would like to acknowledge the collaborative research that has contributed to this doctoral thesis. Specifically, I would like to thank:

- **Dr. Renzo Vanna** and **Andrea Sguassero** for teaching me how to use the SPRi methodology during my doctoral stay in Milan and for helping to analyze the SPRi results (**Section 3.1.1**).

- **Rafael Ramírez Jiménez** for synthesizing some of the AuNPs employed for SPRi comparison (**Section 3.1.2**).

- **Dr. Gabriel Alfranca Ramón** for teaching me about AuNR synthesis and PTT and for paving the way with the AuNP-mediated PTT proof-of-concept studies (**Section 3.2.1**)

- **Dr. Catherine Berry** and **Dr. Anil P. Patel** for the complementary PTT results in 3D cancer cell models (**Section 3.2.1**).

- **Sonia García Embid** for teaching us how to encapsulate AuNRs in chitosan (**Section 3.2.2**).

- **Dr. Carlos Sánchez Somolinos** for showing me how to use the inkjet and for open access to his inkjet set-up (**Section 3.3**).

- **Laura Comas Calmet** and **Dr. Julián Pardo** for the *in vivo* studies of our microcapsules for oral administration in mice (**Section 3.3.9**).

Abbreviations

Abbreviation	Complete name
3D	Three-dimensional
Ab	Antibody
ABTS	2,2'-azino-bis(3-ethylbenzothiazoline-6-sulfonic acid)
AuNP	Gold nanoparticle
AuNPr	Gold nanoprism
AuNR	Gold nanorod
AuNR@CS	Chitosan hydrogel nanocontainer containing AuNRs
AuNS	Gold nanosphere
AuNS@Neutrav	Gold nanospheres functionalised with neutravidin
B-AuNS	Big-size gold nanospheres
BSA	Bovine serum albumin
CCD	Charged Coupled Device
CS	Chitosan
CTAB	Cetyltrimethylammonium bromide
DAPI	4′,6-diamidino-2-phenylindole
DNA	Deoxyribonucleic acid
DLS	Dynamic light scattering
DMEM	Dulbecco's Modified Eagle Medium
DMSO	Dimethyl sulfoxide
DOD	Drop-on-demand
DPBS	Dulbecco's Phosphate Buffered Saline
DTNB	5,5'-dithio-bis(2-nitrobenzoic) acid
EDC	1-ethyl-3-(3-dimethylaminopropyl) carbodiimide
EU	European Union
FDA	Food and Drug Administration
FTIR	Fourier transform infrared
HPLC	High-performance liquid chromatography
HRP	Horseradish peroxidase
ICTs	Information and communication technologies
ICP	Inductively coupled plasma
ICP-AES	Inductively coupled plasma atomic emission spectroscopy
ICP-MS	Inductively coupled plasma mass spectrometry

LED	Light-emitting diodes
LOD	Limit of detection
LSPR	Localised surface plasmon resonance
MES	2-(N-morpholino)ethanesulfonic acid
miRNA	MicroRNAs
mRNA	Messenger RNA
MS	Multiple sclerosis
MTT	3-(4,5-dimethylthiazol-2-yl)-2,5-diphenyltetrazolium bromide
NIR	Near-Infrared
NP	Nanoparticle
OD	Optical density
PB	Phosphate buffer
PBS	Phosphate-buffered saline
PCR	Polymerase chain reaction
PEG	Poly(ethylene glycol)
PMA	Phosphomolybdic acid
POM	Polyoxometalate
PTA	Phosphotungstic acid
PTT	Photothermal therapy
QCM	Quartz crystal microbalances
q-PCR	Quantitative polymerase chain reaction
ReS	SPR response signal units
RNA	Ribonucleic acid
RT	Room temperature
RT-PCR	Real time PCR
S-AuNS	Small-size gold nanospheres
SD	Standard deviation
SEM	Scanning electron microscope
SERS	Surface-enhanced Raman scattering
siRNA	Small interfering RNA
SPR	Surface plasmon resonance
SPRi	Surface plasmon resonance imaging
sulfo-NHS	Sulfo-N-hydroxysuccinimide
TBE	Tris-borate-ethylenediaminetetraacetic acid
TCEP	Tris(2-carboxyethyl) phosphine
TEM	Transmission electron microscopy

TPP	Tripolyphosphate
UV	Ultraviolet
UV-vis	Ultraviolet-visible
WT	Wild-type
ε	Extinction coefficient

Abstract

The application of gold nanoparticles (AuNPs) to the biomedical field is generally framed around the myriad of different applications that would benefit from their incorporation. However, in contrast to the thousands of publications that highlight every year the fantastic potential of AuNPs in the biomedical fields, their real-world application remains scarce, especially for therapeutic purposes in clinical environment. The main objective of this thesis rests on improving the applicability of gold nanoparticles to the biomedical sector by two action lines: 1) the study of the physicochemical properties of different AuNP shapes related with their performance in biosensing and photothermal therapy applications and 2) the search for a complementary manner to improve their inherent properties for therapeutic applications by their entrapment in chitosan hydrogels. In the first part of this thesis, the lack of a suitable clinical methodology for the detection of miRNA led us to pursue new strategies for their detection using AuNPs as signal enhancers due to its highly adequate properties: high density, proper size and easiness for functionalisation with proteins. In addition, the comparative study of different AuNP shapes and different strategies of biofunctionalisation for their interaction with the miRNA are carried out to discover its suitability for a clinical setting miRNA detection. In a second part of the study we continue with the comparative study of different AuNP shapes for photothermal therapy, focusing on its optical properties, cell interaction and effectiveness motivated by the lack of knowledge about AuNP shape importance for this topic. Thanks to the conclusions extracted from this study concerning the low cell internalisation of AuNRs, we propose an innovative strategy entrapping the AuNRs in chitosan hydrogel due to the cell-adhesive chitosan properties which results in a remarkably improvement of the AuNRs efficacy. Finally, a novel methodology for entrapping AuNPs in chitosan hydrogels based on the automatic inkjet technology is developed to improve the encapsulation methodology, which makes the

process more scalable, effective and controllable. This methodology offers a continuous automatic production technology for chitosan microcapsules containing AuNPs providing materials with interesting properties for biomedical applications. As a result, the research carried out as part of this doctoral thesis contributes to strengthen our understanding of the importance of different AuNP shapes for sensing and therapeutic applications, while simultaneously providing new tools to increase their applicability through surface functionalization and entrapment in chitosan hydrogels.

Resumen

Un sinfín de aplicaciones en el campo de la biomedicina se verían beneficiadas por el futuro uso de nanopartículas de oro (AuNPs). Sin embargo, a pesar de las miles de publicaciones científicas que destacan cada año las fabulosas propiedades de estas nanopartículas en este área, su empleo más allá del ámbito científico es testimonial, especialmente cuando hablamos de su uso con finalidades terapéuticas en el ámbito clínico. El objetivo principal de esta tesis consiste en mejorar la aplicabilidad de las nanopartículas de oro con diferentes geometrías mediante dos líneas de acción: 1) el estudio de la relación entre sus propiedades fisicoquímicas y su rendimiento para las aplicaciones de bio-detección y terapia fototérmica y 2) la búsqueda de una manera complementaria de mejorar sus propiedades intrínsecas para aplicaciones terapéuticas mediante su encapsulación en hidrogeles de quitosano. En la primera parte de esta tesis la inexistencia de una metodología clínica adecuada para la detección de miRNA nos ha llevado a buscar nuevas estrategias para su detección mediante el empleo de nanopartículas de oro como amplificadores de la señal de detección gracias a sus idóneas propiedades: elevada densidad, tamaño adecuado y facilidad para su funcionalización con diferentes proteínas. Además, para descubrir su utilidad en la detección de miRNA en condiciones similares a las necesarias en el ámbito clínico, se ha llevado a cabo un estudio comparativo empleando nanopartículas de oro con diversas geometrías y diferentes estrategias de biofuncionalización para su interacción con los miRNA. En la segunda parte de esta tesis se ha continuado con el estudio de la aplicación de diferentes geometrías de nanopartículas de oro para su uso en terapia fototérmica, centrándonos en sus propiedades ópticas, su interacción celular y eficacia, ya que hay una falta de conocimiento acerca de la importancia que tiene la forma de las nanopartículas en este tema. Gracias a las conclusiones extraídas durante este estudio concernientes a la baja internalización celular de los nanorods, hemos propuesto una estrategia innovadora consiste en su

encapsulación en hidrogeles de quitosano motivada por las propiedades de adhesión celular del quitosano que han permitido una mejora remarcable de su eficacia. Finalmente se ha desarrollado una nueva metodología para la encapsulación de nanopartículas de oro en hidrogeles de quitosano empleando la tecnología de eyección automática de tinta o inkjet para mejorar su encapsulación, la cual permite que el proceso sea más fácil de escalar, efectivo y controlable. Esta tecnología ofrece una metodología automática para la producción continua de microcápsulas de quitosano que contengan las nanopartículas de oro en su interior, proporcionando biomateriales con propiedades muy interesante para las aplicaciones biomédicas. Como resultado, la investigación llevada a cabo durante esta tesis doctoral contribuye a ampliar nuestro conocimiento en la importancia del empleo de diferentes geometrías de nanopartículas de oro para las aplicaciones terapéuticas y de detección a la vez que proporciona nuevas herramientas para aumentar su aplicabilidad gracias a la funcionalización de su superficie y a su encapsulación en hidrogeles de quitosano.

1. Introduction

1.1. Biomedical applications of nanoparticles

Over the last few decades, the importance of nanotechnology in our daily lives has increased exponentially. Although nanotechnological advances remain at an early stage of development in comparison with original predictions,[1–3] nanotechnology is already in the market in a wide range of fields as diverse as information and communications technology (ICTs), vehicles, biotechnology, aerospace, the food industry, medical and pharmaceutics, textile, cosmetics, entertainment, construction, energy, catalysis and military.[4,5] However, when talking about nanotechnology appearance in the market, the costumers should pay attention to differentiate products where nanomaterials have been employed as a strategy to attract consumers and enhance the perception of value from those where nanotechnology is really improving the properties of the materials. Because at the nanoscale, when one of its dimensions is reduced between 1 and 100 nm, the behaviour of nanomaterials is different than the macroscopic one due to their reduced dimensions, degree of arrangement or interaction between particles which results in novel or improved physicochemical properties (optical, magnetic, electric, structural, etc.).[6,7] One particular advantage of the dimensions and properties of nanomaterials is their unique ability to interact at the same size scale with most types of biomolecules essential for life and replication: proteins, nucleic acids, carbohydrates and lipids (see **Figure 1**).[7] This advantage is of interest mainly in nanoparticles, which are particles made of a large variety of materials with sizes in the nanoscale. This fact combined with their improved physicochemical properties offers a new world of possibilities in the biomedical field.

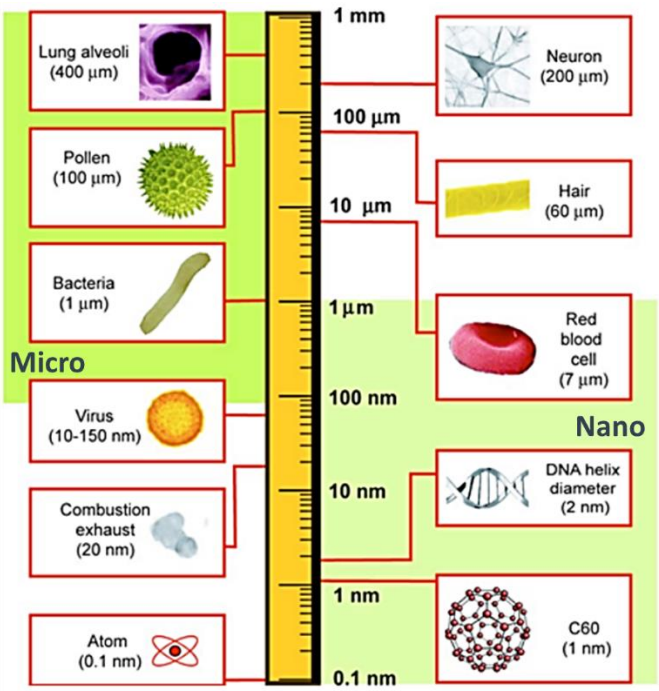

Figure 1. Comparative size scale of different biological elements in the micro and nanoscale. Adapted with permission from[8]

Nanotechnology for biomedical applications, sometimes indistinguishable from the term nanobiotechnology that appeared in the literature in 1995, is revolutionizing the research in the biomedical field.[9] Althought some researchers have insisted in the languisihing of nanomedicine research, on the contrary, innovative nanotechnology-based products are developed as fundamental knowledge about this topic is expanded, as recently highlighted by the Nanomedicine and Nanoscale Delivery Focus Group of the Controlled Release Society.[10] Nanoparticles have noteworthy applications in biomedicine, particularly in diagnostics, drug delivery systems, prostheses and implants.[11] The most commonly employed nanoparticles in the biomedical field includes polymeric, lipid, metallic and other inorganic materials like metal oxides, among others.[12,13] Each nanoparticle poses specific properties that make them useful for different applications. For example, polymeric and lipid nanoparticles are commonly

employed for drug delivery and several of these nanocarriers are already approved by Food and Drug Administration (FDA).[14] Also other types of nanoparticles (NPs) have been approved for treatment, including several hydroxyapatite NPs for bone substitution and several iron oxide NPs for iron deficiency and as imaging agents.[15] In Europe, the Commission of the European Communities has been working on the regulation of nanomaterials in relation to health, safety, environment, research and related measures (see for example communication COM(2008) 366 for more details) and around 15 clinical trials involving nanoparticles have been already registered in the EU Clinical Trials Register. These clinical trials are mainly focused on cancer treatment employing lipid-based, polymeric, magnetic, gold and protein-based nanoparticles.

Apart from their physicochemical properties, the potential application of nanoparticles for biomedical applications increases dramatically when they are combined with biomolecules that provide a specific biological function. Using this approach several functionalities can be added to the nanoparticles to work in a synergistic way, increasing the effectiveness, efficiency and range of applications where these nanoparticles can be of great utility. Such new functionalities can confer properties that allow the nanoparticles to interact and detect specific compounds (for sensing applications) or to direct drugs and/or biomolecules to desired locations (for co-delivery treatments), among others (see **Figure 2**). A large list of biomolecules can be linked to the nanoparticles by an extensive number of methodologies and strategies,[16–18] mainly by the use of polymers that can be linked to the nanomaterial and to the molecule of interest. By this way, nanoparticles can be surface-functionalised with a large list of useful ligands including small molecules (such as drugs and vitamins), lipids, sugars, peptides, fluorophores as well as larger biomolecules like nucleic acids (DNA or RNA), antibodies and cell signalling proteins.[17]

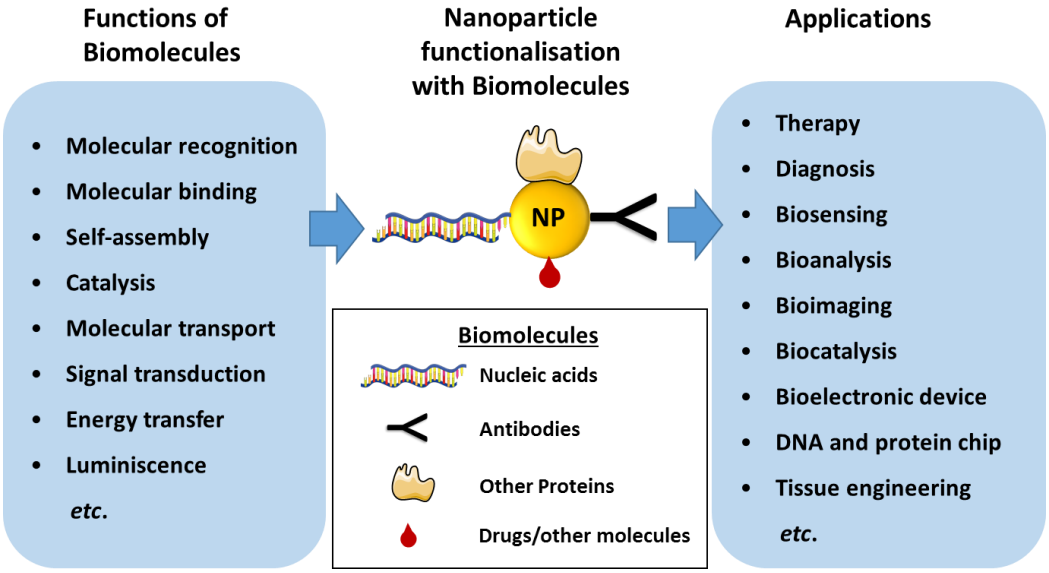

Figure 2. Overview of different biomolecule functions that can be employed to improve nanoparticle properties and their subsequent application in the biomedical field.[19]

From all of the nanoparticles employed for biomedical applications, gold nanoparticles (AuNPs) stand out due to their unique optical properties and their relative inertness and corresponding biocompatibility coupled with the ability to control their size, shape and surface functionalisation on the nano and molecular level, in contrast to other inorganic carriers such as silica nanoparticles, iron oxide nanoparticles and quantum dots.[20] Gold nanoparticles (AuNPs) have shown promising results in a wide-variety of biomedical applications. However, if anything can be derived from the vast amount of literature on the subject it is that there is no universal AuNP for biomedical applications.[20] In contrast, one of the principle advantages of using AuNPs is that they can be engineered specifically for the desired application by the design of the most appropriate size and shape. These are the primary considerations that should be taken into account for AuNP-mediated biomedicines, which will be discussed in detail in the following sections.

1.2. Shape-controlled synthesis of AuNPs

One of the major advantages of employing AuNPs is the vast knowledge concerning the synthesis of different shapes of AuNPs. Although Faraday carried out the first documented studies on gold colloid synthesis in 1857,[21] the previous two decades have witnessed an exponential increase in the number of publications and nowadays thousands of scientific papers concerning gold nanoparticle synthesis are published each year. This exponential increase in the interest of the scientific community is highly related with the development of AuNPs with different shapes (see **Figure 3**). These variety of shapes allow to increase the functionalities and applications where the AuNPs can be of great interest.

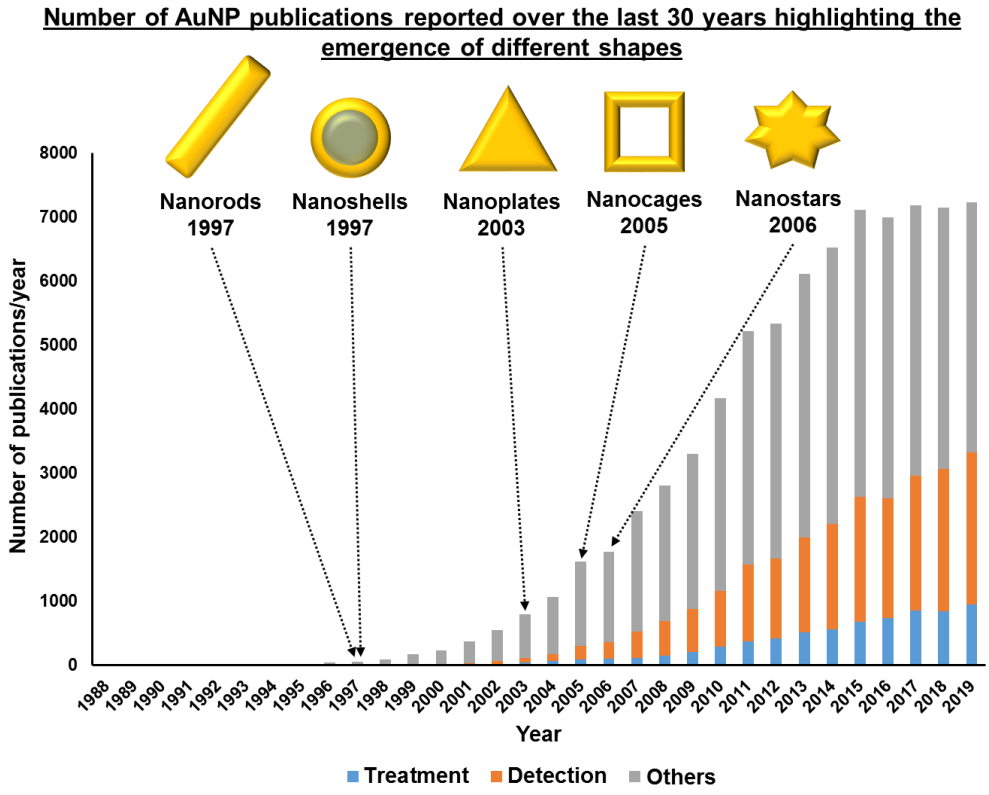

Figure 3. Bar plots showing the increase in scientific publications related with gold nanoparticle along the years. The year when the initial studies concerning the different

shapes of AuNPs were performed are also highlighted, including gold nanorods,[22] gold nanoshells,[23] gold nanoplates,[24] gold nanocages[25] and gold nanostars.[26] The number of publications related with AuNPs and treatment (in blue) and with AuNPs and detection (in orange) is differentiated from the rest of publications (in grey). Search terms: “gold nanoparticles” (top), “gold nanoparticles treatment” (medium), “gold nanoparticles detection” (down). These data were acquired from Scopus database.

Currently, the synthesis of AuNPs with almost any size and geometry can be found in the scientific literature including but not limited to nanospheres, shaped nanorods, nanoshells, nanocages, tetrahedral, icosahedral, octahedral, cubes, dodecahedra, tetrahexahedra, bipyramids, trisoctahedra and triangular nanoprisms (see **Figure 4**). In the majority of cases the size of the AuNP can be controlled with ease by changing one of a few key experimental parameters during their synthesis, e.g. reagent concentration, reaction time, solution pH, reduction potential, ionic strength, and so forth.[27–29] However, for the shape control of the AuNPs a vast list of different synthetic strategies and methodologies can be found in the literature. By this way, nowadays is possible to tune the shape and dimensions of AuNPs by controlling the synthesis to obtain almost any AuNP with particular properties on demand. Sizes and morphologies of AuNPs represent critical factors for determining their properties and other important properties such their interaction with biological structures.[20]

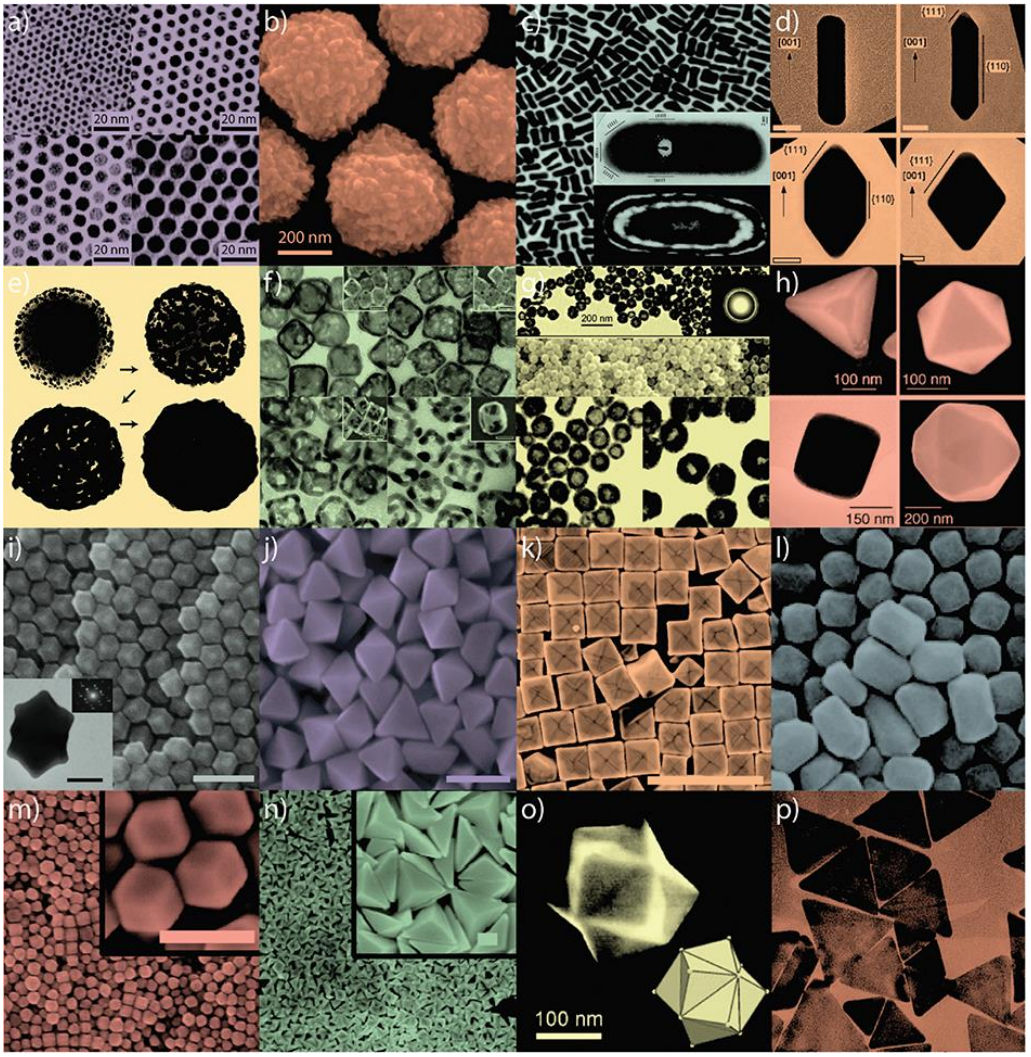

Figure 4. A summary of some of the many gold nanoparticle (AuNP) morphologies that can be accessed *via* conventional synthetic methodologies: small (**a**) and large (**b**) nanospheres, (**c**) nanorods, (**d**) sharpened nanorods, (**e**) nanoshells, (**f**) nanocages/frames, (**g**) hollow nanospheres, (**h**) tetrahedra/octahedral /cubes/icosahedra, (**i**) rhombic dodecahedra, (**j**) octahedra, (**k**) concave nanocubes, (**l**) tetrahexahedra, (**m**) rhombic dodecahedra, (**n**) obtuse triangular bipyramids, (**o**) trisoctahedra, and (**p**) nanoprisms. Reproduced with permission from[30]

The synthesis methods of any type of nanoparticles are normally classified in bottom-up or top-down methodologies (**Figure 5**). Bottom-up or constructive method is the synthesis of nanoparticles from atomic components to molecular clusters and nanoparticles while the top-down or destructive method is the reduction of a bulk material to nanometric-sized particles.[31] Top-down strategies for AuNPs in nanomedicines are less common than bottom-up due to its limitations in size resolution, scalability, colloidal instability in solution and 3D patterning. As examples of top-down strategies employed for AuNP synthesis, plasma etching,[32] electron-beam litography,[33] laser ablation,[34] sputtering[35] and thermal descomposition[36] can be listed. However, the majority of AuNPs for biotechnology are produced by bottom-up methodologies.

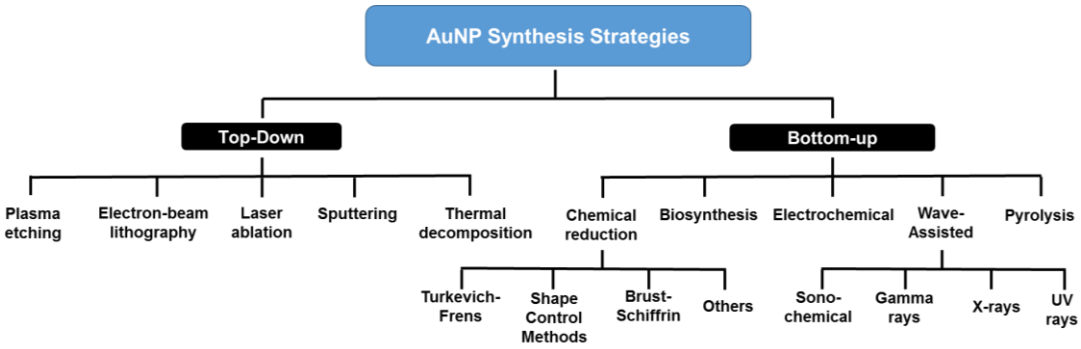

Figure 5. Schematic classification of AuNP synthesis methodologies, divided in top-down and bottom-up.

Bottom-up methodologies available for AuNPs synthesis can be classified in chemical reduction methods, biosynthesis, electrochemical methods, wave-assisted chemical methods and pyrolysis. Although pyrolysis is the most commonly process in industry for large scale nanoparticle production due to its cost effectiveness, continuous processing and high yielding,[31] this technique is not commonly employed for AuNP synthesis probably due to the specificity of the equipment required and the high polydispersity obtained.[37,38] Despite of its infrequent use in AuNP synthesis, wave-assisted chemical methods offer a really useful approach for hybrid nanoparticles made of gold and other materials. For

this purpose different waves are employed to provide the energy ned for the nanoparticle synthesis, including but not limited to ultrasounds for sonochemical synthesis,[39] gamma rays,[40] x-rays,[41] UV-light,[42] visible light[43] or NIR light.[44] Electrochemical synthesis of AuNPs has been proposed as an easy of control, low cost and high quality method,[45] however its use is scarce.

Biosynthesis is a green and environmentally friendly approach for the synthesis of AuNPs that has growth exponentially in recent years. Emerged as a response to avoid the use of expensive, environmentally dangerous and toxic reagents involved in other types of synthetic procedures, biosynthesis also reduces the subsequent toxicity of the nanoparticles in biomedical applications. Biosynthesis employs enzymes, bacteria, plants, fungi or extracts obtained from them to reduce the precursor gold salt. Although a large list of organisms have been employed for AuNP synthesis, biosynthesis is of great interest when the biological compounds contribute to the functionality of the AuNPs, as is the case of AuNPs synthesis with antibacterial and antifungal properties.[46] The main disadvantage of this methods is the polydispersity and low control over the size of the AuNPs[46] along with the inconvenience that anisotropic shapes of AuNPs are extremely difficult to obtain.

Due to the aforementioned considerations of other methodologies and because of its numerous advantages, chemical reductions methods for AuNPs synthesis are by far the most employed until the date. With low cost, a low equipment requirement, simplicity, relative easiness to scale-up and the possibility to control almost perfectly the size and shape of the AuNPs produced, chemical reduction methods represent the preferred method by researchers for designing AuNPs for biomedical applications with desired properties. The most common and extensively utilised methods for gold nanospheres production includes Turkevich-Frens method[47] and Brust-Schiffrin method.[48] However, anisotropic AuNPs possess modified physicochemical properties respect to the spherical ones due

to its shape and these properties described in **Subsection 1.3** are of great utility for some of their biomedical applications.

The synthesis of gold nanospheres (AuNS) is quite simple as confirmed by the precocity of the studies carried out by Faraday in 1857[21] in contrast to the relatively recent development of the rest of AuNPs morphologies (**Figure 3**). In the case of AuNS it is only necessary the increase of the crystalline structure without controlling the place where these atoms are linked. However, to produce an anisotropic shape of AuNPs, the synthetic procedure must control the position where the structure is growing. In a synthesis of metal nanocrystals, three distinct stages can be differentiated: nucleation, transformation of nuclei into seeds and growth of seeds into nanocrystals. In the colloidal synthesis of gold nanocrystals, shape control is achieved by accurately tuning the nucleation and growth processes, which may be under either thermodynamic or kinetic control.[49] When crystal growth is under thermodynamic control, surface energy plays a crucial role in determining the morphology of gold nanocrystals since the surface-area-to-volume ratio is high for nanoparticles, and a crystal in equilibrium tends to have the lowest surface energy for a given volume of material.[49]

Although examples of anisotropic AuNP synthesis in organic solvents have also been reported,[50,51] this text is focused on their synthesis in aqueous media which is the more commonly employed solvent due to its convenience for biomedical applications. Different strategies collected in **Figure 5** are commonly employed for anisotropic AuNP synthesis in aqueous media, including but not limited to adsorbate-directed synthesis, seed-mediated synthesis, template-assisted synthesis and growth-kinetics control. In the adsorbate-directed synthesis a wide variety of molecules such as metal ions, small organic molecules, surfactants, polymers and biomolecules are employed for selectively adsorbing to specific crystal planes, lowering its surface energy and directing shape control of gold nanocrystals. This methodology can be achieved by two different mechanisms: directed growth (the metal atoms addition to the structure only occurs in the

crystal planes without adsorbates) or oriented aggregation (preformed seeds attach between them by the crystal planes not occupied by the adsorbates).

One of the most commonly employed strategies for anisotropic AuNPs synthesis is the seed-mediated synthesis. The nucleation of the nanocrystals is favoured by conditions of high chemical supersaturation, ensuring a rapid growth of all crystal surfaces, what is contraindicated for shape control.[52] For this reason, in seed-mediated synthesis, the nucleation and the growth of seeds into nanocrystals is divided in two different steps with different chemical conditions. In the first step, small and almost monodisperse nanoparticles are generated and subsequently the conditions are altered and more gold ions and other compounds are added to produce the morphological-defined growth. The separation in two steps allows an advantageous rational design of nanocrystal shape through the choice of seed structure and growth conditions.[49]

Template-assisted synthesis and growth kinetics control represent two less employed methods for anisotropic AuNP synthesis. In the template-assisted synthesis of AuNPs, a structure with well-defined dimensions is employed as a template to spatially determine the shape of the AuNP. Traditional templates physically confine the growth of the AuNPs[53] but in the last years other nanometric solids with a specific shape are used as sacrificial templates for anisotropic AuNP synthesis, which adopt the underlying shape of the template.[54,55] By controlling the growth kinetics, it is possible to produce anisotropic AuNPs by substantially slowing down the reaction.[49] This strategy is of great interest for star-shaped or dendritic nanostructures.[56]

From all the previous methodologies for shape-controlled synthesis of AuNPs the use of surfactants as shape-directing agents is the gold standard. A large number of surfactants with different polar head-groups, hydrophobic chains, counterions and molecular structures have been employed for this end, i.e. cetyltrimethylammonium bromide (CTAB) as a usually employed surfactants for

a wide variety of AuNP shapes. However, recently an interesting work carried out by Wall *et al.* employs a green-method without the employment of surfactants or polymers to produce gold nanostars, nanorods, triangular nanoprisms and nanospheres from the same gold seeds. The authors develop a unified theoretical framework for designing shape-controlled nanoparticles just by controlling the concentrations of gold salt, sodium hydroxide, seeds and hydrogen peroxide that provide AuNPs with surface free of non-desired molecules.[57] Although these methods normally involve production on a relatively small scale (miligrams), which represents one inherent disadvantage for potential real world applications, recently a large scale synthesis in the order of grams has been reported.[58]

The AuNP shape not only determines its physicochemical (detailed in next section **1.3**) but also it is crucial for determining other important factors for biomedical applications, such as protein corona formation,[59] cellular internalisation[60,61] and biodistribution,[60,62] among others.

1.3. AuNPs physicochemical properties

Many of the applications were AuNPs can be of great interest are related with their physicochemical properties. As a noble metal, AuNPs stand out due to its chemical inertness, density and electron conductivity. Gold is one of the densest elements, with 19700 kg/m^3 it almost doubles the density of lead (11300 kg/m^3) normally employed as counterweight and it is only slightly overcame by other uncommon transition metals such as Osmium (22600 kg/m^3), Iridium (22400 kg/m^3) or Platinum (21400 kg/m^3). For this reason, gold is probably the best material for applications where nanoparticles with high density are required. Gold is also one of the best electrical conductors with 4.1x10^7 S/m at 20 °C, only slightly poorer than copper or silver, a property of great interest that has been exploited for sensing (see **Section 1.4.1**).

Metallic gold, as is the case of AuNPs, is highly unreactive and as such, artefacts made of gold retain their brilliant lustre for thousands of years without oxidizing. This property is also very useful for using AuNPs in biomedical applications since Au(0) is inert and thus stable nanoparticles do not chemically react with biological elements. In this aspect, gold, in contrast to other heavy metals, does not produce a marked associated-cytotoxicity. Cadmium, lead, chromium and mercury tend to accumulate in living organism and are considered as systematic toxicants that induce multiple organ damage and carcinogenicity.[63] There has been considerable on-going controversy about the cell-toxicity of commonly employed inorganic nanoparticles such as silver or titanium dioxide nanoparticles,[64] this reported toxicity should be analysed carefully. While for silver nanoparticles it has been shown how the toxicity of the nanoparticles increases due to low dissolution and release of silver ions into the medium,[65] for the AuNPs most *in vitro* studies have indicated the complete absence of toxicity where the cases of reported toxicity are mostly associated to their surface-coating coverage, for example for some types of positively charged AuNPs.[64,66] In addition, even if gold in AuNP has shown accumulation in different tissues after intravenous administration,[62,67] it is considered to be a relatively safe nanomaterial for biomedical applications because this accumulation was not associated with any detected toxicity or mortality.[67]

Another advantage of AuNPs is the easiness to attach a large variety of molecules to its surface. Most employed method to anchor molecules to the gold surface is by the employment of thiol-containing molecules that interact by the thiol with the gold surface to form a pseudo-covalent bond, although the gold surface can be covered with other ligands containing different chemical groups such as phosphorous, amine, carboxyl, carbonyl and phenol.[68] Thanks to this facility to attach to the gold surface, AuNPs are usually coated with molecules that confer colloidal stability and improve their properties. This chemical surface coating of the AuNP determines the interaction with all the components of the physiological

medium. This fact is of special importance in the case of nanomedical applications where the AuNPs is exposed to complex biological environment with different components, such as different proteins, ions, hydrophilic or hydrophobic molecules as well as with the other nanoparticles. The interaction of the AuNPs with their environment affect different critical phenomena for their application, *i.e* immune response, extravasation, cellular internalisation or accumulation in a cell-type dependent manner, in addition to their intracellular location and elimination. Although some approaches use the reducing agent required for the AuNP synthesis as a final stabiliser (e.g., citrate), the most interesting results are obtained when the coating is designed specifically for the desired application, as an example, when it can be used for subsequent functionalisation with other molecules of interest. Most frequently, AuNP surfaces are stabilised with coordinating thiol groups where the most common coating agents include different types of polymers and surfactants, e.g. thiolated poly(ethylene glycol) (PEG), thiolated end-capped polystyrene, poly(ethylenimine), thiolate poly(vinyl pyridine), polyamidoamine dendrimers and cetyltrimethylammonium bromide, among others.[68] This facility to link to the gold surface can be also exploited to link functional molecules for specific applications. As an interest example, the use of gold nanoparticles for oligonucleotides delivery has been widely studied.[20]

However, the most important physicochemical property for much of the applications related with the use of AuNPs is their unique optical properties. The optical properties of metal nanoparticles are mainly governed by the surface plasmon effect. When a metal particle is exposed to light, the oscillating electromagnetic field of the light induces a collective coherent oscillation of the free electrons (conduction band electrons) of the metal. This electron oscillation around the particle surface causes a charge separation with respect to the ionic lattice, forming a dipole oscillation along the direction of the electric field of the light (see **Figure 6**).[69] Further, surface plasmon resonance (SPR) of conduction electrons depends on the nature of the metal, but is also sensitive to refractive

index changes around the metal such as changes in the surrounding medium.[28,70] The surface plasmon effect induces a strong absorption of the incident light and it is much stronger for plasmonic nanoparticles (noble metal, especially Au and Ag) than other metals.[69]

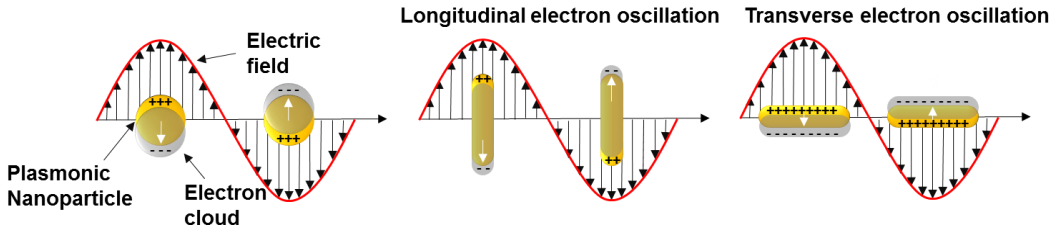

Figure 6. LSPR excitation scheme for plasmonic gold nanospheres and nanorods. Inspired from [71]

When the electromagnetic waves are confined on a metallic nanostructure the localised surface plasmon resonance (LSPR) is produced.[72] The LSPR effect is related with the nature of the metallic material but is particularly affected by the shape of the nanostructure and size. For pseudo-spherical AuNPs, the LSPR band depends on their diameter and remains in the visible region of the electromagnetic spectrum with slight changes of their optical properties.[73] However, when the AuNPs pose an anisotropic shape the optical properties are highly-size dependent and change dramatically depending on their dimensions,[74] with their LSPR peak corresponding with the in-plane dipolar mode lying in the Near-Infrared (NIR) range of the electromagnetic spectrum (see **Figure 7**).[75] As a result of this and the easiness to control the synthesis of AuNPs detailed in **section 1.2**, nowadays is possible to tune the shape and dimensions of AuNPs by controlling the synthesis to obtain almost any AuNP with particular optical properties on demand. The possibility to control the optical properties of the AuNP is crucial for the most important applications in the biomedical field. The optical properties of AuNPs combined with the sensing of biomolecules along with the

light-to-heat transduction properties used for photothermal therapy are described and discussed in the following **Subsections 1.4.1**, and **1.4.2**.

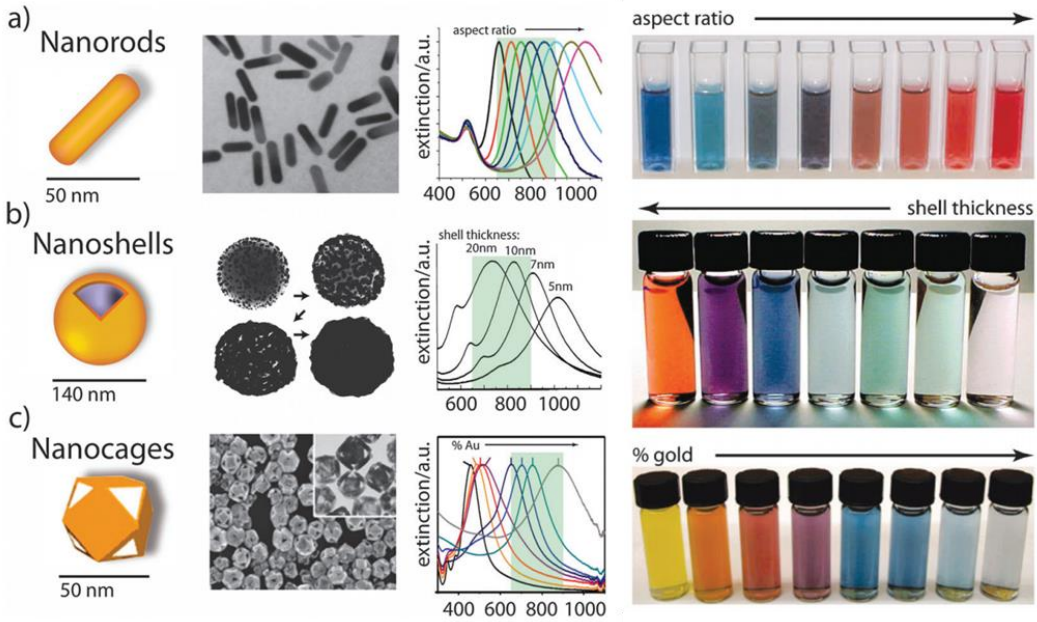

Figure 7. Various gold nanostructures commonly applied in biomedical applications. Graphical illustrations, transmission electron micrographs, and synthetically tunable extinction spectra with their real colour produced by their LSPR including (a) gold nanorods, (b) gold nanoshells, and (c) gold nanocages. Spectral red-shifts and real colours are indicated for increasing aspect ratio, decreasing shell thickness, and increasing gold displacement, respectively. Adapted with permission from.[30,76]

1.4. Applications of AuNPs in biomedicine

If anything can be derived from the vast amount of literature on the subject it is that there is no universal AuNP for biomedical applications.[20] In contrast, one of the principle advantages of using AuNPs is that they can be engineered specifically for the desired application by the design of the most appropriate size, shape, surface coating and functionalisation strategies for each purpose. These

are the primary considerations that should be taken into account for AuNP-mediated biomedicines. Gold nanoparticles (AuNPs) have shown promising results in a wide-variety of biomedical applications, ranging from photothermal therapy,[61] drug delivery,[20] biosensing[77] and imaging techniques such as optoacustic imaging[78] and surface enhanced Raman spectroscopy (SERS).[79] The versatility of AuNPs has been assessed in a diverse set of fields, including but not limited to anticancer,[80] antiviral,[81] stem cell differentiation,[82] gene expression,[20] and to treat a large list of diseases as pancreatitis,[83] diabetes,[84] psoriasis,[85] etc. From the aforementioned applications, the most important research of today and probably their daily use in the future is related with their capability for sensing and treatment.

1.4.1. AuNPs for sensing

In AuNP-based sensing, the analyte (molecule to detect) is recognised by a recognition element linked to the AuNP surface, where the AuNP acts as a transducer that produces a signal-transduction event based on the physicochemical properties of the nanoparticle, which is in turn recognised by a processor (see **Figure 8**). The optical properties, high density, electrical conductivity, stability and ease of surface-functionalisation to link sensing molecules have rendered AuNPs as one of the most frequently studied and extensively employed models for chemical and biological sensing. Consequently, many types of AuNPs specifically designed for detection can be purchased from commercial suppliers and AuNPs can already be found in hundreds of commercial detection kits.[86] Depending on the molecule to detect and the limit of detection to achieve, a large number of strategies have been applied with several levels of complexity and different needs of equipment, from simple and portable colorimetric tests to be used in the moment to complex equipment to massive-sequence DNA. Thousands of publications can be found in the literature with different strategies to detect a vast a number of analytes, so diverse as vapours,

metal ions, anions, small organic molecules, toxic chemicals, drugs, proteins, oligonucleotides, viruses, pathogens and mammalian cells.[87]

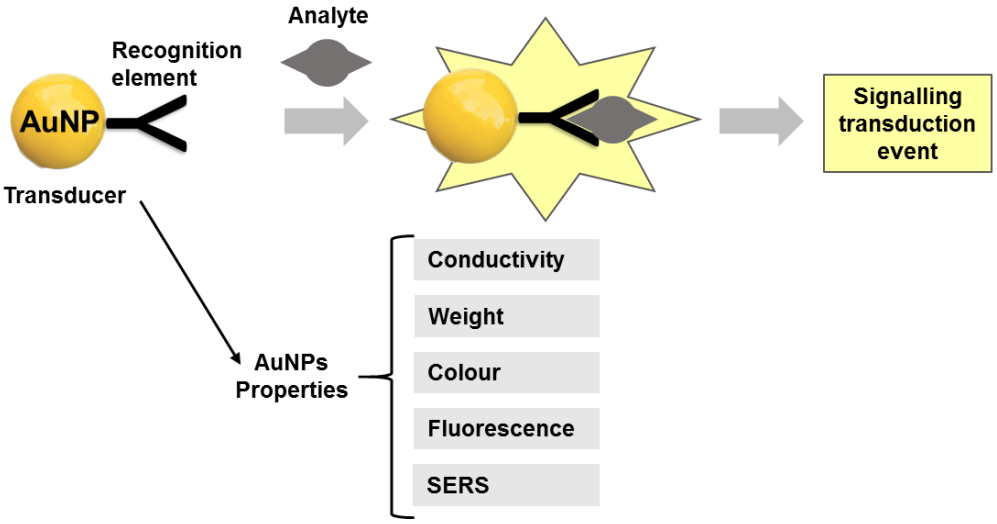

Figure 8. Physical properties of AuNPs that are usually employed for sensing and schematic illustration of an AuNP-based detection system, including the AuNP that acts as a transducer of the recognition between the recognition element and the analyte to produce the signal.

Most AuNPs-based strategies for sensing take advantage of the optical properties of AuNPs and their interaction with light, however another physical property of gold that has been employed for sensing is the electrical conductivity. Several electrochemical sensing strategies have used AuNPs, most frequently whereby the AuNPs are functionalised with molecules that undergo an electron-producing chemical transformation upon interaction with the analyte and the AuNPs serve to conduct and transfer the electrons to the surface of the electrode. This strategy has been employed for a long time and between the pioneers the work carried out by Willner and co-workers in 2003 deserved a special mention. In this work they anchored AuNPs functionalised with flavin adenine dinucleotide to the surface of the electrode to interact with the enzyme glucose oxidase and detect the presence of glucose.[88] Nowadays this strategy is increasingly been exploited using graphene oxide hybridised with gold nanoparticles since graphene oxide is

a very efficient conductor of electrons from the AuNPs to the electrodes and the gold nanoparticles are perfect points for the functionalisation with the detection molecules.[89,90]

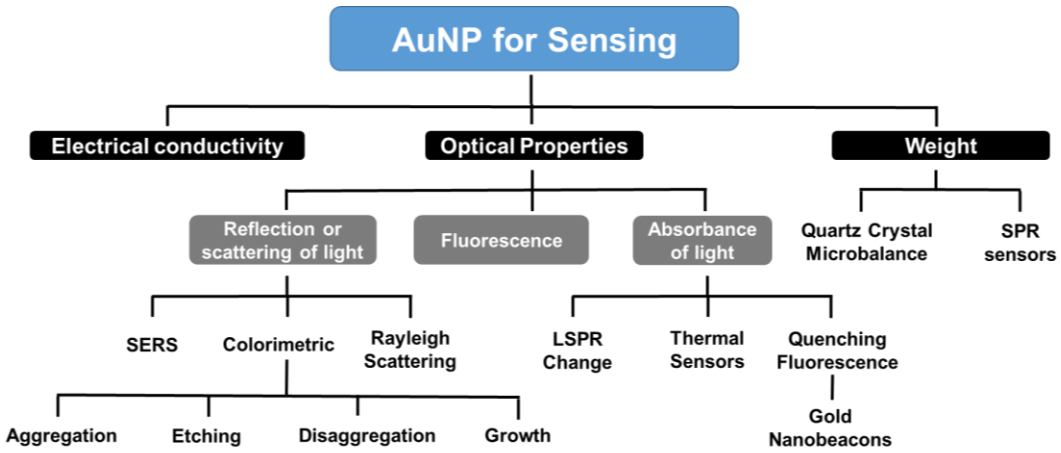

Figure 9. Schematic classification of biosensing techniques that employs AuNPs based on the transducing AuNP physicochemical property used for the sensing technique.

As previously described, most of the strategies including the use of AuNPs for sensing are related with their unique optical properties (**Section 1.3**). In the **Figure 9** it can be found a complete summary of the most usually employed strategies for sensing depending on how the AuNPs interact with the light. Mainly, the sensing employing AuNPs occurs when they absorb, scatter or reflect the light. However, gold nanoclusters, which consist of an aggrupation of gold atoms smaller than conventional AuNPs, present fluorescence behaviour when irradiated at the proper wavelength. Thanks to their ultrasmall size, low toxicity, and their low photobleaching compared with other organic fluorophores, make them excellent probes for biological applications.[91] However, more efforts are still needed to improve their synthesis because of their low quantum yield, which is usually less than 20 %.[92] Another aspect to highlight is that nanoclusters not only are employed for sensing due to their fluorescent properties but also thanks to

their fluorescence properties they can be exploited for imaging of cells and in animal testing.[92]

AuNPs ability to absorb light at specific wavelengths can also be harnessed for sensing and the absorbance spectrum of AuNPs changes depending on the refractive index of the surrounding medium. By this way, the refractive index change produced by an adsorbate on the surface of the AuNP can be used to monitor molecular binding events.[93] This strategy has been proposed for applications as delicate as HIV-detection,[94] however, the slightly changes produced in the absorbance spectrum and the requirement of specific equipment such an spectrophotometer complicate commercial application.

The high light absorption capacity of AuNPs has also been exploited for fluorescence quenching sensing. In fluorescence quenching the AuNPs are employed for decreasing the fluorescence intensity of a molecule. Although the mechanism by which the energy transfer between the molecule to detect and the AuNP is still to be resolved with certainty, the applications on this field are still growing.[95] A very interesting application of this strategy has been employed in the molecular beacons. Firstly described in 1996,[96] molecular beacons are sequences of nucleotides with a fluorophore in an end and a quencher in the other end that specifically recognise complementary sequences of nucleotides. When the complementary sequence is present, the molecular beacon opens and binds to the complementary sequence, decreasing the intensity of the quenching and emitting fluorescence. Since their discovery, molecular beacons have been extensively employed for DNA sequencing and quantitative polymerase chain reaction (q-PCR). AuNPs have appeared as very efficient quenchers for molecular beacons, allowing the *in situ* imaging and silencing of mRNA in living cells.[97]

But probably the most intelligent strategy for taking advantage of AuNPs highly efficient light absorbance properties for sensing is their use in plasmonic-driven

thermal biosensors. Firstly reported by Qin et al.,[98] this type of biosensors employ a gold nanoparticle functionalised with a molecule able to specifically recognise the analyte (most frequently an antibody). By this way, if the molecule to detect is present in the sample the AuNPs interact with it and remain linked to a solid support that after that is irradiated with a laser. If the analyte was present the AuNP produce heat that burns a thermosensitive paper or it is monitored by a specific system such as a thermocouple or an infrared camera. An interesting improvement of the system was achieved by the use of anisotropic AuNPs that enable to use a NIR laser, enabling lower limit of detection and a higher specificity.[99] In recent times, this strategy has been improved by the combination with other photothermal-sensing materials and the lateral flow immunoassay in order to facilitate the processing of the sample.[100]

Although an abundance of complex strategies that employ the scattering or reflexion of light from AuNPs for sensing (e.g. gold-bridged nanoprobes for the identification of single point DNA mutations by Rayleigh scattering),[101] the most important and simple method involves simple change of colour related with changes in the degree of aggregation or morphology of the AuNPs that modify their interaction with light and LSPR absorbance spectrum. Compared with other sensing methods, AuNP-based colorimetric assays are promising because normally the whole reaction occurs without any washing step and the colour-change can be directly assessed with the naked eye. In addition, nowadays such colorimetric assays are easily adaptable to smartphone-based devices to automatically translate the result in quantitative information. Therefore, these approaches remarkably simplify the detection process in less time and reduce costs and without the need of complex equipment. Several strategies have been employed to take advantage of the change of colour, including but not limited to aggregation and disaggregation of the AuNPs, etching to change their shape or reactions that catalyses the growth of the AuNPs.[102] However, these methodologies present some disadvantages such as the limit of detection is quite

limited, difficult to detect more than one analyte and problems in sensitivity and background colour in real complex samples.[102]

One of the most employed recent applications of light scattering employing AuNPs for sensing is the surface-enhanced Raman scattering (SERS). Raman spectroscopy detects inelastic light scattering related to vibrational energy levels of the probed molecules, leading to molecularly specific Raman fingerprints.[103] The main problem of Raman scattering is that it is a highly inefficient process thus resulting in weak signals that are insufficient for sensitive analysis.[104] However, this inefficient process can be dramatically enhanced by the use of surface-enhanced Raman scattering, with enhancement factor of 10^4-10^8.[105] In SERS, the molecule to be detected has to be located in close proximity to plasmonic surfaces of AuNPs and the enhancement of the signal is supposed to be produced by a combination of two mechanisms: an electromagnetic mechanism produced by the local field of plasmonic AuNPs and a chemical mechanism due to charge transfer between the substrate and probed molecules.[106] One of the main advantages of SERS is that it can be also combined with cell microscopy imaging.[107]

Most of the reported strategies for sensing take advantage of the optical properties of AuNPs and their interaction with light, however a small part of them employ other physicochemical property of AuNPs: their high density. As detailed in **section 1.3**, gold is one of the densest elements. Due to its density and the ability to interact with the molecule to detect at the same size level, AuNPs are one of the best candidates if not the best to enhance the signal of molecules in techniques where the signal depends on the mass or density of the complex to detect. In this line, most important sensing techniques where AuNPs are of great utility include surface plasmon resonance (SPR) sensors and quartz crystal microbalance (QCM) sensors. Quartz crystal microbalances (QCM) are ultrasensitive piezoelectric devices that use frequency changes on a quartz crystal resonator to monitor changes in mass arising from molecule binding.[87]

This strategy has been employed mainly for the detection of oligonucleotides by the use of AuNPs-complementary DNAs[108] or the detection of proteins employing AuNPs with a recognition protein.[109]

Surface plasmon resonance (SPR) was initially used to study the details of molecular interactions, but more recently it has emerged as a rapid label-free optical biosensing tool that can be used in a wide variety of fields, including medical diagnostics, environmental monitoring, food safety and security.[110] This optical technique detects the changes in the refractive index of a planar metallic surface (typically silver or gold), which has been functionalised with specific molecular probes to absorb a target analyte, thereby enabling direct real-time detection without the need for prior labelling (see **Figure 10**). However, the main problem of SPR biosensing relies on the low signal produced by most of the biological molecules of interest and their very low concentration. For this reason, an intense area of research in this field is focused on SPR signal enhancement using dual-functional elements that are able to both recognise the target analyte (or the ligand/target interaction) and also increase the refractive index change related to the analyte recognition.[111] Among all these enhancing strategies, AuNP have proven to provide outstanding amplification for the SPR detection signal.[77,112] Furthermore their stability and the ease by which biomolecules can be conjugated to their surface ("biofunctionalisation") makes them even more attractive.[20] For these reasons the use of AuNPs as SPR signal enhancers is one of the most attractive biosensing applications nowadays.

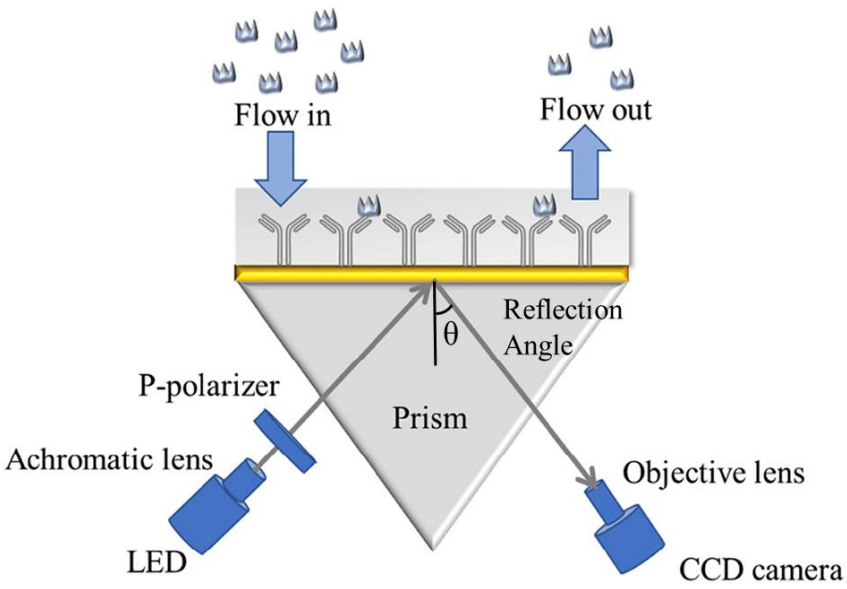

Figure 10. Detection mechanism by Surface Plasmon Resonance (SPR) biosensors. A light beam is reflected on a gold film and the intensity of the light depending on the reflection angle is collected. Depending on the molecules attached to the gold surfaces this reflected light changes its intensity at different reflection angles. Adapted with permission from[113]

1.4.2. AuNPs for treatment

The other main biomedical application where AuNPs have been extensively employed is their use as potential therapeutic agents in medicine. Gold was already employed as a therapeutic agent as far back as 2500 BC.[114] In modern medicine, gold salts were extensively employed in the 1920s for tuberculosis treatment with doubtful results but this therapy laid the foundation for their subsequent successful employment for rheumatic treatment.[114] Gold nanoparticles have been brought to the forefront of disease treatment in recent years because of their facile synthesis and surface modification, excellent biocompatibility and enhanced tuneable optical properties. In this line, the research involving AuNPs has been mainly focused in their application for photothermal treatment and as carriers for the delivery of pharmaceuticals, among other therapeutics. There are currently five clinical trials involving AuNPs

registered in U.S. National Library of Medicine. From them, two are focused in their use as photothermal agents, two are based on their employment as drug carriers and the other one is focused in cavity treatment. However, AuNPs have been recently proposed for other types of treatments, including but not limited to radiotherapy, antibacterial, rheumatoid arthritis and as angiogenesis modulators.

AuNPs are usually employed as drug carriers due to the easiness to functionalise them with a wide variety of molecules. Almost any biomolecule can be anchored to the surface of a gold nanoparticle when its covered with the proper surface coverage and so AuNPs have been extensively employed for the delivery of peptides, enzymes, antibodies, lipids, other drugs and oligonucleotides, among others.[115] AuNPs have been employed to increase drug efficiency or to direct them to the site of action for traditional drug delivery such as antibiotics and anticancer drugs. Antibodies conjugated to the AuNPs have been employed mainly for cancer treatment and to direct nanoparticles to the target cell. Lipids have been anchored to AuNPs to increase their interaction with membranes and as an attempt to treat diseases related to incorrect balances of lipids, like atherosclerosis. AuNPs have also shown interesting results as vaccine platforms due to their advantages over traditional vaccine platforms.[116] In particular, the ability to tune AuNP sizes, shapes and surface properties enables an appropriate design platform to enhance interaction with the target receptors. However, perhaps the most important results have been obtained for delivering oligonucleotides. The use of AuNPs as DNA carriers initially and as RNA carriers some years after have allowed their use for gene transfection and RNA interference allowing to control the expression of potentially almost any protein in the organism in order to try to treat a large list of diseases.[20] Each of these molecules can be linked to the gold nanoparticle or to their organic coverage employing different strategies involving but not limited to covalent linking, ionic interaction or adsorption (the linkage of RNA as an example can be observed in **Figure 11**).

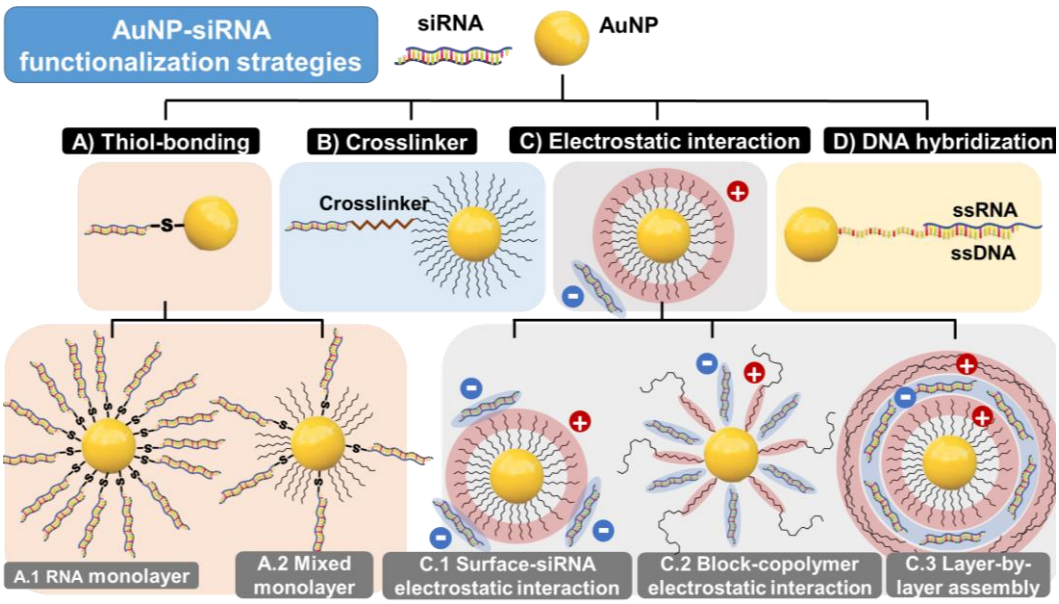

Figure 11. Illustrative example of the most common siRNA functionalisation strategies for AuNPs based on electrostatic association, covalent/coordination bonding and hydrogen bonding. siRNA can be directly linked to the gold surface by thiol-bonding (**A**) to form a RNA monolayer (**A.1**) or a mixed monolayer with other thiolated molecules (**A.2**). Covalent bonding between siRNA and AuNP coating can be obtained by the employment of a crosslinker (**B**). Electrostatic interaction (**C**) takes advantage of negative charge of siRNA to interact with different positively charged parts of the AuNPs, including the surface of AuNP coating (**C.1**), the inner part of block copolymers in the AuNP coating (**C.2**) or different positive layers surrounding the nanoparticle in a layer-by-layer assembly (**C.3**). Specific sequence hybridisation can be obtained using ssDNA linked to AuNP complementary to ssRNA by hydrogen bonding (**D**). Adapted with permission from[20]

Although the enhanced cellular internalisation is one of the main reasons to employ AuNPs for drug delivery, arriving to the target cell site of interest and subsequent specific internalisation represents a complex task in living organisms like humans. Especially in the case of a systemic administration, the AuNP and the drug carried have to avoid several delivery problems (see **Figure 12**). AuNPs should avoid the mononuclear phagocyte system that captures most of nanoparticles and organs that retire most of compounds from blood such as kidneys and liver. AuNPs should protect the drug against serum enzymes

degradation in the case it is necessary. AuNPs with the drug should perform extravasation from blood torrent to the desired tissue across the vascular endothelium. After that, they should be internalised by the target cells which occurs through a host of different mechanisms such as phagocytosis, macropinocytosis, clathrin-mediated endocytosis and caveolae-mediated endocytosis depending on the cell type.[117] After all this process, the drug-AuNP should remain functional to exert its biological function inside the cell. For these reasons, when possible normally a local administration is preferred for AuNP delivery carriers.

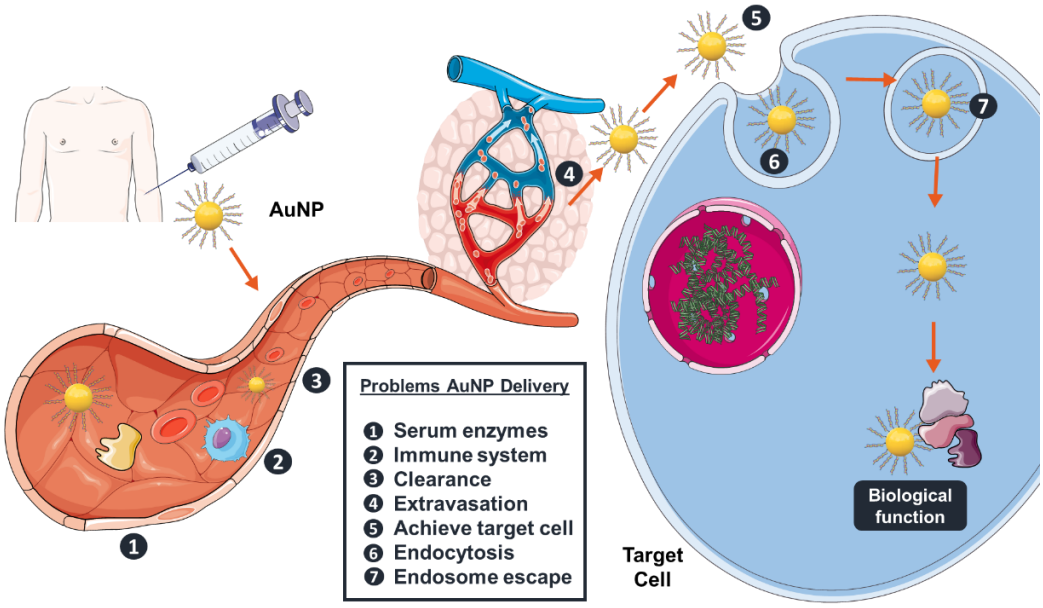

Figure 12. Overview of AuNP delivery problems that must be overcome after systemic administration to achieve and exert its biological function in the target cell. Adapted with permission from [20].

However, another strategy that has been extensively explored for AuNP systemic administration is the employment of target molecules linked to the AuNP. The objective of targeted delivery consists of the predominant accumulation of the desired drug at the zone or cells of interest. To improve the targeting effect, an active targeting approach involving the conjugation of targeting ligands to the

nanoparticle that interacts specifically with molecules in the target cells can be employed.[20] In the case of AuNPs, cell-penetrating peptides, small ligands molecules recognised by cell surface receptors and antibodies are the most commonly utilised.

Although normally gold salts are preferred for arthritis treatment and some approved drugs based on gold salts are already in the market and employed in clinics to this end,[118] some researchers have explored the use of gold nanoparticles for this application. Although it is not clear the mechanism by which gold nanoparticles are useful to treat this disease, in the case of gold salt Auranofin is able to slow disease progression by suppressing inflammation and stimulating cell-mediated immunity.[119] The mechanism of action of this compound is through the inhibition of redox enzymes due to the high affinity for thiol and selenol groups, forming stable and irreversible adducts.[119] It should be highlighted that in the last years the use of gold salts in clinics for arthritis treatment is been replaced by other disease-modifying antirheumatic drugs such as methotrexate due to its higher efficiency and lower number of side-effects.[119] Anti-arthritic activities of AuNPs have been investigated in an effort to avoid these side-effects which include loose stools, abdominal cramping, watery diarrhoea, skin irritations, rash, conjunctivitis or proteinuria.[120,121]

As angiogenesis modulators, AuNPs have shown interesting results and they have even been qualified as the most promising nanoparticles with anti-angiogenic properties.[122] Angiogenesis is the formation of new blood vessels from pre-existing vessels under conditions of hypoxia, inflammation, or vascular injury by the interplay between pro-angiogenic and anti-angiogenic factors that mediate the transition of vascular endothelium through different stages of vascular growth. However, certain diseases such as cancer, inflammation, arthritis, atherosclerosis and some types of blindness are related with pathological angiogenesis. Pathological angiogenesis involves the formation of vessels which are hyperpermeable to plasma and its proteins and possess heterogeneous functions

with irregular sprouting and non-uniformed vessel distribution.[123] The anti-angiogenic effect of AuNPs has been demonstrated in several models, including but not limited to human umbilical vein endothelial cells,[124] human retinal microvascular endothelial cells,[125] *ex vivo* models[126] and *in vivo* tumour models.[127] Multiple molecular pathways have been shown to contribute to the anti-angiogenic effects of AuNPs (see **Figure 13** for details).

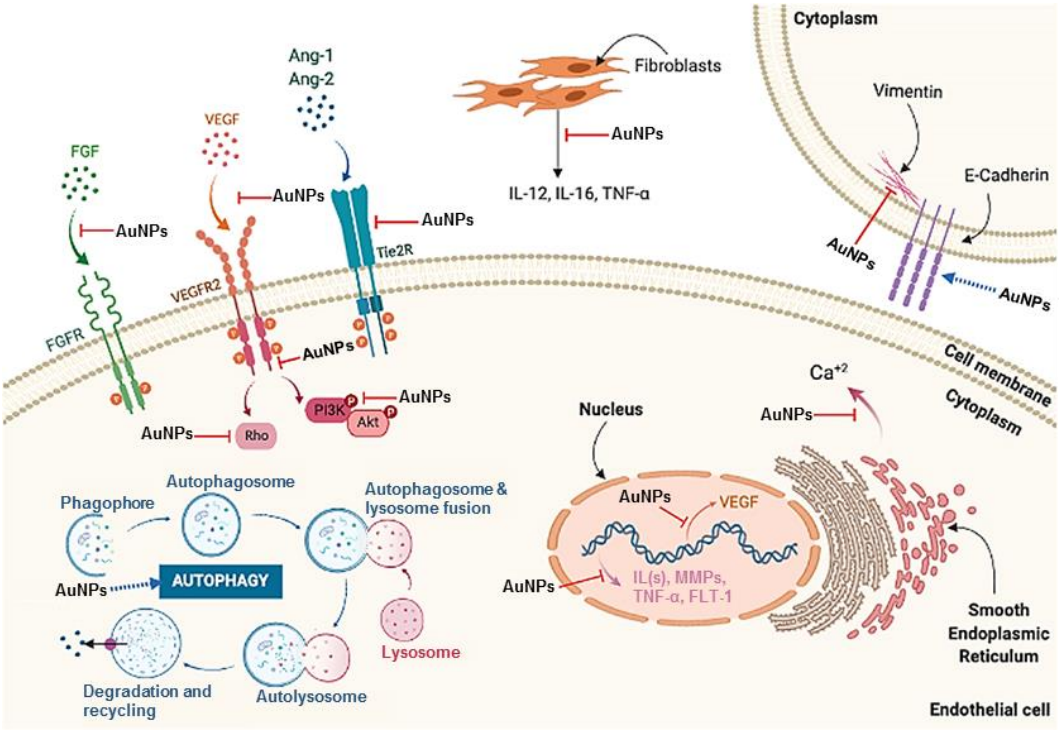

Figure 13. Molecular pathways affected by the anti-angiogenic effects of AuNPs. Anti-angiogenic effects of AuNPs are mediated by suppressing activation of VEGFR2, Tie2R, FGFR, and their downstream signalling pathways. AuNPs suppress intracellular calcium release mediated by VEGF-165. AuNPs upregulate E-cadherin and downregulate vimentin reducing epithelial-to-mesenchymal transition (EMT). AuNPs reduce ILs, MMPs, and TNF-α expression and inhibit neovascularisation via induction of autophagy. Abbreviations in the image: Ang-1, angiopoietin 1; Ang-2, angiopoietin 2; Ca^{2+}, calcium; FGF, fibroblast growth factor; FGFR, fibroblast growth factor receptor; ILs, interleukins; MMPs, matrix metalloproteases; Tie2R, angiopoietin receptor; TNF-α, tumour necrosis factor-α; VEGF, vascular endothelial growth factor; VEGFR, vascular endothelial growth factor receptor. Reproduced with permission from[123]

Other therapeutic applications of AuNPs that have also been exploited include radiotherapy and as antibacterial agents. AuNPs have shown very promising properties as “radiosensitisers” in oncology. Their role as radiosensitisers consists in the enhancement of radiation effects on biological tissues treated with radiotherapy. The use of AuNPs for radiotherapy can be achieved by two different strategies: the employment of external sources of radiation (X-ray and gamma beams) or by brachytherapy, where the source of radiation is located near the target tissue, normally inside the body (see **Figure 14**). When an external source of radiation (X-radiation and/or gamma radiation beams) is applied to the AuNPs the interaction between the photons with the AuNPs produce the emission of low-energy and short-range secondary electrons, which in turn increase the dose deposited in the tissues.[128] Another alternative remains in the employment of traditional brachytherapy radiation sources such as radioisotopes ^{125}I or ^{103}P in combination with the AuNPs. The other strategy consist in the use of AuNPs as sources of radiation in the target tissue either by the use of radioactive AuNPs or by the employment of radiolabelled AuNPs (AuNPs functionalised with radioactive elements), as explained in **Figure 14**.[128]

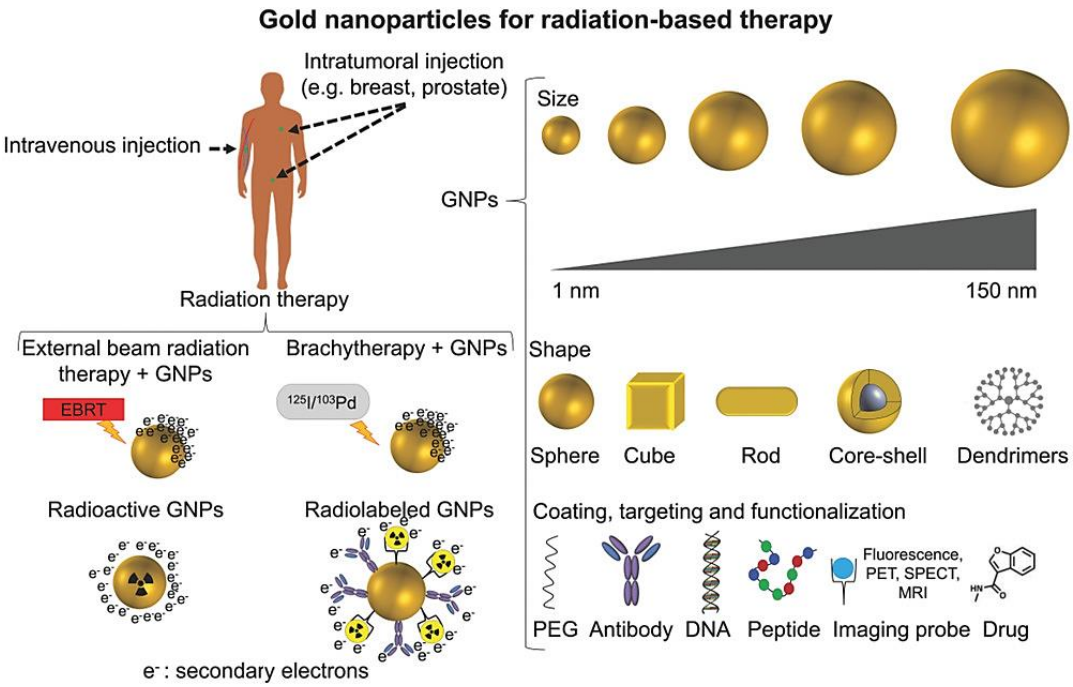

Figure 14. Different radiotherapy scenarios involving GNPs as radiosensitisers to enhance dose deposition. The size, shape, and functionalisation of GNPs can be varied depending on the target organ and requirements of the administration routes. The interaction of GNPs with photons, either through external beam therapy, brachytherapy, radioisotopes, or in/at the GNPs surface, generates secondary products (e.g., photons and electrons), which, in turn, enhances the efficacy of the radiotherapy treatment. Reproduced with permission from[128]

The use of gold nanoparticles as antibacterial agents has been extensively investigated both for combat infections caused by pathological bacteria and for their use in surfaces. Although AuNPs have been classified as nanoparticles with intrinsic antibacterial activity, the best results are obtained when they are combined with other antimicrobial agents.[129] In such applications gold nanoparticles can be functionalised with dozens of antibiotics by several methodologies depending on the final specific application.[130] As an alternative, their conjugation with enzymes with antibacterial activity not only increase their efficacy but also enhance their antibiofilm activity.[129] It should be highlighted that ultrasmall AuNPs (nanoclusters) with core diameters of 0.8 and 1.4 nm have

shown an intrinsic antibacterial activity, especially effective in the case of the smallest ones, suggesting a size-depending effect.[131] Other approaches in the use of AuNPs against bacteria include their use as antibacterial vaccines and taking advantage of their optical properties for laser irradiation in order to kill bacteria, as is explained in subsequent paragraph.

The most important application of AuNPs for biomedical treatment is related with their unique optical properties. As explained in **Section 1.3**, the optical properties of AuNPs are governed by the LSPR effect. This LSPR effect provokes that at specific wavelengths the AuNPs absorb light extremely efficiently and most of the energy of this light is converted in thermal energy in a process named photothermal effect. The photothermal effect has been employed in a wide-variety of biomedical therapeutic applications such as the photothermal therapy (PTT), photothermal antibacterial activity and light-mediated drug release. In addition, the photothermal effect has been exploded for other biomedical applications, as is the case of photothermal sensing (explained in **Subsection 1.4.1**). Photothermal therapy (PTT) involves the use of a light source to produce heat to destroy or weaken the target cells (cancer cells in most of the cases). The destructive effect of increased temperature corresponds to damage of cellular structures, mainly lysosomes, releasing their content and inducing cell death,[132] while the aim of weakening the cells is generally to make them more susceptible to other treatments.[61]

The main problem of photothermal effect is to heat dangerous cells without affecting the surrounding healthy tissues. To avoid this, lasers in the near infrared (NIR) wavelength are employed because the light absorbance of the biological tissues is highly decreased between 750-1200 nm (NIR 'biological window') (see **Figure 15**). Consequently, by using light at this wavelength, radiation can penetrate deeper in the biological tissues without damaging the biological structures. As detailed before, the LSPR absorbance band of anisotropic AuNP

can be fine-controlled (see **Figure 7**), making them one of the best if not the best candidates for nanoparticle-mediated PTT.

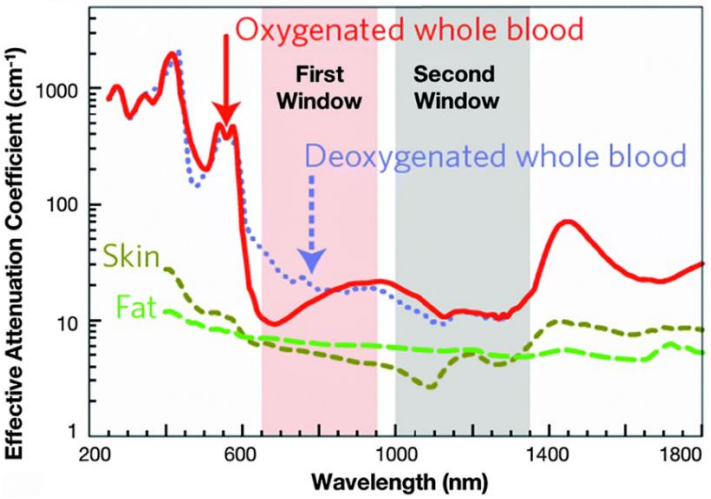

Figure 15. Absorbance spectrum showing the two first optical windows in some biological tissues and fluids. These plots of effective attenuation coefficient (on a log scale) versus wavelength show the quantitative relevance of different body substances (oxygenated blood, deoxygenated blood, skin and fatty tissue) when aiming for deep sub-skin imaging. Reproduced with permission from[133]

As an example of anisotropic AuNPs potential for PTT, the first successful clinical trial in humans involving AuNPs employed a NIR wavelength laser to produce a temperature increase when irradiating silica coated AuNPs to reduce atheroma volume in coronary artery.[134] In this clinical trial, involving 180 patients, a total atheroma volume reduction of 38 % was achieved. Recently, the initial results of a successful clinical trial employing gold nanoshells for the localised ablation of prostate tumours was reported by N. Halas and co-workers.[135] In this study, the feasibility and safety data from 16 cases of patients diagnosed with low- or intermediate-risk localised prostate cancer was assessed. After gold nanoshells infusion and high-precision laser ablation, the evolution of the prostate cancer was monitored by magnetic resonance imaging and biopsies during 12 months. In 15 of the 16 patients, the gold nanoshell-mediated focal laser ablation was

successfully achieved and their treatment protocol did not show serious complications or deleterious changes in genitourinary function. These clinical trials will help usher in novel therapies employing AuNPs for PTT, especially in the cases where PTT employing AuNPs can be combined with traditional therapies as is the case of several types of cancer.

Although several manuscripts describing interesting results employing different AuNPs for PTT are published every day, it is almost impossible to elucidate which is the appropriate shape of AuNPs for a determined application. The lack of standardisation and proper characterisation is one of the major problems in nanomedicines nowadays[136] and makes comparison of studies between different authors almost impossible to compare. In addition, the number of direct comparisons of the physicochemical properties of anisotropic AuNPs is rare and *in vitro* and *in vivo* comparisons of these AuNPs for PTT are almost unheard in literature.[60,137,138] Taking into account that the protein corona can completely change depending on the media and the nanoparticle affecting the cell internalisation and that cell internalisation can differ between different cell lines, any comparison between the optical properties and cellular interaction of different-shape gold nanoparticle for PTT is very useful to seed light to this topic.

1.5. AuNPs hydrogel entrapment

As previously described, AuNPs are being studied intensely for numerous potential biomedical applications, especially for treatment (therapy). However, there has yet to be a clinical breakthrough using gold nanoparticles and, according to the United States National Library of Medicine, only five clinical trials have been proposed to date. One such approach to improve the applicability of AuNPs in real conditions as well as improving some of their properties is their combination within polysaccharide hydrogels. The structural combination of a polymer hydrogel network with a nanoparticle holds the promise of providing superior functionality to the composite material with applications in diverse fields,

including catalysis, electronics, bio-sensing, drug delivery, nano-medicine, and environmental remediation.[139] One of the objectives of such hybrid materials is to provide a synergistic property enhancement of each component.

Hydrogels consist of three-dimensional, highly hydrated networks of polymeric chains electrostatically or covalently cross-linked. Although they can be synthesised by different methods, the ionotropic gelation method is one of the most commonly employed, based on the establishment of electrostatic interactions between the charged polymer chains and an oppositely charged appropriate ion or polyion, which acts as an ionic cross-linker.[140] The polymers employed for hydrogel synthesis can be classified between synthetic polymers (such as polyethylene glycol, poly(hydroxyethyl methacrylate), poly(acryl amide) Poly(vinyl alcohol), poly(N-isopropylacrylamide) and poly(vinylpyrrolidone)) and natural polymers. Natural polymers highlights for biomedical applications for its biocompatibility, biodegradability, and low toxicity.[140] Between the most usually employed natural polymers for hydrogels, gelatin, alginate, cellulose and chitosan are the most usually employed, among others.[141] Gelatin is produced from animal collagen and it is commonly employed in food, medications and cosmetics. Alginate is a negatively charged polysaccharide normally obtained from cell walls of brown algae normally employed as additive in dehydrated products and pharmaceutical preparations and wound dressings. Cellulose is a not-charged polysaccharide with applications in a large number of fields, such as construction, pharmaceuticals, biofuels, fibre and paper production, etc. Chitosan is a positively charged mucopolysaccharide obtained by deacetylation of chitin, a polymer extracted from the exoskeletons of crustacean, insects and the cellular wall of fungi. This polymer has low toxicity and immunogenicity and it is biocompatible, biodegradable, cheap and bioadhesive.[142] The mucoadhesive properties of chitosan are due to the fact that it is one of the richest natural polymers in amino groups.[143]

The innovative combination of nanoparticles and hydrogels create synergistic, unique and potentially useful properties that are not found in the individual components.[139] Although AuNPs-hydrogel hybrid materials have been employed for applications as diverse as SPR-based sensors,[144] antibacterial applications,[145] between the fields where the hydrogels provide new functionalities to AuNPs until date, PTT, thermal-responsive and oral administration highlight. Hydrogels can be of great utility to improve the AuNP applicability for PTT. As an example, hydrogels can be employed for containing AuNPs and anticancer drugs, to obtain nanocomposites for photothermal-chemotherapies.[146,147] They can also be used to increase the cell-adhesion of AuNPs with low cell internalisation in order to provide an effective PTT.[143] Macroscopic hydrogel patch containing two different types of AuNPs have also been implanted adjacent to colorectal tumours to provide a triple-combination therapy using RNA interference, drug release and phototherapy (see **Figure 16**).[148]

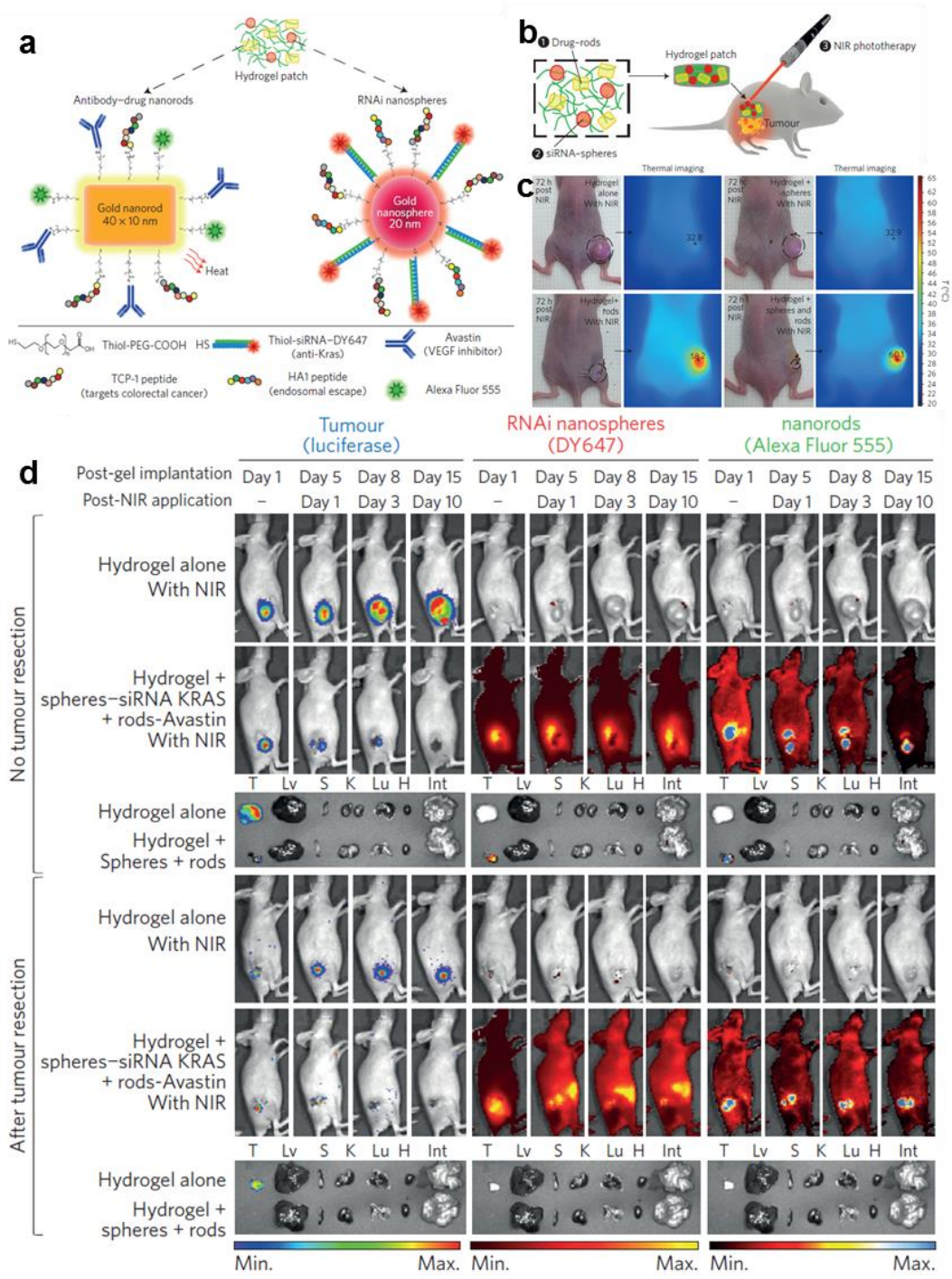
a
Hydrogel patch
Antibody–drug nanorods
RNAi nanospheres
Gold nanorod 40 × 10 nm
Gold nanosphere 20 nm
Heat
Thiol-PEG-COOH
Thiol-siRNA–DY647 (anti-Kras)
Avastin (VEGF inhibitor)
TCP-1 peptide (targets colorectal cancer)
HA1 peptide (endosomal escape)
Alexa Fluor 555
b
Drug-rods
Hydrogel patch
NIR phototherapy
Tumour
siRNA-spheres
c
Thermal imaging
Thermal imaging
d
Tumour (luciferase)
RNAi nanospheres (DY647)
nanorods (Alexa Fluor 555)
Post-gel implantation
Post-NIR application
Day 1 Day 5 Day 8 Day 15
– Day 1 Day 3 Day 10
No tumour resection
Hydrogel alone With NIR
Hydrogel + spheres–siRNA KRAS + rods-Avastin With NIR
T Lv S K Lu H Int
Hydrogel alone
Hydrogel + Spheres + rods
After tumour resection
Hydrogel alone With NIR
Hydrogel + spheres–siRNA KRAS + rods-Avastin With NIR
Hydrogel alone
Hydrogel + spheres + rods
Min. Max.

Figure 16. a) Scheme of implantable hydrogels containing the gold nanorods and siRNA–gold nanospheres with all of the molecules employed for their functionalisation. b) Strategy utilised for in vivo local triple therapy, before and after surgical removal of the tumour in an in vivo colon cancer model mouse. c) Thermographic surveillance of photothermal heating in mice implanted with hydrogels doped with drug–gold nanorods, siRNA–gold nanospheres or their combination, 72 h after the first NIR treatment. d) *Ex vivo* images of tumours and whole body organs (T, tumour; Lv, liver; K, kidneys; S, spleen; H, heart; Lu, lung; Int, intestines) and live imaging of SCID hairless congenic mice with colorectal tumour xenografts implanted with the hydrogels and the NIR treatment, either with no tumour resection or after tumour resection. Adapted with permission from.[148]

The use of stimuli-responsive hydrogels is highly extended, with responsive materials to changes in pH, temperature, electricity, magnetism, light, humidity, redox state or biomolecules.[149] However, the most interesting stimulus-responsive hydrogels for its combination with AuNPs are the thermal-responsive ones, due to the high efficiency of AuNPs as heater producers upon laser irradiation. Commonly studied temperature-sensitive polymers include acrylamide-based hydrogels, especially poly[N-isopropylacrylamide], as well as elastin-like polypeptides.[150] At a temperature-sensitive polymer's lower critical solution temperature, a reversible volume phase transition occurs.[150] At lower temperatures, it is thermodynamically favourable for water molecules to form hydrogen bonds with polar groups on the polymer chains, causing the hydrogel to be in its swollen state. At higher temperatures, the increase in Gibbs free energy causes hydrogen bonding between the water molecules and polymer chains to become thermodynamically unfavourable compared to polymer–polymer and water–water interactions, causing the water to move into bulk solution and the polymer chains to collapse onto themselves diminishing its volume.[150] This effect has been employed for drug release upon laser irradiation,[151] and even for microfluidic valves control using hydrogels with gold nanospheres and gold nanoshells by the employment of two different wavelength lasers.[152] This property could be also used for self-healing hydrogels, control of mechanical properties of the hydrogels or adhesive materials.[153]

Another field where AuNP entrapment in hydrogels could be of great interest is the oral administration. Oral administration of drugs is usually preferred over any other route of administration because it is not invasive and shows patient acceptance and long-term compliance.[154] However, most nanocarriers currently approved by the FDA depend on intravenous administration and no one has been yet approved for oral drug delivery.[155] Only near a dozen of publications have explored this approach for AuNPs and most of them have just explored the biocompatibility, absorption and biodistribution of AuNPs after oral administration. In these studies, gold nanoparticles did not show any acute toxicity *in vivo,*[156–158] and only minor side-effects (e.g. activation of immune system,[159,160] increase of alkaline phosphatase activity[157], etc.) are described but these side-effects were reversible even after 30 days of administration.[160] It is remarkable that AuNPs have rarely been studied for applications after oral administration, but two of the few studies were employing AuNP-chitosan nanoparticles.[161,162] Chitosan has been demonstrated as crucial for the intestine absorption of the AuNPs.[162] In this two studies, chitosan-AuNPs systems have been employed as oral vaccines proof of concept[161] and for colorectal liver metastasis cancer treatment as small interfering RNA delivery agents,[162] with promising and interesting results in both cases. This low employment of oral administered AuNPs is almost certainly due to the fact that most of the AuNPs without chitosan appear in the faecal content without been absorbed by the intestine,[163] probably because of the aggregation and loss of functionality caused by the gastric environment during digestion. Consequently, could be of crucial interest to develop novel strategies to protect and increase AuNPs absorption to facilitate the oral administration of AuNPs.

The hydrogel-AuNP entrapment can be made at different size scales, including nanometric hydrogels (nanogels), micrometric hydrogels (microgels) or macrometric hydrogels (bulk hydrogels). For nanogels production, several methodologies can be applied, including but not limited to the polymerisation in templates (such as miniemulsion, suspension, liposomes, and so forth), cross-

linked micelles, polymer reaction of linear chain, nanoparticles and nanocomplexes or physical nanogels produced by hydrogen bonding, ionic bonding, coordination bonding or hydrophobic interaction or protein denaturation.[164] However, a precise nanogel production control is limited technologically due to its small size and the number of AuNPs that they can carry is very limited. There is an extensive technological development of bulk hydrogel synthesis for biomedical applications,[165,166] however its high size limits is application mainly to tissue engineering, 3D printing and surgically implantable hydrogel patch.

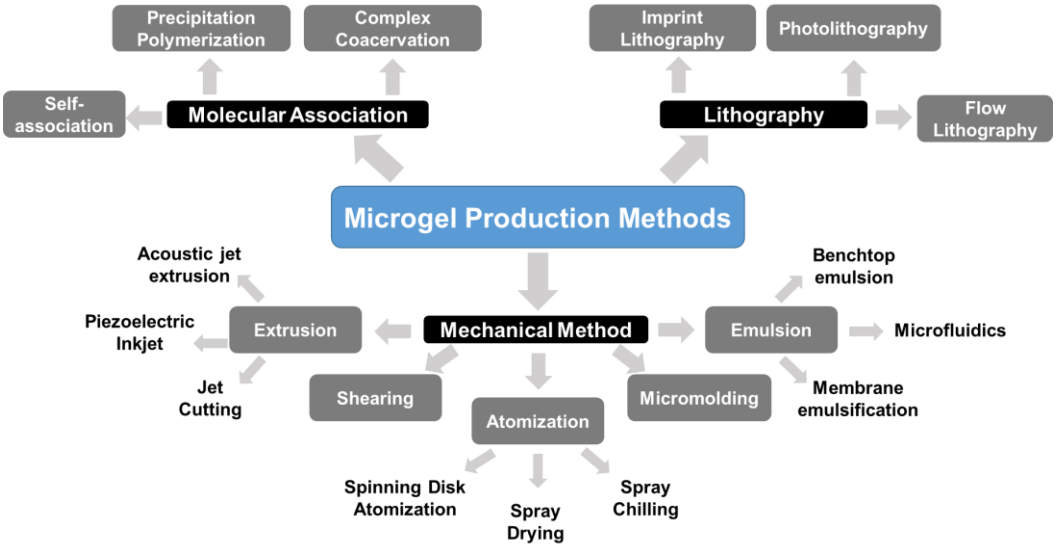

Figure 17. Schematic classification of microgel production methodologies.

Due to its proper ratio between small size and number of AuNPs encapsulation capacity, together with a high controlled synthesis technology development, microgels offer an interesting option for AuNP entrapment for a wide variety of biomedical applications. Microgels have played centre stage in the biomedical sector with an extensive employment in applications such as drug delivery, controlled release and cell/tissue targeting systems.[167] The high number of microgel production technologies can be classified depending on the strategy

employed to provide the micrometric in molecular association methods (such as precipitation polymerisation, self-association or more complex coacervation strategies), mechanical methods and lithographic techniques (see **Figure 17**), such as imprint technology, photolithography and flow lithography.[168,169] Between the mechanical methods, the hydrogels can be produced by extrusion, shearing methods, atomisation, micromolding or emulsion; with several techniques for each of the methods. From all these wide variety of approaches that have been developed to manufacture microgels, all of them have own advantages and disadvantages making them more or less suitable for specific applications.[170]

When talking about microparticle production methodologies, microfluidics is emerging as one of the leading production techniques due to the possibility of having a continuous and automatic production of microparticles with high reproducibility, size control and ease by which to encapsulate molecules in multi-compartments.[171] Although especially useful for microemulsion production or microparticle synthesis that involves several liquid immiscible phases, the use of microfluidic for microgel production presents some challenges when all the components of the microgel are dissolved in the same phase (i.e. aqueous phase). In these cases, a common strategy relies on using an extra non-miscible phase to separate the microdroplets that will form each microgel particle,[172,173] where a subsequent phase separation step is also required.[172] The challenge increases when it is necessary to mix a gelling agent with the polymer, where a careful optimisation of the set up parameters is required in order to avoid the clogging of the system.[172] The need of complex channel geometries for this strategy and the slow production rate of each nozzle along with the fact that AuNPs for biomedical applications are commonly dispersed in aqueous phase make the use of microfluidics for microgel entrapment of AuNPs a complicated and rarely employed technique.

Taking the aforementioned factors into account, inkjet technology represents an alternative technique that should be considered for AuNP hydrogel entrapment in

microparticles for biomedical applications such as, therapeutic agents and for tissue engineering. Although it has been previously employed for gold nanoparticle printing specially for sensor-related applications, inkjet printing represents an entirely unexplored technique for AuNP-containing microgel production. Although this technology has been extensively employed for ink printing in a large number of commercial printers, it has only employed few times for microparticles production made of alginate,[174,175] poly lactic-*co*-glycolic acid[176] or lipids.[177] The inkjet ejection system is formed by a header with a small nozzle (typically 20-100 μm) filled with liquid and with a surrounding piezoelectric element in contact with the fluid (**Figure 18**). A controlled voltage is applied to the piezoelectric and it generates a sudden deformation of the fluid cavity and induces a pressure impulse, origin of the ejected drop.[178] With this method, droplets with sizes in the range of the nozzle orifice diameter and linear speeds of few metres per second are typically generated at frequencies of 1 to 20 kHz.[178] Main advantages of inkjet as a highly interesting technology are excellent control and reproducibility of particle synthesis, high efficiency encapsulation, easiness to scale-up and continuous and automatic production. However, nozzle obstruction in the case of impurities and the need to carefully optimise the ejection parameters to achieve a stable ejection of the fluid makes the inkjet technology a technique that required a trained specialist to optimise the system and a re-optimisation for each system.

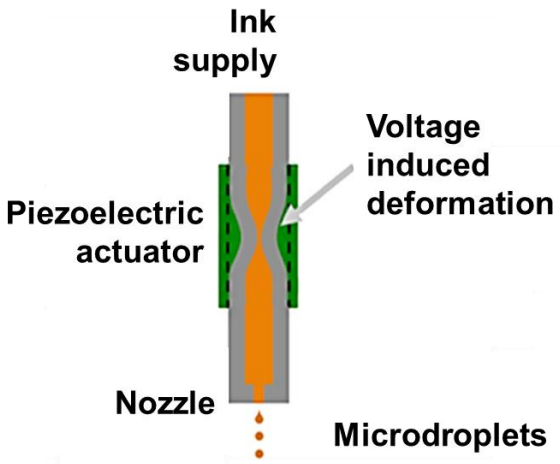

Figure 18. Schematic representation of drop on demand piezoelectric inkjet technology. Adapted with permission from[178]

2. Objectives

The main goal of this thesis consists of improving the potential of AuNPs for biomedical applications by 3 principal objectives: 1) understanding how AuNP shape and surface functionalisation affects their use in biosensing 2) understanding how AuNP shape influence their use for photothermal therapy and 3) how hydrogel encapsulation methodologies can be used to improve their therapeutic application. This research was aligned with the aims of the project Nanogram (Plan Nacional de I+D+I (SAF2014-54763-C2-2-R)) and the project NanoplasmiRNA (European EuroNanoMedII Project (Call 2015)) in order to focus in the next specific objectives:

- Development of novel strategy to take advantage of gold nanoparticle inherent physicochemical properties for their use as SPRi signal enhancers of miRNA sensing, detailed in Section 3.1.1.
- Comparison of different biofunctionalisation strategies, shapes and sizes of AuNPs for the SPRi signal enhancement of miRNAs in order to achieve the most effective AuNP with the best functionalisation for the future clinical setting of this technique, detailed in Section 3.1.2.
- Comparison of different physicochemical properties of AuNRs and AuNPrs related with its applicability as photothermal therapy agents, optimising its synthesis for the application and focusing on its photothermal properties, cell death efficacy and cell interaction, detailed in Section 3.2.1
- Improvement of the AuNPs performance for photothermal therapy by exploring an alternative strategy based on hydrogel encapsulation to increase its cell interaction, detailed in Section 3.2.2
- Optimisation of novel methodologies for high efficiency encapsulation of AuNPs in chitosan hydrogels to increase its future applicability and improve its physicochemical properties, detailed in Section 3.3.

3. Results and discussion

3.1. Harnessing of the physicochemical properties of AuNPs for SPRi signal enhancement

3.1.1. Establishing a universal approach for multiple miRNA detection using a single AuNP SPRi enhancer

Despite the great potential of microRNAs (miRNAs) as circulating stable diagnostic markers or predictive markers of disease progression, they have not yet been screened in large patient cohorts thus delaying their introduction into clinical practice. The small size, low concentrations, varying abundance and sequence similarity of miRNAs make them challenging to detect using current profiling and quantifying methods, such as PCR, deep sequencing and microarrays.[179] Therefore, there is a need to develop new and technologically improved analytical approaches and surface plasmon resonance (SPR) has made a large contribution to the research field of miRNA detection.[180] However, the low molecular weight of miRNAs and their low concentration in clinical samples require of SPR enhancers.[181] In addition, most of the proposed strategies require the use of as many sequence-specific regents as the number of miRNAs sequences to be detected or multiple enhancing steps.

In multiple sclerosis (MS), a highly heterogeneous, chronic and immune-mediated demyelinating disease,[182] a clinical evaluation and magnetic resonance imaging constitute the only available means of diagnosing and monitoring MS.[183] Some miRNAs have been also reported as promising MS markers,[184,185] but these still need to be validated in large patient cohorts. MS is therefore an exemplary and pertinent disease for which the development of efficient and versatile multiplexing miRNA detection methods may help patient care.

The aim of this study is to develop a single, universal SPR enhancer capable of simultaneously detecting multiple miRNAs with sensitivity below pM by a simple approach and without the use of enzymatic reactions, sandwich strategies, partial

sequences hybridisation steps, multiple reagents or multiple enhancing steps. To this end, and as showed in **Figure 19**, we combined: 1) the universal sequence-independent recognition of miRNA thanks to the use of an Ab against all DNA/RNA hybrids,[186] 2) the SPR-enhancing properties of gold NPs due to its physicochemical properties, properly functionalised with the mentioned Ab and 3) the use of a SPR-imaging (SPRi) instrumentation that offers the capability to simultaneously detect in real-time multiple (potentially hundreds) molecular interactions in a multi array format. To the best of our knowledge, anti DNA/RNA Abs have never been conjugated with spherical gold nanoparticles (herein AuNS) for enhanced SPR-based strategies before. Thanks to the employment of neutravidin-coated gold nanospheres (AuNS@Neutrav) that interacted with a previously biotinylated antibody (Ab) against DNA/RNA hybrids, this nano-enhancer guarantees the recognition of any miRNA sequence adsorbed on a surface properly functionalised with different DNA probes at the same time, even at a low ligand concentration, by performing a single enhancing injection.

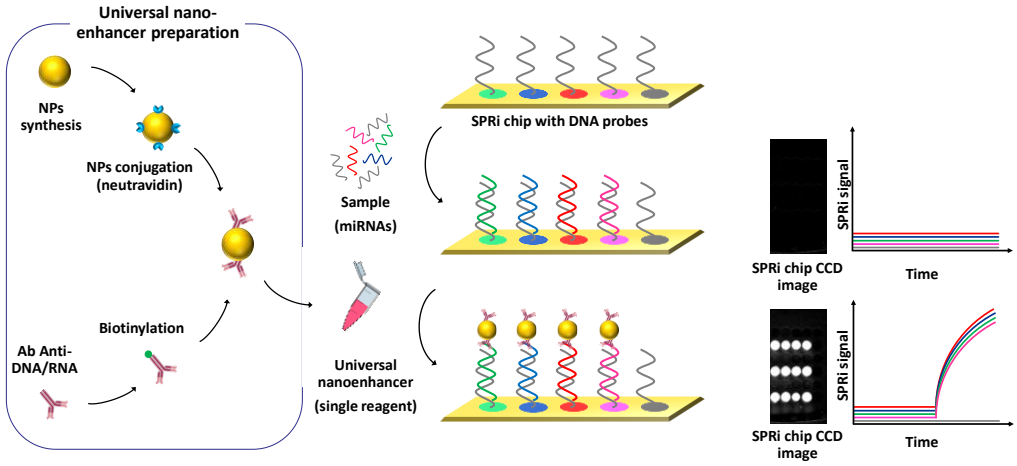

Figure 19. Schematic representation of the strategy used for the simple and simultaneous detection of multiple miRNAs using the same nanoenhancer. Spherical gold nanoparticles (AuNSs) were covalently functionalised with neutravidin in order to interact with a biotinylated antibody anti DNA/RNA hybrids and to recognise the specific hybridisation of each miRNA sequence with the complementary sequence of DNA previously deposited

on the SPRi chip, increasing several orders of magnitude the signal in the SPRi equipment until detectable levels.[77]

3.1.1.1. AuNS preparation

Gold nanoparticles were chosen for this study based on the high density of gold along with the ease by which AuNPs can be functionalised with biomolecules (detailed in the **Introduction section**). These two properties make gold nanoparticles one of the best candidates for SPRi signal enhancement, as SPRi signal is directly proportional to the weight of the molecules attached to the surface. Due to initial problems of stability of different AuNPs during the first trials using SPRi, for this study we decided to employ the simplest and most stable AuNP that we could subsequently functionalise with the proteins needed for the RNA recognition. Spherical gold nanoparticles with a diameter of around 14 nm (AuNS) were stabilised using a PEG-carboxylated coverage employing a previously reported protocol with minimal modifications.[187] The AuNS were prepared using a commonly employed protocol that utilises citrate as the reducing agent, producing AuNS of 14±1 nm with a narrow size distribution (see **Figure 20**). After the synthesis AuNSs were coated with PEG chains with carboxyl end-groups. The coated nanoparticles showed excellent colloidal stability and no sign of aggregation, even after many months of storage. The carboxylic groups of the AuNS surface not only provide a remarkable stability in the buffers employed for SPRi sensing but also enabled the subsequent protein functionalisation (detailed in subsequent section). The gold concentration of the AuNS was quantified by ICP-AES and it can be correlated with its absorbance at 450 nm in order to calculate its extinction coefficient, which resulted 11.3 $mL \cdot mg^{-1} \cdot cm^{-1}$. Taking into account the diameter of the AuNS, the density of gold (19.3 g/cm^3) and assuming a spherical shape it is possible to estimate the nanoparticle gold weight in $1.67x10^7$ g/mol. It should be noted that the possibility and influence of employing

different AuNPs from the AuNS described in this section for the same SPRi application is investigated in **Section 3.1.2**.

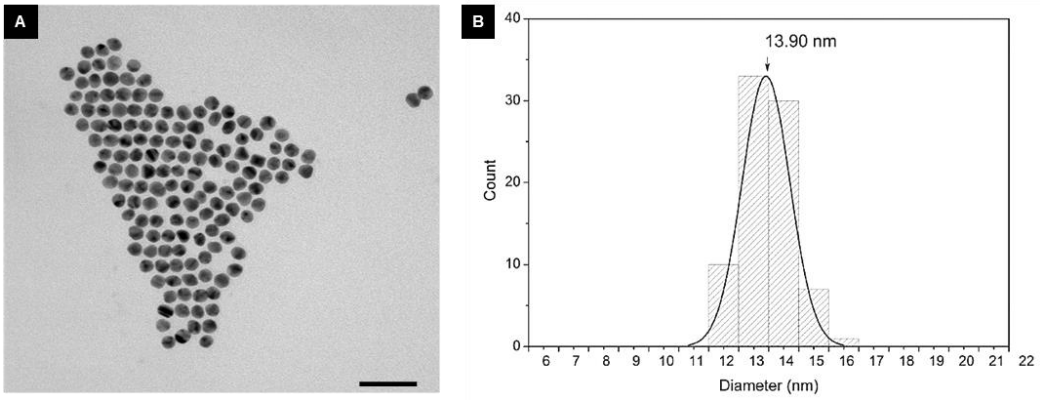

Figure 20. A) Transmission Electron Microscopy (TEM) image of AuNS, scale bar = 50 nm. D) Size distribution of AuNS measured from TEM images. Adapted with permission from[77]

3.1.1.2. AuNS direct functionalisation with Ab anti DNA/RNA

Our first approach consisted in the direct functionalisation of the AuNSs with the antibody against DNA/RNA hybrids by covalent bonding. The antibody was conjugated onto the AuNSs using EDC/sulfo-NHS commonly employed protocol that permits the linkage between the carboxylic end-groups of the PEG with the terminal amine groups of the proteins to form a covalent amide bond. As a proof of concept of this strategy, and in order to understand the maximum number of antibodies that could be linked per nanoparticle, we functionalised the AuNS with antibody against horseradish peroxidase (HRP). The main advantage of this model is that the functionalisation of the AuNPs with the antibody and its functionality can be easily tested and quantified by a simple colorimetric reaction catalysed by the HRP. By this way the AuNPs were functionalised with increasing ratios of Ab:AuNPs, and incubated with HRP. After that, the unbound (not-conjugated) HRP was discarded in the supernatant following centrifugation of the

particles and the activity of the AuNP-bound HRP was monitored by colorimetric reaction of ABTS (2,2'-azino-bis(3-ethylbenzothiazoline-6-sulfonic acid)). The HRP catalyse the reaction of ABTS with hydrogen peroxide producing a change of colour in the ABTS that could be easily monitored by its absorbance at 420 nm. By this approach it was possible to confirm that the anti-HRP antibodies maintain their functionality and calculate the proper number of antibody per AuNS that should be employed for further studies (see **Figure 21**). All the AuNS covalently functionalised with the antibodies possessed a higher activity than the negative controls (without HRP, without the antibody or just by adsorption of the antibody to the AuNS surface without covalent bonding due to the absence of EDC during the functionalisation). From the different AuNS:Ab ratios tested, the ratio 1:3.3 was the selected because it showed the best compromise between high activity and quantity of antibody needed, as can be seen in **Figure 21**.

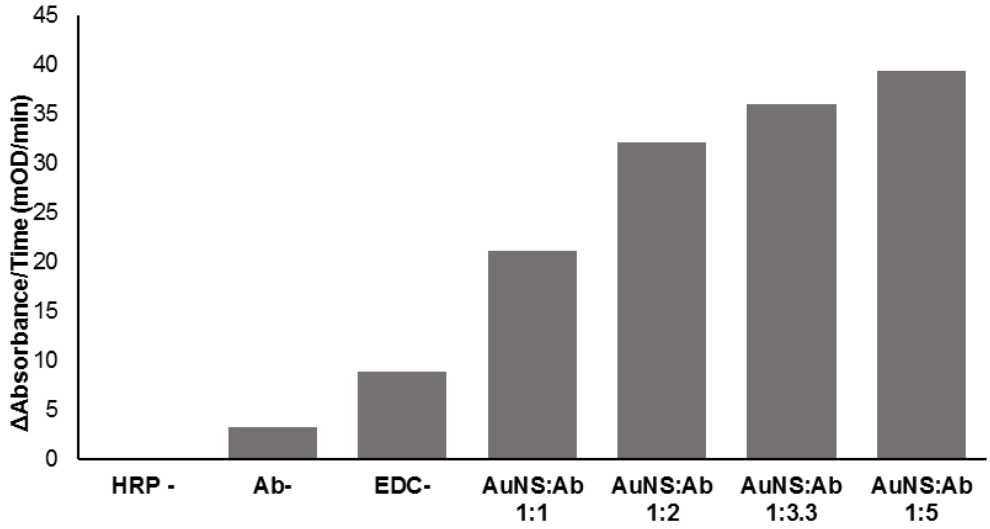

Figure 21. HRP enzymatic activity of various AuNS functionalised with Ab against HRP with increasing AuNS:Ab ratios (1:1, 1:2, 1:3.3 and 1:5) after incubation with HRP. Three negative controls were also tested: the AuNS functionalised with the antibody but not incubated with the HRP (HRP -), the AuNS without antibody (Ab -) and the AuNS linked to the antibody just by adsorption of the antibody to the AuNS surface without covalent bonding due to the absence of EDC during the functionalisation (EDC -). An increasing

HRP activity can be observed due to the covalent bonding of the Ab and the increasing ratio of Ab per AuNS.

Using this strategy, we functionalised in the same manner the AuNS with anti DNA-RNA hybrid antibody and including as a positive control of the functionalisation protocol the previously described anti-HRP antibody. However, even in the parallel case of the anti-HRP linked to the AuNP, which retained its activity, in the case of the AuNPs functionalised with anti-DNA/RNA they were not able to recognise the RNA/hybrid as demonstrated in the SPR sensogram in **Figure 22**. In this experiment, it can be clearly seen how the Ab anti-DNA/RNA alone was able to highly amplify the signal of the miRNA miR-103 while the AuNS functionalised with the Ab anti-DNA/RNA were not able to amplify the signal displaying similar small signal both for the sensing of miR-103 and the negative control that has not been added of miR-572. We attributed this lack of activity to a higher sensibility to denaturation of the anti-DNA/RNA during the functionalisation protocol in comparison with the anti-HRP antibody or to a different orientation of the antibody during the functionalisation caused by the different isoelectric point of both antibodies. For this reason we tried an alternative strategy, described in **Section 3.1.1.3**.

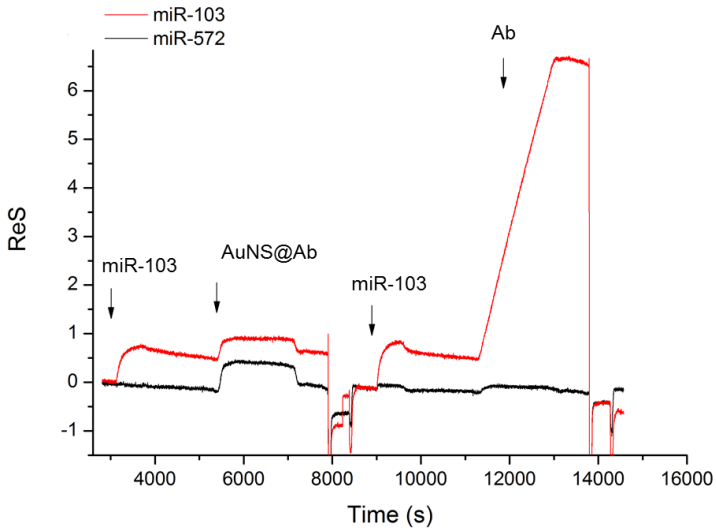

Figure 22. SPRi sensogram of the activity of AuNS functionalised with the Ab anti DNA/RNA hybrid (AuNS@Ab) and just the single Ab anti DNA/RNA hybrid (Ab) after the injection of miRNA miR-103 at 500 nM in the chip spots functionalised with DNA to detect the miR-103 (red) or miR-572 (black) which was not injected. It can be clearly seen that the single Ab anti DNA/RNA hybrid produced a high specific amplification of the signal while the AuNS@Ab only displayed a low non-specific signal.

3.1.1.3. AuNS functionalisation with neutravidin

After the unsuccessful attempt to directly link the antibody to the AuNS surface through a covalent amide bound, we proposed an alternative strategy based on avidin/biotin interaction. This strategy consists of using AuNS functionalised with neutravidin (AuNS@neutravidin) that interacts with anti-DNA/RNA hybrid Ab previously functionalised with biotin. Subsequently, this bio-complex was utilised to recognise the miRNA presented in the SPRi chip enhancing its SPR signal, as previously described (**Figure 19**). In order to define the best approach to guarantee a good neutravidin conjugation, but also to prevent a loss in the stability of the AuNS, we optimised the protocol in order to define the best amount of neutravidin required to functionalise each AuNS. Neutravidin was conjugated onto the AuNPs using the previously described EDC/sulfo-NHS coupling strategy

and the neutravidin conjugation was followed by gel electrophoresis and UV-vis spectroscopy and TEM measurements (**Figure 23**). Among these approaches, gel electrophoresis was mainly used to visually select 32 nM as final optimal neutravidin concentration corresponding to the minimum amount of neutravidin to obtain the functionalisation of all AuNS (i.e. no residual band related to non-conjugated AuNS was visible).

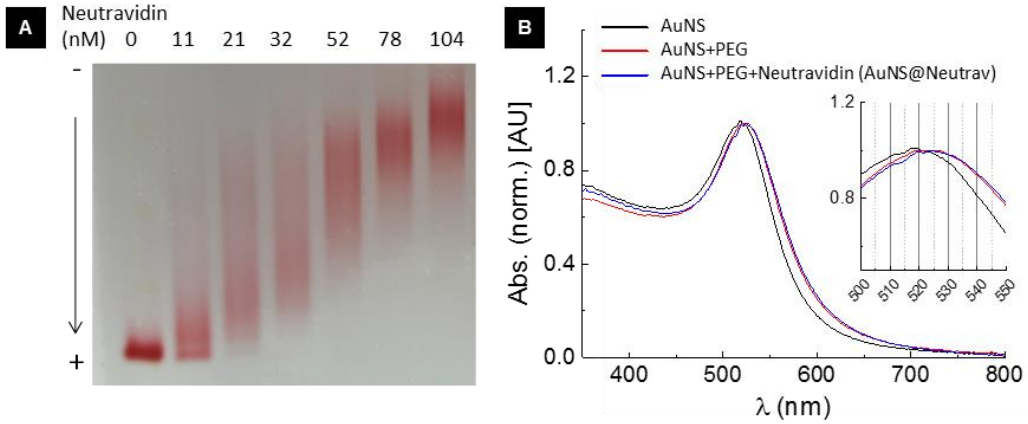

Figure 23. A) Gel agarose electrophoresis used to follow and optimise the conjugation between neutravidin and AuNS with increasing ratio Neutrav/AuNS. The fourth line from the left represent the reaction using 32 nM neutravidin as final concentration and it is the best condition used for further experiments in this study. This condition was selected because the amount of neutravidin used here was the minimum to guarantee the functionalisation of all the AuNS (i.e. no residual bands related to non-conjugated AuNS were visible in this line); B) UV-visible spectra of AuNS (black), AuNS covered by PEG (red) and AuNS@Neutrav (i.e. AuNS+PEG+neutravidin) (blue) showing the small displacement in the LSPR band. Adapted with permission from[77]

In order to precisely quantify the neutravidin that was linked to the AuNS a non-common radiolabelling technique employing iodine-125 radionuclide for protein quantification was carried out.[188] Radio-labelling permits the precise quantification of very low protein levels and is one of the few methods that can be used to measure the amount of protein bound and unbound to the nanoparticles at the same time.[188] For this reason, radiolabelling is a very useful and reliable tool for protein functionalisation of nanoparticles when you are able to easily separate the

non-linked proteins from your nanoparticles. Radiolabelling of proteins with iodine-125 is based on the use of chloramine T that acts at oxidising agent catalysing the covalent binding of iodide to several amino acids of the proteins. Before starting with the neutravidin quantification, we evaluated a separation strategy utilising PD MiniTrap G-10 columns to separate unbound iodine-125 from the proteins (see **Figure 24**). In this study, neutravidin, iodide and tyrosine were passed through the column and eluted in the same conditions that would be employed in the radiolabelling protocol. The eluted fractions of 1 mL were collected and the concentration of each of these compounds was determined by UV-Vis absorbance, showing that all the neutravidin appeared just in the first elution fraction while the iodide and tyrosine appeared between the fourth and the sixth elution fraction, demonstrating that the separation methodology was perfect for our radiolabelling study as the not covalently linked iodide would remain retained in the column.

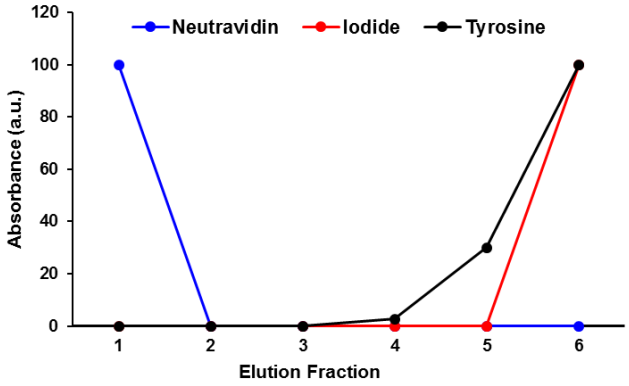

Figure 24. Elution profile of neutravidin (blue), iodide (red) and tyrosine (black) from a PD MiniTrap G-10 column, collecting elution fractions of 1 mL and measuring the UV-Vis absorbance of each compound.

After that the radiolabelling protocol of neutravidin was performed and the functionalisation of the AuNS with the neutravidin-I^{125} was carried out, measuring the gamma emission of both the AuNPs and the supernatants as an internal control and compared with gamma emission of the original amount of neutravidin-

I^{125} employed for the functionalisation. The selected concentration of neutravidin was functionalised employing EDC/sulfo-NHS linkage and compared with a non-covalent absorption control performed in the same conditions but without EDC. Coupling the theoretical average weight of the AuNS ($1.67x10^7$ $g \cdot mol^{-1}$) with data acquired by means of ICP-AES and by radio-labelling protein determination using iodine-125 radionuclide made it possible to quantify the number of neutravidin molecules attached to each nanoparticle (see **Table 1** for details). Surprisingly, 1.60±0.25 neutravidin molecules per AuNSs were linked in the case of non-covalent adsorption, probably due to unspecific adsorption of the proteins to the AuNS surface. However, the results showed that a mean of 2.58±0.19 neutravidin molecules per AuNS were conjugated in the case of EDC/NHS covalent coupling thus demonstrating the utility of covalent conjugation, which was employed in all the subsequent experiments.

Table 1. Radiolabeling results related to the quantification of neutravidin molecules conjugated on average on single AUNS.[77]

	Neutravidin used in the reaction mix (pmol)	**AuNS used in the reaction mix (pmol)**	**Neutravidin linked to AuNS after centrifugation (calc. by Gamma emission)**	***SD (n=3)***	**Neutravidin linked (pmol)**	**Neutravidin/AuNS**	***SD (n=3)***
Neutravidin + AuNS (+EDC)	46.7	1.42	7.82 %	*0.58*	3.65	2.58	*0.19*
Neutravidin + AuNS (-EDC) (non-covalent absorption)			4.84 %	*0.76*	2.26	1.60	*0.25*

3.1.1.4. Interaction of AuNS@neutrav with the Ab anti DNA/RNA and their enhancing efficiency for miRNA detection

After the unsuccessful direct covalent functionalisation attempt described in **Section 3.1.1.3** and taking into account the importance of using a robust and controlled procedure for the production of the nanoenhancer,[189] before

functionalising the AuNS@Neutrav with the biotinylated anti-DNA/RNA antibody, several Ab:biotin molar ratios (1:5, 1:25, 1:50 and 1:75) were tested taking into account a biotinylation reaction yield of around 10 % according to protocol suggested by manufacturer. This test was done in order to compare the activity of the original Ab and with that of the differently biotinylated Abs injected immediately after the injection of a high concentration of miRNA (500 nM) and determine signals at equilibrium binding conditions (**Figure 25a**). As expected, increasing the biotinylation molar ratio led to a progressive reduction in Ab activity due to the chemical modification of the antigen-binding site (**Figure 25a**).

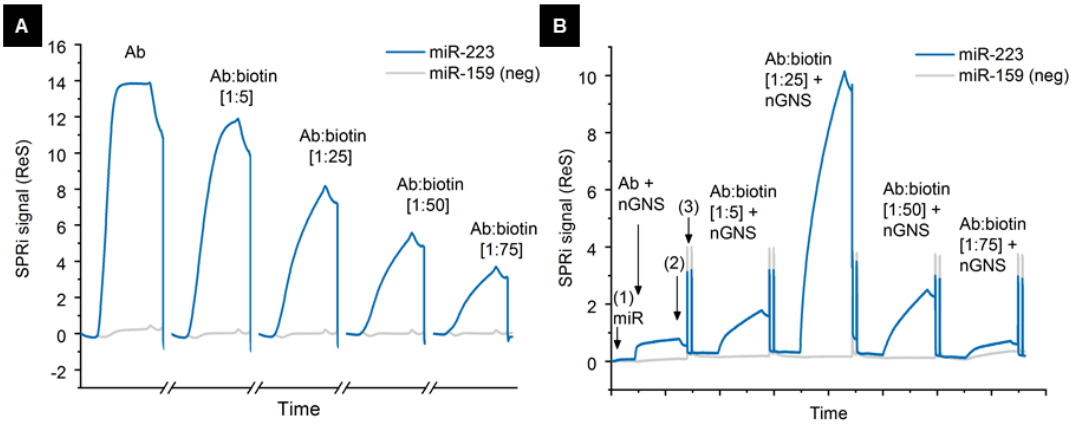

Figure 25. A) Biotinylated Ab activity tests. The sensograms relates the activity of the original Ab and the differently biotinylated antibodies (Ab:biotin molar ratios 1:5, 1:25, 1:50, and 1:75) injected (5 nM, 500 µL, 10 µL ml-1) after the injection of miR-223 (500 nM, 500 µL, 10 µL min-1) (not shown). B) Enhancement test (see **Figure 26** for larger graphs). The sensogram relates the injection of AuNS@Neutrav (0.25 O.D. at Abs. λ 524 nm) mixed with 5 nM of the original Ab and the differently biotinylated antibodies (Ab:biotin molar ratios 1:5, 1:25, 1:50, 1:75) (800 µL, 10 µL min-1) after the injection of 1 nM of miRNA 223 "(1)" (500 µL, 50 µL/min). Each Ab+AuNS injection, was followed by a dissociation phase (running buffer "(2)") and chip regeneration phase (double injection of NaOH 50 mM "(3)"). The signal in A and B are the average of three spots after the subtraction of the signals from the negative references (PolyA sequences) spotted in parallel on the same chip. Both sensograms also show the signal related to miR-159 (not injected).

On the other hand, **Figure 25B** and **Figure 26** show the results when the different Abs were mixed with AuNS@Neutrav and injected in the SPRi machine after the injection of a low concentration of miRNA (1 nM). This experiment was carried out with the aim of selecting the optimal Ab:biotin molar ratio and verifying the best conditions for SPRi enhancement. The biotinylated Abs mixed with AuNS@Neutrav greatly enhanced SPRi, thus confirming AuNS@Neutrav functionalisation, neutravidin activity and Ab coupling. The SPRi signal progressively increased when moving from the non-biotinylated Ab (Ab:biotin molar ratio 1:0) to a ratio of 1:25 biotinylated antibodies, which led to approximately 900-fold enhancement (compared to non-enhanced SPRi miRNA detection), and began to decrease when the higher ratios of 1:50 and 1:75 were used. All of these experiments were carried out with a sequence of miRNA miR-223 that specifically bound DNA with the complementary sequence linked to the chip and compared with a negative control that consisted of a DNA sequence against a miRNA that was not injected, showing a very sequence-specific SPRi response in all the cases. As shown in **Figure 26**, the AuNS@Neutrav alone did not show any significant signal arising from non-specific interactions between the AuNS@Neutrav and the SPRi chip surface. In the same experiment, it can be seen that the original non-biotinylated Abs used alone showed similar enhancement to that observed when the AuNS@Neutrav were mixed with non-biotinylated Abs (19-fold and 17-fold, respectively). This suggests that the non-biotinylated Abs do not spontaneously bind AuNS@Neutrav and that their combination does not lead to any significant additional signal due to non-specific interactions. It is finally worth noting that in these experiments and all of the further experiments involving model or real samples, the mixture of AuNS@Neutrav/Ab used as only enhancing reagent was stable for days without any further purification if stored at 4°C.

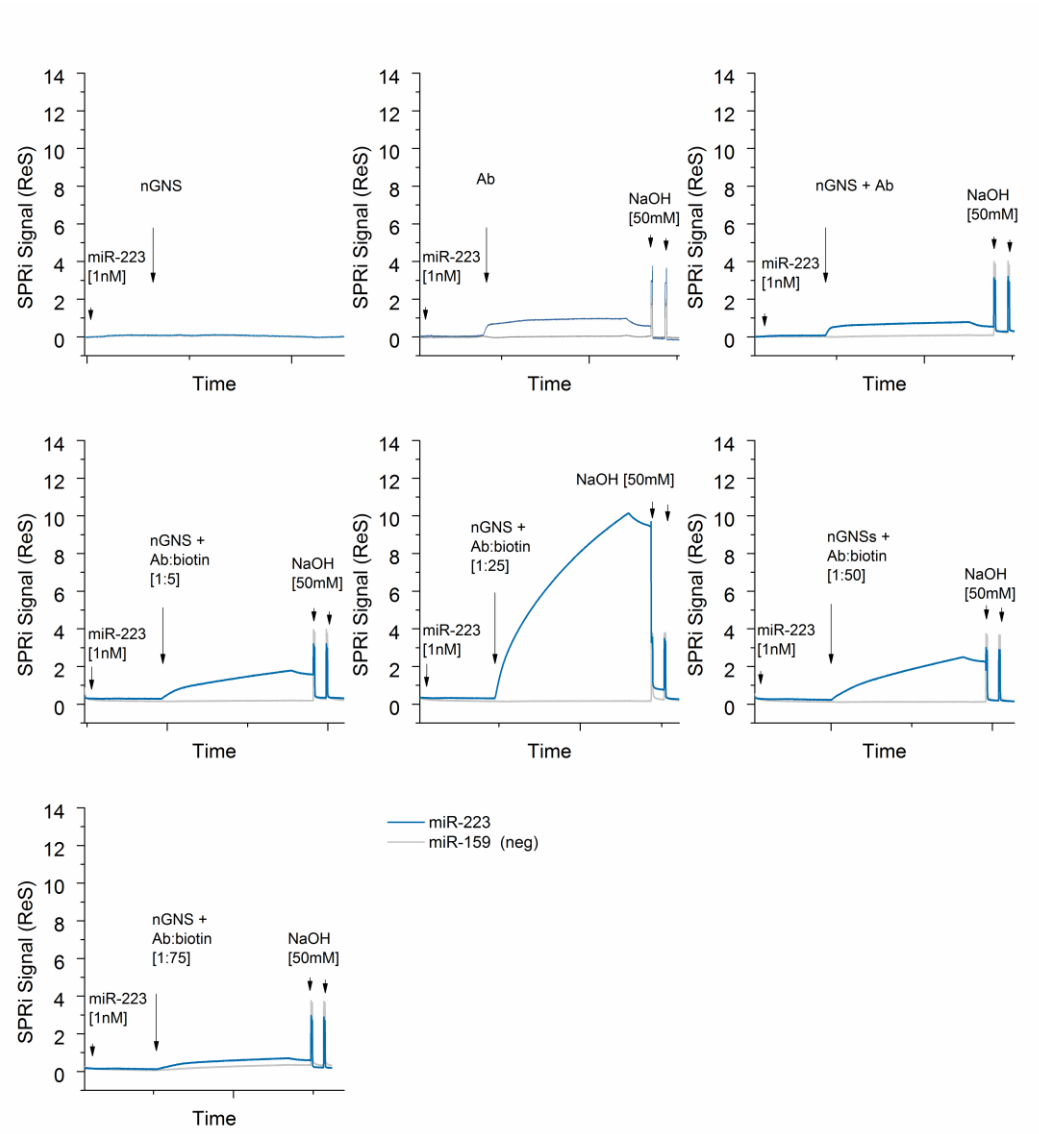

Figure 26. Enhancement derived by AuNS@Neutrav and Ab only. For each panel the injection of miR-223 (1nM, 500 µL, 50 µL/min) is followed by the injection of AuNS@Neutrav alone (0.25 O.D. at Abs. λ 524nm) and anti-DNA/RNA Ab 5 nM or AuNS@Neutrav mixed with differently biotinylated antibodies (ab:biotin molar ratios 1:5, 1:25, 1:50, 1:75) 5 nM (800 µL, 10 µL/min). All the signals were corrected by subtracting the corresponding negative control reference signals (PolyA). For each panel a negative control miRNA spot (miR-159) was also reported as additional negative control signal.[77]

As previously described, the 1:25 ratio of biotinylated antibodies give the better response while increasing the amount of biotins produced a decrease in the SPRi signal. In order to clarify these data and to determine the number of Abs effectively linked to the AuNS@Neutrav, radio-labelling experiments were also used to understand the importance of Ab biotinylation, (**Figure 27C**). They were performed similarly to the methodology employed in **Section 3.1.1.3** but in this case radio-labelling the antibodies instead of the neutravidin, the gamma emissions produced by antibodies was quantified after AuNS@Neutrav interaction. By this way the number of linked Ab can be easily calculated (see more details in **Materials and methods section** and **Table 2**). The result confirmed that, under our experimental conditions and considering all the biotinylation ratios tested, the number of biotinylated Abs linked to each AuNS@Neutrav are between 0.7 to 4.1 and this is compatible with the number of biotin-binding sites provided neutravidin molecules immobilised on the nanoparticles (i.e. 2.58 neutravidin molecules/AuNS multiplied by maximum four neutravidin binding sites = a maximum of ~10 Abs/AuNS@Neutrav). More in details, AuNS@Neutrav conjugated with 1:5 biotinylated antibodies were linked with less than one Ab (0.73); the most active AuNS@Neutrav (i.e. those conjugated with an Ab:biotin ratio of 1:25) were linked with an average of 1.9 Abs, whereas the less active AuNS@Neutrav conjugated with more biotinylated Abs (i.e. at molar ratios of 1:50 and 1:75) were linked with respectively 2.4 and 4.1 Abs. These numbers are also close to the number of biotins supposed to be covalently bound to each Ab considering the biotinylation reaction yield of around 10 % as claimed by manufacturer (i.e. 0.5, 2.5, 5, 7.5 biotin/Ab for 1:5, 1:25, 1:50 and 1:75 molar ratio respectively). As the enhancement factor did not linearly correlate with Ab activity or the number of immobilised Abs (see **Figure 27**), different biotinylation ratios may not only affect Ab activity and functionalisation efficiency but also the orientation of the immobilised Abs. When taking into account these data with the previously described studies of the activity of the biotinylated antibodies alone and together with the AuNS@neutrav (**Figure 27**),

it can clearly be seen that the AuNS@Neutrav linked with high biotin content Abs were less active due to Ab damage, wrong Ab orientation or steric hindrance. In addition the best results were obtained with intermediate biotin ratios because a high biotinylated ratio produced non-functional antibodies and with low biotinylated ratio the antibodies did not link to the particles. These experiments demonstrate that for the preparation of active nanoparticles-Ab conjugates it is required proper screening, control and optimisation steps, as previously described.[190]

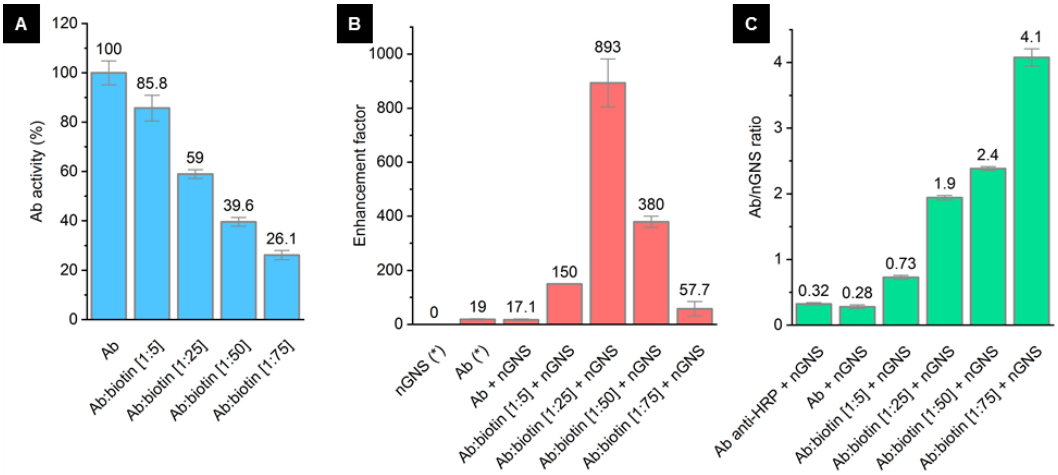

Figure 27. A) Activity of Abs functionalised with increasing amounts of biotin; the SPRi signals were normalised using a non-biotinylated Ab as the reference (100 %). B) SPRi enhancement induced by the original Ab, the AuNS@Neutrav, and the AuNS@Neutrav conjugated with differently biotinylated Abs; enhancement was calculated by dividing the SPRi signals produced by the Ab+AuNS@Neutrav by those produced by 1 nM of miR-223 alone injected before the Ab+AuNS@Neutrav. See the sensograms in **Figure 26** for the enhancement produced by the AuNS@Neutrav and the original Ab alone. C) Results of the radio-labelling experiments; the values refer to the average number of Abs linked to each AuNS@Neutrav (see **Table 2** for details). Adapted with permission from[77].

Table 2. Radiolabelling results related to the quantification of Ab anti DNA/RNA hybrid molecules conjugated on average on single AuNS@Neutrav depending on the Ab biotinylation degree.[77]

	Ab used in the reaction mix (pmol)	**AuNS@Neutrav used in the reaction mix (pmol)**	**% Ab linked to AuNS@Neutrav after centrifugation (calc. by Gamma emission)**	***SD (n=3)***	**Ab linked (pmol)**	**Ratio Ab :AuNS @Neutrav**	***SD (n=3)***
Antibody anti-HRP (negative control)	3.00	0.45	4.81	*0.30*	0.14	0.32	*0.02*
Ab			4.18	*0.46*	0.13	0.28	*0.03*
Ab:biotin (1:5)			10.84	*0.43*	0.33	0.73	*0.03*
Ab:biotin (1:25)			28.94	*0.53*	0.87	1.94	*0.04*
Ab:biotin (1:50)			35.54	*0.44*	1.07	2.39	*0.03*
Ab:biotin (1:75)			60.73	*1.98*	1.82	4.08	*0.13*

3.1.1.5. Analytical performance of miRNA detection

As previously stated, the specificity of the signal produced by the Ab+AuNS@Neutrav can be seen in the sensogram (**Figure 27a**) and the chip CCD differential image (**Figure 28a**), neither of which shows any significant signal related to the chip surface or negative control spots. Two different negative controls (a PolyA sequence used as a blank for the surrounding spot and a specific recognition sequence of the miRNA miR-159 without the injection of this miR-159 used as a negative control) were employed to ensure the specificity of the system and in any of them could be observed any remarkable signal. The interaction between the Ab+AuNS@Neutrav and the SPRi chip was also investigated by SEM at the end of an enhancement experiment without the regeneration steps normally used to remove interacting/adsorbed molecules.

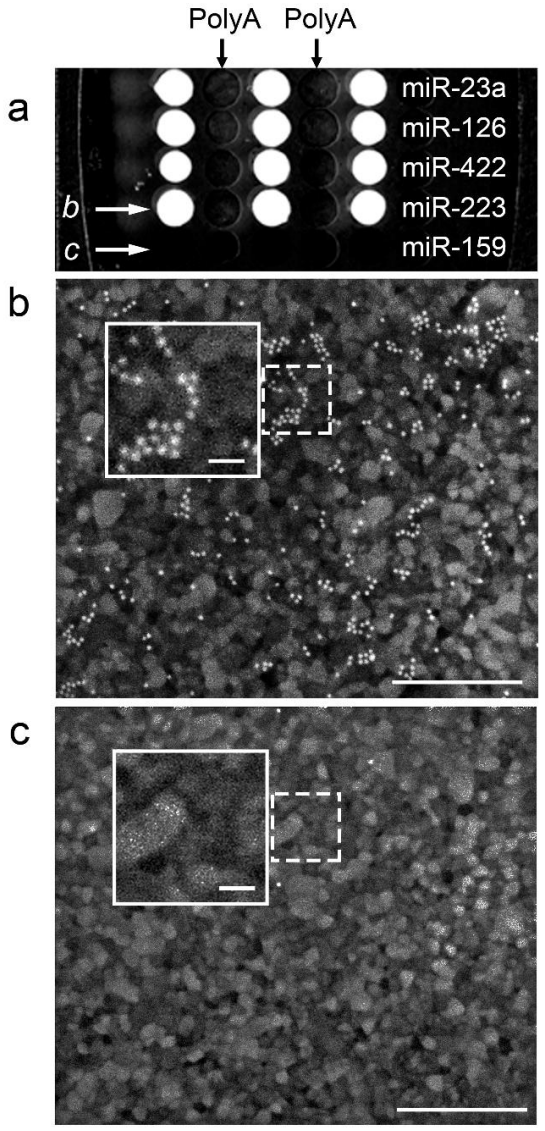

Figure 28. SPRi chip images. a) CCD differential image (reflectivity variation) of the SPRi chip acquired during Ab+AuNS@Neutrav-enhanced detection of four different miRNAs [100 pM]; the PolyA spots were used as references for each miRNA family, miR-159 was used as negative control. The two letters indicate the chip positions visualised by means of SEM (panels below). b) SEM image of the positive spot showing AuNS@Neutrav adsorbed on miR-223:DNA probe hybrids. c) SEM image of one negative spot relating to miR-159, which was not injected in this experiment. Scale bar = 400 nm (200000x). The two regions indicated by the dashed lines are magnified in the boxes enclosed by the solid lines (scale bar = 50 nm (450000x)).[77]

As shown in **Figure 28b** and **Figure 28c**, the positive spots are covered by nanoparticles of the expected size and probably clustered in correspondence with the presence of SH-DNA/miRNAs hybrids; the negative spots do not show any significant interactions and an absence of AuNS on their surface, demonstrating the specificity of the miRNA detection by this strategy. It should be taken into account that both cases have been incubated with the same miRNA solution and the same AuNS@Neutrav-Ab solution and this almost perfect specificity is clearly controlled just by the initial DNA sequence linked to the surface of the chip.

In order to evaluate the enhancing properties and dynamic range of the proposed method, two miRNAs (miR-422 and miR-223) injected in a wide range of concentrations were detected without enhancement, using only the Ab or using the Ab+AuNS@Neutrav. **Figure 29** shows all of the calibration curves, which demonstrate the improvement in detection when using the two enhancing strategies. The dynamic ranges of the three approaches were from about 1 nM to >500 nM for direct detection (1x), from about 50 pM to 100 nM (20x enhancement) for Ab-enhanced detection, and from about 0.5 pM to 1 nM (1000-2000x enhancement) for Ab+AuNS@Neutrav-enhanced detection.

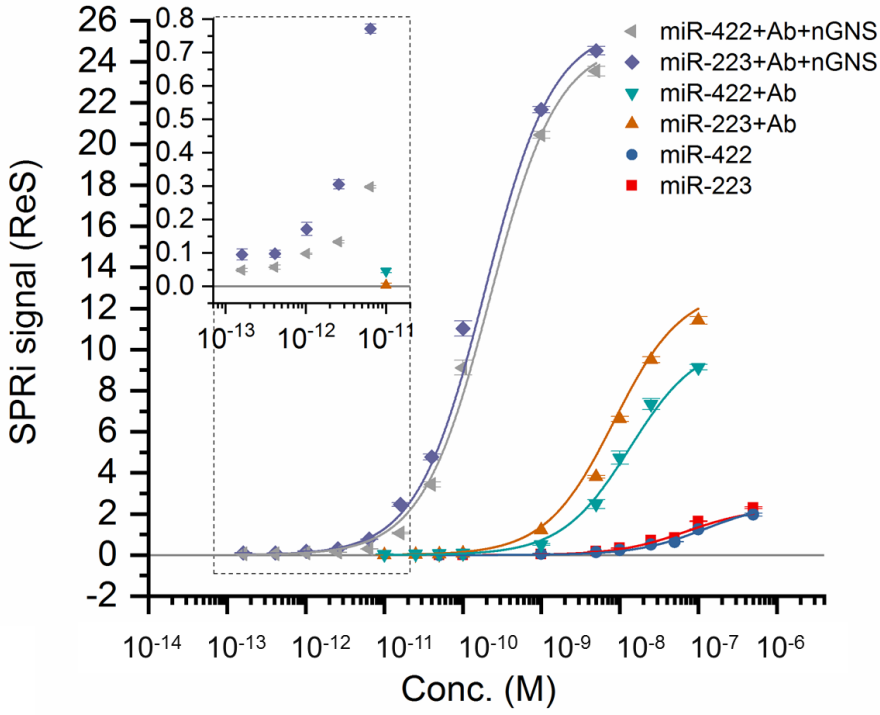

Figure 29. Calibration curves of the detection of miR-422 and miR-223 by means of standard SPRi (blue and red), Ab-enhanced SPRi (jade and orange) and Ab+AuNS-enhanced SPRi (grey and violet) showing the dynamic range and the amplification improvement thanks to the employment of AuNS@Neutrav-Ab.[77]

The sensitivity and the multiplexing capacities of the proposed method were tested by the simultaneous detection of four miRNAs that have been suggested as potential multiple sclerosis biomarkers (miR-422, miR-223, miR-126, and miR-23a).[191–194] These miRNAs were mixed, serially diluted (1:2.5) in running buffer from 0.16 pM to 100 pM, injected in the SPRi instrument, and then detected using Ab+AuNS@Neutrav as a single enhancing reagent at the same time for all the sequences. Most of the binding curves (**Figure 30a**) were clearly separated from noise and their maximum values were plotted using a log-log scale for each miRNA (**Figure 30b**). The data can be interpolated linearly through most of the tested concentrations, and the linear equation was used to calculate the limit of detection (LOD: the average of three replicated blank injections + 3 SD) for each

miRNA: 0.55 pM for miR-422, 0.88 pM for miR-223, 1.19 pM for miR-126, and 1.79 pM for miR 23a. The amounts of detectable miRNA given the 500 µL of injected volume are therefore between 275 and 890 attomoles. These data show that the developed universal enhancement strategy does not seem to be much affected by different sequences as the four calibration curves reside in similar SPRi signals intensity ranges. This is in line with the findings of a previous fluorescence microarray-based study that used an anti-DNA/RNA Ab to analyse small RNA expression.[195]

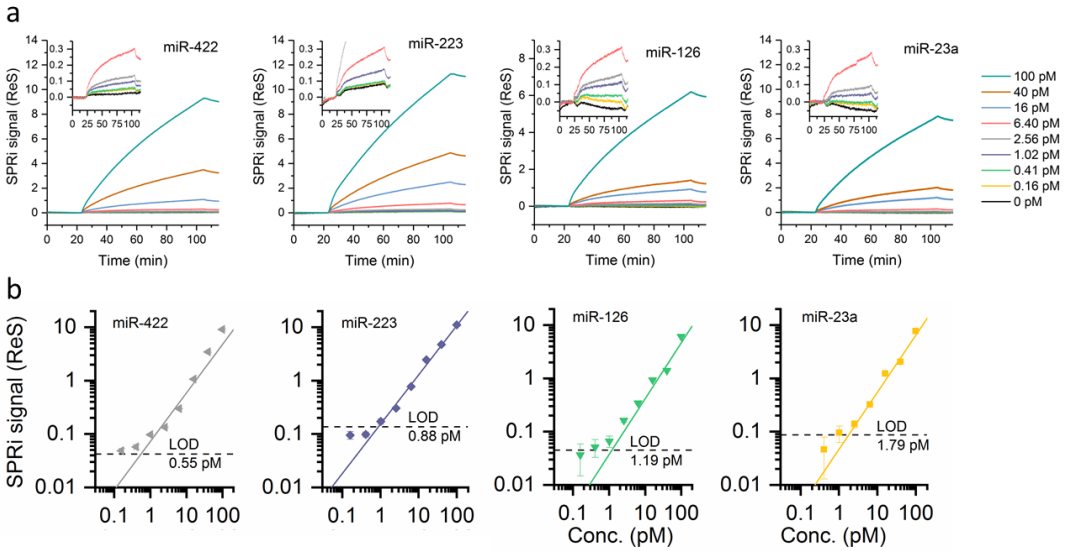

Figure 30. a) Single sensograms related to the enhancing steps for the detection of increasing amount of different miRNAs, performed to define the calibration curves and related to the injection of increasing concentration of miRNAs (500µL, 10 µL/min) each one followed by the injection of Ab+AuNS@Neutrav (800 µL, 10 µL/min) and by the injection of NaOH 50 mM (50 µL, 100 µL/min). All the signals were corrected by subtracting the corresponding negative control reference signals (PolyA). b) Calibration curves of all of the studied miRNA families plotted using a log-log scale and fitted linearly. The LOD values shown were calculated as the blank (0 pM signal + 3 SDs). Fitting curve parameters of miR-23a, miR-126, miR-223 and miR-442, respectively: Y Intercept (-1.33194, -1.42948, -0.81673 and -1.14085) and Slope (1.0689, 1.0482, 0.9225, 0.9096). Adapted with permission from**.**[77]

3.1.1.6. Analysis of miRNA mutation detection

In parallel, the sequence selectivity, necessary in case of mutated miRNA or miRNA isomers detection, was tested by our collaborators Dr. Renzo Vanna and Andrea Sguassero by comparing the SPRi signal obtained after injecting wild-type (WT) miR-23a and miR-23a carrying one or three mutations (**Figure 31**, **Table 6**). These experiments were conducted using different analyte concentration according to the sensitivity range of the three different signal detection approaches: non-enhanced SPRi (miRNA injected at 100 nM), Ab-enhanced SPRi (miRNA injected at 1 nM) and Ab+AuNS@Neutrav-enhanced SPRi (miRNA injected at 100 pM). As shown in **Figure 31**, the use of both Ab and Ab+AuNS increased the selectivity of the SPRi biosensor. When detecting a target with three mutated bases the Ab+AuNS enhancer produced only the 13 % of signal if compared with the signal related to the WT target. In the case of the miR-23a carrying a single mutation, SPRi alone was unable to distinguish it (i.e. 96 % of response signal in comparison with the wild-type sequence), Ab still produced 77 % of the signal but the use of Ab+AuNS@Neutrav reduced the sensor response to 52 %. This demonstrates that Ab, but especially the developed AuNS linked to the Ab enhancement, easily allow recognition of the mutated sequence probably because of the three-dimensional changes arising from the base-base mismatch.

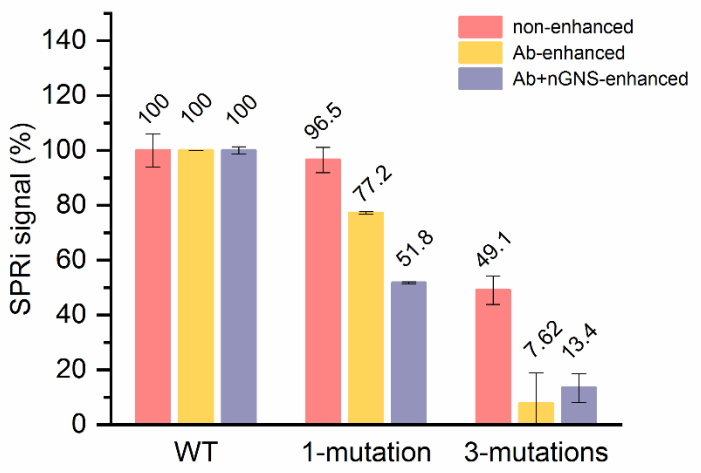

Figure 31. Sequence selectivity. Columns represent the strength of the SPRi signals corresponding to the detection of non-mutated (WT) (100 %) miR-23a, and miR-23a carrying one or three mutations. The three variants were detected by means of non-enhanced SPRi (after injecting miR-23a 100 nM), Ab-enhanced SPRi (after injecting miR-23a 1 nM) and Ab+AuNS@Neutrav-enhanced SPRi (after injecting miR-23a 100 pM) in separate experiments.[77]

3.1.1.7. Analysis of miRNA from human serum

In order to test our approach in a clinical relevant environment, our collaborators Dr. Renzo Vanna and Andrea Sguassero used total RNA extracted from serum samples taken from three healthy control subjects, which were processed as is usually done in pre-clinical research laboratories before RT-PCR quantification.[193,196] Total RNA samples were isolated from serum using a commercial extraction kit, diluted in 500 µL of running buffer, and directly injected into the instrument, followed by the Ab+AuNS@Neutrav. All three samples were automatically and consecutively injected onto the SPRi chip, which had been previously used to define the calibration curves. The four studied miRNAs (miR-422, miR-223, miR-126, and miR-23a), selected because they have previously associated with MS, were then detected and quantified (**Figure 32a**). These data show the varied contents of miRNAs in different samples, as expected and

reported in literature, and show that, at least for these four selected miRNAs, the proposed approach is adequate for the realistic dynamic range for clinical purposes. A parallel quantification by RT-PCR was carried out by our collaborators from Dr. Aija Linē research group thus demonstrating a good agreement between the data obtained by the proposed SPRi approach and demonstrating that the total RNA complex sample does not interfere the SPRi measurement (**Figure 32b**). It is noteworthy that RT-PCR was unable to detect miR-422 in Sample 1, most probably due to a very low concentration in the real sample. On the other hand, our experiments aim to confirm that multiple miRNA can be detected starting from complex samples and passing through standard sample preparation followed by a very simple detection approach.

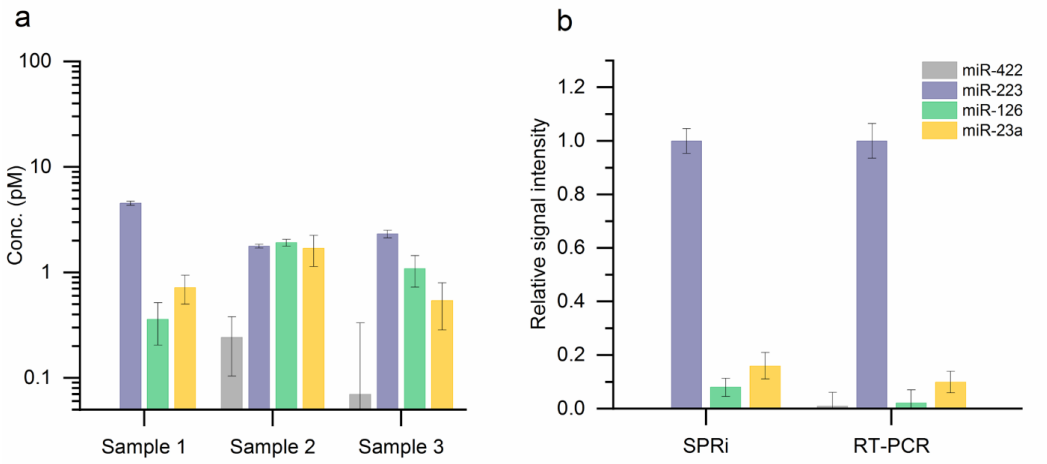

Figure 32. Tests on complex samples. a) Total RNA extracted from serum samples taken from three healthy control subjects were analysed by SPRi. The concentrations of four different miRNAs (miR-223, miR-126, miR-23a, and miR-422) were calculated on the basis of the calibration curves shown in **Figure 28** and were corrected (1:0.687 dilution factor) considering that the RNA extracted from 800 µL of serum was then suspended in a final volume of 550 µL; 500 µL of those were injected (10 µL min-1) followed by 800 µL Ab+AuNS@Neutrav (10 µL min-1). b) Comparison between the new proposed method and miRNA quantification by RT-PCR. The same sample of total RNA extracted from serum (Sample 1) was used as starting material for both quantifications. The relative signal intensity was based on the expression ratio between the four miRNA and miR-223. For SPRi results were used the quantities and the standard deviation reported in a. For

the RT-PCR results relative expression fold between each miRNA and miR-223 were used.[77]

In conclusion, thanks to the careful control of the AuNS functionalisation methodology, the developed strategy shows good signal specificity, high SPRi amplification and permits discrimination of wild type, single- and triple-mutated sequences much better than non-enhanced SPRi. The method also functions for real samples based on total RNA extracted from blood. Consequently, these results confirm that this approach can provide the possibility of detecting a (theoretically unlimited) number of miRNAs using a simple protocol and an easily prepared enhancing reagent, and may further facilitate the development of affordable multiplexing miRNA screening for clinical purposes.

3.1.2. Influence of AuNPs shape, size and functionalisation methodology in SPRi detection of miRNA

After developing the strategy of a universal SPR enhancer based on gold nanoparticles capable of simultaneously detecting multiple miRNAs with sensitivity below pM by a simple approach as previously described in **section 3.1.1**, the lack of information in the literature about the importance of the gold nanoparticle properties and the functionalisation strategy enhanced our curiosity to obtain a deeper understanding of these key technical elements.

Among all the described enhancing strategies for SPR sensing, AuNP have proven to provide good amplification to the SPR detection signal,[197] a high stability[20] and the ease by which biomolecules can be conjugated to their surface ("biofunctionalisation"),[16] making them a recurrently attractive option. Numerous synthetic strategies can be used to obtain almost any shape and size of AuNP.[30] Although the use of AuNP in SPR biosensors is now routine, only a few publications have focused on understanding how physicochemical properties AuNP affect their efficiency as SPR signal nano-enhancers and some results are contradictory. Mitchell et al. reported that no significant different enhancement was revealed by using AuNP with different size ranging from 25 to 50 nm[198] but

the exact concentration or number of colloids used is not evident from the reported results. A study by Uludag et al. reported that 40 nm AuNP produce higher sensor responses and higher sensitivity (LOD around 8-fold lower) if compared with 20 nm AuNP.[199] In that study, the same exact concentration of nanoparticles was employed and this means that, the higher volume and mass of gold nanoparticles produced higher signal.

Only recently, Springer and colleagues made an important contribution in this field, describing theoretically and experimentally that the sensor response enhancement is dependent by sensor sensitivity, by AuNP surface density and by the ability of the AuNP to bind to sensor surface, and dependent on the size of the AuNP.[200] This particular study evaluated five different sizes of colloid (10, 15, 21, 33, 52 nm) and, aiming to present a theoretical model, it has been performed at the equilibrium state. This configuration required to pre-optimise the concentration of each AuNP and to perform enhancer injections with duration up to 20 hours. However, this experimental setting is not useful for the diagnostic applications due to its long duration. For this reason the evaluation of AuNP enhancement in experimental conditions that could be transferred to diagnostic clinic is still necessary. Furthermore, previous studies comparing different AuNP as SPR enhancer did not attempt to compare their enhancement properties by keeping constant both the total amount of gold injected and the theoretical amount of molecular probes immobilised on them (e.g. proteins and antibodies able to recognise the analyte pre-immobilised on the chip surface).

In parallel, if studies focused on the effect of AuNP size are rare, then there are fewer still which attempt to understand the influence of nanoparticle shape on SPR response. The study by Kwon et al. compared three different AuNP shapes (quasi-spherical, cages and nanorods), showing behaviors and responses completely different depending on the shape employed.[201] The study by Mariani et al. investigates the enhancement of SPR response by using silica spheres, gold spheres and silver prisms. They reported relative large different

enhancement properties between the three different nanoenhancers but that large part of variations was due different plasmonic effects related to their chemical composition (i.e silica, gold, silver).[202] Therefore, the shape of different AuNP has been scarcely studied in relation to enhancement properties.

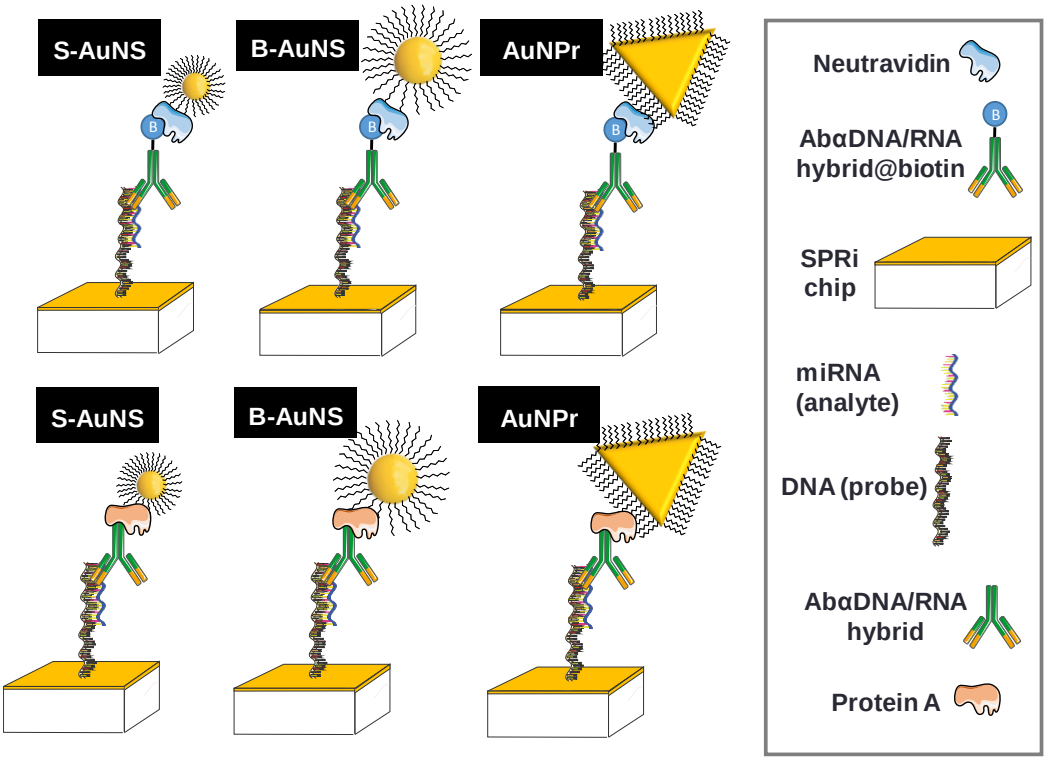

Figure 33. Molecular strategies employed for the miRNA recognition and detection, combining the three types of nanoparticles (small-size gold nanospheres (S-AuNS), big-size gold nanospheres (B-AuNS) and gold nanoprisms (AuNPr)) with the two different proteins (neutravidin and protein A) as linker for antibody (Ab) conjugation. In particular, an Ab against DNA/RNA hybrids is used here to recognise the adsorption of miRNA (analytes) bound to specific DNA (probes) previously spotted on the SPRi chip. This antibody needs to be pre-functionalised with biotin (Ab anti RNA/DNA hybrid@biotin) to be recognised by the neutravidin while it is not needed in the case of the protein A (Ab anti RNA/DNA hybrid).

For all these reasons, the aim of this portion of the research was to evaluate the performance of spherical gold nanoparticles with different sizes and also triangular nanoprisms, along with two different approaches (neutravidin and

protein A) used to conjugate them with a specific Ab for miRNA detection, as SPR nanoenhancers (see **Figure 33**). In particular, in order to reduce the complexity of the study and of the emerging results, here we set as starting point: 1) the use of gold nanoparticles only; 2) the injection of the exact amount of gold nanoparticles (as total mass and not as number of particles); 3) the use of nanoparticle theoretically conjugated with the same amount of active probes and 4) the use of standard experimental procedures normally used for the validation of new diagnostic approaches (i.e reasonable experiment duration, type of chemistry, simple protocols).

3.1.2.1. Preparation and characterisation of AuNP

The SPRi nanoenhancing properties of different sizes of gold nanospheres were evaluated: small-size gold nanospheres of 14 nm (S-AuNS), big-size gold nanospheres of 37 nm (B-AuNS), and triangular gold nanoprisms of 183 nm (AuNPr) (**Figure 34**). Furthermore, gold nanoprisms were chosen due to their planar shape. Although different shapes of AuNP have been compared previously,[201] as far as we know, a planar nanoparticle shape has never been compared with a spherical one and we postulated that the planar nature of the nanoprism would provide better surface coverage and improved interaction with the chip, therefore increasing the signal and sensitivity of the system.

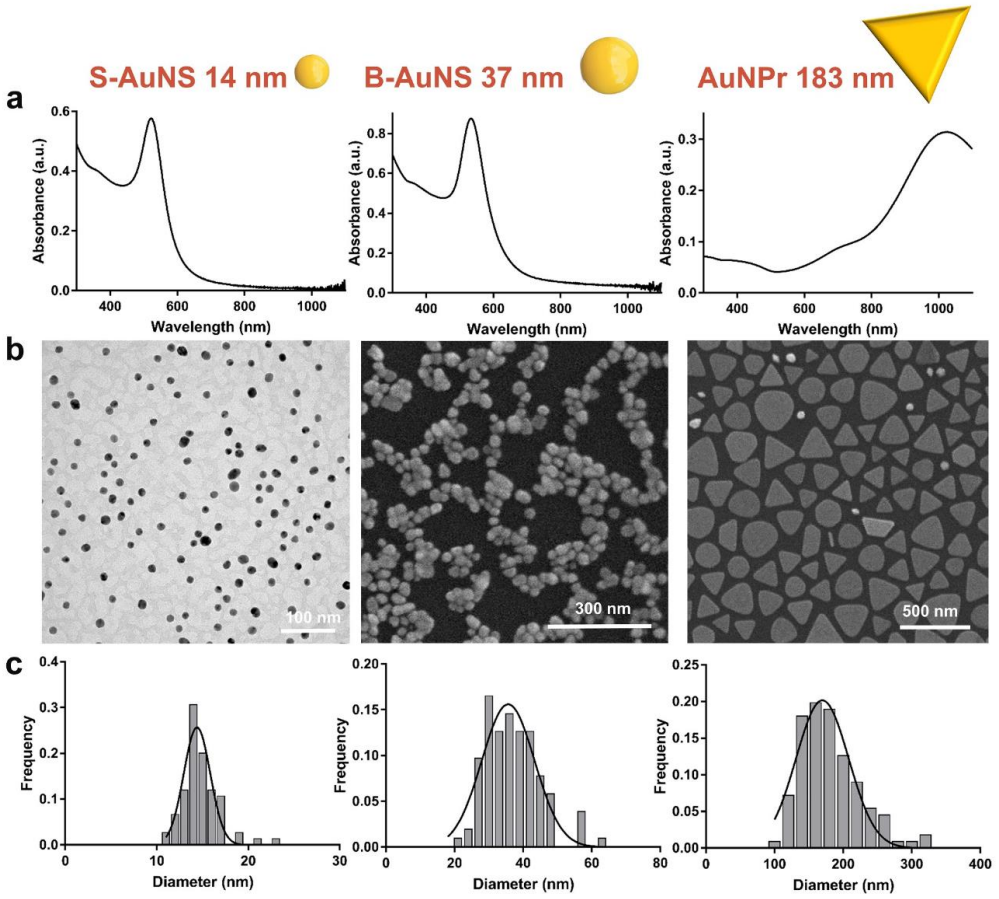

Figure 34. a) UV-Vis spectroscopy of gold nanoparticles showing how the LSPR band varies with shape; b) Representative TEM (S-AuNS; B-AuNS) or SEM (AuNPr) imaging of the three nanoparticles: spheres of 14±3 nm (S-AuNS), spheres of 37±9 nm (B-AuNS) and triangular prisms of 183±47 nm (AuNPr) and c) Size-dispersion histogram each of the nanoparticles using diameters obtained from TEM or SEM images.

S-AuNS and B-AuNS were synthesised using the well-established Frens-citrate methodology changing only a few parameters during the synthesis. Concretely, for small 14 nm nanospheres (S-AuNS) a concentration of 2.5 times of sodium citrate was employed compared with big 37 nm nanospheres (B-AuNS). By employing the same methodology for both gold nanospheres, we ensured that the components on their surface were similar and that the nanoparticles are comparable during all the study. In **Figure 34,** both nanoparticles show a similar

UV-Vis spectrum because they have the same shape, with a narrow Localised Surface Plasmon resonance (LSPR) peak at 522 nm for the S-AuNS and 532 nm for the B-AuNS, which is indicative of a low polydispersity (subsequently confirmed by TEM measurements). The diameters of both gold nanospheres were measured from TEM or SEM images showing a diameter of 14±3 nm for the S-AuNS and of 37±9 nm for the B-AuNS, confirming the low polydispersity of both nanospheres. The mass of both nanoparticles was also calculated by employing the diameter obtained from the TEM images, assuming a complete sphere shape and the density of gold ($19.3 \cdot g \cdot cm^{-3}$), obtaining a mean weight of $1.67x10^{7}$ $g \cdot mol^{-1}$ for S-AuNS and $3.08x10^{8}$ $g \cdot mol^{-1}$ for B-AuNS. The concentration of gold nanoparticles was measured by ICP-AES and correlated with the UV-Vis absorbance in order to ensure the proper concentration in gold mass for each study step.

Triangular gold nanoprisms (AuNPr) were synthesised employing a previously reported methodology.[61] The main advantage of this strategy consists in the avoidance of the toxic surfactant CTAB, commonly employed in the synthesis of anisotropic AuNP and that could affect the subsequent protein stability. However, pseudo-spherical gold nanoparticles that are formed as a by-product of the synthesis must be removed from the AuNPr solution. Separation by gel electrophoresis was used for nanoparticle separation.[28,203] Purification of AuNPr was carried out employing gels with high concentration of agarose allowing the pseudo-spherical gold nanoparticles to enter on the gel, while larger triangular gold nanoprisms remain in the well due to their higher size (see **Figure 35**). In this way, it was possible to easily recover them completely pure from the well, improving considerably the efficiency and the time employed with this methodology. After the purification, AuNPr were almost completely free of nanospheres and showed a size of 183±47 nm as can be seen in **Figure 34**. Their mean weight was also calculated assuming that they had a regular triangular prism shape with a height of 9 nm, resulting in a nanoparticle mass of $1.59x10^{9}$

g·mol^{-1}. In order to increase their stability and to permit the subsequent functionalisation of the AuNP with the protein of interest, the three types of nanoparticles were covered with polyethylene-glycol. These polyethylene-glycol molecules are anchored to the gold surface by thiol groups and possess a carboxylic-end group that allows the covalent linking of proteins by an amide group to the AuNP surfaces.

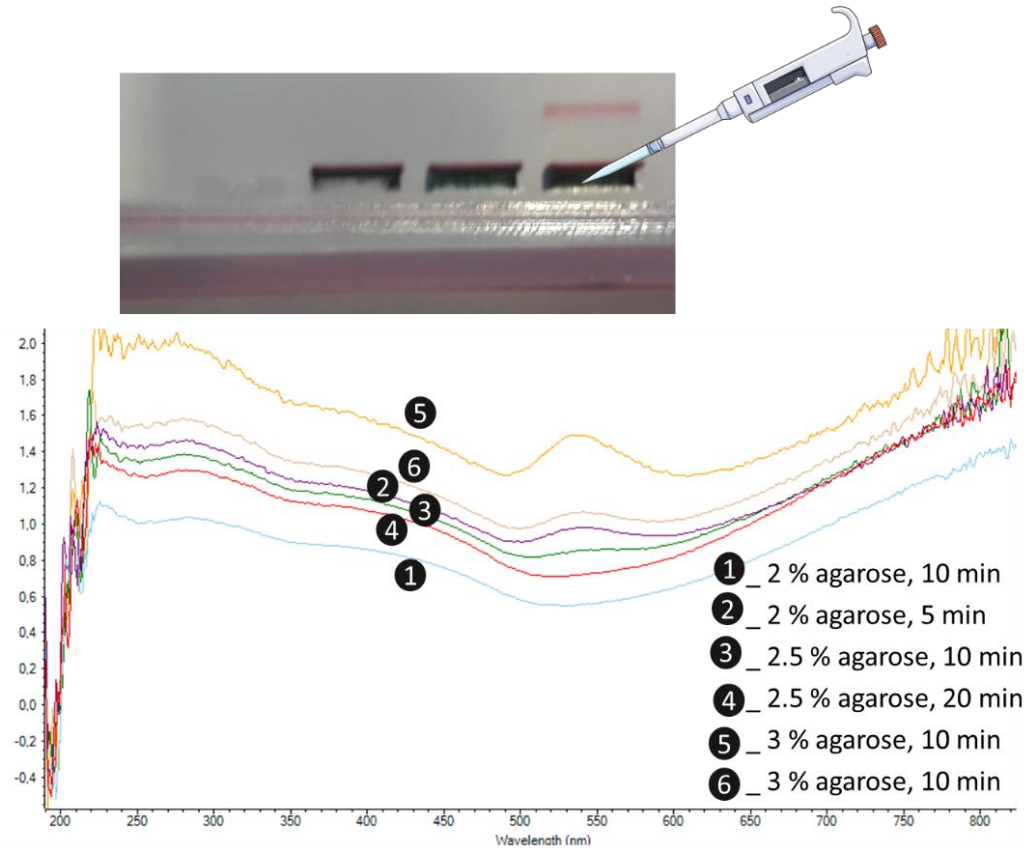

Figure 35. AuNPr purification methodology. In the top a scheme of the methodology employed to purify the nanoprisms consisting in running an electrophoresis with high concentration of agarose and recovering the nanoprisms (green) form the well. In the bottom graph could be seen the UV-Vis spectra of the recovered nanoprisms depending on the electrophoresis parameters employed, showing a clear diminution of the absorbance peak around 540 nm, proportional to the nanosphere presence.

3.1.2.2. Exploring the influence of functionalisation strategy, size and shape of NP on SPR enhancement properties

In order to study the SPR signal enhancement associated to the detection of miRNA as analyte of interest, AuNP were conjugated with an Ab able to specifically recognise the RNA/DNA hybrid forming on the chip surface previously functionalised with specific DNA probes. Although a direct covalently linkage of the Ab to the AuNPs PEG surface was also tried and reported in the previous section, this Ab lost its function during the functionalisation due to a lower stability compared with other antibodies. Each of the three types of AuNP was conjugated with the anti-DNA/RNA Ab by using protein A or neutravidin to evaluate which of these two protein-derived strategies gives better signal enhancement and was more appropriate for the nanoparticle comparison (**Figure 36)**. Neutravidin is a protein from the avidin family that links specifically to biotin. Neutravidin/avidin strategy offers an extraordinary binding affinity (K_d ~$1x10^{-15}$ M),[204] but requires antibody functionalisation with biotin prior to their interaction with the neutravidin-AuNP complexes. On the other hand, the protein A strategy offers a lower binding strength (K_d ~$1x10^{-10}$ M)[205] but permits simpler protocols because it does not require the biotinylation of the target antibody, avoiding the risk of partially deactivating the antibody, as was previously reported (see **Figure 27**).

In order to properly compare these two strategies, the same amount of proteins (neutravidin or protein A) per AuNP surface unit was maintained for each of the three nanoparticles during the functionalisation process (see **Table 3**). The employed ratio of $2.57x10^{-14}$ pmol of proteins·nm^{-2} had been optimised previously for the neutravidin/biotin strategy with gold nanospheres (see **Section 3.1.1.1**). In a similar manner, in the experiments described herein, the same concentration of gold (12.42 µg·mL^{-1}) was injected when comparing the three different nanoparticles in order to evaluate the influence of conjugation strategy, shape and plasmon properties, and trying to keep constant the amount of gold and the amount of active probes theoretically immobilised on the nanoparticles. To test

the conjugation strategy, neutravidin and protein A were bonded covalently to nanoparticles using EDC/NHS reaction and characterised by agarose gel electrophoresis. **Figure 36** show how the increasing number of protein molecules on their surface decreases the mobility of AuNP in the gel due to the higher size of the complex, indicating that the protein is linked to the AuNP surface in all the cases.

Table 3. Properties, functionalisation details and SPR experimental conditions related to each of the AuNPs used in the study.

	S-AuNS 14 nm	B-AuNS 37 nm	AuNPr 183 nm
AuNPs properties			
Size (nm)	14	37	183
LSPR wavelength (nm)	522	532	1000
Extinction coefficient at 450 nm ($mL \cdot mg^{-1} \cdot cm^{-1}$)	11.3	11.2	11.5
Mean weight (g/mol)	$1.67x10^{7}$	$3.08x10^{8}$	$1.52x10^{9}$
Surface Area (nm^2)	$1.09x10^{15}$	$5.06x10^{14}$	$6.59x10^{7}$
Functionalisation details			
Quantity AuNPs used for the functionalisation (µg)	49	60	50
Quantity AuNPs (pmol)	2.93	0.20	0.03
Protein (neutravidin or Protein A) added (pmol)	28	13	17
Ratio Protein/ Au mass (pmol/µg gold)	0.57	0.22	0.34
Ratio Protein/ AuNP (pmol/pmol)	9.6	66.6	514.0
Ratio Protein/Surface ($pmol/nm^2$)	$2.57x10^{7}$	$2.57x10^{7}$	$2.57x10^{7}$
SPR experiments			
Concentration of NPs injected (µg/mL)	12.42	12.42	12.42
Concentration of NPs injected (nM)	0.74	0.04	0.01
Concentration of NPs injected (NP/ml)	$4.5x10^{11}$	$2.4x10^{10}$	$4.9x10^{9}$
Concentration of NPs injected (O.D.)	0.150 (λ=450nm)	0.137 (λ=450nm)	0.68 (λ=1000nm)

After the functionalisation, each neutravidin or protein A-functionalised AuNP was conjugated with the biotinylated or free antibody, respectively. The neutravidin strategy, used to conjugate S-AuNS to the anti-DNA/RNA Ab, produced the best enhancement (i.e. 22-fold the SPR signal derived by the Ab alone used as enhancer) (see **Figure 36**). In contrast, the protein A strategy yielded a 15-fold enhancement. In the case of B-AuNP, neutravidin also provided even better results (i.e. 24-fold the SPR signal derived by the Ab alone) compared with the protein A strategy which did not offer any significant enhancement (i.e. 1.2-fold enhancement). The lack of activity of protein A strategy when coupled with B-AuNP (37 nm) cannot be easily explained by the sole increase of size of colloids. In theory the difference between the surfaces of these two nanoparticles should not compromise the functionalisation of protein A. On the other hand, a possible explanation of both the lower enhancement of protein A when coupled with S-AuNS and the lack of enhancement when coupled with B-AuNS is the lower affinity strength of Protein A if compared with neutravidin/biotin one, which is around $1x10^5$-fold stronger. Starting from this consideration, it may happen that the stability of the target/Ab/protein A/NP complex is less stable than the target/Ab/neutravidin/NP complex. In particular, this could be more evident for B-AuNS considering their much higher molecular mass, around 18-fold heavier if compared with S-AuNS.

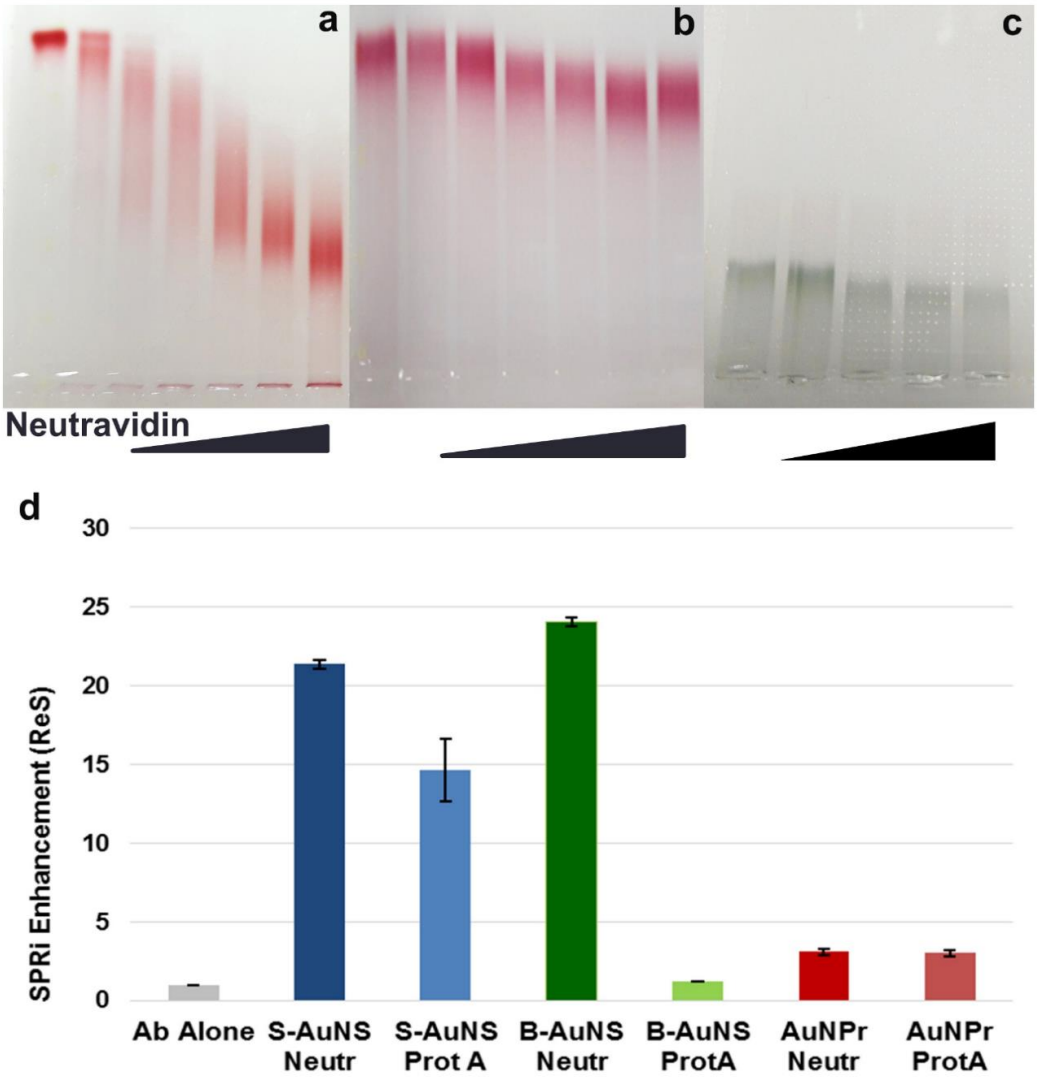

Figure 36. Gel electrophoresis mobility reduction of 14 nm AuNS (S-AuNS) (a), 37 nm AuNS (B-AuNS) (b) and 183 nm AuNPr (c) functionalised with increasing ratios of neutravidin, confirming the protein functionalisation. d) SPR enhancement for the detection of miR223 (1 nM) produced by each functionalisation strategy. The relative enhancement was calculated comparing the NP-derived enhancement with the enhancement derived by the injection of the Ab alone (5 nM) as a reference. All signals are corrected by subtracting signals from the negative references (PolyA sequences) spotted in parallel on the same chip.

At the same time, triangular gold nanoprisms (AuNPr) showed a low enhancement (i.e. three-fold compared with Ab alone, **Figure 36**) with either approach. This surprising low enhancement derived by the use of nanoprisms is again not simply justified by a lack of SPR enhancement of gold nanoprisms. The main reason of the reported low enhancement results from high non-specific adsorption on negative control spots as showed in **Figure 37**. The high planar surface area of these AuNPr could be responsible for this observation due to their flat shape and the high surface of interaction with the chip. At the same time, the density of AuNPr adsorbed on the SPR chip, as measured by SEM analysis, is similar for both positive and negative spots (i.e. 0.7 and 0.5 NP/μm^2, respectively) and more than 40 times lower if compared with density of gold nanospheres adsorbed on the chip after similar experiments (see the next paragraph). This means that gold nanoprisms did not efficiently interact with the chip surface. Also in this case, one limiting factor could be the very high molecular mass of 183 nm nanoprisms (around 90-fold heavier if compared with S-AuNS) that could limit and destabilise the formation of the molecular complex between the target on the surface (DNA/miRNA duplex), the Ab and the nanoparticle (AuNPr). Finally, another influencing factor here is the kinetics of relatively large AuNPr that may require a longer injection time to reach maximum SPR response.

Even if very long injection and/or other approaches can be utilised to optimise colloidal stability and to facilitate their compatibility with SPR experiments, such considerations are beyond the scope of this doctoral thesis. On the contrary, here we aimed to verify and to test the feasibility of using different gold nanoparticles as potential SPR signal enhancer by using as driving criteria reliability, reproducibility and practicality. For this reason, the rest of our study focused on understanding the dependence of the size of AuNS in the SPRi enhancement excluding further detailed investigation of AuNPr.

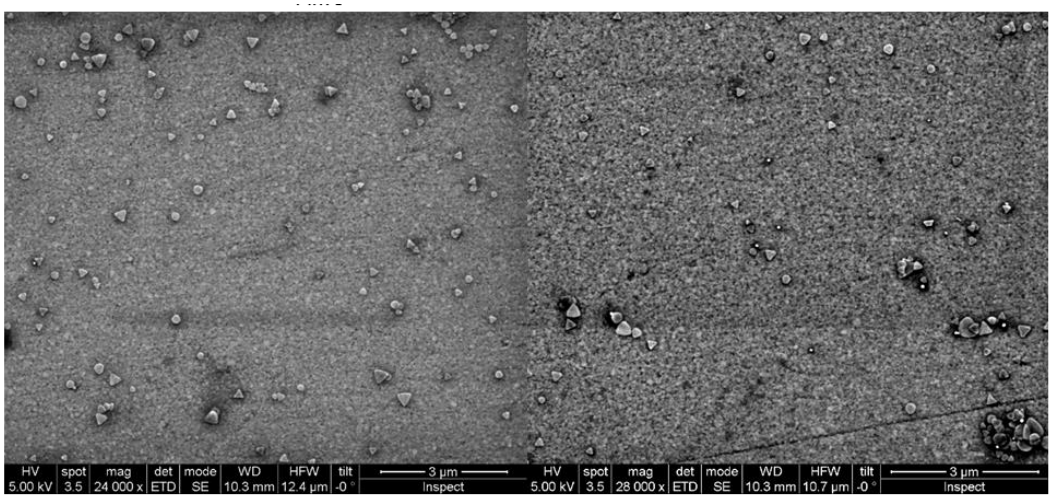

Poly A **miR 223**

Figure 37. SEM image of the surface of the chips (left, spot functionalised with PolyA used as negative reference spot; right, spot functionalised with miR-223 probes) where is possible to see the unspecific adsorption of AuNPr to the chip surface.

3.1.2.3. Detailed comparison of the enhancement of small and big nanospheres

In order to evaluate the enhancement properties of selected NP and to verify the specificity of the studied interactions, we evaluated the SPR response resulting by the use of both small-size (S-AuNS) and big-size (B-AuNS) NP for the enhancement of the signal derived by the injection of an increasing amount of target miRNA (from 0.3 pM to 50 nM). As can be seen in **Figure 38a**, the injection of the same amount of both S-AuNS and B-AuNS for an injection duration of around 1.5 h, produced a very similar signal at each of the tested target concentrations and both reached the maximum signal when injecting 50 nM of target miRNA. In particular, to calculate the signal enhancement we use 1 nM miRNA concentration as the minimum concentration of miRNA giving a detectable SPR signal even without enhancement strategies (**Figure 38a**). At this concentration, we calculated a 950-fold and 1070-fold enhancement comparing the signal derived by S-AuNS and B-AuNS, respectively, with that of non-enhanced SPR. If we compare the NS enhancement with that derived by the Ab

alone, we calculated a 21-fold and 24-fold for S-AuNS and B-AuNS, respectively. In parallel, the test of both nanoparticles resulted in very similar sensitivities with LOD of 1.34 and 1.71 pM (for miR-422 and miR-223, respectively) when using S-AuNS and LOD of 0.87 and 1.48 pM (for miR-422 and miR-223, respectively) when using B-AuNS (**Figure 38d-e**). From these data we can say that both nanoparticles are very good enhancers allowing an ultra-low detection of miRNA at concentrations around pM range. The obtained sensitivity and enhancement factors are in line with those previously reported in literature by Vaisocherova et al. using SPR-imaging coupled with spherical AuNSs with diameter 35 nm (i.e. around 800-fold enhancement with the respect to only miRNA injected at 2 nM and LOD between 0.35 and 0.95 pM).[206]

Even if B-AuNS performed better than S-AuNS, the observed differences between enhancement factors and sensitivities can be considered as very similar if the large difference between the volumes of these two nanospheres is taken into account. As it can be observed in the sensograms reported in **Figure 38b,c** and by the linear fit of calibration curves in **Figure 38d,e**, not only both nanoparticles resulted in similar sensitivities but, at all miRNA target concentrations, they produced similar interaction curves with similar kinetics.

Overall, these results may appear unexpected considering that the larger mass of bigger nanospheres, which theoretically, should increase the SPR response; according to what normally happens when injecting biomolecules on the chip surface. These results could be explained by a low (or very low) surface density of big AuNSs in the chip (low interaction with the probes on the chip) when injected onto the SPR chip, as also previously described.[200] In the mentioned study, Springer et al. reported that the increase of size of AuNP decreases their surface density in the chip due to different reasons including a) steric effect, b) the binding of multiple AuNP to a single Ab and c) the binding of one AuNP to multiple Abs.

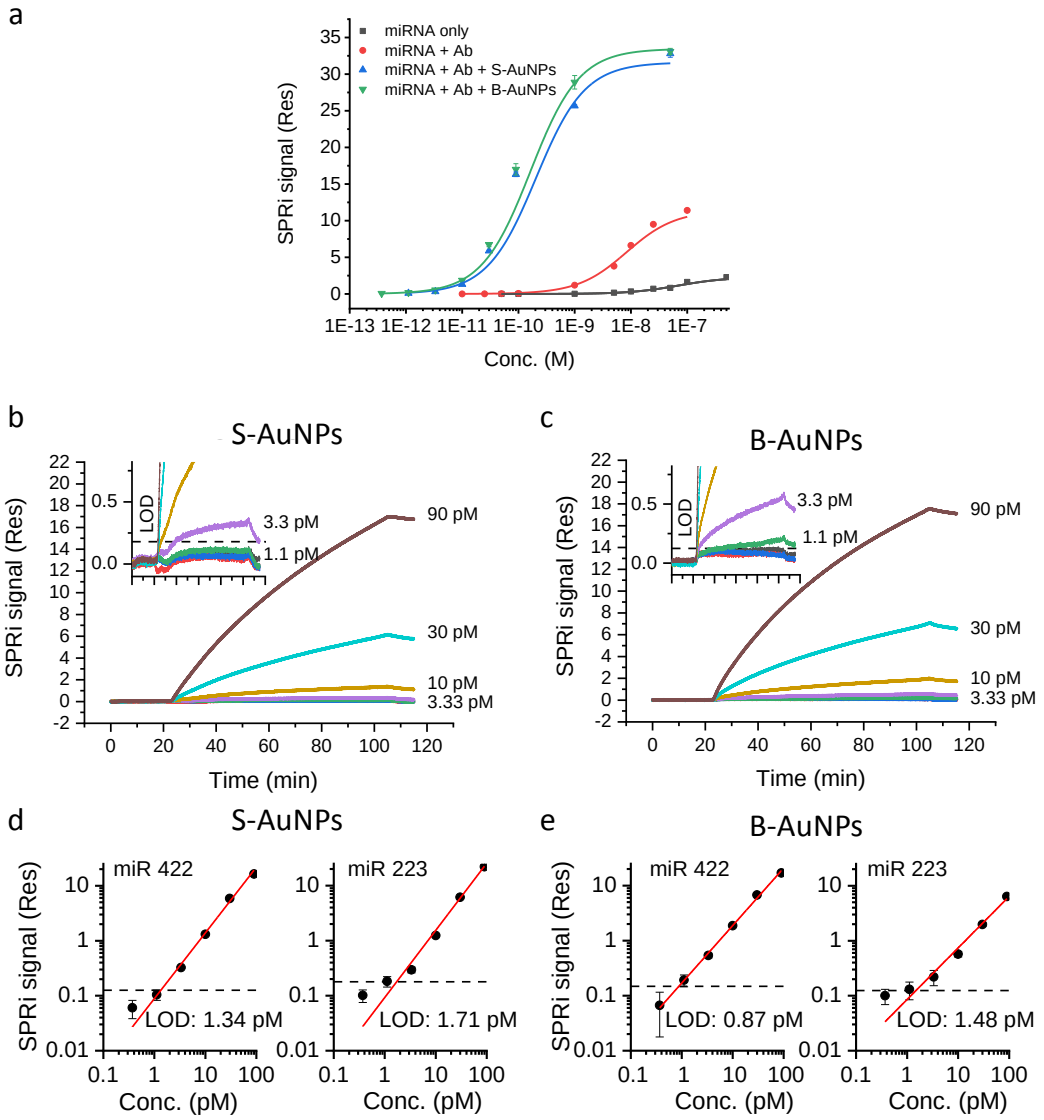

Figure 38. a) calibration curves of the detection of miR-223 by means of: standard SPRi obtained by injecting only the miRNA target (i.e. the analyte) (grey); Ab-enhanced SPRi obtained by injecting the anti-DNA/RNA duplex Ab (red); Ab+AuNS-enhanced SPRi obtained by injecting gold nanospheres (AuNSs) of 14 nm (S-AuNS) and 37 nm (B-AuNS), respectively (blue and green, respectively). miR-223 was injected with different increasing known concentration, from a minimum of 0.37pM to maximum 500 nM, depending to the experiment. b-c) SPRi sensograms of miR-223 corresponding to the calibration curves (green and blue data) reported in panel a. d-e) Calibration curves of miR 223 and 422 plotted for both x and y axis using a log scale with linear fit and used to calculate the LOD.

All signals are corrected by subtracting signals from the negative references (PolyA sequences) spotted in parallel on the same chip.

SEM was used to verify whether the scarce enhancement of B-AuNS was derived from a low number of NP adsorbed on the surface of the chip when using big nanospheres, after injection of 50 nM of three different target miRNA (**Figure 41a-b, Table 4**). The high concentration of miRNA target (50 nM) was chosen in order to easily detect and count AuNSs physically adsorbed on the chip surface, and considering that the Langmuir curve of both S-AuNS and of B-AuNS was almost exactly matched at all concentration.

First of all, SEM measurements confirmed that S-AuNS and B-AuNS specifically interacted with all three miRNA probes (miR 572, miR 39 and miR 223) without significant adsorption of AuNSs on negative control spots (miR-159 (*Arab. Thal*), as also revealed by SPR response (**Figure 41a-b; Table 4**). More important, the SEM data reveal that the number of NP adsorbed on the chip is very similar when comparing S-AuNS and B-AuNS. In detail, the number of small (S-AuNS) nanospheres adsorbed on the chip surface (42.50±15 NP/μm^2) is only 32 % higher if compared with B-AuNS (32.02±11 NP/μm^2) where the SPR signal, as said before, is almost equal, being on average between 34.05±0.4 and 35.06±7 ReS (only 3 % smaller for S-AuNS) (**Figure 41b**). Further SEM experiments proved that S-AuNS adsorbed on the chip surface are not lost by washing steps normally performed between SPR and SEM experiments even if no fixative reagents were used in our protocols (
Figure 39).

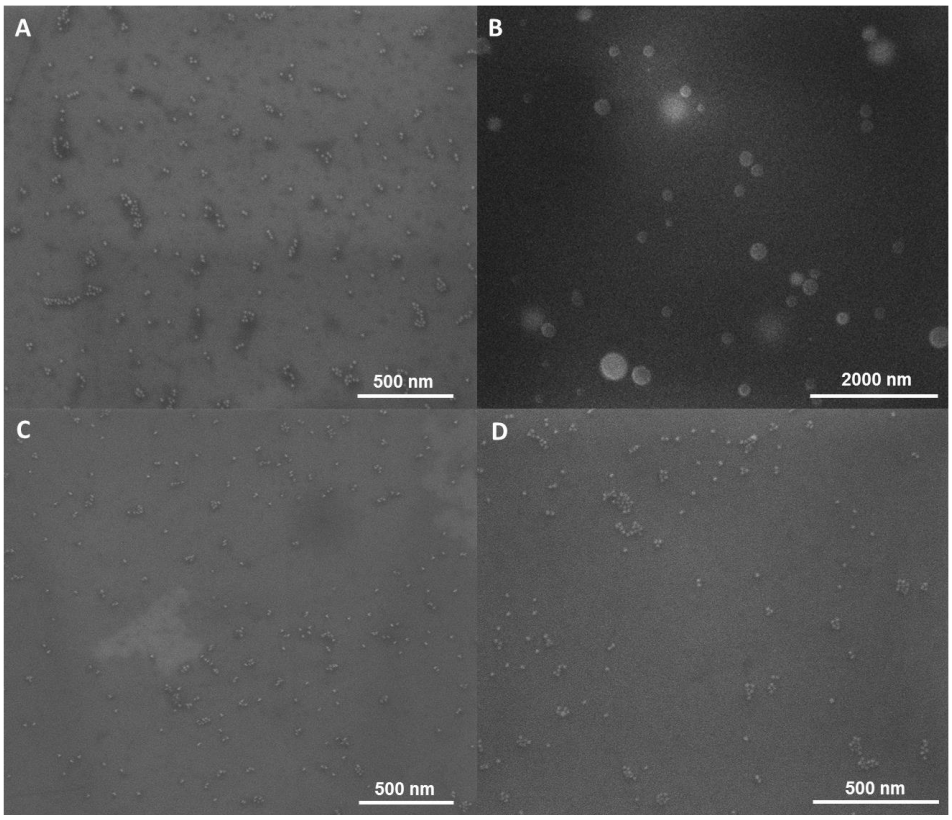

Figure 39. A) AuNP functionalised with neutravidin deposited on a gold surface. B) AuNP functionalised with neutravidin deposited on a gold surface and incubated with glutaraldehyde 3 % in order to fix them. C) AuNP functionalised with neutravidin deposited on a gold surface and washed with abundant ultrapure water. D) AuNP functionalised with neutravidin deposited on a gold surface and incubated with glutaraldehyde 3 % in order to fix them and after that washed with abundant ultrapure water.

We have then calculated the response of both nanoparticles in our sensor system (**Table 4**) dividing the SPRi response by the density of nanoparticles on the surface ($NP \cdot \mu m^{-2}$). The B-AuNS displayed 34 % higher average sensitivity (1.17 $ReS \cdot \mu m^{-2}$) compared with the S-AuNS (0.87 $ReS \cdot \mu m^{-2}$). Accordingly to these data, the plasmonic curves acquired before and after the injection of nanoparticles showed a small shift for B-AuNP (from 57.8 to 56.6 degrees, diff=1.2) if compared with the plasmonic shift of S-AuNP (from 57.7 to 56.9 degrees, diff=0.8) (**Figure 40**).

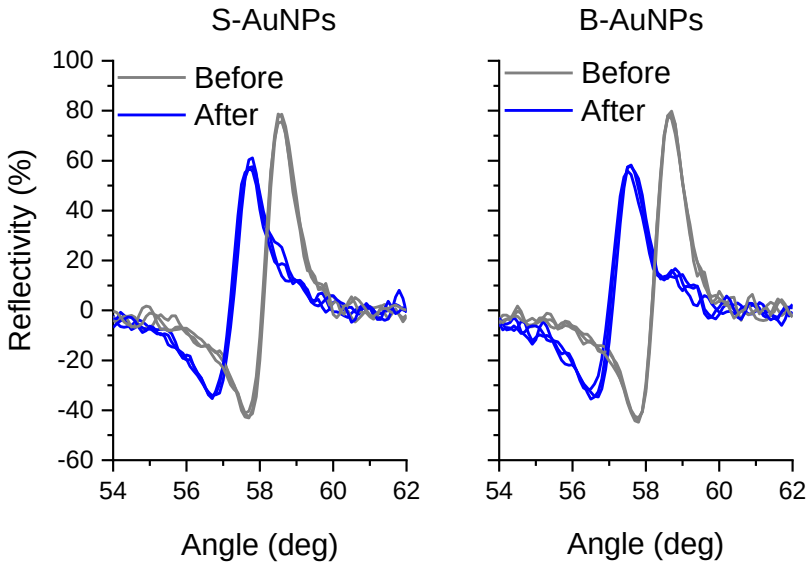

Figure 40. Plasmonic curves of the SPR chips before and after the injection of S-AuNS and B-AuNS- These data are related to the injection of 50nM miRNA and measured for the chip spot associated to miR-233 family.

The mentioned small difference between number of particles adsorbed on the chip in our experiments, giving around the same SPR signal, is largely far from what reported in the study by Springer et al. reporting around 340 % higher density of small Au nanospheres (14 nm, 52 NP/μm^2), compared with big nanospheres (37 nm, 52 NP/μm^2), when the SPR response associated with small Au nanospheres was 66 % smaller. Furthermore, the result observed here is even more significant if we consider that, as showed in **Figure 41b**, the total density of gold adsorbed on the chip, as theoretically estimated by NP counting by SEM, is about 14-fold higher for B-AuNS if compared with S-AuNS.

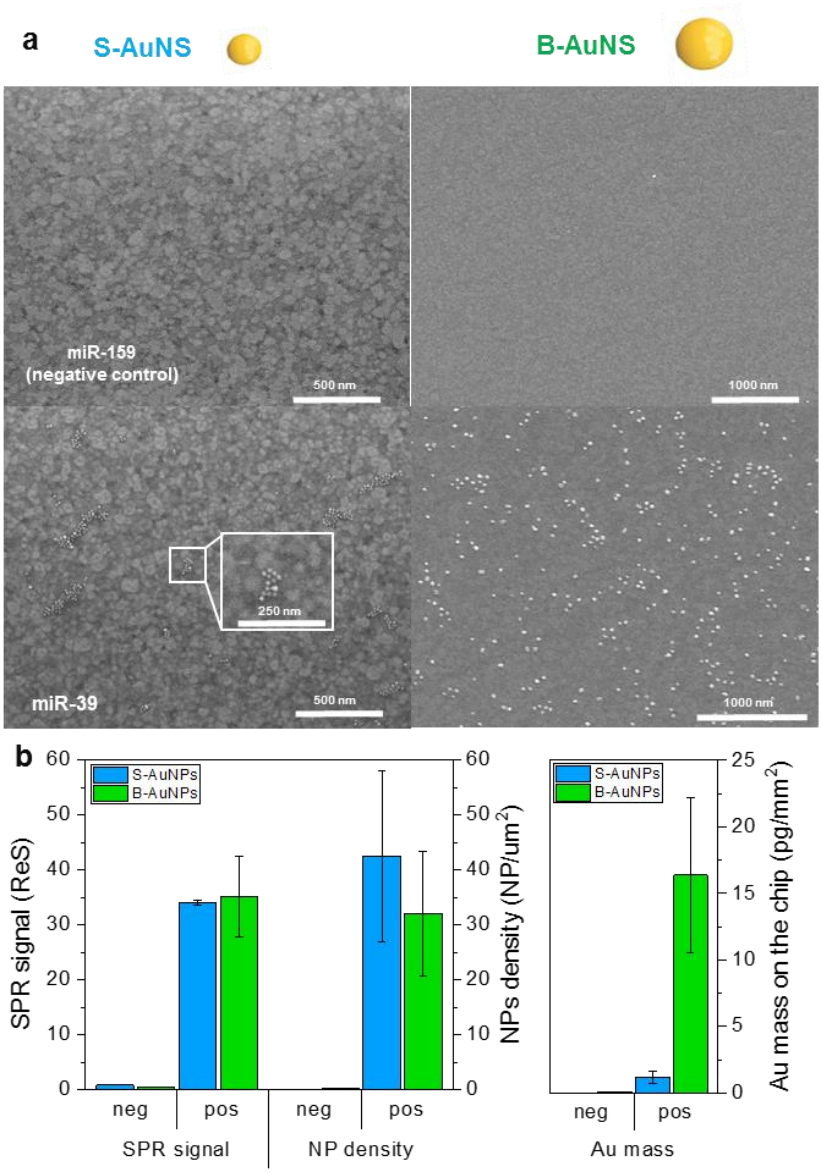

Figure 41. a) SEM images of the chip surfaces employed for miRNA detection using the different spherical NP (S-AuNS and B-AuNS), including the negative control miRNA sequence (miR 159) and a detected sequence (miR 39). The SEM images were acquired after the injection of nanoparticles at 50 nM; b) overview of the average SPR signal, density of NP adsorbed on the chip measured by SEM and estimated amount of gold adsorbed on the chip related to the injection of three different target miRNAs (data is detailed in **Table 4**). In this case both SPR signals and density of NP were not corrected by negative references in order to exactly compare these two parameters. Data related to negative reference spots are reported.

Table 4. Overview of SPR response and SEM results when using S-AuNS and B-AuNS as SPR enhancers.

	S-AuNS	*SD*	B-AuNS	*SD*	% Ratio B-/S-AuNS
SPR signal (ReS)					
Neg. Control (miR-159)	0.83	*0.01*	0.45	*0.05*	
Positive spots (average)	34.05	*0.39*	35.06	*7.31*	103
Nanoparticles adsorbed (NP/μm^2)					
Neg. Control (miR-159)	0.05	*0.06*	0.17	*0.16*	
Positive spots (average)	42.50	*15.54*	32.02	*11.42*	75
Au mass adsorbed on the chip (pg/mm^2)					
Neg. Control (miR-159)	0.001	*0.001*	0.08	*0.002*	
Positive spots (average)	1.18	*0.43*	16.38	*5.84*	1388
Senstivity (ReS*μm^2/NP)					
Positive spots (average)	0.87	*0.29*	1.17	*0.36*	134

The average of positive signals was calculated considering the detection of three miRNA families (miR-39, miR-223, miR-572).

These data raise some interesting questions, especially if seen from a practical point of view. The first point to be discussed is the fact that almost the same number of 14 nm (S-AuNS) and 37 nm (B-AuNS) nanoparticles, produces almost the identical instrumental response expressed as SPR signal even though a large difference (14-fold higher) of gold was adsorbed when injecting B-AuNS. Even if a relative large standard deviation was reported between SEM data related to the three miRNA families studied (mostly due to difficulties in counting the whole active chip surface for each family), the numbers we report reasonably show that both SPR signal and NP density are very similar if compared to previously mentioned studies. From the physical point of view, a larger amount of gold and, more specifically, the larger mass adsorbed on the chip, should be associated to

the change of the overall refractive index of the chip surface, thus giving a larger SPR response. In parallel, we also should consider that possible plasmonic effects would contribute to the final SPR signal considering that small and big nanoparticles have different LSPR (i.e. 522 and 532 nm, respectively). In our experimental set-up, a significant contribution by plasmonic effects should not be considered taking into account the small difference between LSPR of the two particles (just 10 nm) and the wavelength of the SPR light source used (i.e. 810 nm), which is far enough from the LSPR bands of the particles to avoid any influence in the SPR response. Furthermore, even considering plasmonic effects, they would increase the signal of B-AuNS due to their LSPR closer to the light source, which is not what we observed here.

Once excluded that the almost identical SPR response derived by a similar number of small and big NP is due to plasmonic effects we must consider as possible explanation the detecting system which is part of the commercial SPR-imaging instrumentation used here. In fact, according to the technical sheet provided by the manufacturer, the coupling of the CCD camera and the wavelength used here, results in an optical lateral resolution of 40 µm. If we then verify that the probe density of the surface is similar or lower than this size, we can suppose that one single small nanoparticle or one big nanoparticle, both giving a relative large SPR response that saturates the signal if compared with standard protein analytes, may produce a signal that cannot be easily distinguished by a low resolution CCD detector.

In our experimental setting we have two different probes: capturing DNA probes (covalently immobilised on the gold surface) deputed to specifically recognise the miRNA target and the DNA/miRNA duplexes formed during the injections of miRNA. These DNA/miRNA duplexes are actually the real probes recognised by the nanoenhancer made of AuNP conjugated with Ab anti DNA/RNA duplexes. In brief, from experimental data derived by the injection of increasing amount of

miRNA alone (i.e. the Langmuir in **Figure 38a**) we estimated that maximum $2.28x10^{10}$ DNA probes are available on the chip. In parallel, we calculated that when injecting 500 µl of miRNA 50 nM, a maximum of $2.68x10^{9}$ DNA/miRNA duplexes (i.e. the real probes recognised by the Ab conjugated to AuNP) were present on the chip. If we consider that an area of around 3.14 nm^2 is occupied by each single DNA/miRNA duplex, around 99.3 % of the spot's surface is free, guaranteeing around 20 to 30 nm of distance between duplexes. Starting from these data and also by observing the SEM image related to B-AuNS in **Figure 41a**, we can assume that most of nanoparticles are positioned, on average, at a distance close or larger than the optical lateral resolution of the SPRi detector. These data may thus suggest that, when the used SPRi imaging system has not a high lateral optical resolution as in our case, the enhancement by AuNP with larger size may not significantly differ from the enhancement derived by smaller nanoparticles but that, in this case, number of NP play a major role. It is therefore probable that different results may emerges when using other traditional (non-imaging) SPR systems or SPRi systems reporting high lateral optical resolution (e.g. reaching values around 2 or 5 µm).[207,208]

Another point to be discussed is whether the surface density of probes (DNA/RNA duplexes) used in our experimental conditions was low enough to guarantee 1:1 binding ratio between Ab conjugated on the AuNP and the DNA/miRNA duplexes (probes) on the chip surface. Having each Ab a distance between arms of max 14 nm[209] and having DNA/miRNA duplex an average distance of around 30 nm in our experimental setting, Ab mainly interact with the duplexes by 1:1 binding ratio at every miRNA concentration injected in the range tested (from 0.37 pM to 50 nM).

3.1.3. Conclusions

A new and practical simultaneous approach to sub-picomolar multianalyte detection of miRNAs using AuNPs has been developed - without the use of

enzymes or multi-step enhancing protocols. The major advantage is that just one stable and easy-to-prepare reagent consisting of gold nanoparticles functionalised with a commercially available Ab is sufficient for the detection of a (theoretically) unlimited number of miRNAs. In addition, several miRNA sequences can be detected at the same time in one single chip, making this strategy one of the best SPR-based approaches for miRNA detection (**Table 5**). These advantages derive by the coupling of an Ab able to recognise RNA/DNA regardless of sequence with the very good enhancing properties of gold nanoparticles. This protocol also allows better sequence selectivity than the intrinsically low sequence selectivity obtained by means oligonucleotide hybridisation on a bare SPRi chip. Most of these benefits are due to the optimisation of AuNS synthesis and functionalisation: the nano-structured enhancer was thoroughly characterised and with these proper control of the nanoenhancer we were able to amplify the signal of the miRNAs around 900 times and detect attomoles of several miRNA sequences at the same time with a universal nano-enhancer.

Table 5. Comparative table reporting examples of SPR-based miRNA detection strategies on recent years.[77]

Reference	Enhancing strategy	Sandwich free	Sequence Independent enhancing reagents	Enzyme free	Single step (steps number)	Multianalyte (miRNA simultaneously tested)	Detection limits
Vaisocherova *et al* 2015[206]	Sandwich + NPs	no	no	yes	yes	yes (4)	0.35 pM
Wang *et al* 2016[210]	Sandwich + NPs	no	yes	yes	no (2)	no	< 0.1 pM
Wang *et al* 2016[211]	Sandwich + GO-NPs	no	no	yes	yes	no	< 0.1 pM
Zhang *et al* 2013[212]	Sandwich + STRP	no	no	yes	yes	no	17 pM
Liu *et al* 2017[213]	Hairpin + sandwich + NPs	no	yes	yes	no (3)	no	< 0.1pM
Zhou *et al* 2011[214]	Enzyme + NPs	yes	yes	no	no (2)	yes (4)	0.1 pM
Ding *et al* 2015[215]	Hairpin + STRP	yes	no	yes	no (2)	no	1 pM
Fang *et al* 2006[181]	Enzyme + NPs	yes	yes	no	no (2)	yes (3)	10 fM

Qiu *et al* 2015[216]	Enzyme	yes	yes	no	yes	yes (2)	3 fM
Sipova *et al* 2010[186]	Antibody	yes	yes	yes	yes	no	2 pM
Nasheri *et al* 2011[217]	Protein p19	yes	yes	yes	yes	no	4 nM
Qian *et al* 2018[218]	Boronic-NPs	yes	yes	yes	yes	no	0.3 pM
This work: Artiga *et al*[197]	Antibody + NPs	yes	yes	yes	yes	yes (4)	0.5 pM

Different antibody functionalisation strategies and gold nanoparticles of different shape and size have been studied in order to improve and better understand this strategy. For two of the most common functionalisation strategies used to couple antibodies to gold nanoparticles, neutravidin and protein A, we observed how the neutravidin antibody biotinylation is efficient and stable and gave overall better SPR enhancement results. Even if the ProteinA-mediated functionalisation is more practical (e.g. no covalent modification of the antibody is required), this approach showed poor SPR enhancement especially when coupled with big nanoparticles (both spherical and prisms).

In parallel, studies on the SPR enhancement using gold nanoparticles of different shape showed that triangular gold nanoprisms (AuNPr) provide almost no SPR amplification if compared to AuNS, derived by a non-specific adsorption of AuNPr on the chip surface. Comparative experiments on spherical gold nanoparticles functionalised with the same theoretical density of neutravidin and injected in order to use a similar amount of total amount of gold, showed that in our experimental setting a larger size itself did not significantly increase the SPR signal as initially expected. Almost the same SPR signal was observed when using big nanoparticles even if the number of gold nanoparticles directly observed on the chip surface was similar and the amount of immobilised gold was much higher, probably due to optical resolution of SPRi systems. In summary, when the aim is to use nanoparticles as efficient and reliable enhancer of SPR response for real (e.g. diagnostic) applications at commonly used concentrations (O.D.

around 0.15) and using relatively short injection time (max 1.5 h), the best enhancing strategy can be different from what is expected theoretically. The use of standard small (14 nm-diameter) gold nanoparticles, conjugated with Abs by a standard functionalisation neutravidin approach, resulted as the best compromise between analytical performance, experimental feasibility and practicality.

3.2. AuNPs for PTT

3.2.1. Comparison of AuNPs for PTT

As detailed in the introduction, nanoparticle (NP)-mediated photothermal therapy (PTT) is a promising cancer treatment consisting of the use of heat to eradicate tumour cells (thermoablation) or weaken them, thereby making them more susceptible to other treatment(s), where the latter translates into a synergistic therapeutic improvement.[219] Nevertheless, adequately delivering and controlling heat production *in vivo* represents a significant challenge which will be better controlled as soon as we completely understand the correlation between LSPR, heat production and AuNP properties. Although many manuscripts concerning the optical applications of AuNPs are published each day, the direct comparison of their physicochemical properties is almost unheard in the literature, with *in vitro* and *in vivo* comparisons even more rare.[60] Thus if researchers wish to compare two types of nanoparticles it is almost impossible to draw conclusions from separate studies in the literature, where dramatic variations in the nanoparticle sizes, types, surface coatings, LSPR bands, specific photothermal excitation conditions, cell culture environments, and so on, all play their part. Herein we try to shed some light on this issue by comparing different shapes of AuNPs for PTT.

The aim of this study was to directly compare the synthesis, heating capability, extent of cellular internalisation and thermoablation capacity of two types of anisotropic AuNPs: gold nanorods (AuNRs) and nanoprisms (AuNPrs). Gold nanorods are one of the most commonly employed nanoparticles for PTT;[220,221] while gold nanoprisms are rarely employed even if they have showed very interesting PTT properties until now.[132] In order to perform the comparison between both shapes in the most appropriate conditions, the syntheses of both nanoparticles were tuned so that the corresponding nanoparticles posed a strong light absorption at *ca.* 1064 nm (the wavelength of the NIR laser used in this study). Further, both were stabilised with the same PEG coverage. Their heating

conversion efficiency was compared along with their ability to induce cell death and their cellular internalisation, in order to better understand how these two different shapes carry out their function as photothermal agents (**Figure 42**).

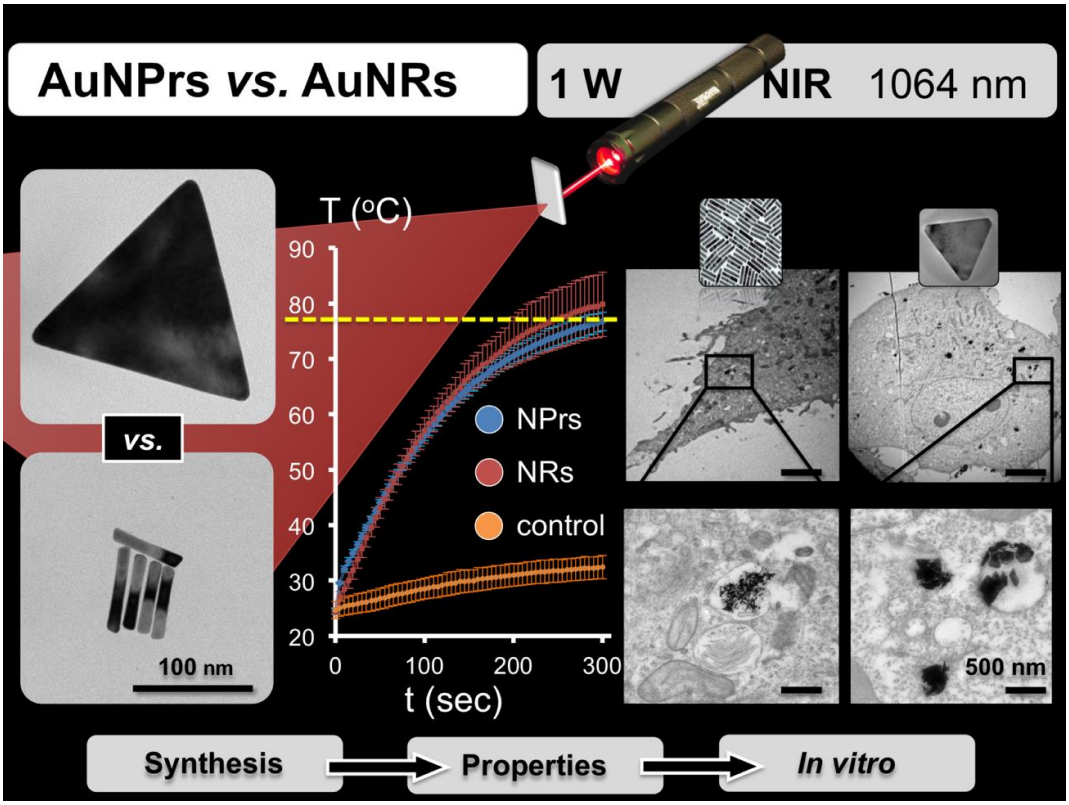

Figure 42. Overview of the comparison between AuNPrs and AuNRs for PTT. Reproduced with permission from[61]

3.2.1.1. Synthesis of AuNPs and characterisation

Where the objective of applying hyperthermia is to destroy malignant tissue(s), one of the main drawbacks concerns avoiding unwanted damage to the surrounding healthy tissues, especially pertinent for those which display high light

absorbance such as skin cells and the blood. One intelligent solution is to employ NIR light in the 'biological window' because between ca. 750-1200 nm the absorption of biological systems is highly decreased, especially for cytochromes (e.g. haemoglobin) that lie in the visible region.[222] Consequently, across this wavelength range, radiation can penetrate deep into tissue without causing significant detrimental effect to biological structures.[223]

The optical properties of metallic nanostructures are shown to be influenced primarily by the localised surface plasmon resonances (LSPRs),[72] as detailed in the **Introduction Section 1.4.3**. In the case of pseudo-spherical AuNPs, its LSPR bands lie in the visible region and when their size changes in size only produce slight changes in their optical properties. However, when anisotropy is added to the AuNP - such as growth of nanorods or nanoprisms - the optical properties of the nanoparticles change dramatically and are highly size-dependent (**Figure 7**).[224] As a result, for anisotropic AuNPs the major contribution to the UV−vis spectrum corresponds to the in-plane dipolar mode lying in the Near-Infrared (NIR) range.[75] The LSPR band of anisotropic AuNPs can be fine-tuned over a large wavelength in the NIR range just by controlling the dimensions of these AuNPs, making them extremely relevant for applications in photothermal therapy.[30,223]

Both AuNRs and AuNPrs exhibit size-dependent optical properties and can be synthesised to exhibit strong absorption in the NIR range. AuNPrs with an LSPR band at *ca.* 1100 nm were synthesised using an adaptation of a previously reported procedure.[75] The main advantage of this methodology is the avoidance of the cationic surfactant cetyltrimethylammonium bromide (CTAB), the most widely used and convenient surfactant for high-yielding syntheses of anisotropic particles such as AuNRs[224] and AuNPrs.[75] One limiting factor is that the cationic surfactant CTAB is a well-known highly toxic component and the need for alternative methods to produce NIR-absorbing AuNPs without CTAB is of great importance, as recently highlighted by Murphy and co-workers, pioneering author

of the seed-mediated approach involving CTAB.[75] In the employed methodology, the principal modifications of this synthetic procedure in order to produce AuNPr with LSPR band near 1064 nm were: i) the addition of potassium iodide at 12.2 µM final concentration and ii) that the gold reduction was performed in three time-lapsed steps, as opposed to two steps, allowing AuNPrs "seeds" to form and grow more slowly (**Figure 43A**). By this way, larger nanoprisms with LSPR band at higher wavelengths were obtained compared with the previously described protocol.[75]

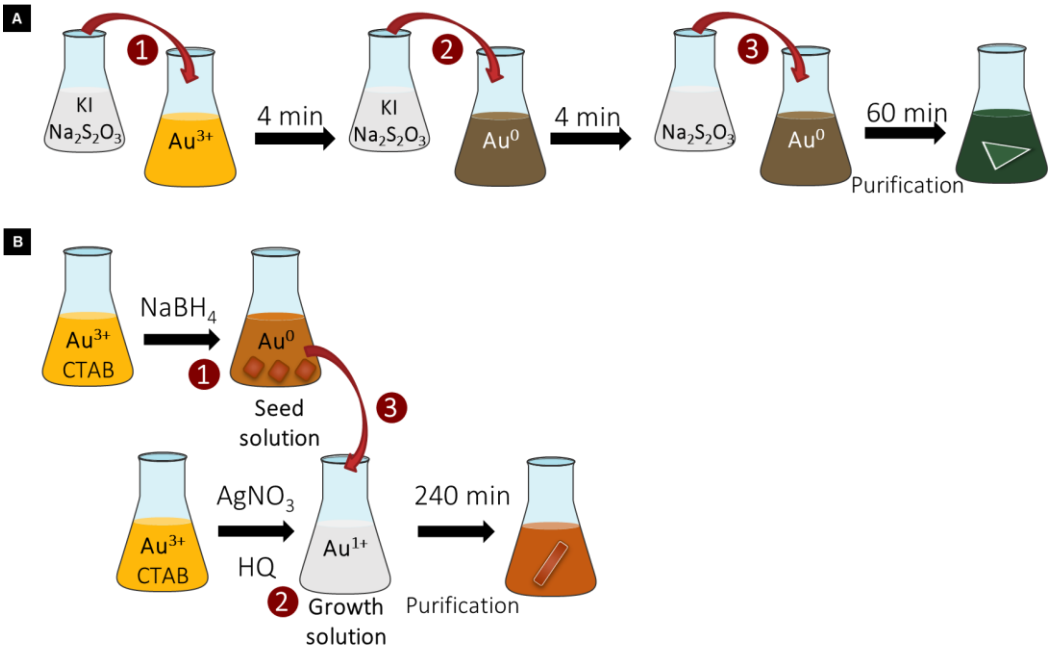

Figure 43. Step-by-step representation of the synthesis of the nanoparticles; **A**) synthesis of gold nanoprisms (AuNPrs); **B**) synthesis of gold nanorods (AuNRs).

The synthesis of AuNRs with LSPR band near 1064 nm was performed following a seed-mediated growth process (**Figure 43b**). After several unsuccessful attempts obtaining AuNRs with small aspect ratios and LSPR bands around 800-900 nm, we identified a highly reproducible procedure[27] and modified it to suit our requirements by some minor modifications and scaled-up (x10). The scale-up

was necessary in order to obtain larger amounts for cell culture studies. This synthesis could also potentially be scaled even higher, if needed, for future applications. Notably, the most significant of our alterations to the published synthetic procedure was that, after seed formation at room temperature, the growth reaction of the AuNRs was carried out at 26 ºC in a water bath to avoid CTAB crystallisation. The reaction was monitored by UV-Vis spectrum as the reaction procedeed, selecting five hours time point as the optimum reaction time to obtain an LSPR wavelength with a maximum of *ca.* 1080 nm (see **Figure 44**).

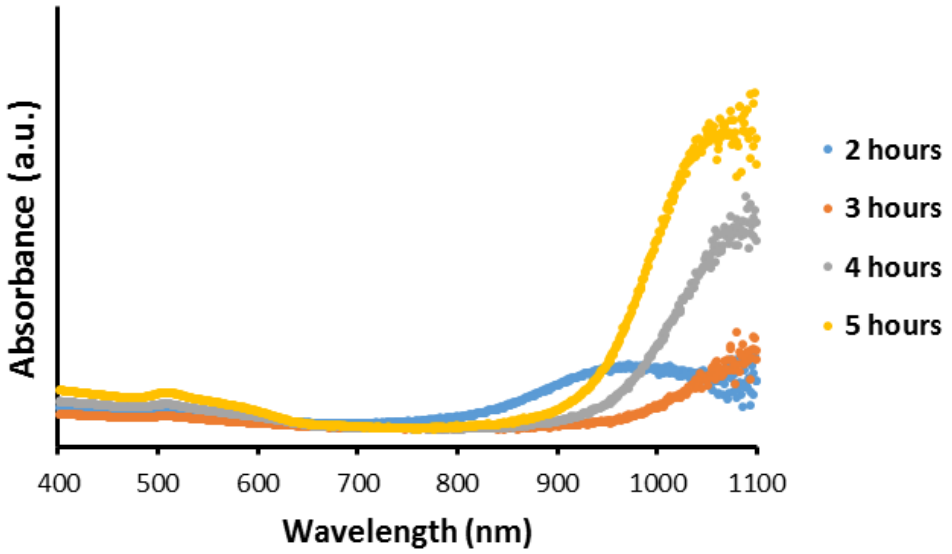

Figure 44. UV-Vis spectra following the formation of gold nanorods over a five-hour time period. Each spectrum corresponds at the same nanorod synthesis at different growth times.

To further increase the colloidal stability of the nanoparticles and their applicability for PTT in cell culture, both nanoparticles were surface-stabilised with heterobifunctional polyethylene glycol (HS-PEG-COOH, MW = 5000 g/mol (5 kDa)).[75] This polymer was elected due to its performance as AuNPrs stabiliser in PTT applications.[132] In order to ensure a proper comparison between both

AuNPs, an excess of the polymer was added to the AuNPs solution to saturate the nanoparticle surface and ensure fully stabilised nanostructures.[75] Sodium borohydride, $NaBH_4$, was required as a reducing agent at a molar ratio of 1:1 with PEG at pH 12 to avoid the formation of S-S bonds between individual PEG molecules (PEG dimers) that impedes its coordination to the AuNPs surface. The PEG stabilisation of the AuNPrs was carried out under sonication of the mixture at 60 ºC for 1 h to speed-up the process, and as an alternative to the reported overnight incubation under mild mixing.[75] A final centrifugation step was performed in order to discard excess of reagents; thereafter the samples were allowed to rest at room temperature for several weeks to sediment and separate the heavier AuNPrs from smaller pseudo-spheres and other pollutants remain in the upper phase.

On the other hand, synthesis surfactants on the surface of AuNRs exist in a dynamic equilibrium with the media, attached by non-covalent mostly hydrophobic interactions.[225] The remaining CTAB impedes the full Au surface coverage by PEG. Thus, by removing as much supernatant as possible during the washing centrifugations it is possible to change that dynamic balance in our favour, decreasing the amount of CTAB on AuNR surface that helps PEG to successfully reach the gold surface and form a conjugated stronger bond thanks to its thiol groups. However, the centrifugation of naked AuNRs in CTAB-depleted medium lead samples to undergo non-desirable shift in their LSPR wavelengths and aggregation. In order to avoid that, an optimised washing-stabilisation protocol was performed. Several parameters were studied, for example the sonication of AuNRs after the synthesis during the first PEGylating step leads to a shift in the LSPR band in the UV-Vis absorbance spectrum which is indicative of the AuNPs dimensions were being severely affected (**Figure 45**). This data demonstrate that AuNRs were more sensible to the sonication process than AuNPrs. Finally, an optimised washing-stabilisation protocol was developed by adding an additional PEG reaction step without sonication at room temperature

overnight after the first washing centrifugation step. By this way the AuNRs remain stable during the subsequent washing steps and once CTAB was completely removed a final PEGylation process was performed to completely saturate the surface giving a LSPR peak near 1040 nm at the end of the PEGylation and washing process (**Figure 45**).

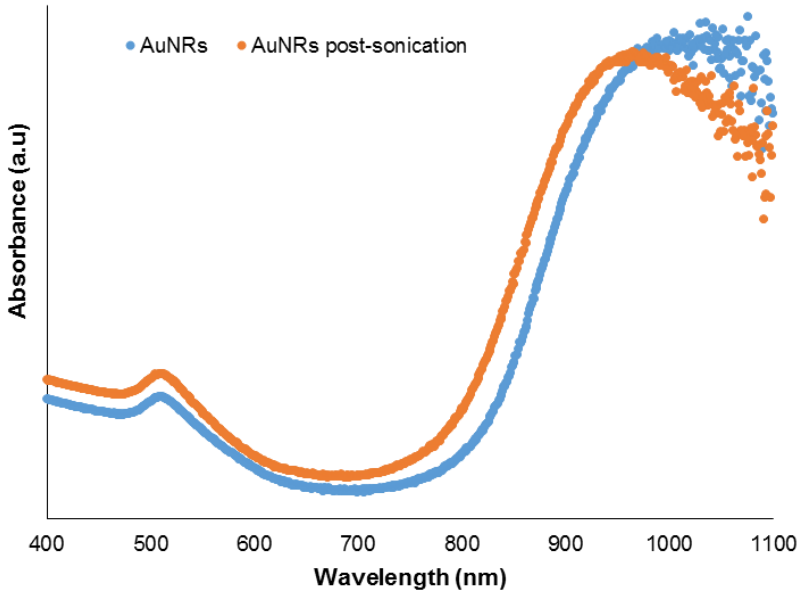

Figure 45. Example of the changes produced in the UV-Vis absorbance by sonication of AuNRs during first PEGylating step. The LSPR peak after 15 min sonication at 60 ºC decrease *ca.* 100 nm, indicating that the sonication affects dramatically the dimensions of the AuNRs. For this reason, the protocol was adapted and the first PEGylating step was carried out without sonication at room temperature overnight in order to avoid this shift.

Both types of nanoparticles were also characterised by ICP, TEM and SEM (**Figure 46**). The UV-Vis spectra of both types of AuNP displayed LSPR bands with sufficient overlap with the 1064 nm laser inside the NIR range (1044 nm for AuNR@PEG and 1100 nm for AuNPr@PEG). Correlating the LSPR absorbance obtained by UV-Vis spectroscopy with the Au concentration obtained from ICP analysis it was possible to obtain a conversion factor (Ɛ) of 29 mL mg^{-1} cm^{-1} for AuNPrs and 74 mL mg^{-1} cm^{-1} for AuNRs. This conversion factor is of great utility

for calculating weight concentration (mg/mL) of gold AuNPs in each sample and the synthesis yield for both synthetic procedures. The respective yields for each synthesis were 71 % for the AuNPrs and 80 % in the case of AuNRs (**Figure 46E**). Both types of AuNPs also showed a strong absorbance peak at *ca.* 530 nm corresponding to a combination of AuNPs transversal absorbance and pseudo-spherical polyhedral gold nanoparticles. Comprehensive analysis of TEM and SEM images were used to calculate the mean surface area of the particles. Briefly, AuNPrs (considered as triangular prisms with 173 nm side and 9 nm constant thickness) possess a surface area of 15.0 m^2/g; while AuNRs (considered as perfect cylinders of 11 nm diameter and 76 nm length) have a surface area of 23.2 m^2/g. Although both nanoparticles obtained from these methods are considered to be stable enough for months and we have corroborated it, each sample was tested before each use by performing UV-Vis spectroscopy. Any shifting of LSPR peak, intensity or shape changes would be considered as direct indications of aggregation or degradation of the AuNPrs, discarding them for the rest of the study.

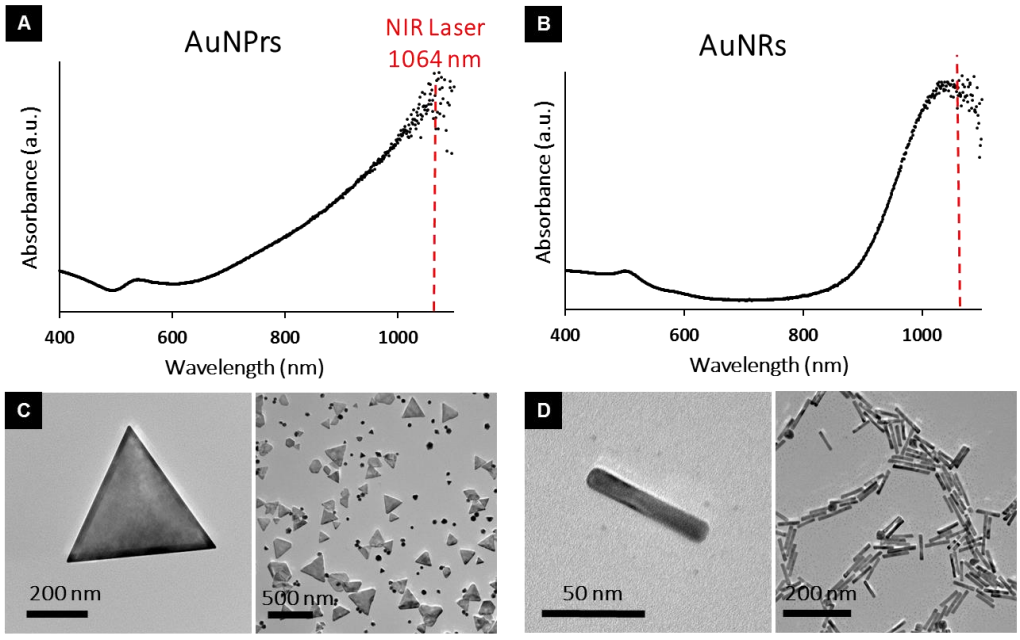

E

	Yield	Length (nm)	Width (nm)	Surface area (m^2/g)
AuNPrs	70.7%	173	9	15.0
AuNRs	79.7%	76	11	23.2

Figure 46. UV-Vis spectroscopy, TEM images and characteristic size and surface area of the particles. A,B) UV-Vis absorbance spectra of AuNPrs (A) and AuNRs (B), with red dotted lines representing the wavelength of the NIR laser (1064 nm). Both nanoparticles possessed a dominant LSPR band in the NIR range overlapping with the wavelength of the laser, 1064 nm. C,D) TEM images of AuNPrs (C) and AuNRs (D). E) From left to right: reaction yield; length, width and surface area of each type of nanoparticle. Adapted with permission from[61]

3.2.1.2. Photothermal Heating Properties of AuNPs

Upon excitation by incident light, sharp local heating can be generated by the ability of nanomaterials to convert light energy into local heating, rendering these particular anisotropic AuNPs as extremely efficient for NIR-induced heating.[74] Several heating trials were performed to evaluate the heating capacity of both

types of AuNPs upon laser irradiation. Thus, an increasing concentration of AuNPrs was tested (from 20 to 150 µg/mL) in order to identify the concentration of AuNPrs that showed the same heating capacity as AuNRs. For these studies, two standard concentrations of AuNRs were used (20 and 100 µg/mL, herein referred to as AuNR20 and AuNR100, respectively) (**Figure 47**). The results revealed a linear initial temperature increase for both the AuNRs and AuNPrs (**Figure 47**). In these initial studies, AuNPr100 (100 µg/mL) heated at a rate of 0.30 ºC/s and gave a final temperature of 87.9±7.8 ºC after 10 min irradiation, which was similar to AuNR20 (0.25 ºC/s and 83.6±6.9 ºC) (**Figure 47**). These concentration values (AuNR20 and AuNPr100) for each nanoparticle revealed similar heating capabilities, with only minor deviation. The AuNRs were found to be far more effective light-to-heat transducers, presumably owing to their higher specific surface area. These optimum concentrations were then also compared with the heating of AuNR100 (100 mg/mL) in order to have a direct comparison of the effect with respect to the weight of gold for each nanoparticle type. AuNR100 displayed the greatest heating effect, characterised by an initial rate of 0.40 ºC/s and a final irradiation temperature of 93.3±6.3 ºC, as well as the highest heating efficiency, transforming 45.3 % of the laser light intensity (1100 mW) at the plate into heat to increase the temperature of the sample with a power of 498 mW. This higher heating capacity of the AuNRs correlates with the higher absorbance intensity of the LSPR peak observed by UV-Vis, with conversion factor (Ɛ) of 29 mL mg^{-1} cm^{-1} for AuNPrs and 74 mL mg^{-1} cm^{-1} for AuNRs. At the other end of the scale, AuNPr20 showed an initial rise in temperature of 0.17 ºC/s and reached 68.3±4.5 ºC after 10 min. The intrinsic heating of the DMEM control should be noted (0.06 ºC/s and 42.2±3.3 ºC), a phenomenon often observed in photothermal therapy applications.[226] Although AuNR20 and AuNPr100 displayed approximately the same overall heating capacities after 10 min irradiation, in order to have a direct comparison at the same concentration, AuNR100 and AuNPr100 were selected for further cellular studies.

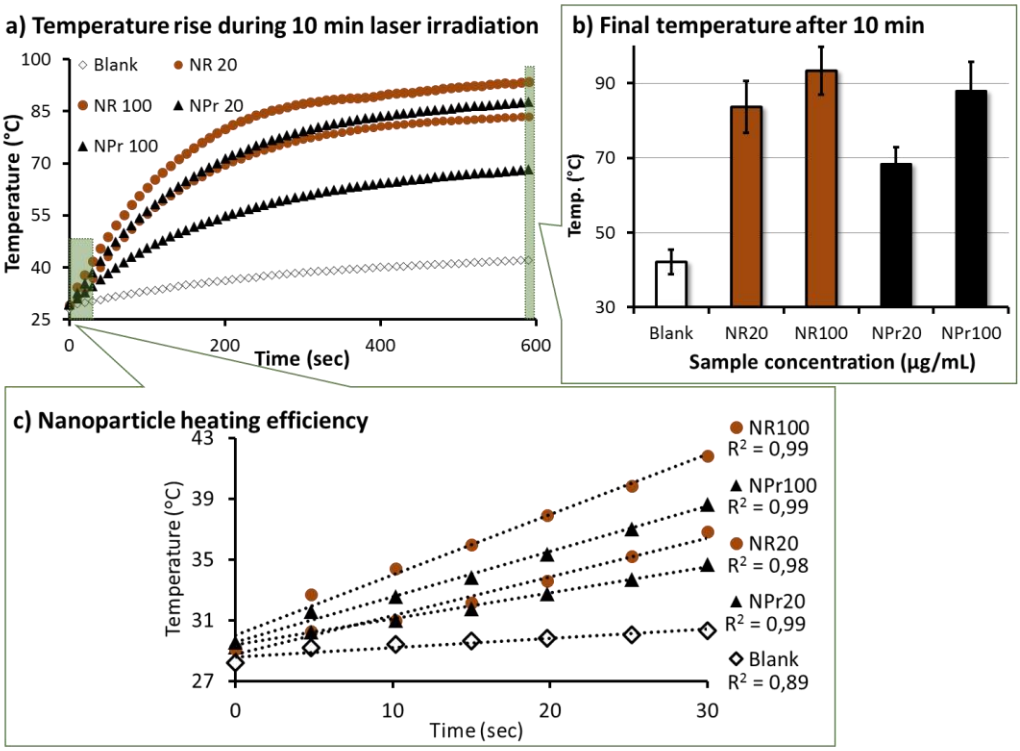

d) Summary of heating properties

Sample	Temperature Increase (°C/s)	Heating Efficiency (%)	Temperature after 10 min irradiation (°C)
Blank	0.06	6.92	42.2±3.3
NR20	0.25	29.03	83.6±6.9
NR100	0.40	45.27	93.3±6.3
NPr20	0.17	19.54	68.3±4.5
NPr100	0.30	34.03	87.9±7.8

Figure 47. Characterisation of the heating capacity of the gold nanoparticles. a) Heating ramps that represent the rise in temperature registered by each type of nanoparticle during the 10 min irradiation period. b) Final temperature of the cell culture medium recorded after 10 min irradiation. c) Plot and linear adjustment of the nanoparticle heating efficiency during the most linear rise in temperature (first 30 seconds). d) Table collecting from left to right: heating efficiency as the representation of the slope of the curve during the first 30 seconds of irradiation, the % of laser intensity that is effectively converted into heat, and the final temperature reached after 10 min laser irradiation. Adapted with permission from[61]

Our collaborators from University of Glasgow, Dr. Anil Pravin Patel and Dr. Catherine Berry, have replicated these comparative studies in depth using a number of different cell lines, with the two AuNRs and AuNPrs produced by us. They compared the heating efficiency in their laboratory with their own laser set up and confirmed our own results previously presented, showing a higher heating efficiency for AuNRs than AuNPrs (see **Figure 48**). As recently highlighted in *Nature Nanotechnology*, an improvement in the reproducibility and transparency of the research in nanobiomedicine is of central importance for the advancements on the field.[227,228] For this reason, the results obtained by our collaborators that complement and corroborate the results obtained in this section of the thesis have been included.

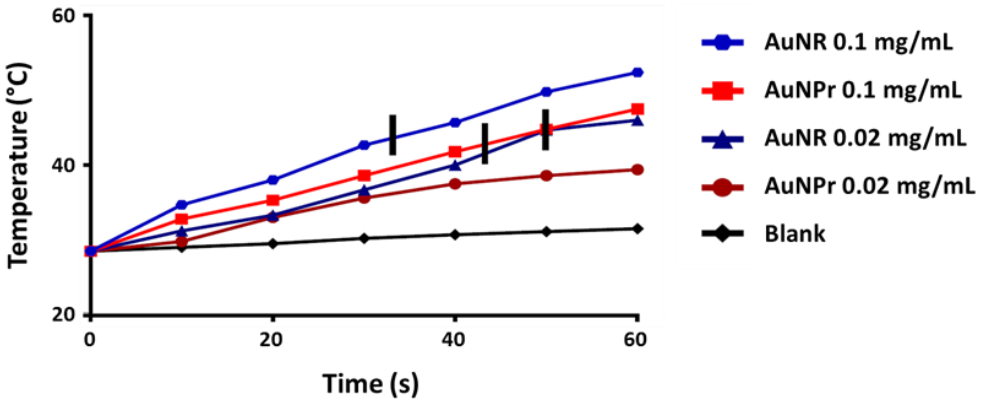

Figure 48. The hyperthermic temperature profiles of both AuNPrs and AuNRs at 0.02 and 0.1 mg/mL concentration during 60 seconds of irradiation with a 1064 nm continuous wave 1 W laser.

Some studies suggest that laser irradiation can change and deform AuNP shape altering the physicochemical properties of the nanoparticle and impeding its use for several cycles of PTT.[229] The stability of the AuNPrs and AuNRs upon laser irradiation was assessed comparing the UV-Vis spectroscopy and SEM imaging before and after the 10-min irradiation period. The apparent increase in the

intensity of the LSPR band after irradiation is caused by the evaporation of water which leads to a subsequent increase of the effective concentration of the particles in solution, however the profile of the UV-vis spectra remained unaltered suggesting that neither nanoparticle type was affected by the laser. This was confirmed by SEM which showed that neither AuNP morphology was affected by the laser irradiation (**Figure 49**). Our results demonstrate that for the conditions tested herein, the AuNPs retain their shape, LSPR properties and colloidal stability.

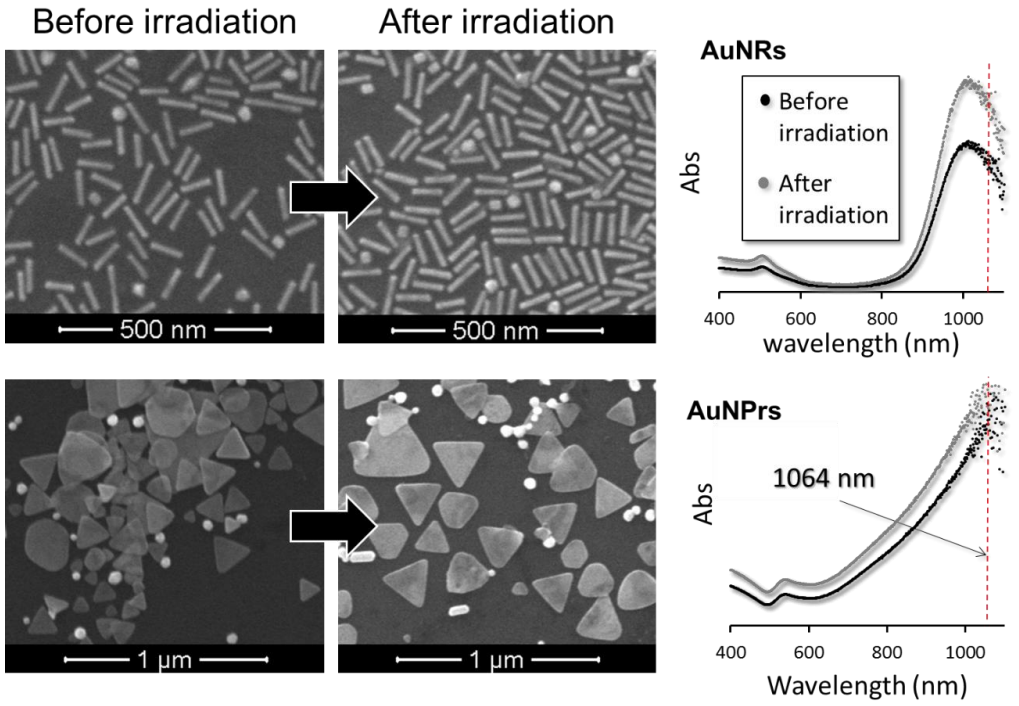

Figure 49. Nanoparticle stability studies. SEM imaging and UV-Vis spectroscopy of the nanoparticles before and after irradiation of the laser for 10 min operating at 1.1 W. The conditions of irradiation affected neither the morphology nor the UV-vis spectra. The increase in the absorbance showed in the UV-Vis is caused by a decrease of the volume of the sample due to evaporation through the process.

This discrepancy with some studies in the literature probably is produced by the laser technology employed during irradiation. While pulsed lasers irradiate the

sample with a huge amount of energy in very short times provoking the deformation of AuNPs,[229] we have employed a continuous wave laser operating at a power output of 1100 mW and illuminating the sample with a power per unit of area of ca. 3.3 W/cm^2 that enable a stable heat production by the AuNP. These results suggest that a continuous wave laser could be preferable to pulsed laser for PTT, especially for applications requiring several irradiation steps, such as a combined therapy for tumour resection.

At this point in our analysis, the higher yield, surface area and heating efficiency all greatly favour the AuNRs over the AuNPrs as photothermal agents; but to delve deeper into this comparison, *in vitro* analyses comparing these particles were necessary. In any case the photothermal effect is a characteristic and versatile property applicable to many biomedical applications including photothermal therapy,[230] drug delivery,[231] optoacoustic imaging[78] and biosensing,[232] among others. Even if we have focussed the rest of our study in the PTT application, the results obtained in this section would be useful for any of the aforementioned applications.

3.2.1.3. Photothermal effect in cells

Prior to their use with cells, AuNPs were sterilised by filtration and gold concentration re-quantified using ICP-AES. Vero cells were incubated with the previously studied concentrations of AuNR100 and AuNPr100 in 96-well plates for 24 h and, only after removing the non-internalised AuNPs, the cells were irradiated for 10 min under the established working laser configuration. The laser intensity (3.3 W/cm^2) was kept intentionally low during both the heating characterisation and throughout the cell irradiation process in order to stay in the range where cell death is mainly governed by an apoptotic process, according to recent studies.[132] Cell death was monitored by phase-contrast microscopy post-irradiation to determine the optimal point for cell viability assays (**Figure 50**).

Previously it had been reported that the cell death after irradiation occurs mainly in the first 5 h after irradiation.[132] According to this data and the phase-contrast images after irradiation, MTT cell viability assays at 5 h post-irradiation were performed (**Figure 50**). The results derived from the MTT assays shown that, although AuNR100 and AuNPr100 concentrations were essentially non-toxic to the Vero cell line before irradiation, applying the laser to cells with AuNR100 reduced viability to 86±3 %; while in the case of AuNPr100 viability was reduced to 44±1 %. Importantly, the irradiated particle-free control cell viability stood at 92±5 %, revealing that the laser itself is not able of inducing significant cell death under the studied conditions. Phase-contrast microscopy of the cells at five-h post-irradiation aptly illustrate how the cells incubated with AuNPr100 are apoptotic/necrotic; whereas cells treated with AuNR100 show morphology commensurate with the control cells. Analysis of final cell culture temperatures following 10 min irradiation showed that the net temperature rises for the same AuNP concentrations (AuNPr100 and AuNR100), one can observe how AuNPr100 reached 47 ºC while AuNR100 reached 45 ºC. It is important to note that the global temperature of the Vero cells without particles reached 43 ºC indicating that cultured cells do display some interaction with the 1064 nm laser beam.

The *in vitro* studies showed that only AuNPr100 was capable of inducing cell death upon irradiation, and at the same time raises the global temperature of the medium higher than AuNR100. Similar tendencies were observed by our collaborators from University of Glasgow when studying the photothermal efficiency of AuNRs and AuNPrs in MCF-7 3D tumour spheroids (**Figure 51**). In this study the AuNPr appeared to be more efficient at killing the cells than AuNPr, both in 2D and 3D. These results are quite surprising when compared with the ones showed in **Section 3.2.1.2**, where AuNRs provide a more efficient light-to-heat conversion. In order to deepen the understanding of this issue, cellular internalisation studies of the AuNPs were performed in subsequent section.

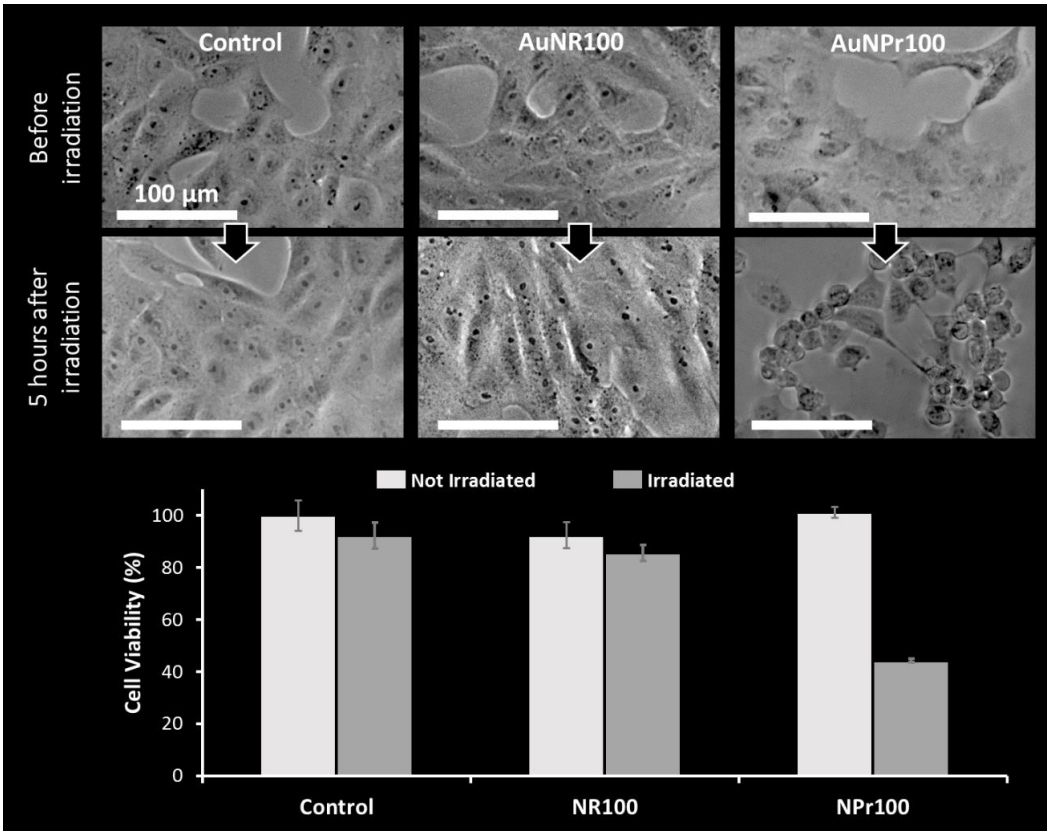

Figure 50. Cell morphology and viability following thermoablation studies. (Top) Cell morphology changes post-irradiation: cells incubated with AuNR100 and AuNPr100 were observed by phase-contrast microscopy for five h post-irradiation; all scale bars correspond to a distance of 100 µm; neither irradiation of nanoparticle-free control nor AuNR100 (100 µg/mL) revealed changes in cell morphology; however, cells incubated with AuNPr100 (100 µg/mL) began showing significant morphological changes from 2 h post-irradiation and peaked at 5 h. (Bottom) MTT assays for cell toxicity and viability of AuNR100 and AuNPr100 (100 µg/mL) of non-irradiated and irradiated cell samples 5 h after laser treatment. Adapted with permission from[61]

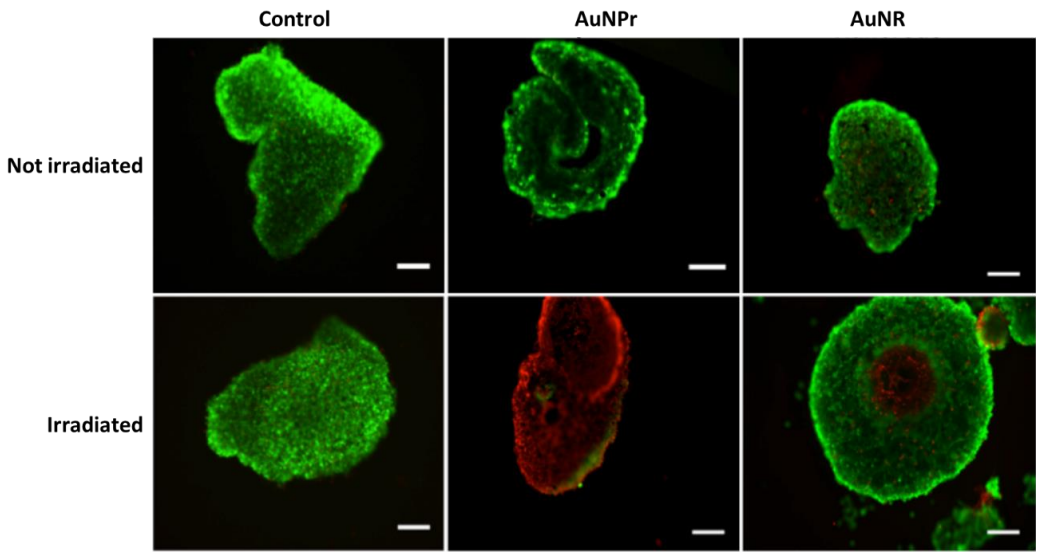

Figure 51. MCF-7 3D tumour spheroids following irradiation with a 1064 nm laser for 1 min. Control cells contain no GNPs. Green fluorescence indicates viable cells and red indicates dead cells. Scale bar = 200 µm. Three independent biological repeats (n=3).

3.2.1.4. Cellular internalisation

Due to the differences observed between the heating efficiency studies where AuNRs showed a higher photothermal conversion and the photothermal effects in cells where AuNPrs acted as the only efficient cell death mediators, next step consisted in the study of the AuNPs cellular internalisation to understand this apparently contradictory data. Cellular internalisation of nanoparticles is a critical issue for biomedical applications. The cellular uptake plays a crucial role in nanoparticle toxicity and affects decisively its application for drug delivery, therapeutics and imaging. For all these reasons, several techniques were explored to elucidate the cellular internalisation of both AuNPs in Vero cells (dark field, TEM microscopy and ICP analysis) using the selected concentrations of AuNPs for PTT (AuNR100 and AuNPr100).

Since AuNPs produce insufficient contrast to be visualized by bright field microscopy alone, the AuNP internalisation was analysed by dark field microscopy/fluorescence (DAPI) (**Figure 52**). In this technique, only the scattered light enters the objective lens, while the directly transmitted is not collected due to a direct-illumination block using a special condenser in the microscope. Due to the higher atomic mass and density of AuNP, the light is scattered by them in a highly specific manner compared with biological molecules,[233] allowing to see regions with AuNPs as bright zones in the dark images. DAPI fluorescence is used to visualise cell nuclei and corroborate how AuNPs are located surrounding cell nuclei. AuNR100 showed no observable internalisation, but AuNPr100 were clearly visible using dark field microscopy. Even if dark field microscopy represent a practical and straightforward technique to assess the cellular internalisation of AuNPrs, without being obliged to resort to other more complex and costly analytical techniques, the differences between AuNPr and AuNR could be caused by a higher contrast capability of AuNPrs or a larger internalisation or a combination of both.

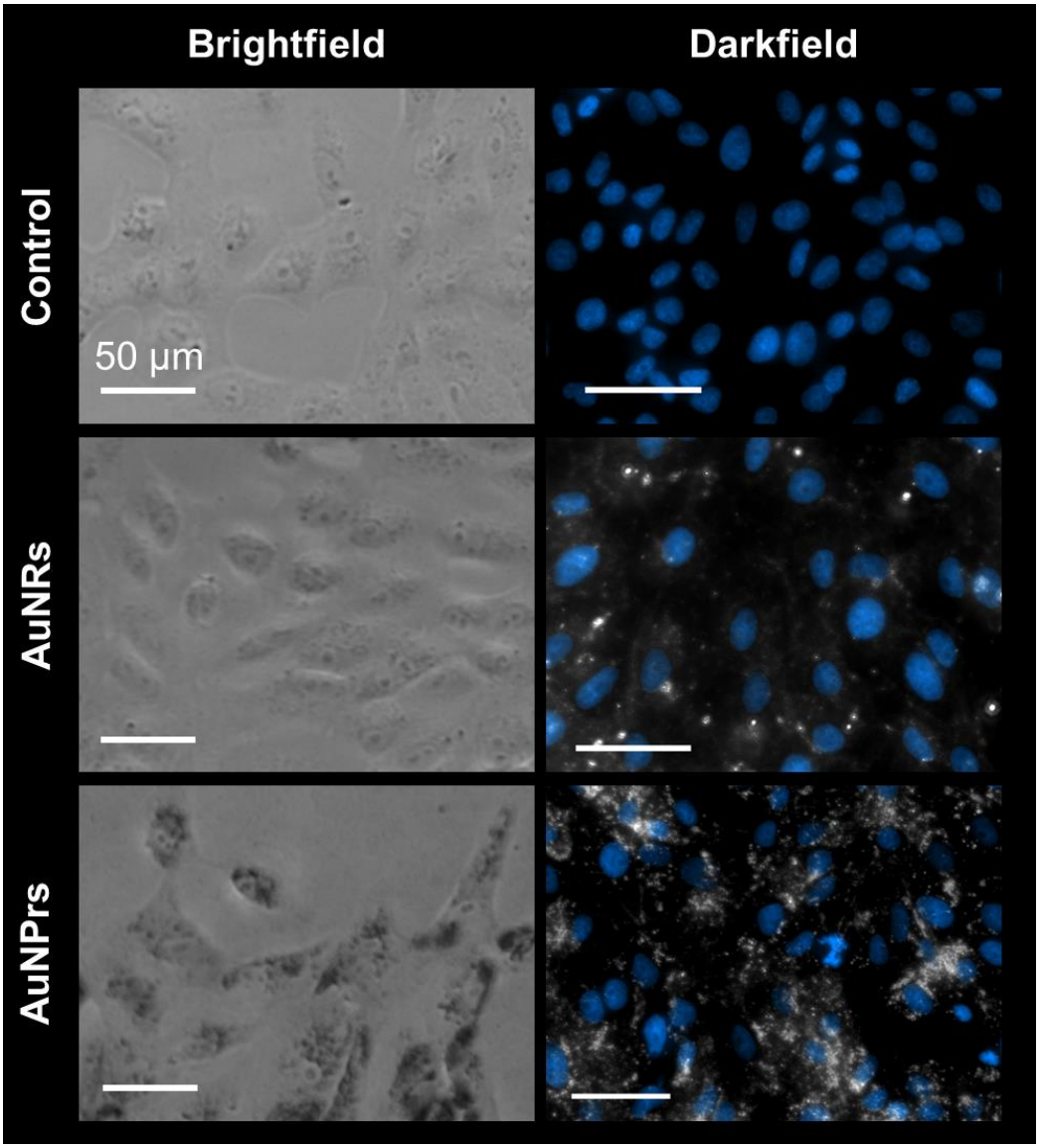

Figure 52. Optical imaging of the cellular internalisation of AuNPs. (Left) Bright-field phase contrast images and (Right) Dark-field images showing the nucleus stained with DAPI (blue), where white contrast areas correspond to AuNPs. This figure illustrates how AuNPrs were homogeneously distributed inside the cytoplasm, were not attached to the cell membrane and did not form extended aggregated structures, while AuNRs were unable to be detected by dark field.

From these images we postulated that there was a greater internalisation of AuNPr than AuNRs, but to gain a better understanding of this we used ICP analysis to precisely quantify the internalisation of Au inside the cells. In a separate experiment, after 24 h incubation of Vero cells with AuNR100 and AuNPr100 concentrations, the amount of internalised gold in the samples was measured by ICP analysis. The data showed that while the concentration of AuNR100 internalised in Vero cells was equal to 0.077 pg of Au/cell, the concentration of internalised AuNPr100 reached 28.73 pg Au/cell, i.e. >370 times higher than for AuNR100. This data are in concordance with the ones obtained by our collaborators from the University of Glasgow (**Figure 53**), where they clearly see a higher internalisation of several magnitude orders in the case of AuNPrs, independent of the concentration of AuNPs employed and both in MCF-7 and MG63 cell lines. This severe variation in AuNPs uptake between nanorods and nanoprisms is probably caused by the different shapes, sizes and/or protein corona formation; as it had already described for other types of gold nanoparticles.[59,234] Different-shaped nanoparticles also show a difference in the curvature and area of their surface that could determine the contact with the cellular membrane. A comprehensive study to exactly understand why this enormous difference is produced could be really interesting in the near future.

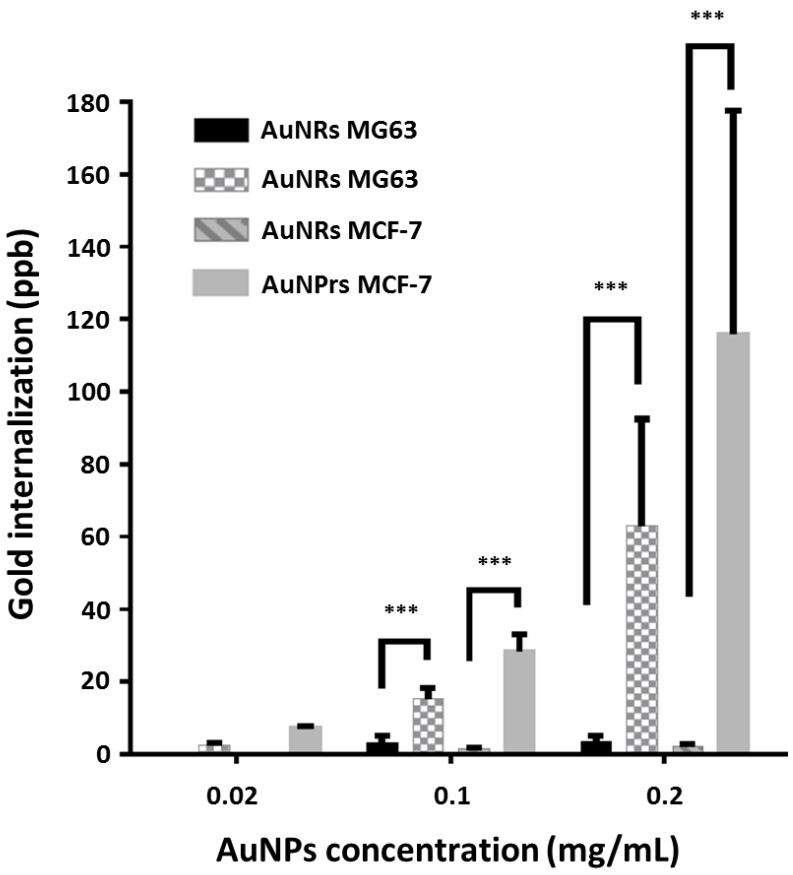

Figure 53. ICP-MS analysis of MG63 and MCF-7 monolayer cells treated with various concentrations of AuNPs at 24 h (n=3, error bars denote SD).

One of the aims of our collaboration with the University of Glasgow was to better understand the cellular internalisation of AuNPs in different cell lines. Scanning Electron Microscopy (SEM) showed that both in the case of AuNPrs and in the case of AuNRs there was a marked increase in the number of cytoplasmic extensions in the form of filopodia, when compared with control groups (without AuNPs), which demonstrated a smooth cell surface (**Figure 54**). These observations occurred independently of the cell line studied (MG63 or MCF7).

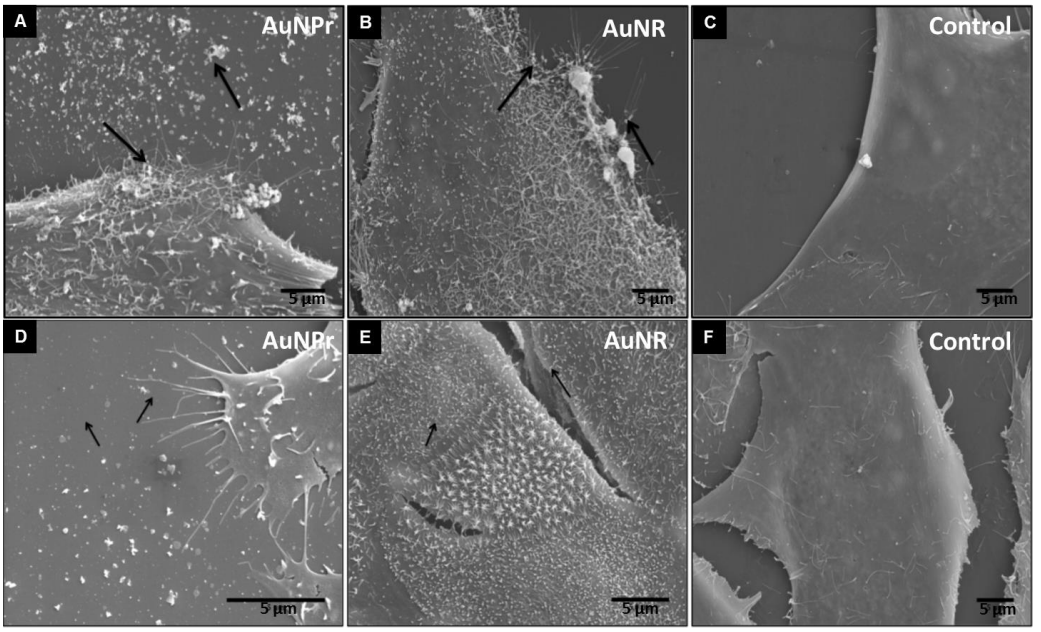

Figure 54. Figure 3-12: SEM images of MG63 cells incubated for 24 h with (A) gold nanoprisms, and (B) gold nanorod, whilst (C) control cells were not incubated with AuNPs and SEM images of MCF-7 cells incubated for 24 h with (D) gold nanoprisms, and (E) gold nanorods, whilst (F) control cells were not incubated with AuNPs. AuNP deposits were observed both on the cell membrane and on the coverslip surface (black arrowheads), inducing a large number of filopodia compared to controls. Scale bar depicts 5 µm.

The precise location of the AuNPs within the cells was obtained using resin-bound cells that were cut with a microtome into ultra-thin slices and stained for electron microscopy investigations. Vero cells were incubated for 24 h with the two samples that contained the same concentration of Au, AuNR100 and AuNPr100, prior being fixed with glutaraldehyde, post-fixed with osmium tetroxide and embedded in Durcupan resin. Semi-thin 1.5 µm sections were cut into finely into ultra-thin sections of <0.08 µm. A reference Vero cell sample was left untreated as a control. Both AuNRs and AuNPrs accumulated inside vesicles and none appeared attached to the plasma membrane, free in the cytoplasm or in the nucleus (**Figure 55**). With this technique, the higher level of internalisation of AuNPrs than of AuNRs was clearly evident, confirming ICP obtained data.

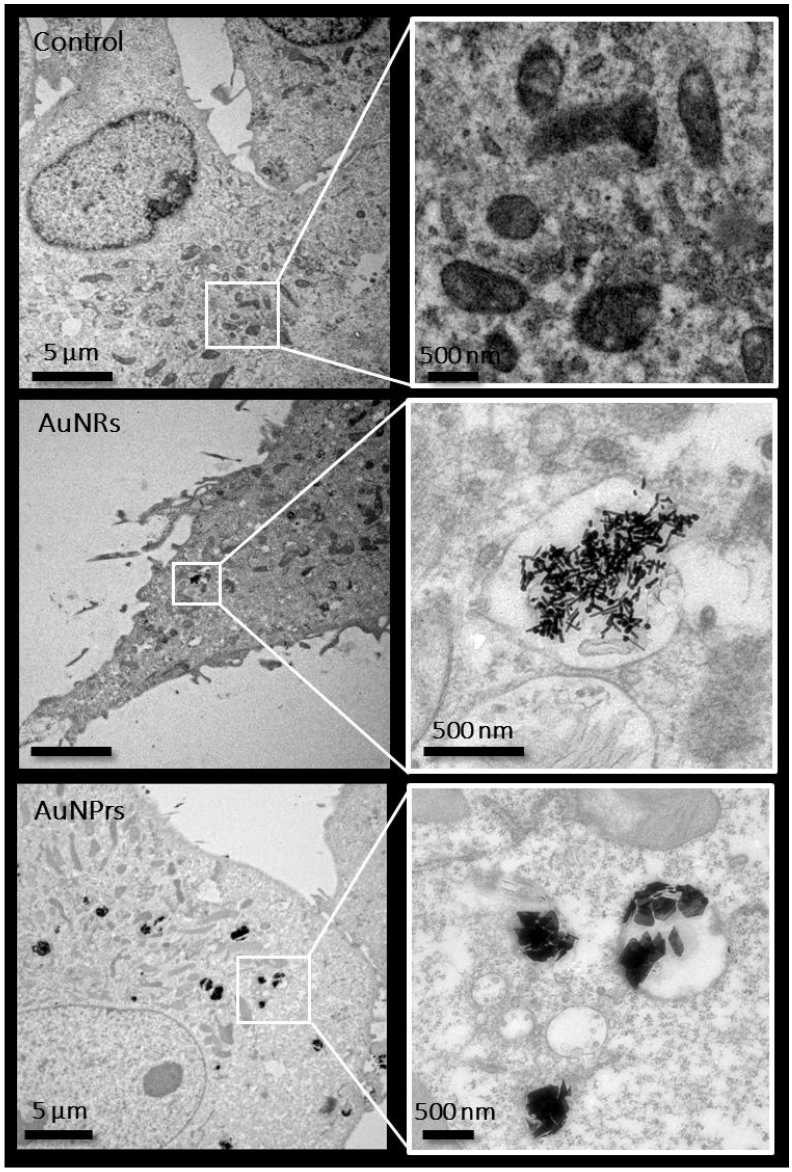

Figure 55. Subcellular localisation of nanoparticles. TEM imaging of ultra-thin slices of fixed cells following 24 h incubation with AuNRs or AuNPrs. AuNPs were distributed inside vesicles; no AuNPs were observed inside the nucleus or attached to the cytoplasmic membrane. Adapted with permission from[61]

As we have demonstrated all along this study, the shape of AuNPs is a critical factor determining the cellular internalisation. In the case of AuNRs, we have

observed poor cellular internalisation, making them incapable of inducing cell death under the conditions employed in this study. It should be noted that many studies on AuNRs for photothermal therapy applications often employ higher concentrations of AuNRs and long irradiation times,[132,235] whereas we routinely aim to employ the minimum required concentration to induce cell death. Furthermore, AuNRs are frequently used as platforms for multi-therapeutic modalities so have vastly more complex surface functionalities than our simple PEG-stabilised AuNRs. The differences observed in this study could be related to the protein corona formation or to differences in the mechanism of internalisation of the particles. Physicochemical properties of AuNPs, such as shape,[59] size[234] and charge[236] have been critical factors determining the formation of the protein corona and cellular internalisation. It has been investigated how differences in these physicochemical properties caused a different scavenger receptor-, caveolin- or clathrin-mediated endocytosis of AuNPs.[234] A common strategy to enhance and to control the rate and amount of AuNPs endocytosis for PTT is the use of targeted uptake.[237] However this strategy enhance enormously the costs, the time-consume and the complexity of the nanomaterials preparation. As an interesting alternative to this strategy, a simple and cheap alternative is proposed and studied in the following **Section 3.2.2.**

3.2.2. Hydrogel entrapment of AuNPs for PTT

In the previous section, AuNRs were demonstrated to posess a high potential for PTT due to their excellent light-to-heat transduction properties, however their efficacy *in vitro* is inadequate because of low cellular internalisation.[61] To overcome this barrier to application, one of the most common solutions found in the literature is the use of post-synthetic functionalisation with molecules to improve cellular internalisation.[220,238] However this can in turn reduce nanoparticle stability, aggregation in cell culture media and so forth; not to mention problems with reproducibility and elevated synthesis costs. In recent years investigators

have highlighted the need for reducing the complexity of nanotherapeutics to allow for clinical translation while simultaneously maintaining their therapeutic effect.[239] It is with this in mind that we have framed the research presented herein, where our hypothesis was that embedding the active photothermal element (in this case the AuNR) in a polymeric cell-adhesive hydrogel we would improve the efficacy of the thermal treatment required to destroy cells without the need for cellular internalisation.

The naturally occurring polymer chitosan has been selected for the entrapment of AuNR. This polymer has low toxicity and immunogenicity and it is biocompatible, biodegradable and bioadhesive.[142] Besides, as chitin is one of the most abundant polymers in nature (obtained from the exoskeletons of crustacean, insects and the cellular wall of fungi), chitosan is readily available and cheap. The mucoadhesive properties of chitosan are due to the fact that it is one of the richest natural polymers in amino groups, available for their interaction with other molecules[240] and that confer the capacity to form hydrogels in the presence of anions by ionotropic gelation. The complementary properties of chitosan to those present in the AuNPs have enabled their use as gold-chitosan hybrid materials with different purposes, including tissue engineering,[241] antibacterial,[242] cancer treatment,[162] sensing[243] and oral delivery of drugs.[162]

In the present work the Keggin-type polyoxometalate (POM) phosphotungstic acid (PTA), was used as an anionic gelling agent that act as an electrostatic crosslinker, for the synthesis of a hybrid organic-inorganic sub-micrometric container based on a chitosan hydrogel. As an illustrative example of their polyvalence, POM-chitosan hybrid materials have also been explored as anticancer drugs,[244] catalysts[245] and antibacterial agents[246] and in all of these applications the encapsulation of AuNPs could be of interest for a number of potential biomedical applications.

The resulting functional container described in this chapter presents biocompatibility and it was a highly efficient heat mediator upon excitation of their localised surface plasmon resonance (LSPR) band with a NIR laser at 1064 nm, which has been used for the photothermoablation of eukaryotic cells *in vitro* due to its cell adhesive properties (**Figure 56**).

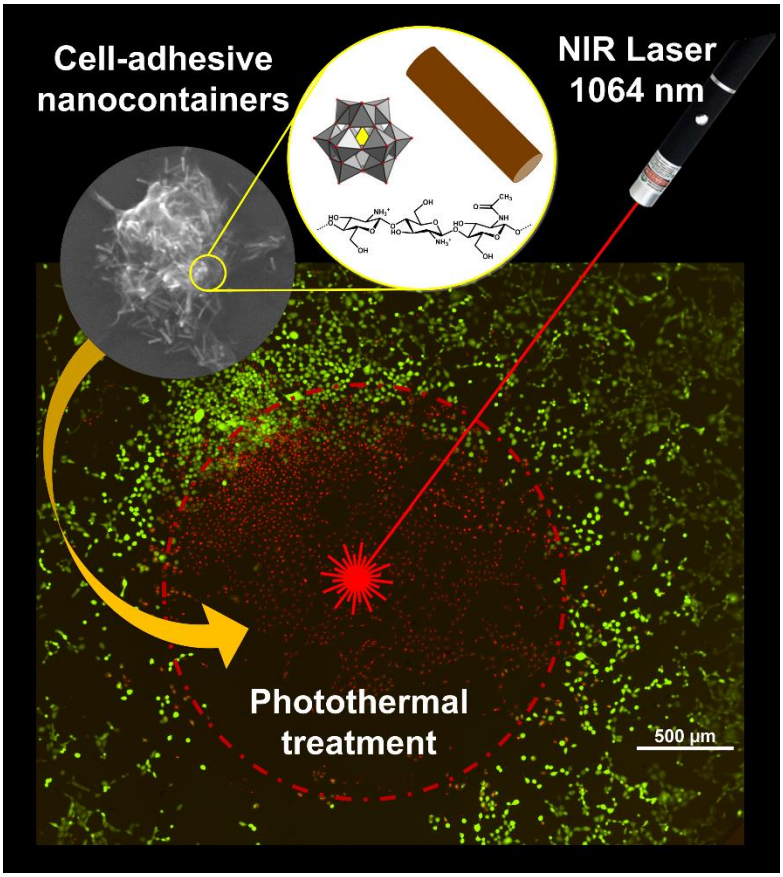

Figure 56. Schematic representation of this study, where AuNRs were entrapped into a chitosan hydrogel to adhere to cell membrane and produce heat that provokes the death of cells upon irradiation with a NIR laser. Adapted with permission from[143]

3.2.2.1. AuNR entrapment in chitosan hydrogels and characterisation

As this study was proposed as a strategy to improve the applicability of AuNRs for PTT in cells with low internalisation rates, the synthesis of high aspect ratio AuNRs was performed following the same previously reported seed mediated growth process in **Section 3.1.1**. As in the previous case, AuNRs were covered with PEG, which is crucial for their cell compatibility (as subsequently detailed in **Section 3.1.2.2**). AuNRs with an LSPR band maximum at 1040 nm were obtained, very close to the 1064 nm wavelength of the laser used in the photothermal therapy and well within the NIR biological window. This is of great importance because, as explained in **Section 1.4.2**, at this wavelength the absorption of light by tissues and cells is highly decreased, meaning that heating will only be produced in the presence of AuNRs and so reducing damage to cells that are not interacting with AuNRs.

The main goal of entrapping this photothermal agent in the cell-adhesive chitosan was to enhance the AuNR interaction with cells, due to the low internalisation of AuNRs showed in **Section 3.2.1.4**. It has been proven that chitosan poses excellent mucoadhesive properties enhancing the retention in mucosal tissues.[247] To take advantage of this property, our hybrid material was synthesised by an ionotropic gelation method, in which the polymer matrix is formed by interaction of the positively charged amino groups in chitosan with a negatively charged gelling agent. In this case, the gelling agent of choice was the Keggin-type polyoxometalate (POM) phosphotungstic acid (PTA), which gives structural stability to the hydrogel matrix (**Figure 57**). We chose PTA based on previous studies illustrating its ability to form spherical and biocompatible nanocapsules.[248]

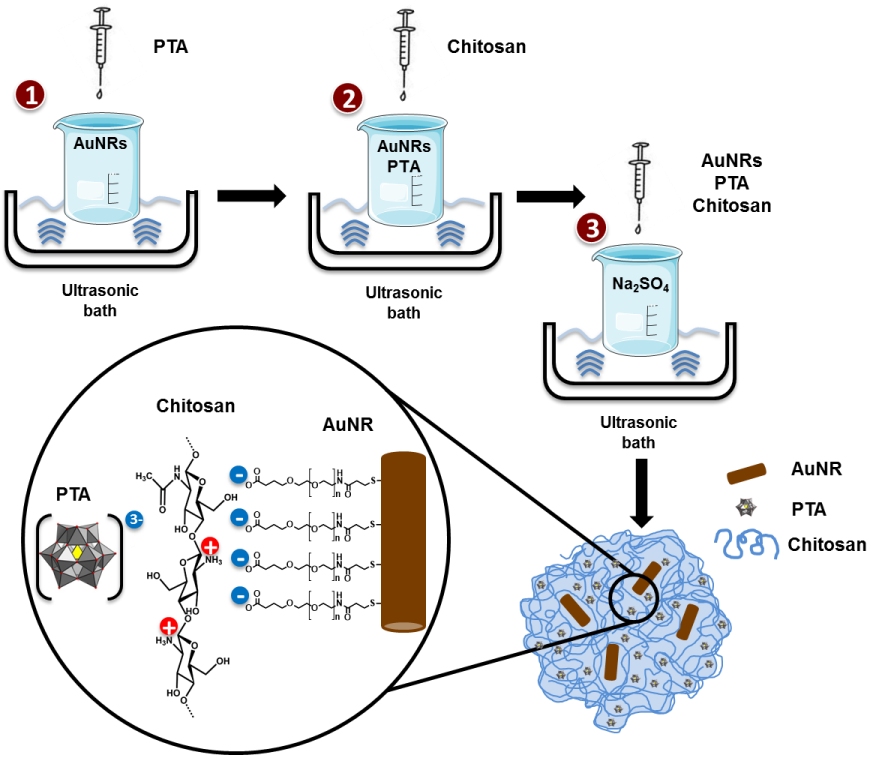

Figure 57. PTA-mediated synthesis of the chitosan hydrogel nanocontainer containing AuNRs (AuNR@CS). Adapted with permission from[143]

In addition to being a simple and rapid synthetic protocol requiring basic experimental equipment, one of the key advantages of this method is that it is performed entirely in aqueous solution, making it compatible with all the components involved in the hybrid hydrogel (CS, PTA and AuNR). After washing to purify, the synthesised hydrogel was fully characterised to investigate the chemical composition, structure and morphology, as well as to confirm the presence of AuNRs in the hydrogel matrix and the suitability of the developed system for its application in PTT.

FTIR spectroscopy was used to determine the composition of hybrid organic-inorganic matrix. FTIR data in **Figure 58** show the most important vibrational

peaks of chitosan: 1630 (primary amide), 1414 ($–CH_2$), 1375 ($–CH_3$) and 1150 cm^{-1} (C–O–C skeletal vibrations). Protonated amino group appears at 1530 cm^{-1} only for the AuNR@CS, probably due to the fact that in the case of AuNR@CS amino groups are electrostatically interacting with negative charges of PTA and/or PEG in the surface of AuNRs. The presence of the POM is largely masked by the chitosan stretches, but can be confirmed by the appearance of small peaks in the AuNR@CS spectrum below 1000 cm^{-1}, corresponding to P-O and W=O stretches. AuNR peaks cannot be observed clearly in the AuNR@CS, because their intensity is too low in comparison with other spectral bands. However, small peaks in the region 3500-3000 cm^{-1} can be observed that correspond to most important peaks of AuNR.

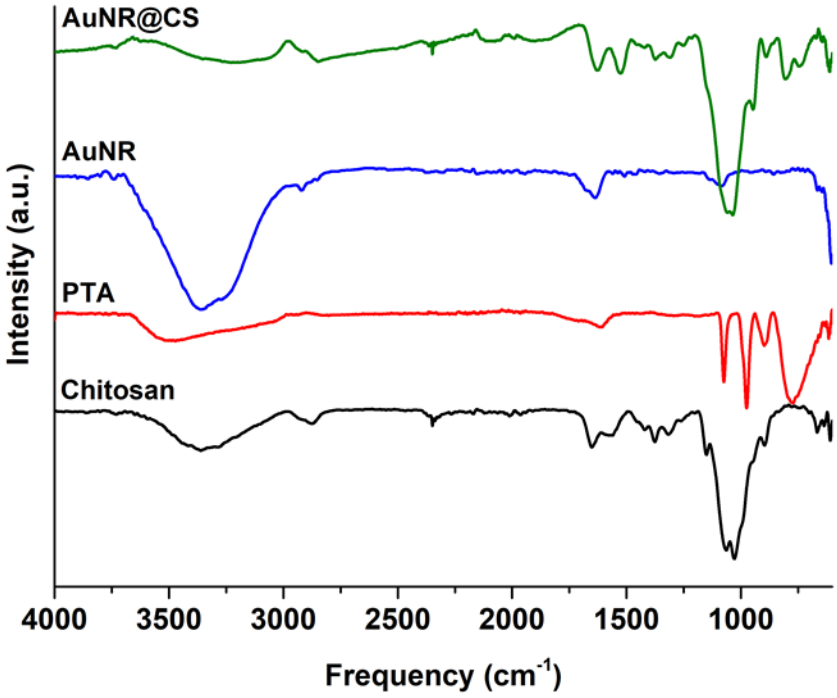

Figure 58. FTIR spectra of AuNR@CS (green), free AuNRs (blue), free PTA (and chitosan. Adapted with permission from[143]

As previously stated the AuNRs possess a distinctive LSPR band at a wavelength of 1040 nm, with a high absorbance at 1064 nm appropriate for PTT using a NIR laser working at this wavelength. Confirmation of the presence of AuNR in the polymer matrix was performed by UV-vis spectrophotometry (**Figure 59**). This technique shows that the characteristic LSPR peak at 1040 nm of free AuNR is still present in AuNR@CS with an almost imperceptible displacement to higher wavelengths, supporting the fact that the plasmonic properties of AuNRs were maintained after their entrapment and that they were virtually not affected by their close proximity within the hydrogel matrix. Both spectra also show an absorbance peak at 505 nm, corresponding to transversal absorbance band of AuNRs. Interestingly the absorbance near 200 nm is increased in the case of AuNR@CS, probably due to the components of the hydrogel more than due to an increase of the light scattering.

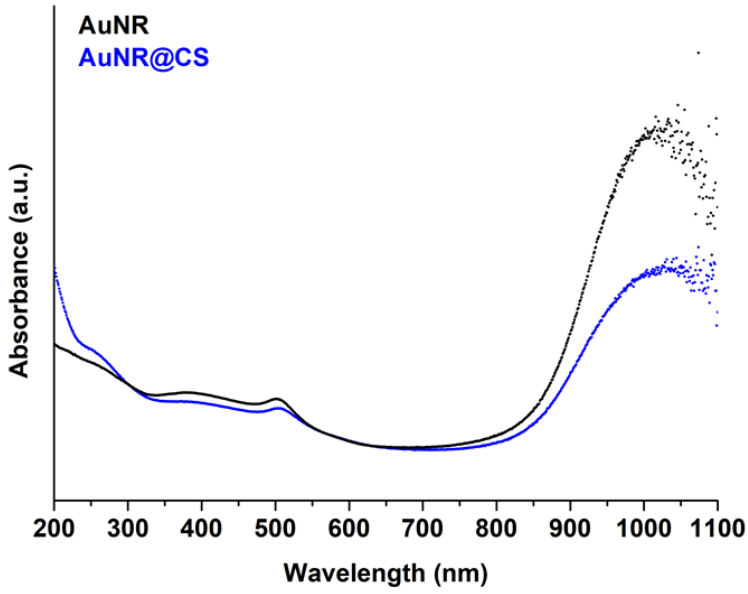

Figure 59. Aqueous UV-vis absorbance spectra comparing free AuNR (black) with AuNR@CS (blue). Adapted with permission from[143]

The quantity of gold corresponding to AuNR entrapped in the hydrogel was quantified using ICP-AES after acid digestion of the samples in *agua regia*. Correlating the Au concentration obtained from ICP-AES analysis of the hybrid matrix with the initial amount of Au added in the synthesis, it was possible to obtain an encapsulation efficiency (mg of encapsulated AuNR/mg of AuNR initially added x 100) of 61 %. Moreover, an AuNR loading (mg of encapsulated AuNR/mg of hydrogel x 100) of 28 % was obtained in the final material.

Due to its fragility, collapsing tendency when dehydrated and easiness to degradation under electron beam, several unsuccessful attempts to visualise the hydrogels employing TEM and SEM were carried out (data not shown). The pre-fixation of AuNR@CS was crucial for SEM imaging to study the morphology of the hybrid matrix and to confirm the presence of the AuNRs inside the chitosan hydrogel (**Figure 60**). SEM images of the AuNR@CS nanocontainers were obtained by fixing the hydrogel by glutaraldehyde covalent crosslinking. Glutaraldehyde acts as a crosslinker between the amino groups in chitosan polymer chains, rigidifying the hydrogel structure and helping to maintain it under electron microscopy conditions. Using this method sub-micron containers ranging from 200 to 500 nm in diameter were observed, all of them containing AuNRs embedded in their structure (**Figure 60B,C**). From **Figure 60B,C** it is possible to observe how the polymeric structure was affected by the microscope conditions (high vacuum) even after glutaraldehyde crosslinking. However, in both images polymer residues are clearly observed surrounding the AuNRs. This sub-micrometric size of the hydrogel structure was confirmed by DLS analysis by means of photocorrelation spectroscopy in which a mean hydrodynamic diameter of 475 nm was obtained. The electrophoretic mobility of the container was also evaluated. In this case, a ζ-potential of +24.4 mV was obtained, which agrees with the composition of the hydrogel, whereby protonated amino groups in the chitosan polymer structure confer a positive potential to the material.

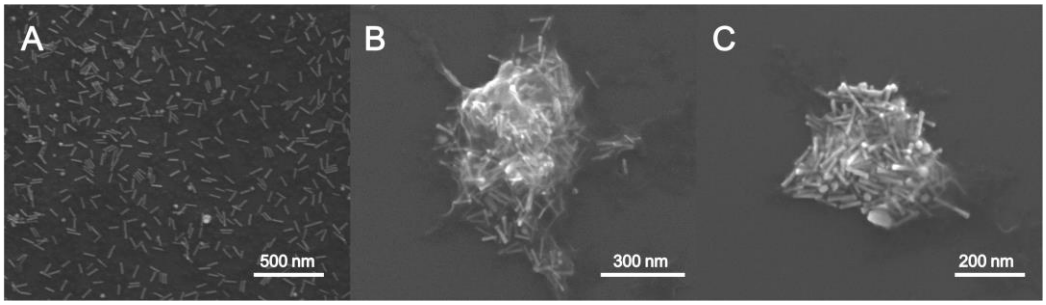

Figure 60. Scanning electron microscopy (SEM) image of AuNR (**A**) and AuNR@CS (**B** and **C**). Adapted with permission from[143]

Although these hydrogels possessed interesting and applicable properties due to the physicochemical characteristics conferred by chitosan and AuNRs, the synthesis method represents a proof-of-concept benchtop synthesis towards hybrid nanomaterial. Consequently, the method presents several drawbacks, in particular the difficulty to control the size of the matrix and the relatively shapeless hydrogel containers obtained which results in a broad size distribution. These drawbacks were the motivating factors behind improving and controlling of the material synthesis using inkjet technologies, described in **Subsection 3.3**.

3.2.2.2. Cytotoxicity of AuNR@CS

The low toxicity of PEGylated AuNRs was demonstrated in **Section 3.2.1.3**. To ensure that the encapsulation process produced a harmless material, the cytotoxicity of the hydrogel nanocontainers was assessed prior to further testing and analysis. Increasing concentrations of sterile nanocontainers, from 0, 10, 50, 100 to 200 µg of capsules/mL (measured by dry weight), were incubated with Vero cells for 24 h, washed and the viability of the cells was evaluated by MTT cell viability assay (**Figure 61**). In this assay, NAD(P)H-dependent cellular oxidoreductase enzymes reduce MTT reagent to its purple coloured product showing both differences in the number of remained viable cells and their metabolic activity. As previously stated, the coverage of AuNRs with PEG resulted

crucial for their biocompatibility as can be observed in **Figure 61**. The nanorods without PEG retained CTAB in their surface that was encapsulated within the AuNRs in the hydrogel (AuNR@CTAB@CS), resulting tremendously toxic in a concentration-related manner. In contrast, the lack of any cytotoxicity from AuNR@CS previously described produced with AuNRs covered with PEG at the highest tested concentration of 200 µg of capsules/mL serves as a first indication of their safety as photothermal agents for future studies.

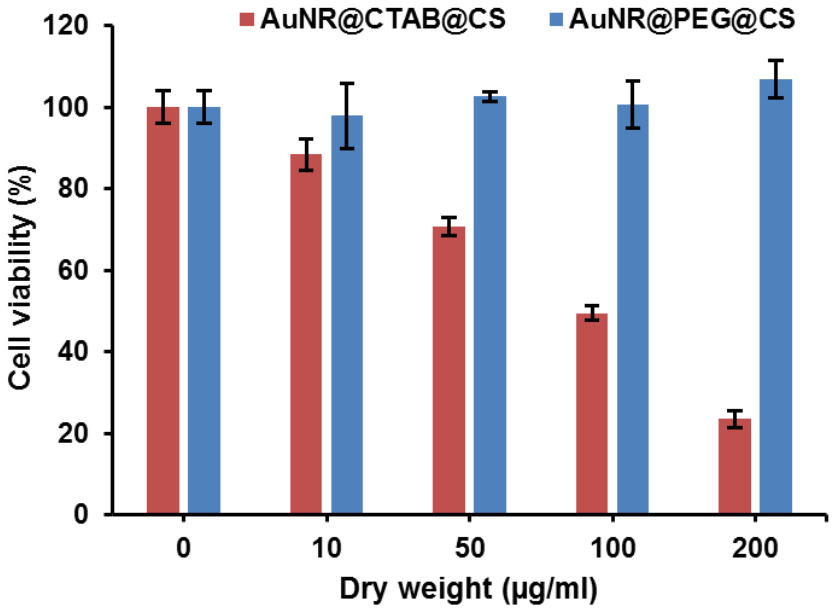

Figure 61. MTT cell viability assay of Vero cells incubated with different concentrations of PEGylated (AuNR@PEG@CS) in comparison with the AuNRs encapsulated without PEGylation (AuNR@CTAB@CS). AuNR@PEG@CS showed no cytotoxicity even at highest concentration of 200 µg/mL while AuNR@CTAB@CS displayed a high cytotoxicity above 10 µg/mL.

3.2.2.3. Heating profiles

One of the main motivations for carrying out this study was the previously described high capability of AuNRs to mediate light-to-heat transduction in comparison with AuNPrs (see **3.2.1.2 Section** for details). In order to evaluate if the entrapment of AuNR as part of the chitosan hydrogel affected their capability to convert light into heat, identical Au concentrations of AuNR and AuNR@CS diluted in Milli-Q water were compared. Their heating capability was investigated over a 10 min period of irradiation using a 1064 nm NIR laser operating at 1100 mW, as in the previous comparison. Compared with the free AuNR, there was only a minor reduction in the initial temperature increase of AuNR@CS (3-7 ^{o}C/min) as can be seen in **Figure 62**. We attribute this reduction in temperature increase to a combination of thermal insulation caused by the hydrogel and weak interactions between the LSPR bands of other nearby AuNRs. In any case, the final global temperatures following ten min of irradiation were highly increased both in the case of AuNR and AuNR@CS at all concentrations studied (see **Figure 62B**) ranging from 57 to 98 ^{o}C depending on the concentration, compared to water control that only reached 43.4 ± 1.3 ^{o}C. These results suggested that irradiation at tested conditions should be harmless for cells and biological tissues without nanoparticles and they also demonstrated the suitability of these nanomaterials for photothermal treatment.

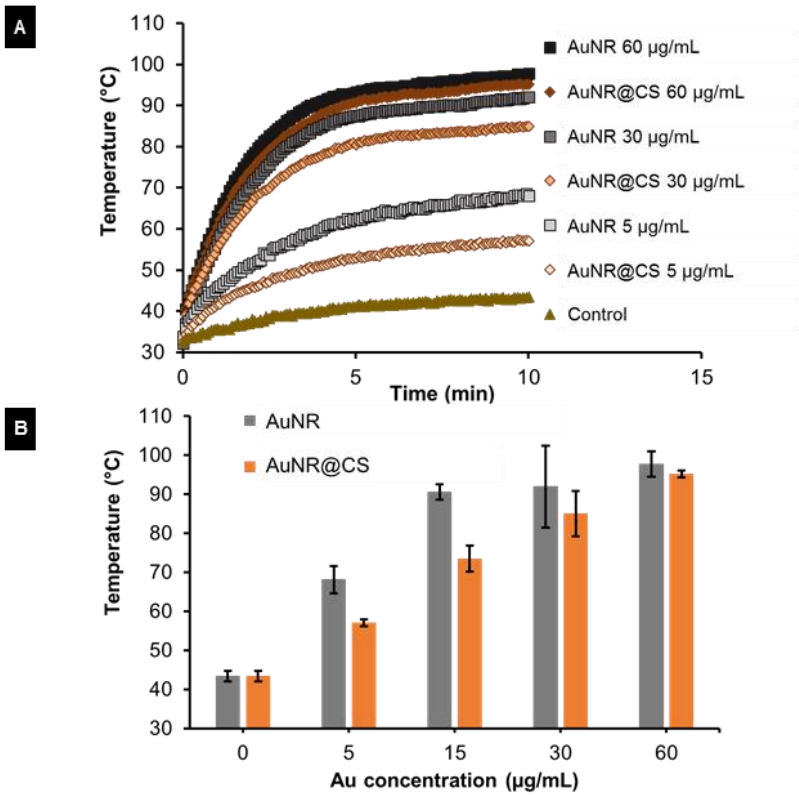

C

AuNR@CS				AuNR			
Au concentration (µg/mL)	Temperature increase (°C/min)	Heating efficiency (%)	Temperature after 10 min irradiation (°C)	Au concentration (µg/mL)	Temperature increase (°C/min)	Heating efficiency (%)	Temperature after 10 min irradiation (°C)
0	2.6	3.3	43.4±1.3	**0**	2.6	3.3	43.4±1.3
5	7.9	10.0	57.1±0.9	**5**	10.6	13.4	68.1±3.5
15	12.4	15.7	73.5±3.3	**15**	19.8	25.1	90.6±2.0
30	17.1	21.7	85.0±5.7	**30**	21.5	27.2	92.0±10.5
60	21.4	27.2	95.2±0.9	**60**	24.3	30.8	97.7±3.2

Figure 62. **A**) Temperature increase during 10 min irradiation of different concentrations (5-60 µg/ml) of AuNR and AuNR@CS. **B**) Final temperature after 10 min irradiation of different concentrations of AuNR and AuNR@CS. **C**) General data table of all tested samples, including concentrations, initial temperature increase, heating efficiency and final temperature after 10 min irradiation. Adapted with permission from[143]

The heating power for each of the tested concentrations was quantified by calculating the initial heating increase per second and assuming that the aqueous solution possess a similar specific heat capacity than water and the plastic wells of the plate would act as thermal insulators (see **Materials and Methods section** and

Figure 63). The heating efficiency was calculated correlating the heating power with the laser potency employed. As a result, the heating efficiency of AuNRs ranged from 13 to 31 % depending on the concentration studied and from 10 to 27 % in the case of AuNR@CS as is described in the **Figure 62**.

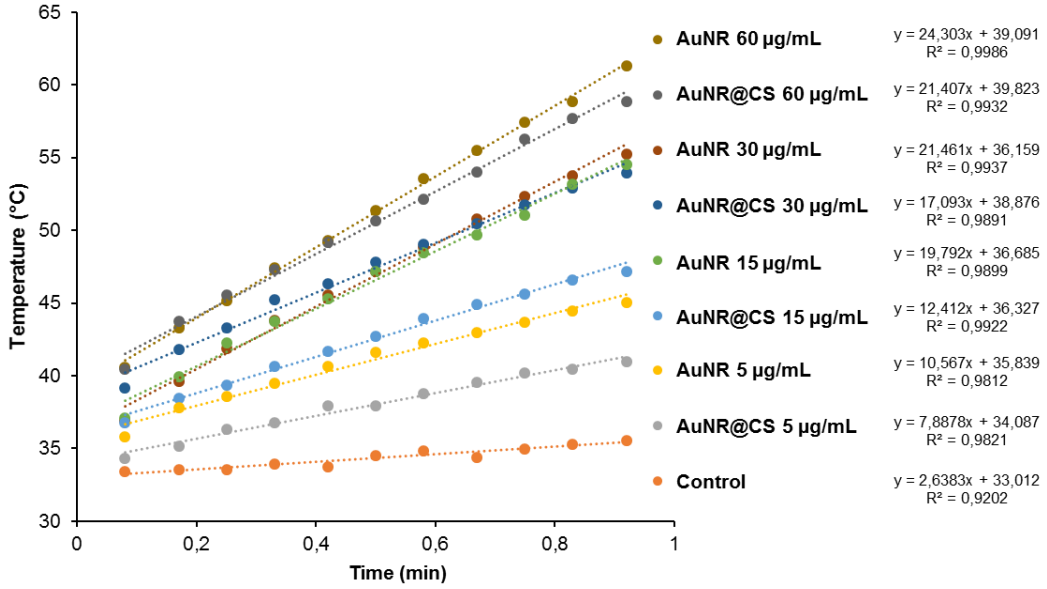

Figure 63. Linear regression of the solution temperature increase vs. the first minute of irradiation for different concentrations of AuNR and AuNR@CS. The slopes of these regressions correspond to the initial temperature increase and was employed to calculate the heating efficiency of each sample. Adapted with permission from[143]

3.2.2.4. Improving in vitro photothermal therapy of AuNR via chitosan entrapment

In the previous section we have shown how the efficient light-to-heat transduction of the AuNRs conferred promising potential for phototermal applications; however, their application is hindered by the fact that AuNRs suffer from very poor cellular internalisation when compared with AuNPrs in the Vero cell line (see **Section 3.2.1.4**). The main objective of this work was that the entrapment of AuNRs in a cationic chitosan hydrogel matrix using an anionic POM as gelling agent allowed us to overcome this limitation. By this way the use of AuNRs, or other AuNPs with low cellular internalisation, in photothermal applications would be improved while simultaneously avoiding the use of complex AuNR surface functionalisation strategies. As a first indicator of the improvement thanks to the chitosan entrapment, optical microscopy images taken during the MTT assays illustrated how the AuNR@CS showed a cell-adhesive behaviour and confirmed that the AuNR@CS were still interacting with the surface of the cells even after several washing steps, as can be seen in **Figure 64**.

The low cytotoxicity combined with cell-adhesive nature of the AuNR@CS make them promising candidates for improving photothermal therapy. Thus, the nanocontainers were incubated with the cells for one day similarly than in the previous study andthe excess of material that was not interacting with cells was removed with PBS before irradiating the cells for 10 min using a 1064 nm NIR laser operating at 1100 mW. This allowed a very localised delivery of heat in cells that contained AuNR, or in which AuNRs were interacting with their surfaces. 5 h after irradiation, morphological changes could be clearly seen in the case of cells incubated with AuNR@CS (**Figure 64**); while no morphological changes were observed in the case of irradiated control cells and irradiated cells previously incubated with AuNR.

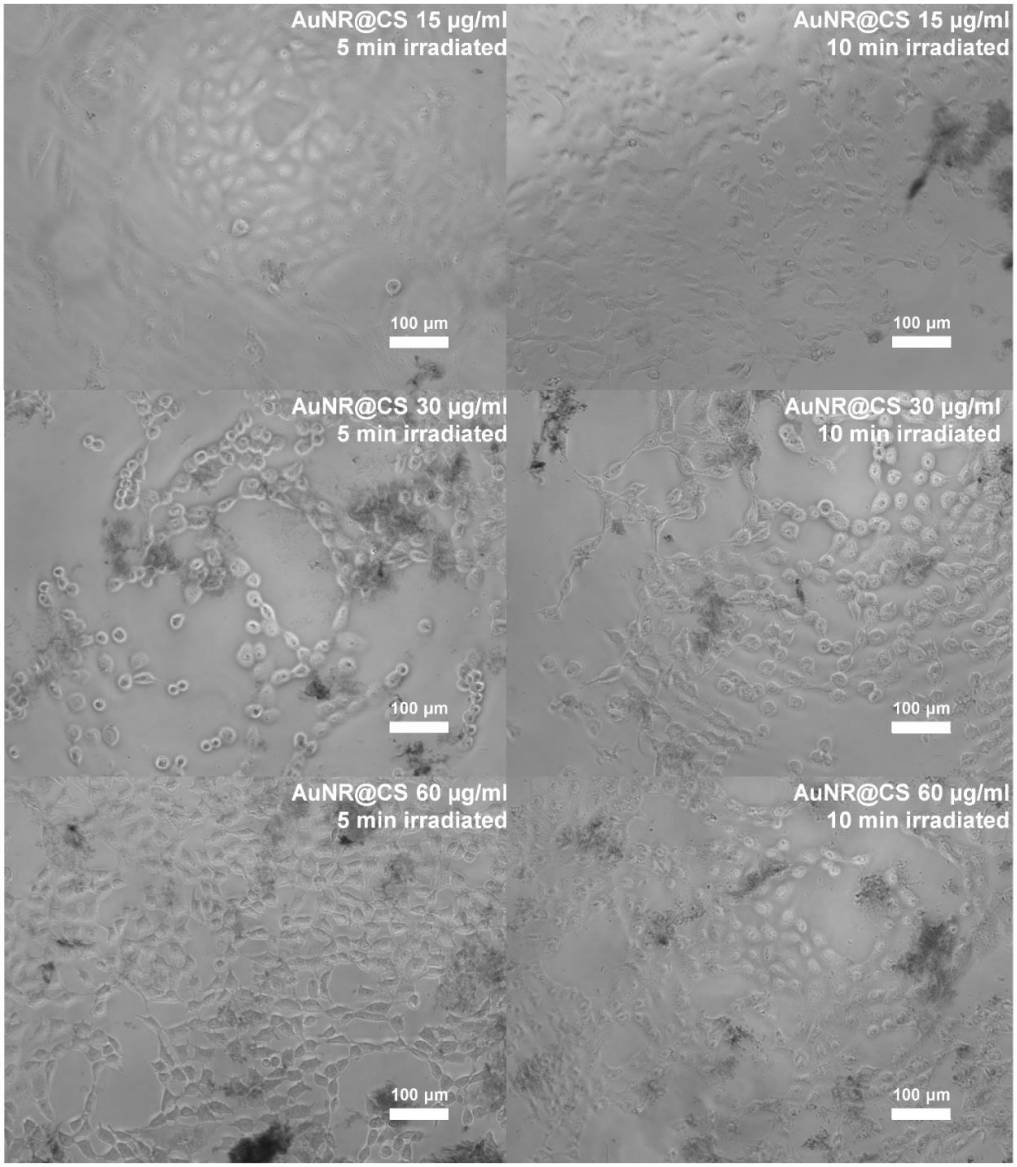

Figure 64. Phase contrast microscopy images taken after 5 h post-irradiation showing the morphology of Vero cells treated with different concentrations of AuNR@CS irradiation for 5 or 10 min, respectively. Adapted with permission from[143]

In order to obtain comparable data to the previous studies involving AuNRs and AuNPrs, MTT cell viability assay was used to quantify the photothermal behaviour

of AuNR@CS five h after irradiation. In addition, this study was carried out five h after irradiation because at this time the effects of apoptosis or secondary necrosis were observed in previous PTT studies.[132] The results of these experiments confirmed that there was no associated toxicity of both AuNR and AuNR@CS in non-irradiated cells. The absence of cell death derived from the laser and the AuNR was confirmed another time using laser-irradiated control cells (without nanorods) and cells incubated with AuNR, respectively. In contrast, for irradiated cells treated with AuNR@CS the cell viability showed a marked decrease to 46.1 ± 7.5 % at a concentration of Au entrapped in the hydrogel of 30 µg/mL and a more dramatic decrease (11.4 ± 1.7 % of unaffected cells) at 60 µg/mL of entrapped Au (corresponding to a dry weight of matrices of 100 and 200 µg/mL respectively) (**Figure 65A**). These data allow us to conclude that AuNR@CS are more effective photothermal agents than AuNPrs, which only displayed 55 % of cell death even employing 100 µg/mL of gold under identical experimental conditions. It should be noted that irradiated cells incubated with AuNR@CS at 60 µg/mL of gold failed to reduce the MTT reagent, indicating severe cellular damage, as observed in **Figure 65D**. In addition, the cellular membranes seems clearly damaged and the absence of round-shape cells is a clear indicator of a hard necrosis instead of a programmed apoptosis. It should be noticed that when the laser was adjusted to irradiate only the central part of the well of cells incubated with AuNR@CS, the frontier between irradiated and not-irradiated cell can be clearly distinguish due to its ability to reduce MTT and form the blue crystals (**Figure 65E**).

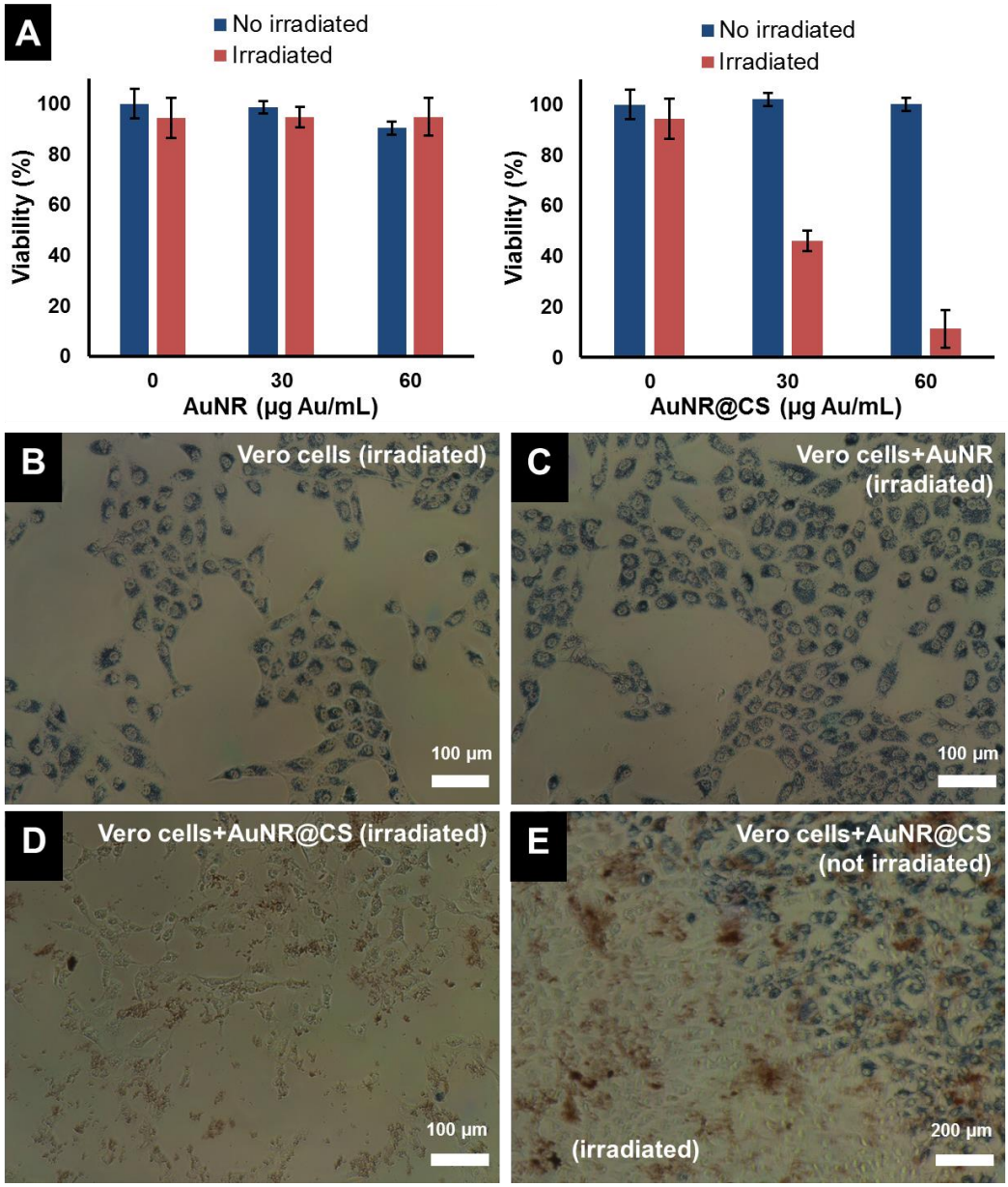

Figure 65. **A**) MTT cell viability of Vero cells incubated with different concentrations of AuNR or AuNR@CS 5 h after laser irradiation. **B-E**) Phase contrast microscopy images of cells during MTT incubation, after irradiation: untreated cells (**B**), 60 µg/mL of AuNR (**C**),60 µg/mL of AuNR@CS (**D**) or 60 µg/mL of AuNR@CS with the laser focused in the

centre of the well and showing a part of the irradiated cells and a part of the non-irradiated cells. Adapted with permission from[143]

To confirm the results and observations from the MTT assay and to study how irradiation of the cells in the presence of the nanomaterials affects the integrity of cell membranes, a commercial LIVE/DEAD™ test was carried out five h after irradiation. In this test, the intracellular esterase activity of live cells transform calcein AM to the green fluorescent calcein; while ethidium homodimer only enters into dead cells with damaged plasma membranes, increasing its red fluorescence when it interacts with nucleic acids. Non-irradiated cells incubated with AuNRs or AuNR@CS, irradiated control cells and cells incubated with AuNR displayed only live cells (**Figure 66A**); however, in the case of cells incubated with AuNR@CS the majority of irradiated cells were red stained, indicating cell death and a severe membrane damage (**Figure 66C**). In addition, when the laser was adjusted to irradiate only the central part of the well of cells incubated with AuNR@CS, hyperthermia affected only cells in the irradiated area, while the remaining cells in the well remained alive (**Figure 66D**). This observation is important to understand how precisely PTT can be for very selecting killing of just the cells with the nanomaterials and irradiated with the laser, but not affecting the surrounding tissues without the nanoparticles or that have not been irradiated. These results confirmed that by entrapping the AuNRs in the cell-adhesive chitosan hydrogel we could dramatically increase their efficiency as photothermal agents *in vitro*, thereby turning ineffective free AuNRs into highly applicable nanomaterials. These promising *in vitro* results provide the first lines of evidence that the AuNR@CS nanocontainers present potential application for the treatment of certain tumours. Further, the hybrid composite would be of particular use in intratumoural administration or after surgical removal of tumours, similar to other recent applications of hybrid gold nanoparticle materials.[148] In addition, these AuNR@CS could be employed for gastrointestinal tumour treatment, as other chitosan hybrid nanomaterials have demonstrated to be able to effectively cross

the intestinal epithelia and displayed tumour reduction with longer survival rates *in vivo*.[162]

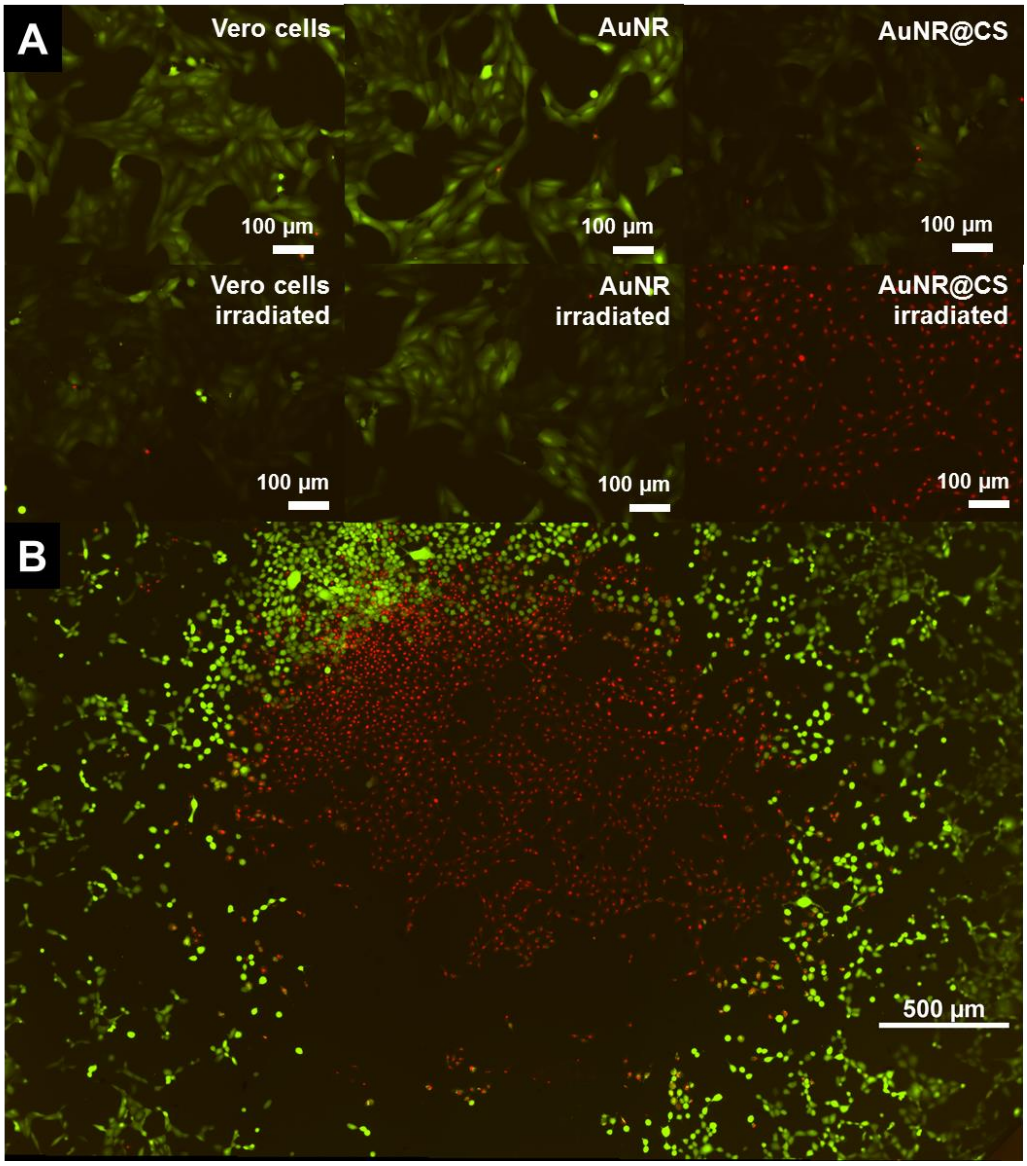

Figure 66. **A**) Fluorescent microscopy images of live/dead test five h post irradiation or not irradiated of untreated cells; treated with 60 µg/mL of AuNR; or with 60 µg/mL of AuNR@CS. Image (**B**) shows an entire 96-well irradiation of 60 µg/mL AuNR@CS with the laser adjusted to irradiate only the central part of the well. Adapted with permission from[143]

3.2.3. Conclusions

In summary, the final goal of the first part of the study was to compare the efficiency of two types of anisotropic AuNPs as PTT mediators. The LSPR bands of gold AuNPrs and AuNRs were adjusted to absorb close to the wavelength of the NIR laser (1064 nm) so that these particles could be evaluated and compared as photothermal agents. Although both AuNPrs and AuNRs showed a high heating efficiency, AuNRs stand out as being more efficient, largely due to their higher specific surface area. Cellular studies with Vero cell line revealed that the AuNPs were essentially non-toxic and were located inside cytoplasmic vesicles, but only the AuNPrs possessed capability to induce cell death, under the conditions tested herein. The explanation of this contradiction between heating efficiency and cell death capacity can be found in the internalisation of both AuNPs, where ICP and TEM studies led us to conclude that AuNPrs internalise more efficiently than AuNRs. These observations, lead us to conclude that AuNPrs are more appropriate candidates for *in vitro* cellular thermoablation. Although AuNRs are important class of photothermal nanoparticles, their cellular internalisation is limited in some cell lines and in most of the cases must be increased using complex and time-consuming surface-functionalisation techniques.

In a second part of the study we have developed a simple strategy to significantly increase the efficacy of AuNRs for photothermal therapy applications *in vitro*. As an alternative strategy, we have entrapped AuNRs in chitosan-based sub-micrometric hydrogels (AuNR@CS) that showed cell-adhesive properties. Importantly, an anionic POM was employed as a gelling agent to form the sub-micrometric hydrogel by ionic interaction with cationic chitosan to capture the AuNRs as part of the hydrogel. The AuNR@CS display almost the same heating properties than the free AuNR and showed no cytotoxicity, even at high concentrations. However, in contrast to the free AuNR, laser irradiation of cells treated with AuNR@CS displayed clear signs of necrosis even employing lower

gold concentrations than in the case of AuNPr. Consequently, our hydrogel entrapment strategy has dramatically increased the *in vitro* efficiency of AuNRs for photothermal therapy applications and could potentially be employed in future intra-tumoural administration, resection of tumours zones after surgery or for oral delivery to treat tumours located in the digestive tract.

Although these hydrogels possessed all of the desired physicochemical characteristics conferred by chitosan and AuNRs, the synthesis route to these hybrid nanomaterials presents several key drawbacks. Notably, it is especially difficult to control the size of the matrix and the overall shape of the nanocontainers. To improve this shortcoming, we proposed that inkjet technology could be harnessed, in a similar way to microfluidics, for the automated and highly reproducible production of large quantities of monodisperse chitosan hydrogels containing AuNRs. Our efforts towards this goal are described in **Section 3.3**.

3.3. New AuNP encapsulation methodology using Inkjet technology

Microencapsulation has played centre stage in the biomedical sector and is crucial for a number of applications ranging from drug delivery and controlled release to cell/tissue targeting systems.[167] Commonly employed microencapsulation techniques such as emulsions, extrusion or spray drying[249] are used for industrial scale microencapsulation, however these methods show several drawbacks including broad size distribution[250], agglomeration of capsules or low encapsulation efficiency.[251] All of these aspects are of paramount importance in drug delivery systems principally because the rate of drug release scales with particle size.[252,253] Inkjet-based microsphere production technology offers the potential to improve such limitations to microencapsulation thanks to excellent control and reproducibility of particle size and efficient encapsulation.[254] Furthermore, from the industrial perspective, inkjet-based technologies represent continuous microdroplet production systems,[178,255] whereby the process can be fully automated. Importantly, such inkjet set-ups can be easily scaled-up using multiple printheads working in parallel with hundreds of inkjet ejection nozzles. Practical aspects such as these can provide advantages for microencapsulation in a number of fields and industries: from the pharmaceutical industry[254] to biomedical applications like cell and bacteria microencapsulation as probiotics for food industry.[256,257]

The use of AuNPs in the biotechnology field range from drug release[20,258] and photothermal therapy[61,135] to biosensing.[197,259] In principle, encapsulating AuNPs in polymers can be employed to improve the applicability of AuNPs for these applications, e.g. in order to enhance stability, provide sustained release and enhance bioavailability of the AuNPs, or to improve other aspects related to their delivery and storage.[260] Another important advantage of AuNPs encapsulated in polymers is the preservation of AuNP optical properties in order to avoid unwanted plasmon shifts due to solvent changing and plasmon hybridization.[261]

Apart from low cytotoxicity and other advantages already described in previous section, chitosan has been used for oral administration of AuNPs by protecting the nanoparticles in the gastrointestinal tract and it is mucho-adhesive, which facilitates the interaction with the intestinal epithelium enabling their absorption from the intestine into the bloodstream.[161,162]

The objective of this work consists of the development of an inkjet methodology for the microencapsulation of AuNPs inside a biocompatible and muco-adhesive chitosan hydrogel. Furthermore we aimed to assess the utility and applicability of these microcapsules for biomedical applications. To this end, we have designed an inkjet microcapsule production strategy to eject microdroplets of a AuNP-containing chitosan solution into a solution which produces an instantaneous ionic gelation of the microgel particles (see **Figure 67**). I*n vitro* biocompatibility studies, a pH stability test and an evaluation of their degradation in simulated gastric medium along with a preliminary study of the applicability for oral administration were used to ascertain their potential as materials for biotechnological applications.

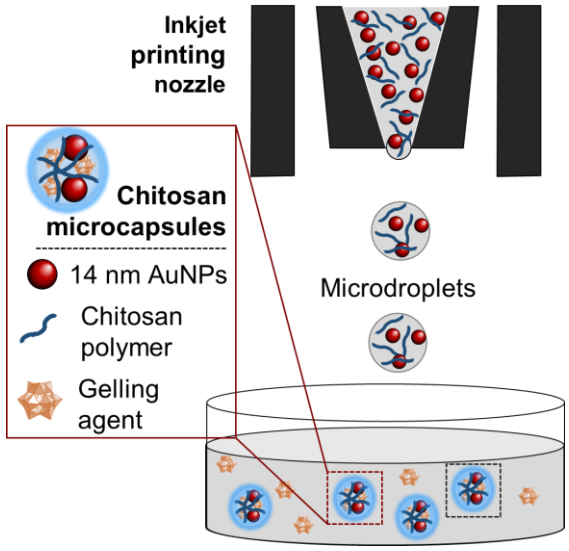

Figure 67. Scheme of the inkjet-based methodology employed for AuNP encapsulation in chitosan hydrogel by the production of microdroplets of AuNPs and chitosan solution,

using a piezoelectric inkjet printhead. The microcapsules are formed by instantaneous ionic gelation when they enter into contact with the gelling agent. Adapted with permission from[262]

3.3.1. AuNP synthesis and preparation

The shape and sizes of AuNPs can be tailored to give the desired physicochemical properties for a variety of different biomedical applications. However, for this AuNP encapsulation study we opted to use simple 14-nm diameter spherical AuNPs as a proof of concept model for the encapsulation by inkjet technology due to the ease of synthesis and high stability. The 14-nm spherical AuNPs (**Section 3.1.1.1**, **Figure 68**) were covered with a PEG surface with carboxylic end-groups to facilitate the ionic interaction with the positively charged chitosan polymer. Another advantage of these AuNPs is their small size, because larger nanoparticles cause an increase in the solution viscosity,[263] which could further complicate the ejection of the solution from the inkjet nozzle. However, we have observed that the addition of the small spherical AuNPs decrease the viscosity of the chitosan, probably due to the electrostatic interaction between the AuNPs and the chitosan amino groups. This decrease in viscosity of the polymer solution has been reported for chitosan solution in the presence of other ions due to the decrease of charge repulsion between ionised amine groups.[264]

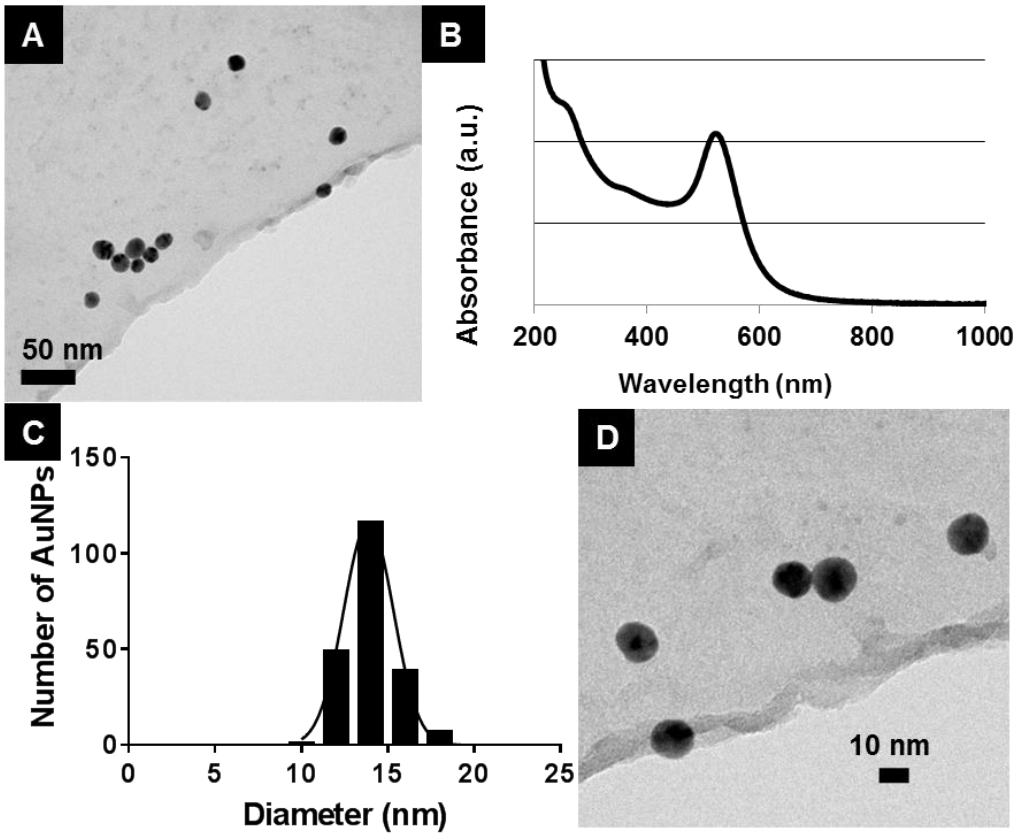

Figure 68. A) TEM image of 14-nm diameter spherical gold nanoparticles (AuNPs) and (**B**) UV-Vis spectroscopy of an aqueous colloidal suspension with the LSPR peak at 522 nm. **C**) Histogram showing the size distribution of the AuNPs employed for inkjet microencapsulation based on the measurements of AuNP diameters in TEM images. Measurements carried out with Image J software. **D**) TEM image at higher magnification of 14-nm diameter spherical AuNPs. These data show the monodispersity, size and morphology of the AuNPs employed as a delivery model for the inkjet encapsulation technology.

3.3.2. Inkjet technology mechanism and experimental set up

The inkjet system employed herein belongs to the drop-on-demand (DOD) inkjet printing type that means that the droplets are ejected due to a controlled external stimulus. In this type of inkjet system, the ejection process is controlled by a piezoelectric element in the inkjet header that remains in contact with the liquid inside the header. When a pulse generator controlled by a computer programme sends a controlled voltage pulse to the piezoelectric element, it causes a deformation on the piezoelectric that provokes a pulse of pressure in the liquid (see **Figure 69**). The microdroplet generation is a complex process that is affected by multiple factors such as surface tension, viscosity and density of the solution along with ejection parameters including orifice dimension, internal architecture of the printhead and specially magnitude and shape of the voltage pulse applied. When a voltage is applied to the piezoelectric actuator it causes a rapid widening of the printhead cavity that involves a local reduction of liquid pressure (see **Figure 69B**). This pressure reduction is transferred all along the printhead as two negative pressure waves in both directions. One of the negative pressure waves is reflected in the upper end of the printhead as a positive pressure wave due to the liquid presence. At the same time the other negative pressure wave is reflected as a negative pressure wave in the orifice. When the pulse voltage ends, the piezoelectric returns to its original position causing another two positive pressure waves in the liquid. Best ejection is obtained when both reflected pressure waves coincide at the same time and in the same position with the new positive pressure waves. When this situation occurs, the reflected negative pressure wave is cancelled by one of the new positive pressure waves. At the same time, the reflected positive wave is combined with the other new positive pressure wave in a new positive pressure wave with double intensity that travels along the liquid to the orifice and provokes the real ejection of the

microdroplet. For this reason, a careful optimisation of the ejection conditions is required for each solution for a stable and controllable ejection.

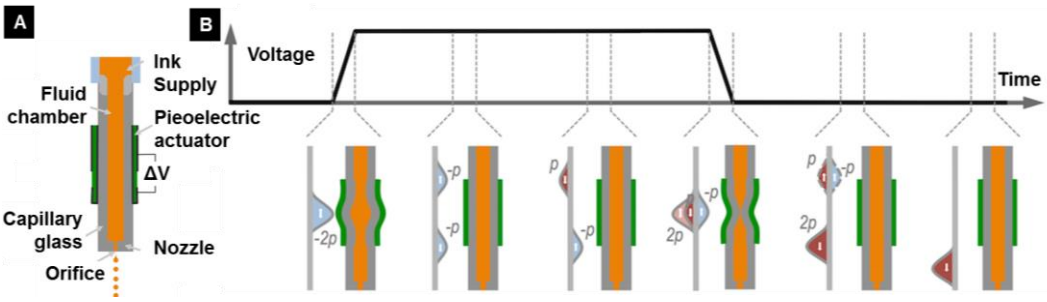

Figure 69. **A**) Detailed schematic structure of a piezoelectric single nozzle printhead. **B**) Pressure perturbation generation, propagation and reflection upon trapezoidal voltage application. Adapted with permission from[178]

Our inkjet microsphere production setup is based on a piezoelectric printhead equipped with a 50-µm nozzle, which determines the size of the ejected microdroplets. The piezoelectric element of the microdispenser is controlled using a multichannel device with software that enables the selection of an electrical waveform with defined parameters (rise, fall and pulse frequency, width, times and voltages). The inkjet set up used in this thesis can be observed in **Figure 70** and refer to **Section 5.6** for precise experimental parameters. The chitosan and AuNPs were filtered and charged in the ink reservoir prior to their ejection employing the inkjet printhead to a gelling agent solution. A bespoke visualisation system based on a strobe LED and a camera synchronised with the inkjet ejection was necessary to photograph the micro-sized droplets ejected at high speed.

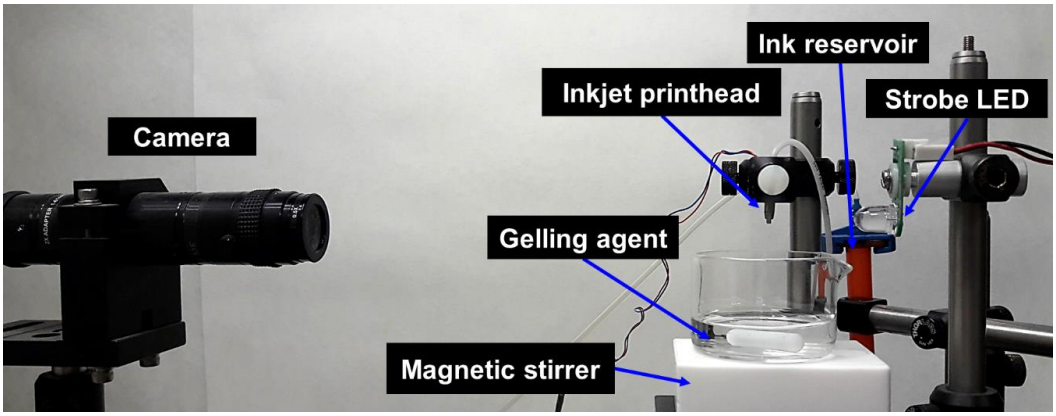

Figure 70. Inkjet set-up employed for the microdroplet generation, with an optical system composed of a camera and the strobe LED synchronised to monitor the microdroplet ejection.

3.3.3. Optimising the chitosan solution ejection

In the first instance, the stable and reproducible ejection of chitosan by inkjet was challenging due to the tendency of chitosan to form micrometric aggregates that affected the ejection by obstructing the fluidics and clogging the nozzle of the inkjet microdispensing device. In order to avoid these issues, all reagent solutions were passed through a 0.45 µm filter prior to their introduction in the reservoir and a carefully washing protocol using an aqueous acetic acid was used to thoroughly clean the whole inkjet fluidic system before and after each printing phase (see **Section 5.6**).

Different electric waveforms to excite the piezoelectric element were studied, including trapezoidal, bipolar and tripolar, and a comprehensive optimisation process was performed controlling all the parameters involved in the excitation pulse including voltages involved, frequency, duration of the rise and fall of the pulse(s) and pulse(s) width(s) as well as other aspects such as pressure applied to the solution in the fluidic system. By changing the electrical pulse applied to the inkjet nozzle, it was possible to continuously control the size of the ejected

chitosan droplets over a large range, *e.g.* from 77 µm using trapezoidal down to 51 µm with tripolar (see **Figure 71**), all the while maintaining a stable and reproducible generation of droplets. This decrease in the microdroplet size is a result of the negative pressure induced by the voltage of the tripolar excitation.[265] Different chitosan concentrations were ejected with the inkjet microdispensing device, until a maximum concentration of 5 mg/mL, above which the nozzle becomes obstructed making ejection impossible. Thus a chitosan concentration of 5 mg/mL was established as our reference and the discharge conditions were optimised to achieve a stable and continuous ejection for long periods of time. For the final optimization steps, the AuNPs were added to the ejected chitosan solution in order to avoid problems due to changes in the fluid properties that could affect the ejection. The optimal ejection conditions were achieved by employing a monopolar electric pulse with a rise time of 3 µs, a dwell time of 15 µs and a fall time of 3 µs, a dwell voltage of 32 V and at a frequency of 3000 Hz allowing a stable ejection during several hours at a rate of 3000 microdroplets per second. The microdroplets were ejected at a velocity of 2.4 m/s.

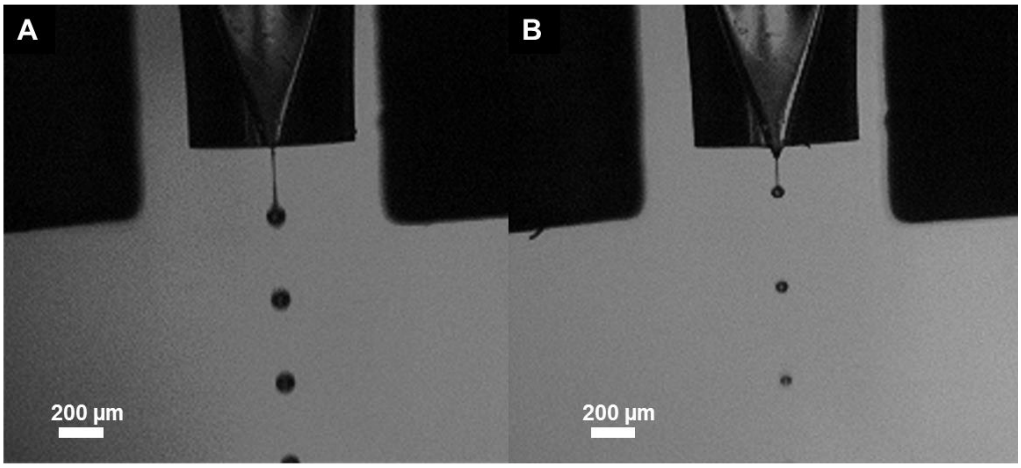

Figure 71. Photographs of inkjet ejection of chitosan 0.1 % (aq.) controlling the size of the microdroplet just by employing different electric pulse waveforms. In this way it was possible to reduce the size from 77 µm (using a trapezoidal waveform) to 51 µm (using a tripolar waveform).

3.3.4. Gelling agent selection

Once the inkjet ejection protocol was optimised, a number of different gelling agents were assayed to form the microcapsule hydrogels. To facilitate the release of the drugs incorporated in the hydrogel in future applications, negatively charged gelling agents were employed to ionically cross-link the positively charged side chains of the chitosan polymer. To obtain a well-defined microcapsule, rapid gelation is required to maintain the shape of the discharged microdroplets when they enter in the gelling agent solution. In the first instance, the selection process was based on a series of gelling agents described frequently in the literature, including sodium sulphate,[143] tripolyphosphate (TPP),[266] phosphomolybdic acid (PMA)[248] and phosphotungstic acid (PTA).[143] Initially, these gelling agents were tested by micropipetting droplets of polymer solution on a receiving solution at different gelling agent concentrations (**Figure 72**). Sodium sulphate was unable to gel the chitosan and phosphomolybdic acid (PMA) was only able to produce a partial gelation of the chitosan and irregular partially gelled microcapsules were formed. Of these four gelling agents, only PTA and TPP were able to completely gel the chitosan solutions at the tested concentrations, so subsequent studies continued with these two gelling agents.

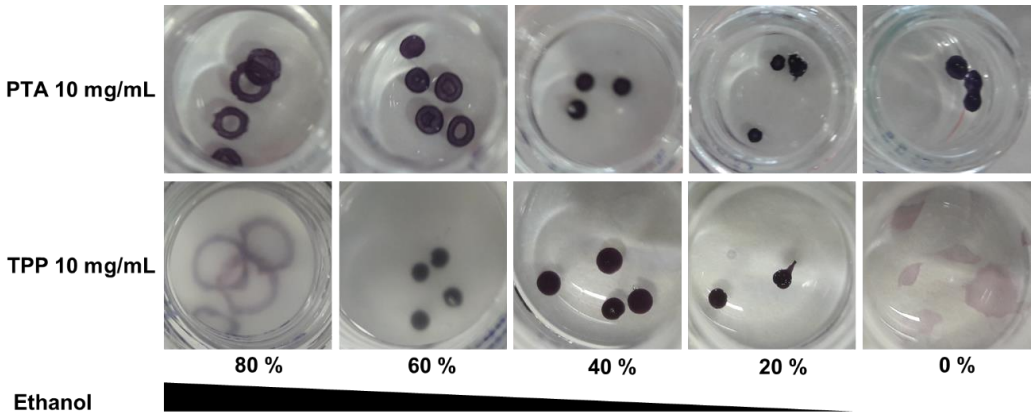

Figure 72. Photographs of AuNPs-chitosan solution droplets micropipetted into a 10 mg/mL solution of PTA or PTT dissolved in an increasing concentration of ethanol (0-80 %).

However, when employed with the microdroplets ejected by the inkjet system, TPP produced slow gelation and as a result heterogeneous amorphous hydrogel fragments were obtained (see **Figure 73**). On the other hand, phosphotungstic acid (PTA) has been proven to serve as an efficient gelation agent for chitosan-based materials[248] and has demonstrated inertness to cell cultures.[143] In this inkjet set-up the PTA proved to be an instantaneous gelling agent that enabled the formation of the chitosan microcapsules directly upon contact with the gelling solution. It should be noted that microdroplets of chitosan tend to float and form planar aggregates when they were ejected over PTA solution in water. To solve this drawback, the density of gelling agent was decreased by dissolving PTA in an ethanol-water mixture where the optimum gelling conditions were obtained using a 10 mg/mL PTA solution, 60 % (v/v) ethanol solution in water. Another advantage of using ethanol is that it ensures the sterility of microcapsules, as demonstrated by the absence of microorganisms studied by sterility samplers (subsequently detailed in **Figure 80**).

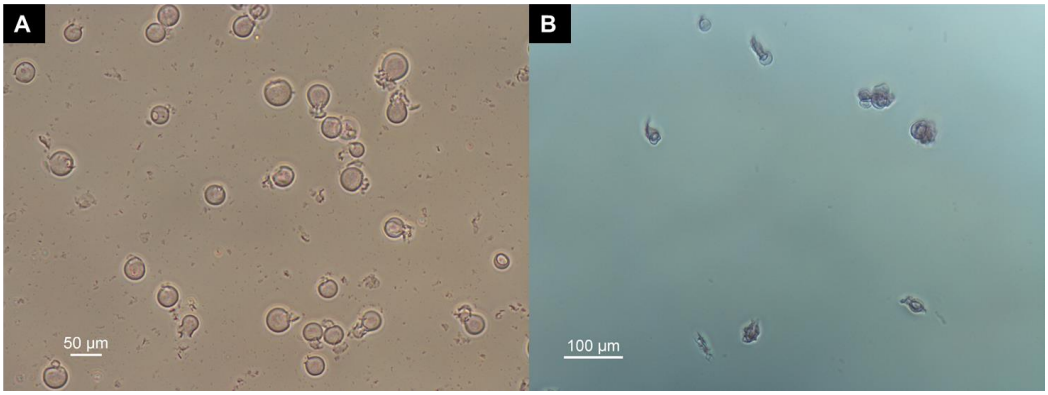

Figure 73. Phase contrast microscopy image of microcapsules synthesised with (A) PTA or (B) TPP as the gelling agent.

3.3.5. Microcapsule production and characterisation

Using this approach with the ejection parameters optimised at the **Section 3.3.3** over the gelling solution composition optimised at the **Section 3.3.4**, sphere-like homogeneous microcapsules of chitosan and PTA containing AuNP were obtained (**Figure 74**). It should be noticed that a controlled agitation of the gelling agent using a magnetic stirrer plate was indispensable to avoid aggregation and fusion of microcapsules during gelation process. These microcapsules were washed with water maintaining the sterility of the samples, concentrated by decantation and their dry weight concentration was measured by freeze-drying. Employing the described methodology, an automatic production rate of 18 mg/hour of microcapsules was achieved thanks to our inkjet system strategy. It should be highlighted that this rate was obtained employing just a single inkjet microdispensing device with a single nozzle. One further advantage of this system is the possibility to scale-up the production by employing several commercially available multi-nozzle headers performing a simultaneous ejection in parallel.

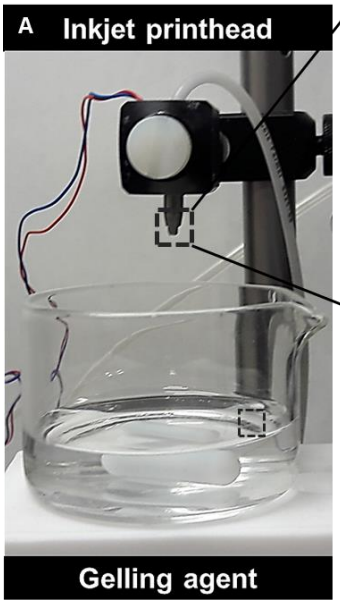

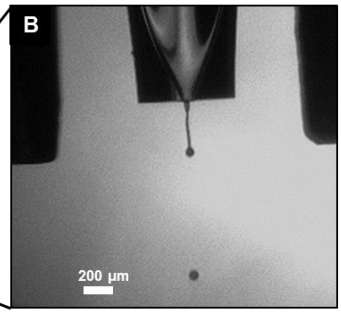

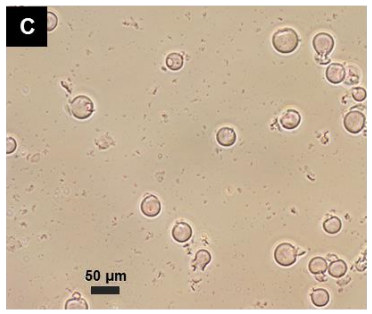

D Characteristics of AuNP microencapsulation by inkjet	
Encapsulation efficiency (%)	92.4 ± 5.8
Gold loading (% Au/dry weight)	2.2 ± 0.1
Rate of production (mg/h)	18
Frequency (microcapsules/s)	3000
Microcapsule Size (µm)	34 ± 4

Figure 74. A) Inkjet system employed for the microdroplet generation. **B)** Photograph of the chitosan and AuNPs droplets ejected from the inkjet printhead at a rate of 3000 microdroplets per second. **C)** Optical contrast-phase microscopy image of AuNPs-chitosan microcapsules in water. **D**) Technical characteristics of the inkjet methodology developed for AuNP microencapsulation in chitosan. Adapted with permission from[262]

Interestingly, the absorbance spectrum of the AuNPs changes when they are encapsulated inside the microcapsules (see **Figure 75**). The LSPR peak is only slightly displaced to *ca.* 545 nm due to the plasmon interactions arising as a result of the physical proximity of the AuNPs to one another. This fact is of great interest because the encapsulation of AuNPs in hydrogels has been extensively employed to protect and modulate the optical properties of the AuNPs for sensing.[267]

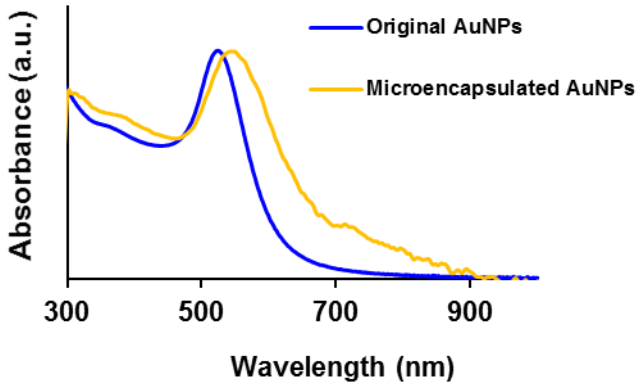

Figure 75. UV-Vis absorbance spectra of the original AuNPs (blue) employed for the ejection and UV-Vis absorbance spectra of the microcapsules containing the AuNPs (yellow).

Under the conditions reported herewithin, the size of the microcapsules was analysed by measuring the diameter in the optical microscopy images showing a monodisperse distribution with a mean diameter of 34 ± 4 µm (**Figure 76A,C**). The presence of the AuNPs and its homogeneous distribution inside all the entire of the microcapsules chitosan hydrogel matrix was confirmed by SEM and TEM confirmed that AuNPs were embedded in the chitosan hydrogel matrix (**Figure 76B,D,E**). The amount of AuNPs encapsulated in the hydrogel was determined by ICP-AES, and correlated to dry the weight to calculate the AuNPs loading of 2.2 wt.% of gold (details of AuNPs encapsulation by inkjet technology are collected in **Figure 74D**), which represent an estimated number of 1.3 million AuNPs per microcapsule calculated form the nanoparticle theoretical weight. The proof-of-concept of our proposed microencapsulation system provides >90 % encapsulation efficiency (based on the initial concentration of AuNPs ejected) compared to other benchtop chitosan hydrogels containing AuNPs which have shown far lower encapsulation efficiencies near 60 %.[143] As an extension of this thesis, the high microencapsulation efficiency of this inkjet methodology could be harnessed for encapsulating expensive particles, pharmaceuticals or compounds

that are prone to degradation, as is the case of AuNPs. This high encapsulation efficiency along with the fact that this inkjet set-up can be easily scaled-up due to its automaticity using multiple commercially available printheads working in parallel with hundreds of inkjet ejection nozzles makes this inkjet technology an interesting option for the pharmaceutical and biomedical industry.

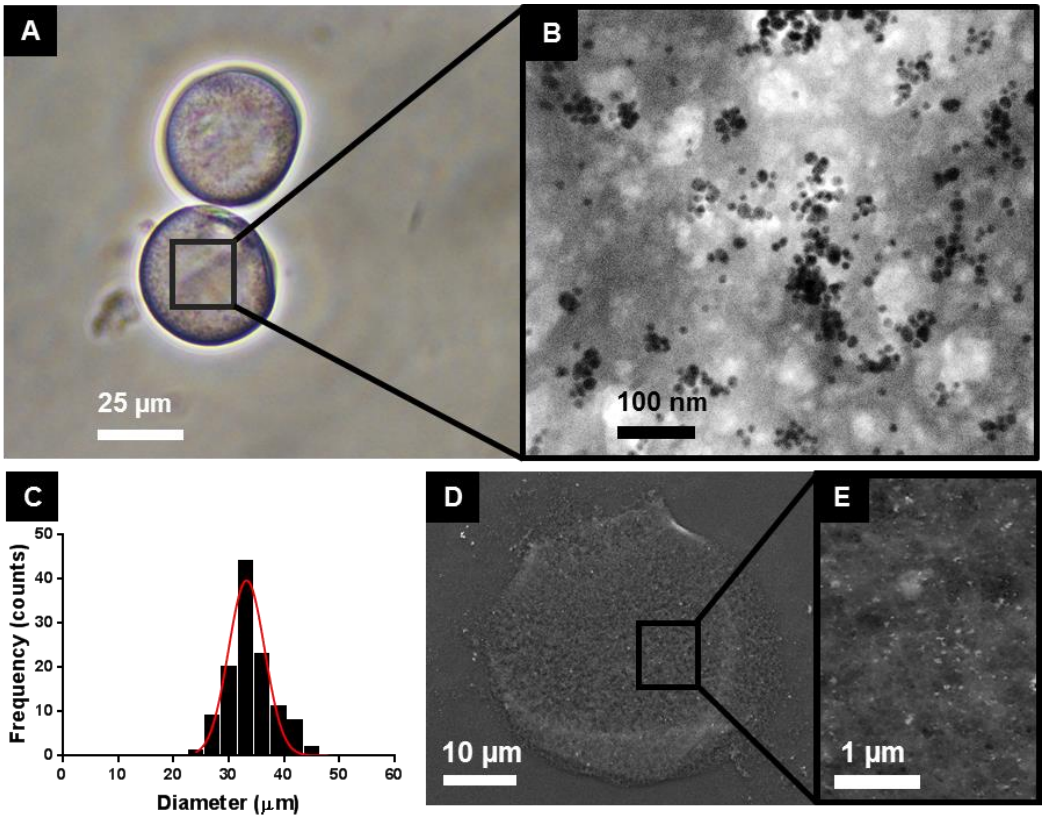

Figure 76. A) Phase contrast optical microscopy image of chitosan microcapsules containing the AuNPs in aqueous media. B) Transmission Electron Microscopy image of the hydrogel structure of the microcapsules containing the AuNPs (visualised as black dots). C) Size distribution histogram calculated from the measurements taken from brightfield microscopy images (diameter: 34 ± 4 µm). D) Scanning electron microscopy (SEM) of the microcapsules, showing a complete microcapsule and an amplification (E) showing the AuNPs embedded in the hydrogel structure. Adapted with permission from [262].

3.3.6. Co-encapsulation of other molecules

In order to know if other molecules of interest could be co-encapsulated at the same time with the AuNPs, a complementary study using a fluorophore as a simple example of co-encapsulation was performed. To this end, Alexa 647 fluorophore was added to the inkjet-ejected solution composed by chitosan, acetic acid and AuNPs and ejected in the microdroplet as other compound of the solution. Inkjet microcapsules were formed similarly as the previously reported ones, without problems during the encapsulation neither phase separation. In order to know if the fluorophore has been properly encapsulated in the microcapsule and maintained its functionality, these microcapsules were observed by fluorescent confocal microscopy. By this technique it was possibly to clearly visualise how the fluorophore was mainly encapsulated in the outer part of the microcapsule and maintained its fluorescent properties (**Figure 77A,B**). In addition, taking confocal images at different heights and performing a Z-stacking, it was possible to 3D reconstruct the morphology of the microcapsules showing its spherical shape and the presence of the fluorophore in all the external part of the microcapsules (**Figure 77C**). This possibility to co-encapsulate other molecules with the AuNPs or several molecules of interest just by their simply addition to the inkjet ejecting solution confers to the inkjet microencapsulation another extra value. Each particular molecule of interest should be tested in the system prior to their application. However the property to easily co-encapsulate several elements at the same time enhance enormously the number of molecules of interest (such as drugs, targeting molecules, reporter molecules, antibodies, other proteins, nucleic acids, among others), functionalities and applications were this microencapsulating system could be of interest in the future.

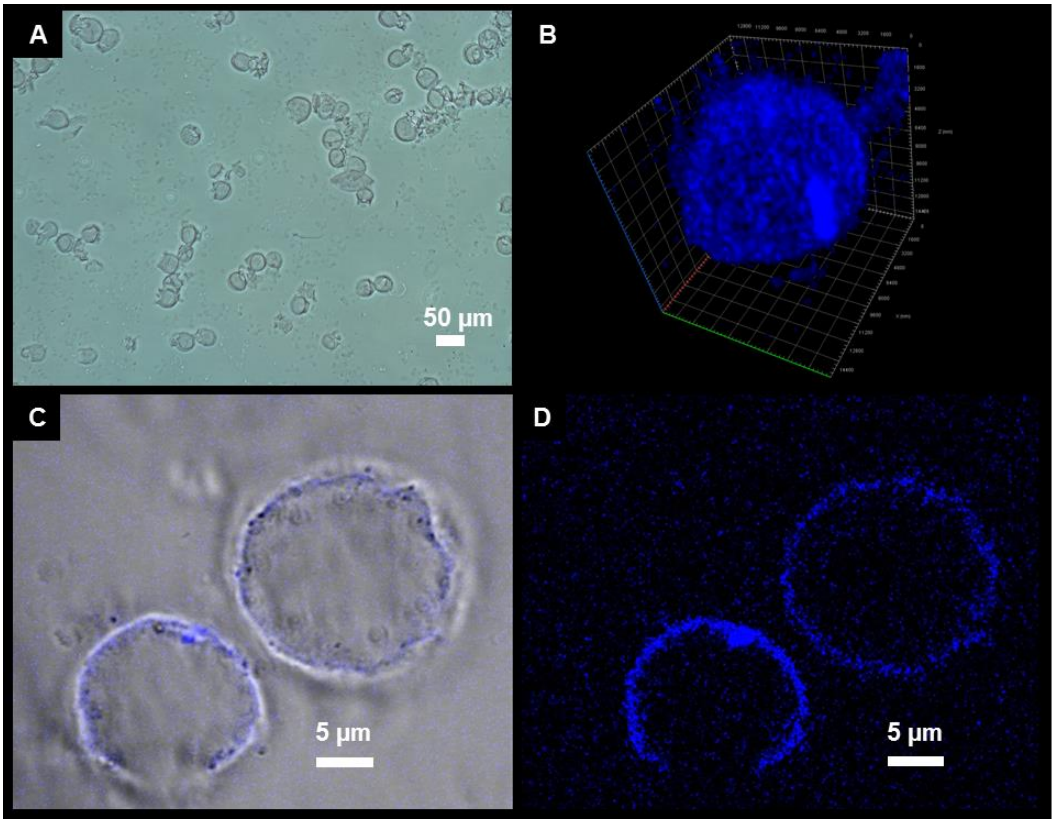

Figure 77. A) Phase contrast optical microscopy image of chitosan microcapsules containing the AuNPs and the fluorophore Alexa 647 in aqueous media. B) 3D reconstruction of the structure of the microcapsules from the fluorophore images obtained with the confocal microscopy. C-D) Confocal microscopy images of the microcapsules containing the AuNPs and the fluorophore Alexa 647. The fluorophore is shown in blue in the overlay of the fluorescence and the bright field channels (C) and in the fluorescence cannel (D). It can be appreciated that the Alexa 647 fluorophore is encapsulated in the external part of the microcapsules produced by inkjet. Adapted with permission from[262]

3.3.7. Liberation of AuNPs from the microcapsule environment

The stability of the inkjet microcapsules in physiological and simulated gastric fluid and in different buffers was studied in order to predict the feasibility of using them as potential drug delivery vehicles. The microcapsules possess stability

over a wide range of pH displaying almost no liberation of AuNPs from pH 2-9, a moderate 10 % release at pH 10-11 and a complete degradation of the microcapsules with AuNPs releases of greater than 60 % at pH higher than 11 (**Figure 78A**). Interestingly, UV-Vis spectra of the AuNPs remained unaltered after their release from the microcapsules in comparison with the original AuNPs and in contrast to the encapsulated ones (**Figure 79, Figure 75**), indicating that they maintain their colloidal stability without any sign of degradation or aggregation. This protective behaviour has already been described for other chitosan-AuNPs hybrid systems that protected the functionality of sensitive molecules from gastric degradation.[161] The stability of our inkjet microcapsules was studied by incubation in simulated gastric fluid that simulates the pH and ion concentration to which microcapsules would be exposed during a potential oral administration route. The release of AuNPs in simulated gastric fluids was studied after 1, 4 and 24 hours of incubation at 37 °C. Overall the inkjet microcapsules maintained their integrity displaying only minor release of AuNPs (< 10 %) in simulated gastric fluid under all the tested conditions after 24 hours (**Figure 78B**), making them potential candidates for oral administration of AuNPs.

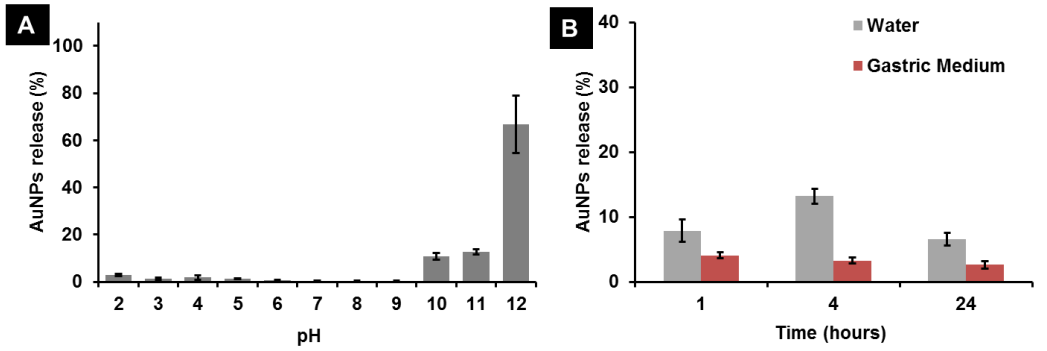

Figure 78. A) pH-dependent release of AuNPs from microcapsules measured after 24 hours of incubation. B) AuNPs release in water and in simulated gastric fluids after incubation times of 1, 4 and 24 hours. Adapted with permission from[262]

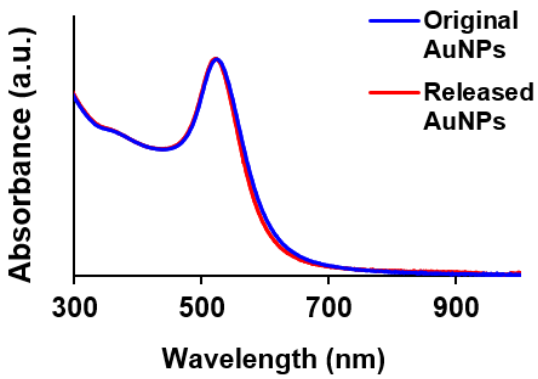

Figure 79. UV-Vis absorbance spectra of AuNPs comparing the AuNPs released from the microcapsules after exposure to pH 12 (Released AuNPs) with the AuNPs spectra before their inkjet microencapsulation (Original AuNPs). It can be seen how their spectra is maintained almost equally, indicating the stability of the AuNPs after their release without signs of aggregation or degradation.

3.3.8. Cell biocompatibility of microcapsules

In the first instance these microcapsules are intended for biomedical applications, so was important to verify their biocompatibility as well as the sterility of the inkjet production methodology. The inkjet production of the microcapsules in sterile conditions was achieved by filtering all the solutions prior to introduction in the inkjet microfluidic channels. Furthermore, the inkjet production is carried out in a laminar flow cabinet and the ejection over a gelling solution with an ethanol content of 60 % also help to prevent microbiological contamination. The presence of several microorganisms the microcapsules solution was analysed using commercial detection kits. The presence of coliform organisms was tested using the Coli-Count™ Sampler, the presence of aerobic bacteria using HPC Total Count Sampler and the presence of yeast or moulds employing the Yeast and Mould Sampler (see **Section 5.6.6** for sterility analysis details). Three different batches of microcapsules were analysed and no microorganisms were detected in any of the testers neither in any of the batches (see **Figure 80**). Such routine

analysis verifies the potential of materials produced using our inkjet methodology and provides confidence for more detailed *in vitro* and *in vivo* studies.

Figure 80. Photographs of sterility testers analysing the presence of microorganisms, comparing a negative control (sterile water), two different batches of microcapsules with AuNPs (microcapsules 1 and 2) and a positive control of contamination (ground sample). Coliform organisms were tested using the Coli-Count™ Sampler (blue), aerobic bacteria

using HPC Total Count Sampler (red) and yeast or moulds employing the Yeast and Mould Sampler (yellow).

As mentioned previously, the cell adhering properties in this type of hydrogel are useful for a wide variety of applications, such as oral delivery[19,20] and nanoparticle-mediated photothermal therapy.[143] For this reason, the cytotoxicity of the inkjet microcapsules was studied *in vitro* as a preliminary indication of safety for their applicability as drug or nanoparticle carriers for the previous related applications. The HeLa cell line was selected as *in vitro* model for cell culture compatibility due to its frequent use as a standard for cytotoxicity trials. After a 24-hour incubation period of the microcapsules with HeLa cells the interaction between the inkjet microcapsules and cells was studied using optical microscopy and showed no signs of cellular toxicity or damage (**Figure 81**).

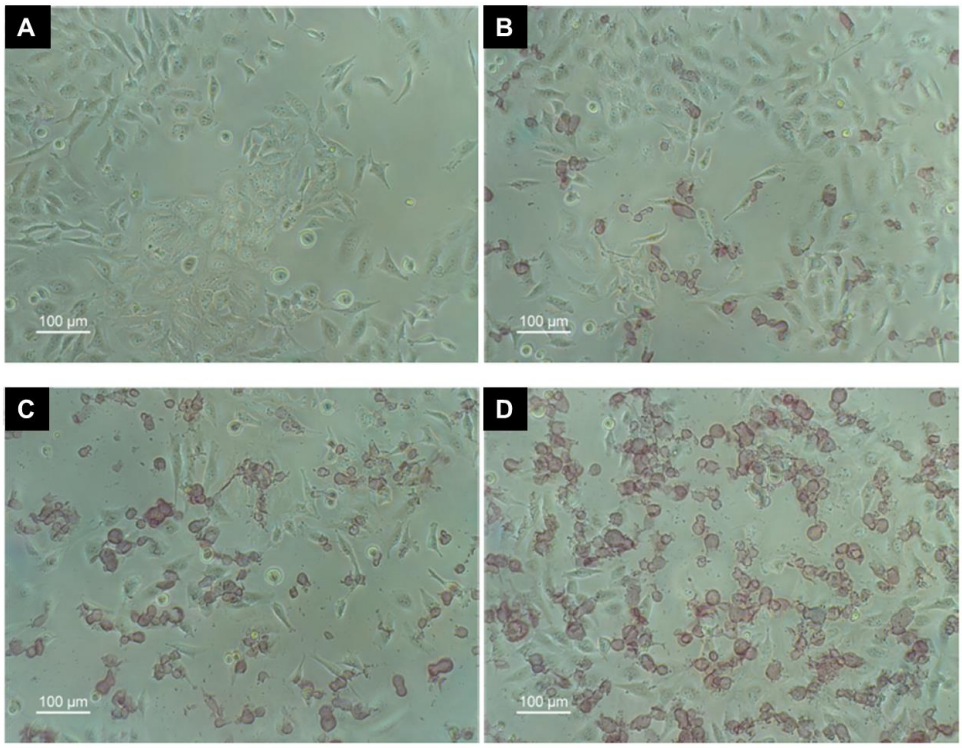

Figure 81. Microscopy images of HeLa cells incubated for 24 hours with 0 (**A**), 50 (**B**), 100 (**C**) and 200 (**D**) µg/mL of microcapsules. The AuNPs confer a red-colour to the inkjet microcapsules, which show similar sizes to the cells.

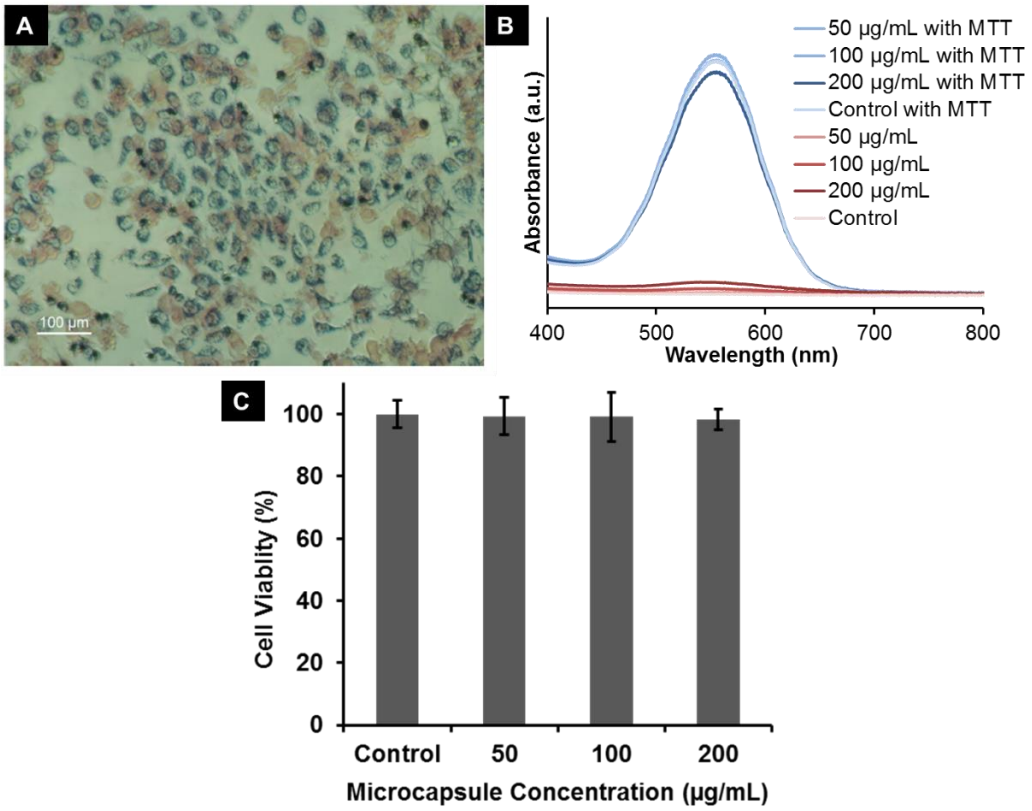

Figure 82. A) Microscopy image of HeLa cells incubated for 24 hours with the microcapsules after the MTT assay. B) Absorbance UV-Vis spectra of the cells incubated with the microcapsules treated or not treated with MTT at different microcapsules concentrations treated or not with MTT, showing a negligible interference of the microcapsules in the MTT assay. C) HeLa cell viability test by MTT of the microcapsules containing the AuNPs incubated at different concentrations for 24 hours incubation, showing no sign of toxicity.

To confirm the apparent absence of cell toxicity, MTT cell viability assays after 24 hours of HeLa cells incubation with the microcapsules were carried out. In order to ensure that the coloured properties of the microcapsules due to the presence of AuNPs (**Figure 82A**) would not affect the result of the colorimetric MTT assay, a control sample of cells incubated with the microcapsules without MTT treatment was used as internal blank for each concentration. However, in any case, the absorbance of the microcapsules was almost negligible compared with the MTT

treated cells (**Figure 82B**). The MTT cell viability assays showed no cytotoxicity (or alteration to cell metabolism) after 24 hours of incubation of the microcapsules with the HeLa cell line, even at the highest tested concentration (200 µg/mL) (**Figure 82C**).

3.3.9. Microcapsule oral administration in mice

After verifying that these microcapsules did not display toxicity to eukaryotic cells and that they were able to protect the encapsulated AuNPs from degradation in simulated gastric medium, the next step was to perform a preliminary evaluation of the biodistribution of AuNPs following oral administration in mice. This portion of the research was carried out with our collaborators Dr. Julian Pardo Jiménez and Ms. Laura Comas from University of Zaragoza at the Centro de Investigación de Biomedicina en Aragón (CIBA). 100 µL of the inkjet chitosan microcapsules at 10 mg/mL carrying the AuNPs and the fluorophore Alexa 647 were administered orally in 4 mice and compared with a similar control group treated with the same gold amount of the bare AuNPs and a control group of 2 mice just treated with water. The fluorescence of the microcapsules was recorded *in vivo* to track to localisation of the microcapsules four hours after the administration employing a IVIS Lumina II, an sensitive imaging system that records the fluorescence *in vivo* (**Figure 83**).

Unfortunately, the negative control experiment of mice without oral administration exhibited a high background of fluorescence due to the content of the gastrointestinal tract. However, the microcapsules were observed in the gastrointestinal tract due to their higher intensity compared with the negative control and AuNP control. Based on these images the exact organ, or region of that organ, cannot be ascertained. It should be noted that in the case unfunctionalised orally-administered AuNPs, the fluorescence in the gastrointestinal tract is significantly smaller than the microcapsules with AuNPs

and Alexa 647. This could indicate a fluorescence quenching phenomena provoked by the AuNPs or more probably alterations in the alimentation of the mice or in the velocity of the intestinal transit.

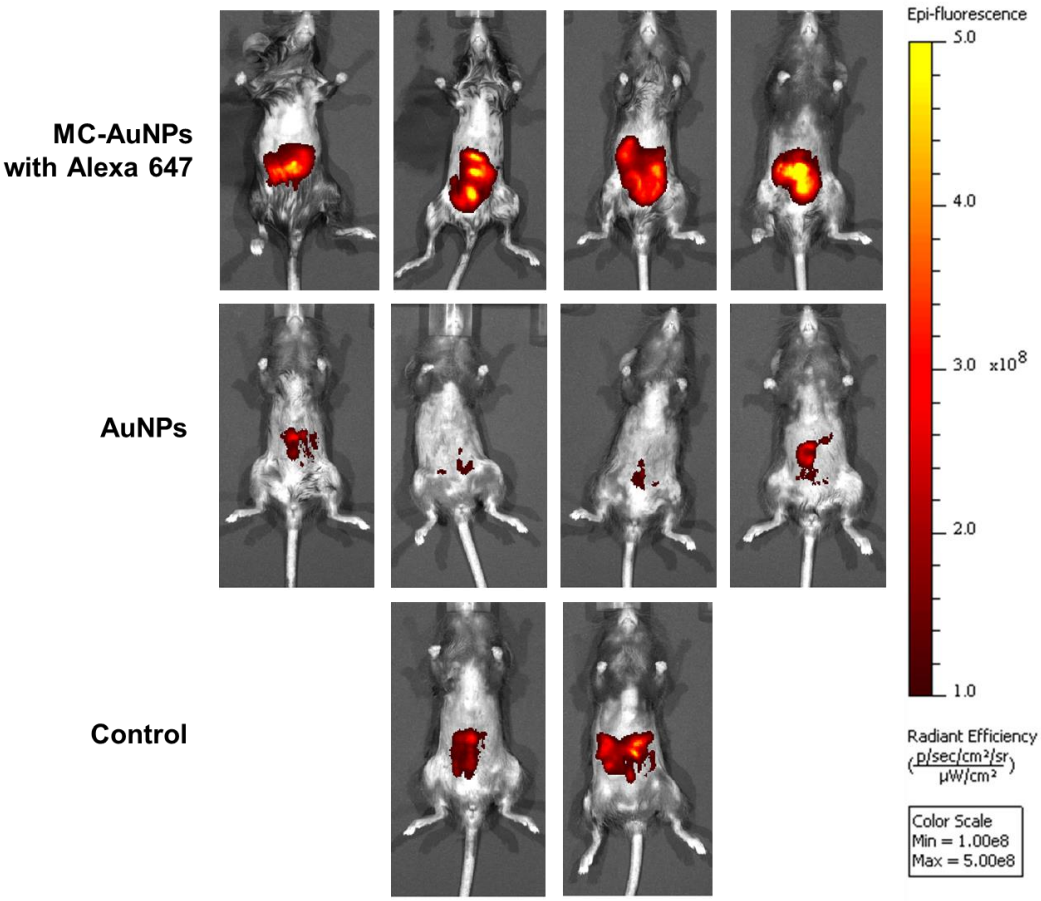

Figure 83. Fluorescence images of the mice 4 hours after oral administration of microcapsules containing the fluorophore Alexa 647 and the AuNPs (upper), the same quantity of bare AuNPs (medium) or administration of water as a negative control (down).

The organs of the mice were also extracted 4 hours after the oral administration and were digested with piranha solution followed by *aqua regia* to quantify the content of Au in each organ using ICP-MS. A large amount of Au was remained in the stomach similar to the case of free AuNPs and microencapsulated ones. The lack of gold in the liver indicates that the AuNPs do not enter into the

bloodstream where there would be a risk of metal bioaccumulation. A slightly increase in the ileum and duodenum retention could be observed in the case of the encapsulated AuNPs, however this gold content is almost depreciable in comparison with the total amount administered. Interestingly, the microencapsulation of the AuNPs conferred the ability to increase the colon retention seven times more than the bare AuNPs probably due to the mucoadhesive characteristics of the chitosan (**Figure 84**). For all these reasons, all these preliminary results suggest that this microencapsulation methodology could be of interest for the encapsulation of AuNPs and/or drugs for applications requiring a localised treatment of the colon. Furthermore, ability to achieve a local delivery without the risk of AuNPs entering in the bloodstream means that we will continue to explore this research line.

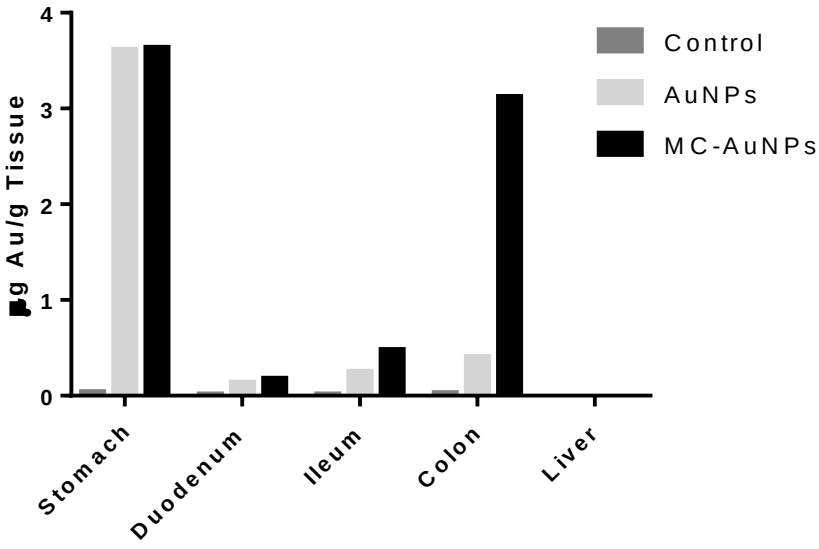

Figure 84. Au biodistribution in different organs 4 hours after the oral administration of the microcapsules. Four mice per group were administered orally with water (Control), the free AuNPs (AuNPs) or the inkjet produced microcapsules containing the AuNPs (MC-AuNPs) and the organs were extracted after 4 hours. The gold content of each of the organs was analysed by ICP-MS. It should be highlighted that colon retention for microcapsule encapsulated AuNPs is 7 times more than the bare AuNPs

3.3.10. Conclusions

In conclusion, we have developed an innovative inkjet microencapsulation methodology for trap nanoparticles within polymeric hydrogels. To the best of our knowledge, this is the first time that inkjet technology has been employed for AuNP encapsulation or for generating chitosan microcapsules. This novel approach enables an automatic production of microcapsules at a high speed and productivity, making the strategy stand out due to its high production efficiency, degree of control over the size of the microdroplets as well as the size and shape homogeneity of the corresponding microcapsules. The proof-of-concept 30 μm diameter AuNP-chitosan microcapsules show no cytotoxicity and are highly resistant over a wide range of pH and to degradation in simulated gastric medium. Furthermore, this preparation methodology facilitates the production of sterile microcapsules. This combination of attributes makes this production methodology highly relevant to a number of biotechnological applications where drug, compound or nanoparticle encapsulation, protection and delivery play key roles. Our preliminary studies on oral administration of these microcapsules showed a seven-fold increase in the colon retention with respect to the bare AuNPs.

4. Conclusions

This thesis proposes new routes to improve the utility and biotechnological application of gold nanoparticles (AuNPs) in biomedical sensing and therapy. In the first instance, AuNPs possess high density and surface functional chemistry enabling the possibility to functionalise with proteins, both of which render them as useful SPRi enhancement materials for biosensing applications. Thanks to these physicochemical properties, a methodology has been developed to detect attomolar quantities of several miRNA sequences at the same time with just one single stable and easy-to-prepare nanoparticle reagent, which, importantly, avoids the use of enzymes and multi-step enhancing protocols. From this study, it can also be concluded that a comprehensive characterisation and optimisation of the gold nanoparticle functionalisation with proteins is of great utility to achieve highly functional nanoparticles for the desired application. To this end, from the matrix of biofunctionalisation strategies and AuNP shapes and sizes tested in this thesis, gold nanospheres of 14 nm functionalised with neutravidin along with biotinylated antibodies proved to be the best compromise between analytical performance, experimental feasibility and practicality for the application of AuNP in SPRi sensing. Future studies should focus on evaluating the feasibility of this approach for miRNA detection market.

The SPR biosensing research highlighted how different shapes of AuNPs are critically important considerations when studying the applicability of AuNPs for a determined application, since the physicochemical properties and biocompatibility of each nanoparticle shape vary so significantly. This thesis shows how AuNPrs and AuNRs are extremely efficient light-to-heat transducers, where the heating efficiency of AuNRs are superior. However AuNR-mediated cell-death was shown to be extremely poor due to their low cellular internalisation, which stand in contrast with the excellent performance of AuNPrs for PTT *in vitro*. In order to

overcome the poor performance of AuNr-induced PTT *in vitro*, a simple strategy consisting of AuNR entrapment in cell-adhesive sub-micrometric chitosan hydrogels was developed. These AuNR@chitosan hydrogels showed no cytotoxicity and displayed almost identical heating properties to free AuNR. Importantly, however, the *in vitro* efficiency for PTT was improved dramatically, even improving on the AuNPr ability for PTT by the need of a lower gold concentration for a higher cell death. This high *in vitro* efficiency encourages future research on AuNR@chitosan hydrogels for *in vivo* PTT, focusing on their interaction with different tissues and organ, the administration pathways and the AuNR release and elimination.

Although the aforementioned AuNR@chitosan hydrogels performed well for PTT applications, the synthetic method for these hydrogels presented several drawbacks including high polydispersity and potential issues with reproducibility, common to benchtop syntheses, which thus motivated the quest for a novel AuNP@chitosan encapsulation method. This thesis has demonstrated how inkjet technology can be employed for AuNPs microencapsulation, providing an automatic and continuous production of microcapsules at high speed and with high AuNP encapsulation efficiency. This proof-of-concept AuNP@chitosan microcapsules showed no cytotoxicity, presented a highly resistance against degradation and showed an enhanced colon retention in preliminary studies of oral administration in mice. Future research on inkjet technology should focus on co-encapsulation of anisotropic AuNPs and other pharmaceuticals in order to take advantage of their NIR optical properties for therapy and sensing. Also trying to understand its interaction with the intestinal epithelium would be highly interesting for its future application as oral delivery microcapsules.

On the basis of all the studies collected in this thesis and analysing them as a whole, it is possible to conclude that the shape of AuNPs and the biofunctionalisation strategy employed are crucial parametres for its performance in sensing and photothermal therapy. It has been proved how by developing a

precise control of its synthesis, biofunctionalisation and a thorough characterisation it is possible to select and design the apropiate AuNP for each case. In addition, it has been showed how the improvement of AuNPs properties can be carried out by the development and optimisation of chitosan hydrogel entrapment methodologies. However, some questions remain still unknown. Why different AuNPs shapes showed different biodetection properties or cell internalisation profiles or how hydrogel encapsulated AuNPs interact with living systems are questions that remain to discover after this thesis. These questions, along with the results obtained during this thesis and the future possibilities related to these studies alredy detailed during this conclusion section, represent a highy interesting starting point for future studies expanding the knowledge about AuNP applicability for treatment and biosensing.

Conclusiones

Esta tesis muestras algunas formas de mejorar la utilidad y aplicación biotecnológica de las nanopartículas de oro para detección y terapia. En la primera parte de la misma, la elevada densidad de las AuNPs junto con la química funcional de su superficie que permite su funcionalización con proteínas, las convierten en materiales de gran utilidad para la amplificación de la señal SPRi para aplicaciones de bio-detección. Gracias a estas propiedades fisicoquímicas, se ha desarrollado una metodología para detectar cantidades attomolares de varias secuencias de miRNA al mismo tiempo detectadas empleando un solo reactivo consistente en nanopartículas estables y fáciles de preparar que evita el uso de enzimas y protocolos de amplificación en múltiples pasos, lo cual es de gran importancia para el sector. Además de este estudio, se demuestra que una caracterización y optimización exhaustivas de la funcionalización con proteínas es de gran utilidad para producir nanopartículas altamente funcionales para la aplicación deseada. Para este fin, de la matriz de formas y tamaños de AuNPs junto con las distintas estrategias de funcionalización con proteínas testadas en esta tesis, las nanoesferas de oro de 14 nm funcionalizadas con neutravidina que interaccionan específicamente con los anticuerpos modificados con biotina han demostrado poseer el mejor compromiso entre rendimiento analítico, viabilidad experimental y practicidad para la futura aplicación real de AuNPs en detección mediante SPRi. Sería recomendable que los estudios futuros se centren en evaluar la viabilidad de esta estragia en el mercado de detección de miRNA.

Durante la investigación realizada en bio-detección mediante SPR queda demostrado que la geometría de las AuNPs es una consideración de vital importancia cuando se estudia la aplicabilidad de las AuNPs para una aplicación concreta ya que las propiedades fisicoquímicas de cada forma de nanopartícula

y su interacción con los componentes biológicos varían drásticamente. Esta tesis demuestra cómo tanto los AuNRs como los AuNPrs son transductores extremadamente eficientes de luz en calor, siendo la eficiencia de calentamiento de los AuNRs superior. Sin embargo, la muerte celular mediada por los AuNRs fue extremadamente baja debido a su baja internalización celular, lo que contrasta con el excelente rendimiento de los AuNPrs para PTT *in vitro*. Para solucionar el bajo rendimiento en PTT *in vitro* de los AuNRs se desarrolló una estrategia simple consistente en su encapsulación en hidrogeles de quitosano sub-micrométricos con elevada adhesión celular. Estos hidrogeles AuNR@chitosan no presentaban citotoxicidad y poseían propiedades de calentamiento casi idénticas a los AuNRs libres. Cabe destacar, además, que la eficiencia en PTT *in vitro* fue mejorada drásticamente, incluso mejorando la de los AuNPr ya que se necesitaba una concentración de oro menor para producir una mayor muerte celular. Esta alta eficiencia *in vitro* es alentadora para continuar con la futura investigación de estos hidrogeles AuNR@chitosan para su uso en PTT *in vivo*, centrándose en la interacción de estos materiales con los diferentes tejidos y órganos, las posibles vías de administración y la liberación de AuNR y su eliminación.

A pesar de que los hidrogeles de AuNR@chitosan funcionaban bien para aplicaciones de PTT, la metodología de síntesis empleada para estos hidrogeles presentaba varias desventajas como polidispersidad y ciertos problemas de reproducibilidad, lo que motivó la búsqueda de un nuevo método de encapsulación de nanopartículas de oro en hidrogeles de quitosano. Este tesis ha demostrado como la tecnología inkjet puede ser empleada para la microencapsulación de AuNPs, al mismo tiempo que esta tecnología permite una producción continua y automática de microcápsulas a alta velocidad y con una elevada eficiencia de encapsulación de AuNP. Estas microcápsulas AuNP@chitosan producidas como prueba de concepto no presentaron citotoxicidad celular, presentaron una alta resistencia frente a la degradación y

demostraron aumentar la retención en el colon en un ensayo preliminar de administración oral en ratones, tal y como se pretendía. La futura investigación en tecnología inkjet continuando con este tema debería centrarse en la co-encapsulación de AuNPs anisotrópicas junto a otros fármacos para beneficiarse de sus propiedades ópticas en el NIR para terapia y detección. También intentar enteder su interacción con el epitelio intestinal sería muy interesante para su future aplicación como microcápsulas de administración oral.

Empleando como base los estudios descritos en esta tesis y analizándolos en su conjunto, es posible concluir que la forma de las nanopartículas de oro y la estrategia de biofuncionalización empleada son consideraciones cruciales para su actividad en biodetección y terapia fototérmica. Se ha demostrado cómo desarrollando un control preciso de su síntesis, biofuncionalización y una minuciosa caracterización es posible seleccionar y diseñar las nanopartículas de oro apropiadas para cada caso. Además, se ha descrito cómo la mejora de las propiedades de las nanopartículas de oro puede alcanzarse mediante el desarrollo y optimización de metodologías para la encapsulación de AuNPs en hidrogeles de quitosano. Sin embargo, algunas cuestiones permanecen aún sin respuesta. Por qué las diferentes formas de AuNPs presentan propiedades de biodetección o perfiles de internalización celular tan diferentes o cómo las AuNPs encapsuladas en hidrogeles de quitosano interaccionan con los sistemas vivos son preguntas que quedan por descubrir después de esta tesis. Estas preguntas, junto a los resultados obtenidos durante esta tesis y las posibilidades de continuar estos estudios en el futuro previamente descritas, represantan un punto de partida altamente interesante para futuros estudios que expandan el conocimiento acerca de la aplicabilidad de las nanopartículas de oro en biodetección y terapia.

5. Materials and methods

5.1. Materials

All reagents, chemicals and solvents were supplied by *Sigma Aldrich Chemical Company Ltd.*, *Merck, Scharlab, Fisher Scientific*, *Strem Chemicals, Invitrogen, Lonza, Panreac or Acros Organics* and used without further purification, unless stated otherwise.

5.2. Instrumentation

Unless otherwise stated, the following instrumentation was used to obtain the analytical data herewithin:

Transmission Electron Microscopy (TEM) images were collected using a FEI Tecnai T20 (FEI Europe, Eindhoven, Netherlands) working at 200 kV.

Scanning Electron Microscopy (SEM) images were collected using a field emission SEM Inspect F50 with an EDX system INCA PentaFETx3 (FEI Company, Eindhoven, The Netherlands) in an energy range between 0-30 keV. Nanoparticles dimensions and counting in the images from SEM and TEM were analysed employing the software ImageJ.

UV-Vis spectra were acquired employing a Cary 50 Probe® spectrophotometer from Varian or a Jasco V670.

Dynamic Light Scattering and Electrophoretic mobility (Zeta Potential) were evaluated using a Brookhaven 90Plus DLS instrument (NY, USA).

Freeze-drying was performed in a Telstar cryodos freeze-dryer (Spain) with an Agilent technologies DS 102 vacuum pump.

For the Near Infrared (NIR) laser irradiation, all samples were irradiated using a 3 W Laser Quantum Ventus laser (1064 nm) at a power output of 1100 mW for

10 min, which corresponds with a power per surface of *ca.* 3.3 W cm^{-2} at the sample position. The temperature was registered every 5 sec using a software program developed by The University of Zaragoza using a Fibre Optic Temperature Sensor TPT-62 (Fiso Technologies Inc.).

Inductively coupled plasma atomic emission spectroscopy (ICP-AES) or inductively coupled plasma mass spectrometry (ICP-MS) was performed using an Optima 8300 (Perkin Elmer®) in the Servicio Central de Análisis de Bizkaia from SGIker of Universidad del País Vasco (EHU).

Both bright-field, dark field and standard fluorescence images of the cells were obtained with a Nikon Eclipse Ti with FPS system equipped with a phase contrast system, dark field visualisation system and 387±11/447±60 nm (DAPI) cube filter connected to NIS-Elements Microscope Imaging Software.

The composition of the hydrogel and its components was analysed by Fourier Transform Infrared (FTIR) spectroscopy analysis in a JASCO FT/IR-4100 Fourier transform infrared spectrometer in a frequency range of 600–4000 cm^{-1} with a resolution of 2 cm^{-1} and a scanning number of 32.

The images of the biodistribution of the fluorescent microcapsules in mice were acquired employing a quantitative fluorescent and bioluminescent imaging equipment IVIS Lumina II (LifeSciences).

5.3. AuNPs synthesis and characterisation

Prior to use, all glassware was washed with *aqua regia* and rinsed thoroughly with Milli-Q water from Millipore Q-POD® system.

5.3.1. Gold nanospheres (AuNS) synthesis

5.3.1.1. Synthesis of gold nanospheres of 14 nm (AuNS)

Gold nanospheres (AuNSs) with a diameter of 14 nm and a maximum absorbance peak (LSPR) at 520 nm, were prepared using the Frens-citrate approach and then

coated with alpha-Thio-omega-(propionic acid) octa(ethylene glycol) (HS-PEG-COOH) of 458 Da (Iris Biotech GmbH) or with alpha-(11-Mercapto-undecanoylamido)-omega-carboxy dodeca(ethylene glycol) (HS-FA-PEG-COOH, from Iris Biotech GmbH) of 818 Da applying the previously reported methodology with minor modifications.[77] Briefly, 195 mL of tetrachloroauric acid ($HAuCl_4$) (Strem Chemicals) at 1.2 mM was heated until boiling and 5 mL of sodium citrate at 163 mM were added and maintained at reflux conditions for 30 min protected from the light. Finally, the solution was cooled to room temperature and stored at 4 °C.

After that, 10 nM bare gold nanospheres (calculated from ICP-AES quantification) were mixed with 0.028 % sodium dodecyl sulphate, 50 µM of HS-PEG-COOH or HS-FA-PEG-COOH and NaOH 25 mM and incubated for 16 h in agitation at room temperature. The nanoparticles were washed 3 times by centrifugation for 30 min at 18000 g and 4 °C. The pellet of nanoparticles was resuspended in ultrapure water and stored at 4 °C, a temperature at which they remain stable for several months if protected from direct light. Extinction coefficient (11.3 $mL \cdot mg^{-1} \cdot cm^{-1}$) was calculated correlating their UV-vis absorbance at 450 nm with the gold content measured by ICP-AES. The theoretical mean mass of gold of AuNS was calculated from the diameter of nanoparticles measured from TEM images assuming a spherical shape and the gold density value (19.3 $g \cdot cm^{-3}$), corresponding with $1.67x10^7$ $g \cdot mol^{-1}$ (See **Table 3** for more details).

5.3.1.2. Synthesis of gold nanospheres of 37 nm (B-AuNS)

AuNS with a diameter of 37 nm (B-AuNS) were prepared by dissolving 0.23 mmol tetrachloroauric acid ($HAuCl_4$) in 195 mL of ultrapure water and heating the solution until boiling point. Sodium citrate (0.33 mmol) in 5 mL of water was added and the boiling solution was kept under magnetic agitation protected from the light for 30 min. After cooling, PEGylation of B-AuNS with heterobifunctional alpha-Thio-omega-carboxy poly(ethylene glycol) (HS-PEG-COOH, from Rapp

Polymere) of 5 KDa was performed by preparing a mixture of B-AuNS at 1.91 nM, SDS 0.028 % and HS-PEG-COOH 3.42 µM. After this, NaOH 25 mM was added and the mixture incubated with mild agitation at room temperature for 16 h. The excess of PEG was subsequently removed by centrifugation at 18000 g for 15 min. This process was performed three times in order to remove all the excess of PEG. The extinction coefficient was 11.2 $mL \cdot mg^{-1} \cdot cm^{-1}$ at 450 nm (see **Table 3** for more details).

5.3.2. Gold nanoprisms (AuNPr) synthesis

5.3.2.1. Gold nanoprisms (AuNPr) synthesis for SPRi detection of miRNA

Triangular gold nanoprisms (AuNPr) with LSPR at 1000 nm were synthesised according to a previously reported methodology with minor modifications.[61] Briefly, 200 mL 2 mM $HAuCl_4$ (aq) were mixed with 140 mL 0.5 mM $Na_2S_2O_3$ (aq) containing 20 µL 0.1 M KI (aq) and, after 4 min, another 140 mL 0.5 mM $Na_2S_2O_3$ (aq) containing 20 µL 0.1 M KI (aq) was added. After another 4 min, 60 mL 0.5 mM $Na_2S_2O_3$ (aq) was slowly added to the solution and the resulting mixture was left reacting for 60 min RT. AuNPr were stabilised by adding heterobifunctional alpha-Thio-omega-carboxy poly(ethylene glycol) (HS-PEG-COOH, from Rapp Polymere) in a ratio PEG:nanoprisms of 2:1 (in mg). After that, the pH was raised to 12 with the addition of 2M NaOH (aq). Finally, the mixture was sonicated for 60 min at 60 ºC and the resultant AuNPr were centrifuged at 5000 g, 15 min to remove unreacted reagents and by-products. While the supernatant was discarded, the precipitate was resuspended in the same volume of water and two further washing steps were performed using the same conditions. The nanoprisms covered with PEG were loaded (mixed with sucrose 20 mg/mL) in wells within an agarose gel (2.5 %) immersed in an electrophoresis cuvette filled with TBE 0.5x in order to remove spherical AuNP which were by-products of the reaction. The electrophoresis separation was run at 120 V for 15 min, after which time the pseudo-spherical gold nanoparticles entered in the gel while the

nanoprisms stayed in the wells from where they could be recovered with a pipette. Extinction coefficient was calculated to be 11.5 $mL \cdot mg^{-1} \cdot cm^{-1}$ at 400 nm (See **Table 3** for more details).

5.3.2.2. Gold nanoprisms (AuNPr) synthesis for PTT

AuNPrs with LSPR at *ca.* 1100 nm were prepared using a modification of the previously reported procedure (**Figure 43**). Briefly, 60 µL 0.1 M KI solution was added to 220 mL 0.5 mM $Na_2S_2O_3$ (aq.) and 110 mL of this dilution (KI + $Na_2S_2O_3$) was added slowly to 200 mL 2 mM $HAuCl_4$ (Sigma-Aldrich) (aq) over a period of *ca.* 30 sec and aged for 4 min undisturbed. A second addition of 110 mL of KI + $Na_2S_2O_3$ was made and was once again allowed to stand for 4 min before one final addition of 70 mL $Na_2S_2O_3$. The final solution was kept undisturbed for 60 min. The concentration of AuNPrs was calculated using their LSPR peak absorbance at *ca.* 1100 nm and applying a conversion factor (Ɛ) 29 $mL \cdot mg^{-1} \cdot cm^{-1}$. Note: Ɛ was obtained from combined UV-vis spectroscopy/ICP analyses.

AuNPrs were covered with PEG as previously added to the nanoparticles was prepared in a 1:2 ratio (NPs:PEG) of the total weight of gold used in the synthesis. PEG was diluted in 1 mL Milli-Q and a determined volume of a 10 mg/mL stock solution of $NaBH_4$ (Sigma-Aldrich) was then added to reach 1:1 molar ratio of PEG:$NaBH_4$. The entire volume of the PEG-$NaBH_4$ solution was completely added to AuNPrs, and adjusted to pH 12 with 2 M NaOH (Sigma-Aldrich) under mild mixing. Finally, the solution was sonicated for 1 h at 60 ºC, and then centrifuged at 4,400 g for 15 min at room temperature to precipitate the AuNPrs and separate them from excess PEG and unreacted starting materials. Pellets were resuspended in Milli-Q water and centrifuged three times at 4,400 g for 9 min at room temperature. These final samples were diluted to one quarter of their original volume and aliquoted in 50 mL centrifuge tubes and allowed to rest at room temperature for several weeks. After this time the larger, heavier AuNPrs sediment at the bottom of the centrifuge tubes and the upper layer of the solution

(containing the smaller, lighter polyhedral gold particles) could be removed. All nanoparticles suspensions were sterilised with 0.22 µm MilliPore® filters prior addition to cell cultures.

5.3.3. Gold nanorods (AuNRs) synthesis

A modified procedure, based on a previously reported seeded-mediated growth method,[27] was used to prepare high aspect ratio gold nanorods, with LSPR bands higher than 1000 nm (**Figure 43**).

To prepare the seed solution a stock of 1 M $NaBH_4$ (Sigma-Aldrich) (aq) dissolved in 1 M NaOH (Sigma-Aldrich) (aq) was prepared and diluted 100 times in Milli-Q water, giving a final concentration of 0.01 M $NaBH_4$ (Sigma-Aldrich) in 0.01 M NaOH. Then, 5 mL of 1 mM $HAuCl_4$ (aq) and 5 mL of 0.2 M hexadecyltrimethylammonium bromide (CTAB purchased from Sigma-Aldrich) (aq) were mixed together. CTAB was dissolved to homogeneity in a water bath at 37 ºC. 460 µL of the previously prepared $NaBH_4$/NaOH stock solution was then added, resulting in a light-brown mixture within seconds, evidence of the presence of Au^0 seeds. This brownish mixture was allowed to stand for no more than a few min before use in the growth solution.

The growth solution was prepared by mixing 50 mL of 1 mM $HAuCl_4$ and 50 mL of 0.2 M CTAB solution, followed by the addition of 700 µL 0.1 M $AgNO_3$ (Panreac®). Then 1 mL 0.5 M hydroquinone (Alfa Aesar®) was added and the resulting mixture was stirred until the solution became transparent and colourless. Finally, 1.6 mL seed solution was added. The growth reaction mixture was aged for 5 h at 26 ºC in a water bath.

After that AuNRs were washed and covered with SH-PEG-COOH 5 kDa. Several centrifugation-washing steps were required after each reaction to clean AuNRs from excess surfactant. In order to maintain the colloidal stability while obtaining PEG-stabilised AuNRs, various PEGylation steps were performed between

washing steps. Firstly, 5 mg of heterobifunctional HS-PEG-COOH (5 kDa) diluted in 1 mL Milli-Q water were added to 37 µL of a freshly made 1 mg/mL $NaBH_4$ (aq.) and left undisturbed for several min at room temperature. Then, the growth solution was centrifuged at 15,000 g, 15 min, 30 ºC, and pellets were resuspended in 100 mL Milli-Q water, followed by the addition of 1 mL of previously prepared PEG solution. Finally, the pH was raised by adding 100 µL of 1 M NaOH to the resultant solution (obtaining a pH value of 10.5 - 11) and the sample was aged overnight (20 h) at room temperature, trying to avoid that the temperature drops below 25 ºC to avoid CTAB crystallisation. The next day, an identical PEGylation step was performed. The sample was centrifuged (15,000 g, 15 min, 30 ºC) followed by the resuspension of the pellets in 100 mL Milli-Q water to remove PEG excess and remaining CTAB from nanoparticles, and 1 mL of previously prepared PEG solution was added. The pH was raised again (obtaining a pH value of 10.5 - 11). The resulting mixture was then sonicated for 15 min at 60 ºC, followed by another centrifugation at the same conditions to remove excess PEG. Pellets were resuspended in 100 mL Milli-Q water and one last centrifugation was performed at the same conditions to concentrate the sample, which pellets were resuspended in a final volume of 15 mL in Milli-Q water. Samples were stored at room temperature and the concentration of nanorods was obtained applying a conversion factor of (Ɛ) 74 mL mg^{-1} cm^{-1} at their LSPR (1044 nm). Ɛ was obtained from combined UV-vis spectroscopy and ICP analyses. All nanoparticles suspensions were sterilised with 0.22 µm MilliPore® filters prior addition to cell cultures.

5.3.4. Characterisation techniques for nanomaterials

All gold nanoparticles were characterised by UV-Vis, TEM or SEM and, depending on the case, the following techniques:

5.3.4.1. Ellman assay

For the determination of the degree of saturation of gold nanoparticles functionalised with thiolated polyethyleneglycol chains it was employed a procedure based on the Ellman's assay previously reported with minor modifications.[268] After the incubation of the gold nanoparticles with the thiolated chains, the supernatant with the excess of thiolated chains is collected to perform the quantification assay. The number of exchanged chains was given by the difference between the amount determined by this assay and the initial amount of chains in the incubation mixture with the nanoparticles. In the employed conditions, 218 µL of supernatant or calibration samples were mixed with 55 µL of tris(hydroxymethyl) aminomethane 1 M pH 8 and 27 µL of DTNB (5,5'-dithio-bis(2-nitrobenzoic) acid) 2 mM in NaAc 50 mM. The mixture was mixed by pipette stirring and the absorbance at 412 nm is measured.

5.3.4.2. Photothermal Characterisation of Nanoparticles

Note that, prior to these measurements, the NPs were incubated in DMEM medium for 24 h (37 ºC, 5 % CO_2) in order to simulate cell culture conditions, and to provide additional information about possible changes in their size and/or shape that may affect their optical properties, stability and so forth. Conformational changes were monitored using UV-Vis and SEM imaging during the process. Each concentrated stock of NPs was mixed with DMEM to a final volume of 300 µL per well, giving a final concentration of 20, 100, 120, and 150 µg/mL for NPrs, and of 20 and 100 µg/mL for NRs. To be able to correlate the heating curves of these experiments to the conditions used for cell irradiation, the final volume contained no more than 10 % water. Blank was performed irradiating 300 µL of DMEM. A linear regression of the heating curves during the first 30 seconds of irradiation was calculated in order to obtain the temperature increase per second. The specific heat and density values of the DMEM were

approximated to those of water and the heat needed to produce this temperature increase in each well was determined.

The heating profiles were measured using a homogeneous laser beam adjusted to the bottom area of one single well on each irradiation (96-well-plates) for 10 min. All measurements were reproduced in triplicates to obtain mean values and standard deviation errors. To avoid pre-heating adjacent samples by heat diffusion and/or diffraction of the beam, one empty well was located between sample rows. The temperature probe was rinsed and cooled in Milli-Q water before collecting new data.

5.3.4.3. ICP-AES and ICP-MS

The gold content of each of the samples was quantified by ICP-AES or ICP-MS depending on the concentration. 100 µL of the samples were previously digested by addition of 100 µL of a 3:1 sulfuric acid (Sigma-Aldrich) (96 %)/hydrogen peroxide (Sigma-Aldrich) (33 %) solution and incubated 15 min at room temperature. After that, 300 µL of a 1:3 nitric acid (65 %)/hydrochloric acid (37 %) solution were added. Samples were incubated for 2 h at room temperature and at 60 °C for 15 min and they were finally diluted with Milli-Q water up to 20 mL. All samples were prepared and analysed in duplicate or triplicate depending on the experimental requirements.

5.4. AuNPs protein functionalisation and characterisation

5.4.1. Direct covalent functionalisation with Antibody

A mixture of 40 µL of 1-ethyl-3-(3-dimethylaminopropyl) carbodiimide (EDC) at 10 mg/mL and 61 µL of sulfo-N-hydroxysuccinimide (sulfo-NHS) at 10 mg/mL, both dissolved in 2-(N-morpholino)ethanesulfonic acid (MES) at 10 mM pH 5, was prepared and incubated 10 min room temperature. 20 pmol of AuNS covered with PEG-COOH and 175 µL of 10 mM MES pH 5 were added and the samples were incubated at 37 °C for 30 min at 120 rpm agitation. After that, they were

centrifuged in 1.5 mL microtubes at 13400 rpm for 25 min at 4°C, the supernatant was discarded and 500 µL of 10 mM MES pH 5 containing the proper amount of the antibody against HRP or antibody against DNA/RNA hybrid (normally 66 pmol) were added. The samples were incubated at 37 °C for 30 min at 120 rpm agitation and they were centrifuged for 25 min at 13400 rpm and 4°C. The supernatant was discarded and 500 µL of bicarbonate buffer pH 8 10 mM were added. The samples were incubated for 30 min at 37 °C and 120 rpm agitation and they were centrifuged for 25 min at 13400 rpm and 4°C. After that, 500 µL of 10 mM MES pH 5 containing 20 mg/mL of bovine serum albumin (BSA) were added, the samples were incubated for 60 min at 37 °C and 80 rpm agitation and they were centrifuged for 35 min at 13400 rpm and 4°C. The supernatant was discarded and the pellet was resupended in 10 mM sodium phosphate buffer pH7.

5.4.2. HRP activity assay

For the HRP activity assay, 100 µL of the AuNS functionalised with the antibody against HRP were incubated with 400 µL of a HRP solution at 0.6 µg/mL in 12.5 mM sodium phosphate buffer pH 7 for 30 min at 37 °C. After that the samples were centrifuged in 1.5 mL microtubes at 13400 rpm for 25 min at 4°C, supernatants were discarded and pellets were resuspended in 400 µL of 20 mM sodium phosphate buffer pH 7. After that, 10 µL of each sample were mixed with 300 µL of MES at 10 mM pH 5 containing 1 mM 2,2'-azino-bis(3-ethylbenzothiazoline-6-sulfonic acid) (ABTS) and 1 mM H_2O_2 freshly prepared. The absorbance was recorded immediately after the addition and every 5 minutes for another two times.

5.4.3. Functionalisation with neutravidin or protein A

The protocol was the same for the three types of AuNP and the two different proteins (i.e. neutravidin (Thermo Fisher Scientific, product nr. 31000) and protein

A (Sigma)), just adjusting the concentration of the AuNP and the protein in order to maintain the same ratio protein/AuNP surface area (i.e. $2.57 \cdot 10^7$ pmol/nm^2) (see **Table 3**). A mixture of 60 µL of 10 mM EDC (Sigma), 12 µL of sulfo-NHS 10 mM (Sigma) (aq.) and 48 µL of water was prepared and added to 250 µL of AuNP at a concentration of 200 µg/mL for the S-AuNS and AuNPr and a concentration of 240 µg/mL for the B-AuNS. The solution was left under mild agitation for 15 min and then centrifuged (20 min) at 13200 g for S-AuNS, 2300 g for B-AuNS. Alternatively, AuNPr were washed using a PD Minitrap G-10 (GE Healthcare) column previously equilibrated with water. The supernatant was discarded and AuNP were resuspended in 880 µL of phosphate buffer pH 5.2 (1 mM). Neutravidin or Protein A solution in PBS was added (until a final concentration of 32 nM for S-AuNS, 15 nM for B-AuNS and 19 nM for AuNPr) and the suspensions were left under mild agitation for 18 min. 160 µL 100 mM taurine (Sigma) in sodium borate buffer (pH=9, 100 mM) was added and the suspensions were leaved under mild agitation for 10 min. AuNP were centrifuged for 20 min (13200 g for S-AuNS, 2300 g for B-AuNS and 600 g for AuNPr), the supernatant was discarded and AuNP were resuspended in 10 mM PBS at pH 7.4.

5.4.4. Gel electrophoresis characterisation

The conjugation of the different AuNPs and neutravidin or protein A was followed by gel electrophoresis and also verified by means of ultraviolet-visible (UV-vis) spectroscopy. For gel electrophoresis experiments AuNPs functionalised with the proteins were resuspended in 20 µL of sucrose 20 mg mL^{-1}, instead of buffer, loaded onto 0.6 % agarose gel, and the electrophoretic run was held for 30 min at 225V in TBE 0.5X, pH 8.

5.4.5. Functionalisation with Antibody through neutravidin or Protein A

Antibody against the hybrid DNA/RNA was purchased from Covalab (Mab0105-P clone D5H6). Before its use, at least two cycles of Ab dialysis were done in

order to remove the amine groups of the storage buffer that could decrease the yield of the biotinylation process. Dialysis (2 h at RT for each cycle) was performed using Slide-A-Lyzed mini dialysis unit 3.5K MWCO (Thermo Fisher Sci., 69550) and using 10 mM PBS at pH 7.4 as buffer to obtain a final Ab concentration of 3.33 µM. NHS-PEG4-Biotin (4 mM) was freshly prepared and added to the Ab solution in order to obtain the proper molar ratio of Ab:biotin for the optimisation of the synthesis (5, 25, 50 and 75 biotin:Ab molar ratios, see **subsection 3.1.1.4**). In any case, the ideal Ab:biotin molar ratio and, consequently, the best biotinylation performances should be finely tuned when using a new biotin-reagent or a new Ab batch. After about 1 h of incubation with the NHS-PEG4-Biotin, two other cycles of dialysis were performed to remove the unreacted biotin. At the end of the dialysis process, the volume of antibody was measured in order to calculate the final concentration of the biotinylated antibody. Conversely, the protein A conjugation strategy did not require the step of antibody biotinylation, since protein A is able to recognise and bind the Fc region of the antibody. Therefore, after dialysis, bare Ab 3.33 µM was stored in fridge until its direct conjugation with nanoparticles functionalised with protein-A.

Nanoparticles and antibody were diluted in 10 mM PBS at pH 7.4 Tween 0.01 % that was the SPRi running buffer. The optical density (OD) of nanospheres of 14 nm and 37 nm (measured at 450nm) to inject in SPRi were 0.15 and 0.137; while the final OD of the nanoprisms (measured at LSPR) was 0.68. These OD were calculated to inject in the instrument the same concentration of gold (12.42 µg/mL) for the three types of nanoparticles in order to do not have different SPRi signal due to the different quantity of gold injected (see **Table 3)**. The suspension containing the nanoparticles and Ab at a final concentration of 5 nM was leaved under mild agitation for 30-45 min before the injection in SPRi.

5.4.6. Radiolabelling quantification

A previously described radio-labelling protein quantification method[188] was used with minor modifications to measure neutravidin/GNS conjugation and antibody functionalisation. Briefly, 5 µg of protein (neutravidin or Abs) were incubated with 5 µCi of $Na^{125}I$ (PerkinElmer) and 15 µg of chloramine T as an oxidising agent for 15 seconds at room temperature in a total volume of 30 µL of 0.5 M sodium phosphate, pH 7.5. The reaction was immediately terminated by adding 17.5 µL of 0.5 M sodium phosphate, pH 7.5, containing 6.7 µg of tyrosine and 150 µg of potassium iodide. The radio-labelled protein was purified using PD MiniTrap G-10 columns (GE Healthcare Life Sciences, Fairfield, CT, USA), and its concentration was determined using a Pierce Coomassie Plus (Bradford) assay kit (Thermo Fisher Scientific, Waltham, USA). The radio-labelled neutravidin and Ab were subsequently used for the conjugation/functionalisation studies. After neutravidin/GNS conjugation and Ab functionalisation of the nGNS, the nanoparticles were centrifuged and the gamma emission of them and the supernatant were measured for 60 seconds using a LKB Wallac 1282 Compugamma Universal Gamma Counter. Each sample was prepared and measured in triplicate.

5.5. Hydrogel entrapment of AuNPs

5.5.1. Synthesis of chitosan-encapsulated gold nanorods (AuNRs@CS)

Polyethylene glycol-stabilised gold nanorods (AuNR) were synthesised according to **Section 5.3.3**. For the AuNR entrapment in chitosan hydrogel, 1 mL of a 2 mg/mL (measured by dry weight and previously sterilised by filtration with a 0.22 µm Low Protein Binding Durapore® (PVDF) MilliPore® filters) aqueous AuNR solution was transferred to a glass vial. Under ultrasonication, 0.5 µmol of PTA (144 µL of a 10 mg/mL, Sigma-Aldrich) was slowly pipetted into the AuNR solution. 2 mL of 5 mg/mL chitosan (medium molecular weight, Sigma-Aldrich) in

1 % v/v acetic acid was then pipetted into the PTA/AuNR suspension and mixed for 2 min under sonication. This mixture was then added to a separate tube containing 5 mL 50 mM Na_2SO_4 solution, under sonication for 2 min. The reaction suspension was centrifuged at 6700 g for 3 min. The supernatant was discarded and the product was resuspended and centrifuged once more at 4300 g for 3 min. The precipitate was resuspended in water. All the experiments for AuNR entrapment were performed under sterile conditions in a laminar flow hood (Telstar PV-30/70). The concentration of the sub-micrometric containers in water suspension was obtained by measuring the dry weight of 0.5 mL of sample after freeze-drying in a Telstar cryodos freeze-dryer (Spain) with an Agilent technologies DS 102 vacuum pump. The composition of the hydrogel and its components was analysed by FTIR spectroscopy analysis with dried samples. Dynamic Light Scattering and Electrophoretic mobility (Zeta Potential) of the hybrid matrixes were evaluated at a concentration of 0.05 mg/mL in water or KCl 1 mM, respectively.

5.5.2. AuNRs@CS hydrogel characterisation

5.5.2.1. AuNRs@CS fixation for SEM imaging

AuNR@CS samples were covalently crosslinked with glutaraldehyde prior to electron microscopy imaging to fix their supramolecular structure. 1 mg of the AuNR@CS hydrogel was incubated for 1 h in a 1.5 % glutaraldehyde solution in PBS. The nanomaterials were then washed with Milli-Q water *via* three successive centrifugation cycles (5500 g for 5 min per cycle).

5.5.2.2. AuNRs@CS photothermal profiles

The heating profiles were measured using a homogeneous laser beam adjusted to the bottom area of one single well on each irradiation (96-well-plates) and measurements were reproduced in triplicates to obtain mean values and standard deviation errors. To avoid pre-heating adjacent samples by heat diffusion and/or diffraction of the beam, one empty well was located between sample rows. The

temperature probe was rinsed and cooled in Milli-Q water before collecting new data.

Each concentrated stock of nanomaterials was diluted in Milli-Q water to a final volume of 200 µL per well, giving a final concentration of 0, 5, 15, 30 and 60 µg of gold/mL of AuNRs or AuNR@CS. These heating curves were also used to calculate the heating potency and efficiency of both nanomaterials at the studied concentrations. For this purpose, a linear regression of the heating curves during the first 60 seconds of irradiation was calculated in order to obtain the temperature increase per second. The specific heat and density values of the suspensions were approximated to those of water and the heat needed to produce this temperature increase in each well was determined. The heating efficiency was calculated using these heat values and the laser power of 1100 mW.

5.6. AuNPs encapsulation in chitosan by Inkjet

5.6.1. Chitosan solution ejection

The inkjet based microsphere production setup employed relies on a piezoelectric printhead MJ-ABP-01-50 from Microfab Technologies, Inc. with a nozzle of 50 µm. The piezoelectric element of the microdispenser is addressed by using a multichannel JetDrive III device (CT-MC3-4) also from Microfab. Software associated (JetSerer™, Microfab) enables the selection of an electrical waveform (8 point bipolar trapezoidal waveforms) with well-defined waveform parameters (rise, fall and pulse width, times and voltages) and the pulse frequency. Pressure and vacuum to control the inkjet dispenser is provided by a CT-PT-4 (Microfab). The software and electronics also allow to control the strobe LED and the acquisition of the camera to observe the droplet formation process (see **Figure 70** for more details). All the solutions were filtered before been introduced in the inkjet ejecting system with filters 0.2 µm, except the chitosan solution that was filtered with a filter of 0.45 µm (Millex-HV REF SLHV033RS), before been ejected using the inkjet system.

5.6.2. Benchtop protocol used for gelling agent selection

A solution of 5 mg/mL of chitosan with 0.72 mg/mL of AuNPs was micropipetted droplet by droplet over vials containing 2 mL of different gelling agents at the tested concentration with increasing concentrations of ethanol. The spheres produced were photographed just after the gelification.

5.6.3. Microcapsule production

After a carefully optimisation of the system parameters, the most consistent ejection was obtained employing the following experimental conditions. 1 mL of chitosan of low molecular weight (50-190 KDa, Merck) at 10 mg/mL in acetic acid 1 % was mixed with 400 µL of acetic acid 10 % (aq.) and 600 µL of AuNS at 2.4 mg/mL. The solution was filtered prior to their addition to inkjet system. This solution was ejected employing monopolar electric pulse with a rise time of 3 µs, a dwell time of 15 µs and a fall time of 3 µs, a dwell voltage of 32 V and at a frequency of 3000 Hz. The microdroplets ejected with the inkjet over 20 mL of gelling agent solution composed by PTA at 10 mg/mL in 60 % (vol/vol) ethanol (aq.) in mild magnetic stirrer agitation. It was important to carefully wash the inkjet system after the ejection employing 3 volumes of acetic acid 1 % (aq.) in order to avoid future blocking problems due to chitosan residues. After that, the microcapsules were washed 3 times with 10 mL of Milli-Q water by 1 h of decantation in sterile conditions. The concentration of the microcapsules in dry weight was calculated by measuring the weight of 0.2 mL of sample after freeze-drying. The morphology and size of the microcapsules was measured from photographs taken from optical brightfield microscopy images. The gold content inside the hydrogel was quantified by ICP-AES.

5.6.4. Co-encapsulation of Alexa Fluor 647 Alkyne

The fluorophore Alexa Fluor 647 Alkyne (Invitrogen) was encapsulated in the inkjet microcapsules using the following methodology. The microcapsules were

produced as previously described and Alexa 647 at a final concentration of 10 µg/mL was added to the ejection solution for incorporation into the microcapsules. The microcapsules were characterised by confocal microscopy imaging employing a Zeiss LSM 880 confocal microscope with an objective 63X, zoom 1.0 and laser source of 633 nm. The 3D reconstruction was performed using the software Zen Blue 2.3 Lite.

5.6.5. AuNPs release from chitosan microcapsules

To study the release of the AuNPs, the microcapsules were incubated with different media. For the pH resistance assay the microcapsules were incubated with sodium phosphate 10 mM at different pHs (2-12). For the oral delivery simulation, simulated gastric medium was employed (NaCl at 34.2 mM at a pH of 1.76).[269] The microcapsules were diluted in the different media until 200 µg/mL in a total volume of 500 µl and were incubated at 37 ℃ with agitation for 1, 4 and 24 h. After that the microcapsules were centrifuged at 3000 rpm for 5 min in a centrifuge MiniSpin plus and 300 µL were collected for their analysis by UV-Vis spectroscopy and ICP-AES. Experiments were performed in triplicate.

5.6.6. Sterility testing

The sterility tests were performed according to the supplier instructions, analysing the presence of several microorganisms. The presence of coliform organisms was tested using the Coli-Count™ Sampler, the presence of aerobic bacteria using HPC Total Count Sampler and the presence of yeast or moulds employing the Yeast and Mould Sampler. In detail, the Sampler case was filled with 18 mL of sterile water and 100 µL of sample were added, the Sampler was inserted into the case and maintained in contact with the sample for 30 seconds. After that, the liquid was discarded, the Sampler was reinserted and it was incubated for 48 h at 32 °C for Yeast and Mould, 48 h at 35 °C HPC Total Count and 24 h at 35 °C for Coli-Count™ Sampler.

5.7. SPRi detection of miRNA using AuNPs as signal enhancers

5.7.1. DNA thiols reduction

Diethyl pyrocarbonate-treated Rnase- and Dnase-free water was used to prepare the thiol-modified DNA and RNA solutions. The oligonucleotide sequences (Eurofins Genomics) were purified by means of high-performance liquid chromatography (HPLC) by the manufacturer. Lyophilised thiols were resuspended with 400 µL of tris(2-carboxyethyl) phosphine (TCEP) 50 mM and the solution was agitated for 60 min at RT. 100 µL of sodium acetate 3 M was added to the thiols solution. 1.2 mL of ethanol 100 % was added and the solution was stored at -20°C for 45 min. After this step, the solution was centrifuged for 10 min at 15,000 g and the supernatant discarded. Finally, the pellet was dried for 30-45 min under air flow. The correct volume of ultrapure-water was added to the pellet in order to obtain a final concentration of the SH-DNA of 100 µM.

Oligo-DNA and microRNA sequences are reported in **Table 6**. The $PolyT_9$ was use in order to stabilize the self-assembled monolayer (SAM) of DNA sequences and to increase the accessibility of the DNA probe sequence to the miRNA target.

Table 6. Oligonucleotide sequences. DNAc is the DNA complementary probe. Underlined and bolded letters are mutated oligonucleotides. "SH" is the thiol group; "C_6" means -$(CH_2)_6$ -.[77]

Name	SEQUENCE (5' --> 3')
miR-422 RNA	ACUGGACUUAGGGUCAGAAGGC
miR-422 DNAc 5-S	SH-C_6-TTTTTTTTTGCCTTCTGACCCTAAGTCCAGT
miR-223 RNA	UGUCAGUUUGUCAAAUACCCCA
miR-223 DNAc 5-S	SH-C_6-TTTTTTTTTTGGGGTATTTGACAAACTGACA
miR-23a RNA	AUCACAUUGCCAGGGAUUUCC
miR-23a RNA 1-mut (Single base mis-match)	AUCACAUUGCC**U**GGGAUUUCC
miR-23a RNA 3-mut (Three base mis-match)	AUC**U**CAUUGCC**U**GGGAU**C**UCC
miR-23a DNAc 5-S	SH-C_6-TTTTTTTTTGGAAATCCCTGGCAATGTGAT
miR-126-3p RNA	UCGUACCGUGAGUAAUAAUGCG
miR-126-3p DNAc 5-S	SH-C_6-TTTTTTTTTCGCATTATTACTCACGGTACGA
miR-159 (Arab. Thal.) DNAc 5-S	SH-C_6- TTTTTTTTTTAGAGCTCCCTTCAATCCAAA
PolyA (25 bp) DNAc 5-S	SH-C_6-AAAAAAAAAAAAAAAAAAAAAAAAA

5.7.2. SPRi chip preparation

Bare gold SPRi biochips (HORIBA Scientific SAS, Palaiseau, France) were cleaned with Piranha solution (3:1 sulfuric acid, 96 % : hydrogen peroxide, 33 %) for 20 min at room temperature and washed with ultra-pure water before use. The spotting procedure was performed using a SPRi-Arrayer (SPRi-Arrayer, HORIBA Scientific SAS, Palaiseau, France) composed by Xtend metal-ceramic capillary pin of 700 µm of diameter that pick up the oligo-DNA and immobilise it through a

contact printing to the gold surface of the chip with high precision. Thiol modified oligo DNA at the concentration of 100 µM were diluted in PBS-Tween 0.075 % in order to obtain a final concentration of 33 µM for the DNA and 0.05 % for the surfactant. In details, 4 µL of DNA were diluted in PBS-Tween 0.075 % in a total volume of 12 µL. Each miRNA family was represented by three positive spots alternatively spotted with three negative control spots, represented by Poly A sequences. This spotting scheme guaranteed a controlled system to minimise the differences due to the different positions of the molecules on the chip surface. The binding between DNA-oligo probes and the chip was guaranteed by the covalent binding between the thiol group of oligo and gold, without any modification of the chip surface. Other specific settings of the spotting were: RT and relative humidity of 70 %, washing of the pin with ethanol 10 % and drying by air four times between the different samples to be immobilized on the gold surface. Once finished the spotting procedure, the SPRi biochips were incubated overnight at RT with a relative humidity of 75 % controlled using a saturated salt solution of sodium chloride. After this incubation, the SPRi biochips were blocked with a solution of PolyA DNA 5-S (10 µM) in water for 3-4 h at room temperature. Finally, biochips were washed in ultrapure water, dried and immediately used or stored in fridge at 4 °C.

5.7.3. SPRi detection

The SPRi experiments were carried out using XelPleX (HORIBA Scientific SAS, Palaiseau), a fully automated high-throughput SPR-imaging system equipped with a LED light source with wavelength 810 nm and with a CCD camera (IEEE 1394, 16 bit, 752x582 pixels) thus obtaining a final optical lateral resolution of 40 µm. Each experiment was preceded by the SPRi conditioning that consist in the flow of the running buffer (PBS and Tween 0.01 %) for 20 min. All the spots on the biochip were manually selected and the system calculated a plasmonic curve for each spot. Before the SPRi experiment, an incidence angle or multiple incidence angles (about 3-4 angles) were selected and positioned to the

maximum slope of the plasmonic curves in order to guarantee the maximum changes of reflectivity related to plasmonic angle changes. The calibration of the instrument was performed to normalise the CCD response for each spot during the experiment by injecting 200 µL of sucrose 3 mg ml^{-1}. The SPR response used here was expresses as "ReS" (used as default unit by the standard software) that, in our experimental setting, corresponds to a mass shift of around 90 pg/mm^2. miRNAs (500 µL), Ab (800 µL) and Ab+nanoparticles (800 µL) were injected at a flow rate of 10 µL/min to ensure the best interaction between the analytes and the probes. The regeneration solution, NaOH 50 mM (100 µL), was injected once or twice at flow rate of 100 µL/min; the optimisation of this conditions had been performed in a previous study by our collaborators.[77] The concentration of miRNAs varied as specified for each experiment. The concentration of Ab, when injected alone, was 5 nM; the concentration of all nanoparticles was always (12.42 µg/mL). This concentration corresponds to OD 0.15 and 0.137 for nanospheres of 14 nm and 37 nm (measured at 450 nm), respectively, and OD 0.68 of the nanoprisms (measured at 1000 nm). All SPR signals reported in the study are corrected by subtracting the SPR signal associated to PolyA spots used as reference spots associated to each miRNA family. miR-159 (from *Arab. Thal.)* was used as negative control miRNA family because not present in humans and never injected here.

5.7.4. SEM quantification of AuNPs

For the SEM counting of AuNP on the surface of SPRi chip, 50 nM of the corresponding miRNA were detected as previously described with each of the nanoparticles without the subsequent regeneration steps. After that, SPR chips were visualised by SEM and at least 5 images (one from each part of the sport: centre, top, button left and right) were acquired from each of the three spots corresponding to each miRNA sequence. The density of nanoparticles on the surface of the chip was calculated from these images using the software ImageJ.

5.7.5. Limit of detection

The limit of detection (LOD) was calculated measuring the SPR response of each nanoparticle after the injection of different concentrations of miRNA (90, 30, 10, 3.33, 1.1 and 0.37 pM). For each miRNA, the LOD signal was calculated as the average of three SPRi-enhanced signals obtained after the injection of running buffer summed to three times the corresponding standard deviation (i.e. average of background signal + 3 SD). This value (Y) was inserted in the fitting equation of the calibration curves getting the related value (X) that correspond to the minimum concentration of analyte detectable by the instrument with statistical significance. The miRNA concentration corresponding to each LOD signal was calculated using the fitting equations reported in **Figure 38**.

5.7.6. Test from real human samples

The tests on complex samples were performed using blood from three healthy control subject enrolled at IRCCS Fondazione Don Carlo Gnocchi. The subjects included in this study gave written informed consent in accordance with the protocols approved by the ethics committee of the same institution and according to the principles of the Declaration of Helsinki. Peripheral blood was collected in BD Vacutainer® SST™ II Advance Tubes (Becton Dickinson, Franklin Lakes, NJ, USA). At the end of clotting time (60 min), serum was obtained by centrifugation at 1800 g for 10 min at room temperature. The clear supernatant was aliquoted into RNase/DNase-free tubes and stored at −80 °C until use. Serum was then thawed on ice, centrifuged at 16,000 g for 5 min at 4 °C and then total RNA was extracted from 200 µL of serum using spin column chromatography (miRNeasy Serum/Plasma, Qiagen GmbH, Hilden, Germany) according to protocol suggested by manufacturer. RNA was eluted by adding 15 µL of RNase-free water for each column. A total of 60 µL of RNA obtained from 800 µL of serum was then resuspended in 550 µL and analysed by SPRi.

For the RT-PCR analysis part of the RNA sample used for the SPRi quantification was used also for the RT-PCR quantification following the protocol previously described.[196] In brief, the purified RNA sample was firstly used for retro-transcription using the cDNA universal synthesis kit (miRCURY LNA™ Universal cDNA synthesis kit, Exiqon Inc., Vedbaek, Denmark). RT-PCR amplification was performed using a specific LNA™-individual microRNAs assay (Exiqon Inc.) to detect the four miRNA target according to the manufacturer's instructions. The quantification was done using Step One system (Applied Biosystem, Foster City, CA) in 10 µl of reaction mix containing SYBR GREEN master mix (Exiqon Inc.), specific primer set and 4 µl of cDNA. Manual baseline and threshold were set manually on the instrument for the evaluation of row Cq value for each miRNA.

5.8. Cell culture

5.8.1. Cell lines

All photothermal studies were performed using Vero cell line (kidney epithelial cells from African green monkey), acquired from the American Type Culture Collection (ATCC: CCL-81). The inkjet microcapsules viability study was performed using HeLa cell line, acquired from Amsbio (Ref. SC034-Puro).

5.8.2. Cell culture conditions

Cells were cultured at 37 ºC in a 5 % CO_2 atmosphere in Dulbecco's modified Eagle's medium (DMEM, purchased from Lonza®) supplemented with 10 % foetal bovine serum (FBS), 2 mM glutamine and 100 U/mL penicillin/streptomycin. Phosphate buffered saline (PBS) and Dulbecco's Phosphate Buffered Saline (DPBS) supplemented with Ca^{2+} and Mg^{2+} were purchased from Lonza® (Basel, Switzerland).

5.8.3. Viability assays

5.8.3.1. MTT assay

After cell incubation with the nanomaterials, washing and convenient experimental protocol (i.e. laser irradiation for PTT), cell medium was removed and cells were incubated with 200 µL of DMEM containing 10 µL of 5 mg/mL 3-(4,5-dimethylthiazol-2-yl)-2,5-diphenyltetrazolium bromide (MTT, purchased from Invitrogen™) in the dark, under culture conditions, for 90-105 min. Finally, the plate was centrifuged at 1250 g for 30 min using an Eppendorf centrifuge 5810R with an A-4-62 rotor, the supernatant was removed and the formazan crystals were solubilised with 100 µL of dimethyl sulfoxide (DMSO). After mixing, the optical density at 555 nm was recorded using a Multiskan GO UV/Vis microplate spectrophotometer from Thermo Scientific. Experiments were performed in quintuplet to determine the standard deviations. Experiments were reproduced in triplicate to verify the reproducibility of the results. The cell viability percentage of each sample was calculated using the following formula, with 100 µl of DMSO as blank:

$$\%\ of\ viable\ cells\ = \frac{OD\ of\ treated\ sample - OD\ of\ blank}{OD\ of\ control\ cells\ without\ NPs - OD\ of\ blank} \times 100$$

For the inkjet microcapsules viability study, 2.5×10^3 HeLa cells per well were seeded in a 96-multiwell plate and the day after they were incubated with each of the concentrations of the biomaterials for 24 h. At this point, cells were washed 2 times with 200 µL of DPBS and the rest of MTT protocol was performed as previously described. Samples were compared with blanks of cells incubated with the microcapsules but without addition of MTT.

5.8.3.2. Live/dead cell viability assays

LIVE/DEAD™ Viability/Cytotoxicity Kit tests (Invitrogen™) were performed according to the instructions of the supplier. Briefly, DMEM of irradiated samples and their respective controls was removed after 5 h under standard culture conditions. Thereafter, cells were incubated for 30 min at room temperature (protected from light) with 100 µL of DPBS containing calcein (2000 times diluted from the stock solution) and Ethidium Bromide homodimer (500 times diluted from stock solution). Finally, bright field and fluorescent images of the cells were acquired using a Nikon Eclipse Ti microscope with PFS system equipped with a phase contrast system and 472±30/520±35 nm (GFP) and 531±46/593±40 nm (TRITC) cube filter connected to NIS-Elements Microscope Imaging Software. Images of all studied conditions were acquired employing identical optical parameters in the microscopy in order to be comparable.

5.8.4. Internalisation of AuNPs

5.8.4.1. Quantification of gold using ICP-AES/ICP-MS

$5x10^4$ Vero cells were seeded in a 24-multiwell plate and grown overnight under standard cell culture conditions (37 ºC, 5 % CO_2). Afterwards, the medium was removed and 500 µL nanoparticles in DMEM at selected concentrations were added: AuNRs 100 µg/mL and AuNPrs at 100 µg/mL (see **results and discussion section**). The cells were left for 24 h incubating with nanoparticles to allow their internalisation. In the case of the control cell samples (cells without nanoparticles for cell counting and for blank subtraction) the medium was replaced with fresh one. Following, cells were washed thoroughly 2 times with 500 µL of PBS and trypsinised with 100 µL of trypsin at 37 ºC for 5 min. Afterwards cells were collected with 400 µL of DMEM and transferred to Eppendorf vials for acid digestion. Replicate cells were counted using Trypan Blue. To digest the samples, cell pellets (of blank cells and cells incubated previously with each nanomaterial) and by separate the corresponding quantities of nanomaterials that

had been incubated with the cells were treated with 100 µL of Piranha solution (3:1 sulfuric acid, 96 % : hydrogen peroxide, 33 %) for 15 min at room temperature followed by 300 µL *aqua regia* (1 : 3 nitric, 65 % : hydrochloric acid, 37 %) for 2 h at room temperature. Subsequently the samples were incubated at 60 ºC for 15 min and diluted with Milli-Q water to 20 mL. All samples were performed in duplicate and evaluated by ICP-AES and/or ICP-MS.

5.8.4.2. Dark-field microscopy

Fixed cells are required for dark-field microscopy imaging, therefore $5x10^4$ Vero cells/well were seeded on a glass coverslide placed in a 24-multiwell plate and grown overnight under standard cell culture conditions (37 ºC, 5 % CO_2). The following day, nanoparticles in DMEM at the optimised concentrations (100 µg/mL) were added to each well and incubated for 24 h (final volume of H_2O <10 %). Cells were washed four times with DPBS, fixed in 4 % paraformaldehyde for 20 min at 4 ºC, washed twice with DPBS and incubated for 10 min with DAPI for nuclei labelling. The coverslips were mounted on glass microscope slides using 6 µL of Prolong® Diamond Antifade Mountant from Life Technologies®.

5.8.4.3. Intracellular localisation of AuNPs by TEM

To determine the intracellular localisation of the AuNPs, cells were analysed via TEM. $2x10^4$ Vero cells were seeded in an 8-well chamberslide (permanox, Nunc) and incubated 24 h under standard cell culture conditions. Thereafter, cells were incubated for 24 h with the optimised concentration of AuNRs and AuNPrs (100 µg/mL). Then, cells were washed with PBS to remove free nanoparticles and fixed with 2.5 % glutaraldehyde in 0.1 M phosphate buffer (PB) for 1 h at 4 ºC. Afterwards, the cells were washed four times with 0.1 M PB to remove glutaraldehyde. Samples were then post-fixed with 2 % osmium tetroxide, rinsed, dehydrated and embebed in Durcupan resin (Fluka, Sigma-Aldrich, St. Louis, USA). 1.5 µm semi-thin sections were cut with an Ultracut UC-6 (Leica, Heidelberg, Germany) and stained with 1 % toluidine blue. Finally, ultra-thin

sections (0.08 μm) were cut with the microtome, stained with lead citrate (Reynolds solution) and examined by TEM operating at 80 KeV.

5.8.5. Photothermal studies in cells

5.8.5.1. Thermoablation conditions

Vero cells were seeded at a density of $5x10^3$ cells per well in a 96-multiwell plate and incubated under cell culture standard conditions. After 24 h the medium was replaced for fresh DMEM with the desired concentrations of each nanomaterial (ranging from 0 to 100 μg of gold/mL with a final water concentration of 10 %) and incubated for another 24 h under culture standard conditions. Thereafter, the cells were washed twice with DPBS to remove any excess of remaining particles or dead cells and fresh phenol red-free DMEM was added. Samples were performed in triplicate and irradiated for 10 min with temperature control set at 37 ºC. Non-irradiated samples of cells with and without nanomaterials and irradiated cells (without nanomaterials) were used as controls. 5 h after irradiation, cells were analysed by microscopy imaging, MTT assay or Live/Dead assay.

5.8.5.2. Heating characterisation in cells

Vero cells were seeded at a density of $5x10^3$ cells per well in a 96-multiwell plate and incubated under cell culture standard conditions. After 24 h the medium was replaced for fresh DMEM with the desired concentrations of each nanoparticle (see **results and discussion section**) and incubated for another 24 h under the same conditions. Thereafter, the medium was removed, the cells were washed twice with DPBS to remove any excess of non-internalised particles or dead cells and a fresh phenol red-free DMEM was added. Plates were irradiated for 10 min with temperature control set up to 37 ºC. Samples were performed in triplicate. Non-irradiated samples of cells with and without NPs, together with irradiated cells (without NPs) were used as controls. The heat produced by the NPs was registered during 10 min laser NIR-irradiation and monitored by a software

developed by The University of Zaragoza using a Fiber Optic Temperature Sensor TPT-62 (Fiso Technologies Inc.).

5.9. Oral administration in mice

Pathogen-free female 7-week C57BL/6 mice were acquired from The Jackson Laboratory and were maintained in the CIBA installations (IACS-Universidad de Zaragoza). Animals were maintained according to the institutional animal use and care regulation of the Centro de Investigaciones Biomedicas de Aragón (CIBA, Zaragoza, Spain). All animal experiments were conducted according to the law RD53/2013 and approved by the Ethics Committee for animal experiments from the University of Zaragoza that is an accredited animal welfare body. Animals were separated depending on the sample administered in order to avoid contamination of the results due to coprophagy.

100 µL of microcapsules at 10 mg/mL or the equivalent concentration of AuNPs in Au content were administered using a gastric cannula. After 4 h, the mice were sacrificed in a CO_2 chamber, images of the biodistribution of the fluorescent microcapsules were acquired employing a IVIS Lumina II employing a Cy5.5 filter set with excitation passband of 615-665 nm and emission passband of 695-770 nm and the different organs were extracted, weighted and frozen at -80 ºC. The organs were freeze-dried, calcined at 600 ºC during 45 minutes. The calcined organs were digested with 200 µL of Piranha solution (3:1 sulfuric acid, 96 % : hydrogen peroxide, 33 %) and 200 µL of *aqua regia* (1:3 nitric, 65 % : hydrochloric acid, 37 %) during 1 h at 70 ºC. Samples were diluted with Milli-Q water to 20 mL the gold content was quantified by ICP-MS.

6. Bibliography

1 J. Corbett, P. A. McKeown, G. N. Peggs and R. Whatmore, *CIRP Ann.*, 2000, **49**, 523–545.

2 A. L. Porter and F. A. Rossini, *Sci. Public Policy*, 1990, **17**, 229–234.

3 R. Zajtchuk, *Disease-a-Month*, 1999, **45**, 453–495.

4 T. Rycroft, S. Larkin, A. Ganin, T. Thomas, J. Matheson, T. Van Grack, X. Chen, K. Plourde, A. Kennedy and I. Linkov, *Environ. Sci. Nano*, 2019, **6**, 356–365.

5 E. Inshakova and O. Inshakov, *MATEC Web Conf.*, 2017, **129**, 1–5.

6 M. A. El-Sayed, *Acc. Chem. Res.*, 2001, **34**, 257–64.

7 G. M. Whitesides, *Nat. Biotechnol.*, 2003, **21**, 1161–1165.

8 C. Buzea, I. I. Pacheco and K. Robbie, *Biointerphases*, 2007, **2**, MR17-71.

9 J. M. Laval, J. Chopineau and D. Thomas, *Trends Biotechnol.*, 1995, **13**, 474–481.

10 J. P. Martins, J. Neves, M. De Fuente, C. Celia, H. Florindo, N. Günday-türeli, A. Popat, J. L. Santos, F. Sousa, R. Schmid and J. Wolfram, *Drug Deliv. Transl. Res.*, 2020, **10**, 726–729.

11 A. P. Ramos, M. A. E. Cruz, C. B. Tovani and P. Ciancaglini, *Biophys. Rev.*, 2017, **9**, 79–89.

12 K. McNamara and S. A. M. Tofail, *Adv. Phys. X*, 2017, **2**, 54–88.

13 E. Calzoni, A. Cesaretti, A. Polchi, A. Di Michele, B. Tancini and C. Emiliani, *J. Funct. Biomater.*, 2019, **10**, 4.

14 Y. H. Choi and H. K. Han, *J. Pharm. Investig.*, 2018, **48**, 43–60.

15 D. Bobo, K. J. Robinson, J. Islam, K. J. Thurecht and S. R. Corrie, *Pharm. Res.*, 2016, **33**, 2373–2387.

16 R. M. Fratila, S. G. Mitchell, P. Del Pino, V. Grazu and J. M. De La Fuente, *Langmuir*, 2014, **30**, 15057–15071.

17 R. A. Sperling and W. J. Parak, *Philos. Trans. R. Soc. A Math. Phys. Eng. Sci.*, 2010, **368**, 1333–1383.

18 R. Mout, D. F. Moyano, S. Rana and V. M. Rotello, *Chem. Soc. Rev.*, 2012, **41**, 2539–2544.

19 T. Nagamune, *Nano Converg.*, 2017, **4**, 9.

20 Á. Artiga, I. Serrano-Sevilla, L. De Matteis, S. G. Mitchell and J. M. De La Fuente, *J. Mater. Chem. B*, 2019, **7**, 876–896.

21 M. Faraday, *Philos. Trans. R. Soc. London*, 1857, **147**, 145–181.

22 Y. Y. Yu, S. S. Chang, C. L. Lee and C. R. C. Wang, *J. Phys. Chem. B*, 1997, **101**, 6661–6664.

23 R. D. Averitt, D. Sarkar and N. J. Halas, *Phys. Rev. Lett.*, 1997, **78**, 4217–4220.

24 D. Ibano, Y. Yokota and T. Tominaga, *Chem. Lett.*, 2003, **32**, 574–575.

25 J. Chen, F. Saeki, B. J. Wiley, H. Cang, M. J. Cobb, Z. Y. Li, L. Au, H. Zhang, M. B. Kimmey, X. Li and Y. Xia, *Nano Lett.*, 2005, **5**, 473–477.

26 C. L. Nehl, H. Liao and J. H. Hafner, *Plasmon. Met. Nanostructures their Opt. Prop. IV*, 2006, **6323**, 63230G.

27 L. Vigderman and E. R. Zubarev, *Chem. Mater.*, 2013, **25**, 1450–1457.

28 B. Pelaz, V. Grazu, A. Ibarra, C. Magen, P. del Pino and J. M. de la Fuente, *Langmuir*, 2012, **28**, 8965–70.

29 J. Piella, N. G. Bastús and V. Puntes, *Chem. Mater.*, 2016, **28**, 1066–1075.

30 E. C. Dreaden, A. M. Alkilany, X. Huang, C. J. Murphy and M. a El-Sayed, *Chem. Soc. Rev.*, 2012, **41**, 2740–79.

31 A. M. Ealias and M. P. Saravanakumar, *IOP Conf. Ser. Mater. Sci. Eng.*, 2017, **263**, 032019.

32 C. K. Chu, Y. C. Tu, Y. W. Chang, C. K. Chu, S. Y. Chen, T. T. Chi, Y. W. Kiang and C. C. Yang, *Nanotechnology*, 2015, **26**, 075102.

33 K. Bi, Y. Chen, Q. Wan, T. Ye, Q. Xiang, M. Zheng, X. Wang, Q. Liu, G. Zhang, Y. Li, Y. Liu and H. Duan, *Nanoscale*, 2019, **11**, 1245–1252.

34 J. Simon, V. P. N. Nampoori and M. Kailasnath, *Optik (Stuttg).*, 2019, **195**, 163168.

35 Y. Yuan, Y. Wang, H. Wang and S. Hou, *J. Electroanal. Chem.*, 2019, **855**, 113495.

36 X. Wang, W. Zhang, X. Gong, X. Hu and X. Yao, *J. Nanoparticle Res.*, 2019, **21**, 192.

37 P. Majerič, D. Feizpour, B. Friedrich, Ž. Jelen, I. Anžel and R. Rudolf, *Materials (Basel).*, 2019, **12**, 10–12.

38 N. Lasemi, C. Rentenberger, R. Pospichal, A. S. Cherevan, M. Pfaffeneder-Kmen, G. Liedl and D. Eder, *Appl. Phys. A*, 2019, **125**, 1–12.

39 M. Abbas, Y. Xue, J. Zhang and J. Chen, *Fuel Process. Technol.*, 2019, **187**, 63–72.

40 X. Li, L. Liu, Z. Xu, W. Wang, J. Shi, L. Liu, M. Jing, F. Li and X. Zhang, *Sensors Actuators, B Chem.*, 2019, **287**, 267–277.

41 M. C. Molina Higgins and J. V. Rojas, *Appl. Surf. Sci.*, 2019, **480**, 1147–1155.

42 G. A. Filip, B. Moldovan, I. Baldea, D. Olteanu, R. Suharoschi, N. Decea, C. M. Cismaru, E. Gal, M. Cenariu, S. Clichici and L. David, *J. Photochem. Photobiol. B Biol.*, 2019, **191**, 26–37.

43 K. Sen, K. Kowlgi, G. Koper and H. T. Wolterbeek, *Int. J. Nanotechnol. Appl.*, 2011, **5**, 173–180.

44 G. González-Rubio, P. Díaz-Núñez, A. Rivera, A. Prada, G. Tardajos, J. González-Izquierdo, L. Bañares, P. Llombart, L. G. Macdowell, M. A. Palafox, L. M. Liz-Marzán, O. Peña-Rodríguez and A. Guerrero-Martínez, *Science (80-.).*, 2017, **358**, 640–644.

45 R. Herizchi, E. Abbasi, M. Milani and A. Akbarzadeh, *Artif. Cells, Nanomedicine Biotechnol.*, 2016, **44**, 596–602.

46 A. E. Adebayo, A. M. Oke, A. Lateef, A. A. Oyatokun, O. D. Abisoye, I. P. Adiji, D. O. Fagbenro, T. V. Amusan, J. A. Badmus,

T. B. Asafa, L. S. Beukes, E. B. Gueguim-Kana and S. H. Abbas, *Nanotechnol. Environ. Eng.*, 2019, **4**, 1–15.

47 G. Frens, *Nat. Phys. Sci.*, 1973, **241**, 20.

48 M. Brust, M. Walker, D. Bethell, D. J. Schiffrin and R. Whyman, *J. Chem. Soc., Chem. Commun.*, 1994, **1**, 801–802.

49 J. Xiao and L. Qi, *Nanoscale*, 2011, **3**, 1383–1396.

50 W. Niu, Y. Duan, Z. Qing, H. Huang and X. Lu, *J. Am. Chem. Soc.*, 2017, **139**, 5817–5826.

51 J. Neng, C. Xiang, K. Jia, X. Nie and P. Sun, *Appl. Sci.*, 2019, **9**, 935.

52 M. Grzelczak, J. Pérez-Juste, P. Mulvaney and L. M. Liz-Marzán, *Chem. Soc. Rev.*, 2008, **37**, 1783–1791.

53 Z. Li, C. Kübel, V. I. Pârvulescu and R. Richards, *ACS Nano*, 2008, **2**, 1205–1212.

54 D. Wan, X. Xia, Y. Wang and Y. Xia, *Small*, 2013, **9**, 3111–3117.

55 A. Shakiba, S. Shah, A. C. Jamison, I. Rusakova, T. C. Lee and T. R. Lee, *ACS Omega*, 2016, **1**, 456–463.

56 T. Huang, F. Meng and L. Qi, *Langmuir*, 2010, **26**, 7582–7589.

57 M. A. Wall, S. Harmsen, S. Pal, L. Zhang, G. Arianna, J. R. Lombardi, C. M. Drain and M. F. Kircher, *Adv. Mater.*, 2017, **29**, 1605622.

58 B. P. Khanal and E. R. Zubarev, *Chem. - A Eur. J.*, 2019, **25**, 1595–1600.

59 B. D. Chithrani, A. A. Ghazani and W. C. W. Chan, *Nano Lett.*, 2006, **6**, 662–668.

60 Y. Wang, K. C. L. Black, H. Luehmann, W. Li, Y. Zhang, X. Cai, D. Wan, S.-Y. Liu, M. Li, P. Kim, Z.-Y. Li, L. V. Wang, Y. Liu and Y. Xia, *ACS Nano*, 2013, **7**, 2068–2077.

61 G. Alfranca, Á. Artiga, G. Stepien, M. Moros, S. G. Mitchell and J. M. de la Fuente, *Nanomedicine (Lond.)*, 2016, **11**, 2903–2916.

62 G. Alfranca, L. Beola, Y. Liu, L. Gutiérrez, A. Zhang, A. Artiga, D.

Cui and J. M. de la Fuente, *Nanomedicine*, 2019, **14**, 3035–3055.

63 P. B. Tchounwou, C. G. Yedjou, A. K. Patlolla and D. J. Sutton, *Mol. Clin. Environ. Toxicol.*, 2012, **101**, 133–164.

64 R. Gupta and H. Xia, *J Env. Pathol Toxicol Oncol*, 2018, **37**, 209–230.

65 S. Kittler, C. Greulich, J. Diendorf, M. Koller and M. Epple, *Chem. Mater.*, 2010, **22**, 4548–4554.

66 A. Sukhanova, S. Bozrova, P. Sokolov, M. Berestovoy, A. Karaulov and I. Nabiev, *Nanoscale Res. Lett.*, 2018, **13**, 44.

67 A. L. Bailly, F. Correard, A. Popov, G. Tselikov, F. Chaspoul, R. Appay, A. Al-Kattan, A. V. Kabashin, D. Braguer and M. A. Esteve, *Sci. Rep.*, 2019, **9**, 1–12.

68 P. Zhao, N. Li and D. Astruc, *Coord. Chem. Rev.*, 2013, **257**, 638–665.

69 X. Huang and M. A. El-Sayed, *J. Adv. Res.*, 2010, **1**, 13–28.

70 B. Pelaz, G. Charron, C. Pfeiffer, Y. Zhao, J. M. de la Fuente, X.-J. Liang, W. J. Parak and P. Del Pino, *Small*, 2013, **9**, 1573–84.

71 J. Xavier, S. Vincent, F. Meder and F. Vollmer, *Nanophotonics*, 2018, **7**, 1–38.

72 M. E. Stewart, C. R. Anderton, L. B. Thompson, J. Maria, S. K. Gray, J. A. Rogers and R. G. Nuzzo, *Chem. Rev.*, 2008, **108**, 494–521.

73 W. Shi, J. Casas, M. Venkataramasubramani and L. Tang, *ISRN Nanomater.*, 2012, **2012**, 659043.

74 R. K. Kannadorai, G. G. Y. Chiew, K. Q. Luo and Q. Liu, *Cancer Lett.*, 2015, **357**, 152–159.

75 B. Pelaz, V. Grazu, A. Ibarra, C. Magen, P. del Pino and J. M. de la Fuente, *Langmuir*, 2012, **28**, 8965–70.

76 E. C. Dreaden, M. A. Mackey, X. Huang, B. Kang and M. A. El-Sayed, *Chem. Soc. Rev.*, 2011, **40**, 3391.

77 A. Sguassero, Á. Artiga, C. Morasso, R. R. Jimenez, R. M. Rapún, R. Mancuso, S. Agostini, A. Hernis, A. Abols, A. Lin, A. Gualerzi, S.

Picciolini, M. Bedoni, M. Rovaris, F. Gramatica, J. M. De Fuente and R. Vanna, *Anal. Bioanal. Chem.*, 2019, **411**, 1873–1885.

78 C. Bao, N. Beziere, P. Del Pino, B. Pelaz, G. Estrada, F. Tian, V. Ntziachristos, J. M. De La Fuente and D. Cui, *Small*, 2013, **9**, 68–74.

79 J. L. Campbell, E. D. SoRelle, O. Ilovich, O. Liba, M. L. James, Z. Qiu, V. Perez, C. T. Chan, A. de la Zerda and C. Zavaleta, *Biomaterials*, 2017, **135**, 42–52.

80 L. Han, J. Zhao, X. Zhang, W. Cao, X. Hu, G. Zou, X. Duan and X. J. Liang, *ACS Nano*, 2012, **6**, 7340–7351.

81 A. M. Paul, Y. Shi, D. Acharya, J. R. Douglas, A. Cooley, J. F. Anderson, F. Huang and F. Bai, *J. Gen. Virol.*, 2014, **95**, 1712–1722.

82 X. Zhao, Q. Huang and Y. Jin, *Mater. Sci. Eng. C*, 2015, **54**, 142–149.

83 W. Feng, H. Guo, T. Xue, X. Wang, C. Tang and B. Ying, *RSC Adv.*, 2016, **6**, 60171–60179.

84 P. S. Randeria, M. A. Seeger, X.-Q. Wang, H. Wilson, D. Shipp, C. A. Mirkin and A. S. Paller, *Proc. Natl. Acad. Sci.*, 2015, **112**, 5573–5578.

85 H. Nemati, M. H. Ghahramani, R. Faridi-Majidi, B. Izadi, G. Bahrami, S. H. Madani and G. Tavoosidana, *J. Control. Release*, 2017, **268**, 259–268.

86 M. Cordeiro, F. F. Carlos, P. Pedrosa, A. Lopez and P. V. Baptista, *Diagnostics*, 2016, **6**, 43.

87 K. Saha, S. S. Agasti, C. Kim, X. Li and V. M. Rotello, *Chem. Rev.*, 2012, **112**, 2739–2779.

88 Y. Xiao, F. Patolsky, E. Katz and J. F. Hainfeld, 2003, **299**, 1877–1881.

89 L. Wu, X. Lu, X. Fu, L. Wu and H. Liu, *Sci. Rep.*, 2017, **7**, 1–7.

90 J. Peng, Y. Feng, X. X. Han and Z. N. Gao, *Anal. Methods*, 2016, **8**, 2526–2532.

91 Y. Wang, L. Hu, L. Li and J.-J. Zhu, *J. Anal. Test.*, 2017, **1**, 1–19.

92 L.-Y. Chen, C.-W. Wang, Z. Yuan and H.-T. Chang, *Anal. Chem.*, 2015, **87**, 216–229.

93 J. H. Lee, H. Y. Cho, H. K. Choi, J. Y. Lee and J. W. Choi, *Int. J. Mol. Sci.*, 2018, **19**, 2021.

94 J. H. Lee, B. C. Kim, B. K. Oh and J. W. Choi, *Nanomedicine Nanotechnology, Biol. Med.*, 2013, **9**, 1018–1026.

95 D. Ghosh and N. Chattopadhyay, *J. Lumin.*, 2015, **160**, 223–232.

96 S. Tyagi and F. R. Kramer, *Nat. Publ. Gr.*, 1996, **14**, 303–308.

97 X. Liu, X. Xu, Y. Zhou, N. Zhang and W. Jiang, *ACS Appl. Mater. Interfaces*, 2019, **11**, 35548–35555.

98 Z. Qin, W. C. W. Chan, D. R. Boulware, T. Akkin, E. K. Butler and J. C. Bischof, *Angew. Chemie - Int. Ed.*, 2012, **51**, 4358–4361.

99 E. Polo, P. del Pino, B. Pelaz, V. Grazu and J. M. de la Fuente, *Chem. Commun.*, 2013, **49**, 3676.

100 S. Li, Y. Zhang, W. Wen, W. Sheng, J. Wang, S. Wang and J. Wang, *Biosens. Bioelectron.*, 2019, **133**, 223–229.

101 X. Ma, S. Song, S. Kim, M. sun Kwon, H. Lee, W. Park and S. J. Sim, *Nat. Commun.*, 2019, **10**, 1–13.

102 C. C. Chang, C. P. Chen, T. H. Wu, C. H. Yang, C. W. Lin and C. Y. Chen, *Nanomaterials*, 2019, **9**, 1–24.

103 S. S. Sinha, S. Jones, A. Pramanik and P. C. Ray, *Acc. Chem. Res.*, 2016, **49**, 2725–2735.

104 D. Wu, Y. Chen, S. Hou, W. Fang and H. Duan, *ChemBioChem*, 2019, **20**, 2432–2441.

105 S. Y. Ding, J. Yi, J. F. Li, B. Ren, D. Y. Wu, R. Panneerselvam and Z. Q. Tian, *Nat. Rev. Mater.*, 2016, **1**, 1–16.

106 S. Xu, S. Jiang, J. Wang, J. Wei, W. Yue and Y. Ma, *Sensors Actuators, B Chem.*, 2016, **222**, 1175–1183.

107 S. Picciolini, N. Castagnetti, R. Vanna, D. Mehn, M. Bedoni, F. Gramatica, M. Villani, D. Calestani, M. Pavesi, L. Lazzarini, A.

Zappettini and C. Morasso, *RSC Adv.*, 2015, **5**, 93644–93651.

108 P. Abdul Rasheed and N. Sandhyarani, *Anal. Chim. Acta*, 2016, **905**, 134–139.

109 B. Della Ventura, M. Iannaccone, R. Funari, M. P. Ciamarra, C. Altucci, R. Capparelli, S. Roperto and R. Velotta, *PLoS One*, 2017, **12**, 1–14.

110 J. Homola, *Chem. Rev.*, 2008, **108**, 462–493.

111 E. E. Bedford, J. Spadavecchia, C. Pradier and F. X. Gu, *Macromol. Biosci.*, 2012, **12**, 724–739.

112 T. Špringer, M. L. Ermini, B. Špačková, J. Jabloňků and J. Homola, *Anal. Chem.*, 2014, **86**, 10350–10356.

113 J. Zhou, Q. Qi, C. Wang, Y. Qian, G. Liu, Y. Wang and L. Fu, *Biosens. Bioelectron.*, 2019, **142**, 111449.

114 S. J. Berners-Price and A. Filipovska, *Metallomics*, 2011, **3**, 863–873.

115 H. Daraee, A. Eatemadi, E. Abbasi, S. F. Aval, A. Akbarzadeh, H. Daraee, A. Eatemadi, E. Abbasi, S. F. Aval and M. Kouhi, *Artif. Cells, Nanomedicine, Biotechnol.*, 2016, **44**, 410–422.

116 F.-Y. Kong, J.-W. Zhang, R.-F. Li, Z.-X. Wang, W.-J. Wang and W. Wang, *Molecules*, 2017, **22**, 1445.

117 R. L. Kanasty, K. A. Whitehead, A. J. Vegas and D. G. Anderson, *Mol. Ther.*, 2012, **20**, 513–524.

118 S. Medici, M. Peana, V. Marina, J. I. Lachowicz, G. Crisponi and M. Antonietta, *Coord. Chem. Rev.*, 2015, **284**, 329–350.

119 C. Roder and M. J. Thomson, *Drugs R. D.*, 2015, **15**, 13–20.

120 C. L. Brown, M. W. Whitehouse, E. R. T. Tiekink and G. R. Bushell, 2008, **16**, 133–137.

121 H. Lee, M. Lee, S. H. Bhang, B. Kim, Y. S. Kim, J. H. Ju, K. S. Kim and S. K. Hahn, *ACS Nano*, 2014, **8**, 4790–4798.

122 H. S. Shah, S. A. Joshi, A. Haider, U. Kortz, N. ur-Rehman and J. Iqbal, *RSC Adv.*, 2015, **5**, 93234–93242.

123 R. S. Darweesh, N. M. Ayoub and S. Nazzal, *Int. J. Nanomedicine*, 2019, **14**, 7643.

124 S. B. F. A. Bhat, P. R. Singh, P. Elumalai, S. Das, C. R. Patra and J. Arunakaran, *Cell Prolif.*, 2016, **49**, 678–697.

125 H. B. Song, J. Wi, D. H. Jo, J. H. Kim, S. Lee, T. G. Lee and J. H. Kim, *Nanomedicine Nanotechnology, Biol. Med.*, 2017, **13**, 1901–1911.

126 S. Vimalraj, T. Ashokkumar and S. Saravanan, *Biomed. Pharmacother.*, 2018, **105**, 440–448.

127 F. A. N. Pan, W. E. I. Li, W. Yang, X. Y. A. N. Yang, S. Liu, X. I. N. Li, X. Zhao, H. U. I. Ding, L. I. Qin and Y. Pan, *Oncol. Lett.*, 2018, **16**, 3083–3091.

128 M. Laprise-pelletier, T. Simão and M. Fortin, *Adv. Healthc. Mater.*, 2018, **7**, 1701460.

129 M. Natan and E. Banin, *FEMS Microbiol. Rev.*, 2017, **41**, 302–322.

130 P. Khandelwal, D. K. Singh and P. Poddar, *ChemistrySelect*, 2019, **4**, 6719–6738.

131 S. K. Boda, J. Broda, F. Schiefer, J. Weber-heynemann, M. Hoss, U. Simon, B. Basu and W. Jahnen-dechent, *Small*, 2015, **11**, 3183–3193.

132 M. Pérez-Hernández, P. Del Pino, S. G. Mitchell, M. Moros, G. Stepien, B. Pelaz, W. J. Parak, E. M. Gálvez, J. Pardo and J. M. De La Fuente, *ACS Nano*, 2015, **9**, 52–61.

133 E. Hemmer, A. Benayas, F. Legare and F. Vetrone, *Nanoscale Horizons*, 2016, **1**, 168.

134 A. N. Kharlamov, A. E. Tyurnina, V. S. Veselova, O. P. Kovtun, V. Y. Shur and J. L. Gabinsky, *Nanoscale*, 2015, **7**, 8003–8015.

135 A. R. Rastinehad, H. Anastos, E. Wajswol, J. S. Winoker, J. P. Sfakianos, S. K. Doppalapudi, M. R. Carrick, C. J. Knauer, B. Taouli, S. C. Lewis, A. K. Tewari, J. A. Schwartz, S. E. Canfield, A. K. George, J. L. West and N. J. Halas, *PNAS*, 2019, **116**, 18590–18596.

136 M. Faria, M. Björnmalm, K. J. Thurecht, S. J. Kent, R. G. Parton, M.

Kavallaris, A. P. R. Johnston, J. J. Gooding, S. R. Corrie, B. J. Boyd, P. Thordarson, A. K. Whittaker, M. M. Stevens, C. A. Prestidge, C. J. H. Porter, W. J. Parak, T. P. Davis, E. J. Crampin and F. Caruso, *Nat. Nanotechnol.*, 2018, **13**, 777–785.

137 A. L. Durán-Meza, D. S. Moreno-Gutiérrez, J. F. Ruiz-Robles, A. Bañuelos-Frías, X. F. Segovia-González, A. M. Longoria-Hernández, E. Gomez and J. Ruiz-García, *Nanoscale*, 2016, **8**, 11091–11098.

138 Q. Chen, H. Qi, L. Ruan and Y. Ren, *Nanomaterials*, 2017, **7**, 416.

139 P. Thoniyot, M. J. Tan, A. A. Karim, D. J. Young and X. J. Loh, *Adv. Sci.*, 2015, **2**, 1–13.

140 I. Serrano-Sevilla, Á. Artiga, S. G. Mitchell, L. De Matteis and J. M. de la Fuente, *Molecules*, 2019, **24**, 2570.

141 S. Rafieian, H. Mirzadeh, H. Mahdavi and M. E. Masoumi, *IEEE J. Sel. Top. Quantum Electron.*, 2019, **26**, 154–174.

142 I. Younes and M. Rinaudo, *Mar. Drugs*, 2015, **13**, 1133–1174.

143 Á. Artiga, S. García-Embid, L. De Matteis, S. G. Mitchell and J. M. de la Fuente, *Front. Chem.*, 2018, **6**, 234.

144 J. Wang, S. Banerji, N. Menegazzo, W. Peng, Q. Zou and K. S. Booksh, *Talanta*, 2011, **86**, 133–141.

145 E. Marsich, A. Travan, I. Donati, A. Di Luca, M. Benincasa, M. Crosera and S. Paoletti, *Colloids Surfaces B Biointerfaces*, 2011, **83**, 331–339.

146 R. Chen, X. Zheng, H. Qian, X. Wang, J. Wang and X. Jiang, *Biomater. Sci.*, 2013, **1**, 285–293.

147 N. Zhang, X. Xu, X. Zhang, D. Qu, L. Xue, R. Mo and C. Zhang, *Int. J. Pharm.*, 2016, **497**, 210–221.

148 J. Conde, N. Oliva, Y. Zhang and N. Artzi, *Nat. Mater.*, 2016, **15**, 1128–1138.

149 Q. Shi, H. Liu, D. Tang, Y. Li, X. Li and F. Xu, *NPG Asia Mater.*, 2019, **11**, 64.

150 L. E. Strong and J. L. West, *Wiley Interdiscip. Rev. Nanomedicine*

Nanobiotechnology, 2011, **3**, 307–317.

151 S. R. Sershen, S. L. Westcott, N. J. Halas and J. L. West, *J. Biomed. Mater. Res.*, 2000, **51**, 293–298.

152 S. R. Sershen, G. A. Mensing, M. Ng, N. J. Halas, D. J. Beebe and J. L. West, *Adv. Mater.*, 2005, **17**, 1366–1368.

153 C. Dannert, B. T. Stokke and R. S. Dias, *Polymers (Basel).*, 2019, **11**, 275.

154 S. Mitragotri, P. A. Burke and R. Langer, *Nat. Rev. Drug Discov.*, 2014, **13**, 655–672.

155 J. Reinholz, K. Landfester and V. Mailänder, *Drug Deliv.*, 2018, **25**, 1694–1705.

156 J. F. Hillyer and R. M. Albrecht, *J. Pharm. Sci.*, 2001, **90**, 1927–1936.

157 J. Cancino-Bernardi, V. S. Marangoni, J. C. F. Besson, M. E. C. Cancino, M. R. M. Natali and V. Zucolotto, *Chemosphere*, 2018, **213**, 41–52.

158 A. K. Patlolla, S. A. Kumari and P. B. Tchounwou, *Int. J. Nanomedicine*, 2019, **14**, 639–647.

159 O. V. Zlobina, S. S. Pakhomy, A. B. Bucharskaya, I. O. Bugaeva, G. N. Maslyakova, N. G. Khlebtsov, B. N. Khlebtsov and V. A. Bogatyrev, *Saratov Fall Meet. 2013 Opt. Technol. Biophys. Med. XV; Laser Phys. Photonics XV*, 2014, **9031**, 90310P.

160 A. B. Bucharskaya, G. N. Maslyakova, S. S. Pakhomy, O. V. Zlobina, I. O. Bugaeva, N. A. Navolokin, B. N. Khlebtsov, V. A. Bogatyrev, N. G. Khlebtsov and V. V. Tuchin, *J. Innov. Opt. Health Sci.*, 2016, **09**, 1642004.

161 G. Barhate, M. Gautam, S. Gairola, S. Jadhav and V. Pokharkar, *Int. J. Pharm.*, 2013, **441**, 636–642.

162 S. H. Kang, V. Revuri, S. J. Lee, S. Cho, I. K. Park, K. J. Cho, W. K. Bae and Y. K. Lee, *ACS Nano*, 2017, **11**, 10417–10429.

163 C. A. Smith, C. A. Simpson, G. Kim, C. J. Carter and D. L. Feldheim, *ACS Nano*, 2013, **7**, 3991–3996.

164 Y. Amamoto, H. Otsuka and A. Takahara, *Synthesis and Characterization of Polymeric Nanogels*, 2012, vol. 10.

165 J. Saroia, W. Yanen, Q. Wei, K. Zhang, T. Lu and B. Zhang, *Bio-Design Manuf.*, 2018, **1**, 265–279.

166 A. Vedadghavami, F. Minooei, M. H. Mohammadi, S. Khetani, A. Rezaei Kolahchi, S. Mashayekhan and A. Sanati-Nezhad, *Acta Biomater.*, 2017, **62**, 42–63.

167 M. N. Singh, K. S. Y. Hemant, M. Ram and H. G. Shivakumar, *Res. Pharm. Sci.*, 2010, **5**, 65–77.

168 A. C. Daly, L. Riley, T. Segura and J. A. Burdick, *Nat. Rev. Mater.*, 2020, **5**, 20–43.

169 T. Farjami and A. Madadlou, *Food Hydrocoll.*, 2017, **62**, 262–272.

170 Y. Wang, L. Guo, S. Dong, J. Cui and J. Hao, *Adv. Colloid Interface Sci.*, 2019, **266**, 1–20.

171 L. Y. Chu, A. S. Utada, R. K. Shah, J. W. Kim and D. A. Weitz, *Angew. Chemie - Int. Ed.*, 2007, **46**, 8970–8974.

172 L. Mazutis, R. Vasiliauskas and D. A. Weitz, *Macromol. Biosci.*, 2015, **15**, 1641–1646.

173 J. Park, A. Byun, D. H. Kim, S. S. Shin, J. H. Kim and J. W. Kim, *J. Colloid Interface Sci.*, 2014, **426**, 162–169.

174 Q. Gao, Y. He, J. zhong Fu, J. jiang Qiu and Y. an Jin, *J. Sol-Gel Sci. Technol.*, 2016, **77**, 610–619.

175 C. López-Iglesias, A. M. Casielles, A. Altay, R. Bettini, C. Alvarez-Lorenzo and C. A. García-González, *Chem. Eng. J.*, 2019, **357**, 559–566.

176 R. A. Fletcher, J. A. Brazin, M. E. Staymates, B. A. Benner and J. G. Gillen, *Talanta*, 2008, **76**, 949–955.

177 J. C. Stachowiak, D. L. Richmond, T. H. Li, F. Brochard-Wyart and D. A. Fletcher, *Lab Chip*, 2009, **9**, 2003–2009.

178 J. Alamán, R. Alicante, J. I. Peña and C. Sánchez-Somolinos, *Materials (Basel).*, 2016, **9**, 910.

179 A. Kappel and A. Keller, *Clin. Chem. Lab. Med.*, 2017, **55**, 636–

647.

180 S. Szunerits, J. Spadavecchia and R. Boukherroub, *Rev. Anal. Chem.*, 2014, **33**, 153–164.

181 S. Fang, H. J. Lee, A. W. Wark and R. M. Corn, *J. Am. Chem. Soc.*, 2006, **128**, 14044–14046.

182 M. M. Goldenberg, *Pharm. Ther.*, 2012, **37**, 175–84.

183 F. D. Lublin, S. C. Reingold, J. A. Cohen, G. R. Cutter, A. J. Thompson, J. S. Wolinsky, B. Banwell, F. Barkhof, B. Bebo, P. A. Calabresi, M. Clanet, R. J. Fox, M. S. Freedman, A. D. Goodman, J. A. Lincoln, C. Lubetzki, A. E. Miller, X. Montalban, P. W. O. Connor and M. P. Sormani, *Neurology*, 2014, **83**, 278–86.

184 M. Guerau-de-Arellano, H. Alder, H. G. Ozer, A. Lovett-Racke and M. K. Racke, *J. Neuroimmunol.*, 2012, **248**, 32–39.

185 A. Junker, R. Hohlfeld and E. Meinl, *Nat. Rev. Neurol.*, 2011, **7**, 56–59.

186 H. Šípová, S. Zhang, A. M. Dudley, D. Galas, K. Wang and J. Homola, *Anal. Chem.*, 2010, **82**, 10110–10115.

187 J. Conde, A. Ambrosone, V. Sanz, Y. Hernandez, V. Marchesano, F. Tian, H. Child, C. C. Berry, M. R. Ibarra, P. V Baptista, C. Tortiglione and J. M. de la Fuente, *ACS Nano*, 2012, **6**, 8316–8324.

188 S. Puertas, M. de Gracia Villa, E. Mendoza, C. Jiménez-Jorquera, J. M. de la Fuente, C. Fernández-Sánchez and V. Grazú, *Biosens. Bioelectron.*, 2013, **43**, 274–280.

189 F. Fernández, F. Sánchez-Baeza and M. P. Marco, *Biosens. Bioelectron.*, 2012, **34**, 151–158.

190 T. Špringer, X. Chadtová Song, M. L. Ermini, J. Lamačová and J. Homola, *Anal. Bioanal. Chem.*, 2017, **409**, 4087–4097.

191 A. Keller, P. Leidinger, J. Lange, A. Borries, H. Schroers, M. Scheffler, H. P. Lenhof, K. Ruprecht and E. Meese, *PLoS One*, 2009, **4**, e7440.

192 M. B. Cox, M. J. Cairns, K. S. Gandhi, A. P. Carroll, S. Moscovis, G. J. Stewart, S. Broadley, R. J. Scott, D. R. Booth and J. Lechner-Scott, *PLoS One*, 2010, **5**, e12132.

193 C. Fenoglio, E. Ridolfi, C. Cantoni, M. De Riz, R. Bonsi, M. Serpente, C. Villa, A. M. Pietroboni, R. T. Naismith, E. Alvarez, B. J. Parks, N. Bresolin, A. H. Cross, L. M. Piccio, D. Galimberti and E. Scarpini, *Mult. Scler. J.*, 2013, **19**, 1938–1942.

194 A. Junker, M. Krumbholz, S. Eisele, H. Mohan, F. Augstein, R. Bittner, H. Lassmann, H. Wekerle, R. Hohlfeld and E. Meinl, *Brain*, 2009, **132**, 3342–3352.

195 Z. Hu, A. Zhang, G. Storz, S. Gottesman and S. H. Leppla, *Nucleic Acids Res.*, 2006, **34**, 52.

196 R. Mancuso, A. Hernis, S. Agostini, M. Rovaris, D. Caputo and M. Clerici, *J. Transl. Med.*, 2015, **13**, 1–7.

197 A. Sguassero, Á. Artiga, C. Morasso, R. R. Jimenez, R. M. Rapún, R. Mancuso, S. Agostini, A. Hernis, A. Abols, A. Linē, A. Gualerzi, S. Picciolini, M. Bedoni, M. Rovaris, F. Gramatica, J. M. de la Fuente and R. Vanna, *Anal. Bioanal. Chem.*, 2019, **411**, 1873–1885.

198 J. S. Mitchell, Y. Wu, C. J. Cook and L. Main, *Anal. Biochem.*, 2005, **343**, 125–135.

199 Y. Uludag and I. E. Tothill, *Anal. Chem.*, 2012, **84**, 5898–5904.

200 T. Špringer, M. L. Ermini, B. Špačková, J. Jabloňků and J. Homola, *Anal. Chem.*, 2014, **86**, 10350–10356.

201 M. J. Kwon, J. Lee, A. W. Wark and H. J. Lee, 2012, **84**, 1702−1707.

202 S. Mariani, S. Scarano, M. L. Ermini, M. Bonini and M. Minunni, *Chem. Commun.*, 2015, **51**, 6587–6590.

203 M. Hanauer, S. Pierrat, I. Zins, A. Lotz and C. Sönnichsen, *Nano Lett.*, 2007, **7**, 2881–2885.

204 P. C. Weber, D. H. Ohlendorf, J. J. Wendoloski and F. R. Salemme, *Science (80-.).*, 1989, **243**, 85–88.

205 L. Cedergren, R. Andersson, B. Nilsson, M. Uhlén and B. Jansson, *Protein Eng. Des. Sel.*, 1993, **6**, 441–448.

206 H. Vaisocherová, H. Šípová, I. Víšová, M. Bocková, T. Špringer, M. Laura Ermini, X. Song, Z. Krejčík, L. Chrastinová, O. Pastva, K.

Pimková, M. Dostálová Merkerová, J. E. Dyr and J. Homola, *Biosens. Bioelectron.*, 2015, **70**, 226–231.

207 G. Steiner, V. Sablinskas, A. Hübner, C. Kuhne and R. Salzer, *J. Mol. Struct.*, 1999, **509**, 265–273.

208 R. Rella, J. Spadavecchia, M. G. Manera, P. Siciliano, A. Santino and G. Mita, *Biosens. Bioelectron.*, 2004, **20**, 1140–1148.

209 T. R. Sosnick, P. A. Seeger, J. Trewhella, D. C. Benjamin and J. Novotny, *Biochemistry*, 1992, **31**, 1779–1786.

210 Q. Wang, R. Liu, X. Yang, K. Wang, J. Zhu, L. He and Q. Li, *Sensors Actuators, B Chem.*, 2016, **223**, 613–620.

211 Q. Wang, Q. Li, X. Yang, K. Wang, S. Du, H. Zhang and Y. Nie, *Biosens. Bioelectron.*, 2016, **77**, 1001–1007.

212 D. Zhang, Y. Yan, W. Cheng, W. Zhang, Y. Li, H. Ju and S. Ding, *Microchim. Acta*, 2013, **180**, 397–403.

213 R. Liu, Q. Wang, Q. Li, X. Yang, K. Wang and W. Nie, *Biosens. Bioelectron.*, 2017, **87**, 433–438.

214 W. J. Zhou, Y. Chen and R. M. Corn, *Anal. Chem.*, 2011, **83**, 3897–3902.

215 X. Ding, Y. Yan, S. Li, Y. Zhang, W. Cheng, Q. Cheng and S. Ding, *Anal. Chim. Acta*, 2015, **874**, 59–65.

216 X. Qiu, X. Liu, W. Zhang, H. Zhang, T. Jiang, D. Fan and Y. Luo, *Anal. Chem.*, 2015, **87**, 6303–6310.

217 N. Nasheri, J. Cheng, R. Singaravelu, P. Wu, M. T. McDermott and J. P. Pezacki, *Anal. Biochem.*, 2011, **412**, 165–172.

218 S. Qian, M. Lin, W. Ji, H. Yuan, Y. Zhang, Z. Jing, J. Zhao, J. F. Masson and W. Peng, *ACS Sensors*, 2018, **3**, 929–935.

219 L. M. Maestro, P. Haro-González, A. Sánchez-Iglesias, L. M. Liz-Marzán, J. García Solé and D. Jaque, *Langmuir*, 2014, **30**, 1650–8.

220 Y. Liu, M. Yang, J. Zhang, X. Zhi, C. Li, C. Zhang, F. Pan, K. Wang, Y. Yang, J. Martinez De La Fuentea and D. Cui, *ACS Nano*, 2016, **10**, 2375–2385.

221 L. Zou, H. Wang, B. He, L. Zeng, T. Tan, H. Cao, X. He, Z. Zhang,

S. Guo and Y. Li, *Theranostics*, 2016, **6**, 762–772.

222 Y. Huang, A. C. Chen and M. Hamblin, *SPIE Newsroom*, 2009, **9**, 1–3.

223 E. C. Dreaden, M. a Mackey, X. Huang, B. Kang and M. a El-Sayed, *Chem. Soc. Rev.*, 2011, **40**, 3391–404.

224 W. Shi, J. Casas, M. Venkataramasubramani and L. Tang, *ISRN Nanomater.*, 2012, **2012**, 659043.

225 P. del Pino, B. Pelaz, Q. Zhang, P. Maffre, G. U. Nienhaus and W. J. Parak, *Mater. Horiz.*, 2014, **1**, 301–313.

226 S. Hwang, J. Nam, S. Jung, J. Song, H. Doh and S. Kim, *Nanomedicine*, 2014, **9**, 2003–2022.

227 H. S. Leong, K. S. Butler, C. J. Brinker, M. Azzawi, S. Conlan, C. Dufès, A. Owen, S. Rannard, C. Scott, C. Chen, M. A. Dobrovolskaia, S. V. Kozlov, A. Prina-Mello, R. Schmid, P. Wick, F. Caputo, P. Boisseau, R. M. Crist, S. E. McNeil, B. Fadeel, L. Tran, S. F. Hansen, N. B. Hartmann, L. P. W. Clausen, L. M. Skjolding, A. Baun, M. Ågerstrand, Z. Gu, D. A. Lamprou, C. Hoskins, L. Huang, W. Song, H. Cao, X. Liu, K. D. Jandt, W. Jiang, B. Y. S. Kim, K. E. Wheeler, A. J. Chetwynd, I. Lynch, S. M. Moghimi, A. Nel, T. Xia, P. S. Weiss, B. Sarmento, J. das Neves, H. A. Santos, L. Santos, S. Mitragotri, S. Little, D. Peer, M. M. Amiji, M. J. Alonso, A. Petri-Fink, S. Balog, A. Lee, B. Drasler, B. Rothen-Rutishauser, S. Wilhelm, H. Acar, R. G. Harrison, C. Mao, P. Mukherjee, R. Ramesh, L. R. McNally, S. Busatto, J. Wolfram, P. Bergese, M. Ferrari, R. H. Fang, L. Zhang, J. Zheng, C. Peng, B. Du, M. Yu, D. M. Charron, G. Zheng and C. Pastore, *Nat. Nanotechnol.*, 2019, **14**, 902–902.

228 M. Faria, M. Björnmalm, K. J. Thurecht, S. J. Kent, R. G. Parton, M. Kavallaris, A. P. R. Johnston, J. J. Gooding, S. R. Corrie, B. J. Boyd, P. Thordarson, A. K. Whittaker, M. M. Stevens, C. A. Prestidge, C. J. H. Porter, W. J. Parak, T. P. Davis, E. J. Crampin and F. Caruso, *Nat. Nanotechnol.*, 2018, **13**, 777–785.

229 A. B. Taylor, A. M. Siddiquee and J. W. M. Chon, *ACS Nano*, 2014, **8**, 12071–12079.

230 H. N. Green, S. D. Crockett, W. E. Grizzle, E. L. Rosenthal and S.

B. Mirov, *Int. J. Nanomedicine*, 2014, **9**, 5093–5102.

231 J. Liu, C. Detrembleur, B. Grignard, M.-C. De Pauw-Gillet, S. Mornet, M. Treguer-Delapierre, Y. Petit, C. Jérôme, E. Duguet, C. W. V. Gmbh and C. Kgaa, *Chem. Asian J.*, 2014, **9**, 275–88.

232 E. Polo, P. del Pino, B. Pelaz, V. Grazu and J. M. de la Fuente, *Chem. Commun.*, 2013, **49**, 3676–8.

233 M. Hu, C. Novo, A. Funston, H. Wang, H. Staleva, S. Zou, P. Mulvaney, Y. Xia and G. V. Hartland, *J. Mater. Chem.*, 2008, **18**, 1949–1960.

234 X. Cheng, X. Tian, A. Wu, J. Li, J. Tian, Y. Chong, Z. Chai, Y. Zhao, C. Chen and C. Ge, *ACS Appl. Mater. Interfaces*, 2015, **7**, 20568–20575.

235 J. R. Melamed, R. S. Edelstein and E. S. Day, *ACS Nano*, 2015, **9**, 6–11.

236 L. Treuel, D. Docter, M. Maskos and R. H. Stauber, *Beilstein J. Nanotechnol.*, 2015, **6**, 857–873.

237 M. R. K. Ali, H. R. Ali, C. R. Rankin and M. A. El-Sayed, *Biomaterials*, 2016, **102**, 1–8.

238 L. Fan, Y. Zhang, F. Wang, Q. Yang, J. Tan, R. Grifantini, H. Wu, C. Song and B. Jin, *Biomaterials*, 2016, **76**, 399–407.

239 M. Barz, *Nanomedicine*, 2015, **10**, 3093–3097.

240 H. Yi, L.-Q. Wu, W. E. Bentley, R. Ghodssi, G. W. Rubloff, J. N. Culver and G. F. Payne, *Biomacromolecules*, 2005, **6**, 2881–2894.

241 R. Seyedebrahimi, S. Razavi and J. Varshosaz, *J. Clust. Sci.*, 2020, **31**, 99–108.

242 R. Kalaivani, M. Maruthupandy, T. Muneeswaran, M. Singh, S. Sureshkumar, M. Anand, C. M. Ramakritinan, F. Quero and A. K. Kumaraguru, *Int. J. Biol. Macromol.*, 2020, **146**, 560–568.

243 A. Diouf, M. Moufid, D. Bouyahya, L. Österlund, N. El Bari and B. Bouchikhi, *Mater. Sci. Eng. C*, 2020, **110**, 110665.

244 L. Pérez-álvarez, L. Ruiz-rubio and B. Artetxe, *Carbohydr. Polym.*, 2019, **213**, 159–167.

245 M. A. Rezvani and Z. N. Oghoulbeyk, *Appl. Organomet. Chem.*, 2019, **33**, e5241.

246 L. De Matteis, S. G. Mitchell and J. M. De La Fuente, *J. Mater. Chem. B*, 2014, **2**, 7114–7117.

247 T. M. M. Ways, W. M. Lau and V. V. Khutoryanskiy, *Polymers (Basel).*, 2018, **10**, 267.

248 L. De Matteis, S. G. Mitchell and J. M. de la Fuente, *J. Mater. Chem. B*, 2014, **2**, 7114–7117.

249 S. Rokka and P. Rantamäki, *Eur. Food Res. Technol.*, 2010, **231**, 1–12.

250 J. Chen, Q. Wang, C. M. Liu and J. Gong, *Crit. Rev. Food Sci. Nutr.*, 2017, **57**, 1228–1238.

251 K. Wazarkar, D. Patil, A. Rane, D. Balgude, M. Kathalewar and A. Sabnis, *RSC Adv.*, 2016, **6**, 106964–106979.

252 W. J. Duncanson, T. Lin, A. R. Abate, S. Seiffert, R. K. Shah and D. A. Weitz, *Lab Chip*, 2012, **12**, 2135–2145.

253 C. Berkland, K. Kim and D. W. Pack, *J. Control. Release*, 2001, **73**, 59–74.

254 S. Hauschild, U. Lipprandt, A. Rumplecker, U. Borchert, A. Rank, R. Schubert and S. Förster, *Small*, 2005, **1**, 1177–1180.

255 B. Derby, *Annu. Rev. Mater. Res.*, 2010, **40**, 395–414.

256 A. K. Anal and H. Singh, *Trends Food Sci. Technol.*, 2007, **18**, 240–251.

257 G. Orive, E. Santos, D. Poncelet, R. M. Hernández, J. L. Pedraz, L. U. Wahlberg, P. De Vos and D. Emerich, *Trends Pharmacol. Sci.*, 2015, **36**, 537–546.

258 A. M. Goodman, O. Neumann, K. Nørregaard, L. Henderson, M. R. Choi, S. E. Clare and N. J. Halas, *Proc. Natl. Acad. Sci. U. S. A.*, 2017, **114**, 12419–12424.

259 H. Yang, Y. Li, D. Wang, Y. Liu, W. Wei, Y. Zhang, S. Liu and P. Li, *Chem. Commun.*, 2019, **55**, 5994–5997.

260 N. A. Liechty, W. B., Kryscio, D.R., Slaughter, B. V. and Peppas,

Annu. Rev. Chem. Biomol. Eng., 2010, **1**, 149–173.

261 H. Kang, J. W. Lee and Y. Nam, *ACS Appl. Mater. Interfaces*, 2018, **10**, 6764–6771.

262 Á. Artiga, F. Ramos-sánchez, I. Serrano-sevilla, L. De Matteis, S. G. Mitchell, C. Sánchez-somolinos and J. M. De Fuente, *Part. Part. Syst. Charact.*, 2020, **37**, 2000026.

263 M. A. K. Abdelhalim, M. M. Mady and M. M. Ghannam, *Lipids Health Dis.*, 2011, **10**, 208.

264 J. Desbrières, C. Martinez and M. Rinaudo, *Int. J. Biol. Macromol.*, 1996, **19**, 21–28.

265 C. Leigh Herran, Y. Huang and W. Chai, *J. Micromechanics Microengineering*, 2012, **22**, 085025.

266 S. Sreekumar, F. M. Goycoolea, B. M. Moerschbacher and G. R. Rivera-Rodriguez, *Sci. Rep.*, 2018, **8**, 1–11.

267 S. I. Y. Diouf, D. J. Williams, S. Seifert, A. Londoño-calderon, M. T. Pettes, J. Sheehan and M. A. Firestone, *Polym. Chem.*, 2019, **10**, 6456–6472.

268 V. Sanz, J. Conde, Y. Hernández, P. V. Baptista, M. R. Ibarra and J. M. De La Fuente, *J. Nanoparticle Res.*, 2012, **14**, 917.

269 M. R. Marques, R. Loebenger and M. Almukainzi, *Dissolution Technol.*, 2011, **18**, 15–28.